

The development and study of self-assembling branched amphiphilic peptide bilayer coated iron
oxide and gold nanoparticles

by

Pavithra Natarajan

B.Sc., St. Xavier's College (Autonomous), University of Mumbai, 2014

AN ABSTRACT OF A DISSERTATION

submitted in partial fulfillment of the requirements for the degree

DOCTOR OF PHILOSOPHY

Department of Biochemistry and Molecular Biophysics
College of Arts and Sciences

KANSAS STATE UNIVERSITY
Manhattan, Kansas

2020

Abstract

The self-assembling branched amphiphilic peptides interdigitate to form water-filled bilayer delimited vesicles called BAPCs. The peptide bilayer is highly stable due to the inter and intramolecular hydrogen bonding, and the hydrophobic interactions, between peptides of the same and opposite leaflets. We substituted the water-filled core of BAPCs with electron dense iron oxide (BAPc-MNBs) and gold nanoparticles (BAP-AuNPs) by coupling the peptides to their surface. The controlled assembly of the peptides on the nanoparticles, verified by Förster resonance energy transfer assay, further provided experimental evidence that the peptides assemble as a bilayer membrane. The peptide bilayer coated metallic nanoparticles were developed to serve as tools to investigate the surface properties of the branched amphiphilic peptides and as entities that find application in bioanalysis, bioimaging and delivery. Therefore, the newly developed nanoparticles expand the applications of branched amphiphilic peptides beyond their current use as delivery systems. The magnetic property of BAPc-MNBs facilitate sorting and isolation of cells that internalize them and the molecules that bind to their surface. Colorimetric quantification assay used to determine the cellular uptake of BAPc-MNBs revealed that epithelial cells utilized multiple endocytic routes to internalize the nanoparticles. However, the water-filled BAPCs were endocytosed mainly via clathrin mediated and macropinocytic pathways. Hence, we could identify the similarities and differences between the cellular interactions of BAPCs with different core compositions and obtain a fundamental understanding of their cellular uptake routes. In vivo studies further demonstrated that BAPc-MNBs are good quantitative tools. They were widely distributed to different organs in C57BL/6 mice and showed difference in biodistribution between melanoma tumor bearing mice and mice without tumors. BAPc-MNBs are also being explored as probes to quantify the binding of nucleic acids to the

peptide bilayer. Thus, the newly developed peptide bilayer coated metallic nanoparticles show great potential as probes to study the surface binding properties of BAPCs and as entities that can be used for various applications.

The development and study of self-assembling branched amphiphilic peptide bilayer coated iron oxide and gold nanoparticles

by

Pavithra Natarajan

B.Sc., St. Xavier's College (Autonomous), University of Mumbai, 2014

A DISSERTATION

submitted in partial fulfillment of the requirements for the degree

DOCTOR OF PHILOSOPHY

Department of Biochemistry and Molecular Biophysics
College of Arts and Sciences

KANSAS STATE UNIVERSITY
Manhattan, Kansas

2020

Approved by:

Co-Major Professor
Sherry D. Fleming

Approved by:

Co-Major Professor (primary)
John M. Tomich

Copyright

© Pavithra Natarajan 2020.

.

Abstract

The self-assembling branched amphiphilic peptides interdigitate to form water-filled bilayer delimited vesicles called BAPCs. The peptide bilayer is highly stable due to the inter and intramolecular hydrogen bonding, and the hydrophobic interactions, between peptides of the same and opposite leaflets. We substituted the water-filled core of BAPCs with electron dense iron oxide (BAPc-MNBs) and gold nanoparticles (BAP-AuNPs) by coupling the peptides to their surface. The controlled assembly of the peptides on the nanoparticles, verified by Förster resonance energy transfer assay, further provided experimental evidence that the peptides assemble as a bilayer membrane. The peptide bilayer coated metallic nanoparticles were developed to serve as tools to investigate the surface properties of the branched amphiphilic peptides and as entities that find application in bioanalysis, bioimaging and delivery. Therefore, the newly developed nanoparticles expand the applications of branched amphiphilic peptides beyond their current use as delivery systems. The magnetic property of BAPc-MNBs facilitate sorting and isolation of cells that internalize them and the molecules that bind to their surface. Colorimetric quantification assay used to determine the cellular uptake of BAPc-MNBs revealed that epithelial cells utilized multiple endocytic routes to internalize the nanoparticles. However, the water-filled BAPCs were endocytosed mainly via clathrin mediated and macropinocytic pathways. Hence, we could identify the similarities and differences between the cellular interactions of BAPCs with different core compositions and obtain a fundamental understanding of their cellular uptake routes. In vivo studies further demonstrated that BAPc-MNBs are good quantitative tools. They were widely distributed to different organs in C57BL/6 mice and showed difference in biodistribution between melanoma tumor bearing mice and mice without tumors. BAPc-MNBs are also being explored as probes to quantify the binding of nucleic acids to the

peptide bilayer. Thus, the newly developed peptide bilayer coated metallic nanoparticles show great potential as probes to study the surface binding properties of BAPCs and as entities that can be used for various applications.

Table of Contents

List of Figures	xiii
List of Tables	xv
Acknowledgements	xvi
Dedication	xviii
Chapter 1 - Understanding the influence of experimental factors on bio-interactions of nanoparticles: Towards improving correlation between in vitro and in vivo studies.....	1
Introduction.....	1
Synthesis and functionalization of iron oxide and gold nanoparticles with biocompatible ligands.....	5
Biodegradable polymers and carbohydrates	6
Lipids and liposomes	7
Peptides and amino acids	8
Antibodies and proteins	10
Nucleic acids/ aptamers	11
Correlation and discrepancies between in vitro and in vivo studies.....	13
Nano-bio interactions in vitro	16
Influence of various experimental parameters	16
Cells and culturing techniques	16
Media composition and protein corona.....	18
Dosage and time.....	19
Influence of NPs with different surface compositions on cellular interactions	21
Toxicity of NPs and their effect on Reactive Oxygen Species (ROS) generation	21
Cellular uptake mechanism and pathways	26
Immune responses to NPs.....	30
Nano – biointeractions in vivo.....	33
Effect of route of administration on biodistribution of NPs	33
Systemic toxicity and immune response to NPs	38
Conclusion	42
References.....	42

Chapter 2 - Synthesis and characterization of multifunctional Branched Amphiphilic Peptide bilayer conjugated gold nanoparticles	61
Introduction.....	61
Materials and methods	65
Solid phase peptide synthesis.....	65
Synthesis of BAP-AuNPs using dodecanethiol capped gold nanoparticles.	65
Replacement of Trifluoroacetic Acetate (TFA-salt) peptide counter ion with chloride.	66
Synthesis of citrate capped gold nanoparticles.	67
Modification of citrate capped gold nanoparticles with peptide bilayer.....	67
Transmission Electron Microscopy (TEM) and Energy Dispersive X-ray (EDX).....	68
FRET experiment.....	69
CD spectroscopy measurements.	70
Thermo-Gravimetric Analysis (TGA).	70
Results and discussion	71
Generation of Branched Amphiphilic Peptide (BAP) bilayer on gold nanoparticles in toluene.....	71
Aqueous citrate capped gold nanoparticles synthesis – A green chemistry approach..	74
Branched amphiphilic peptide monolayer self-assembly on citrate capped gold nanoparticles.	76
Branched amphiphilic peptide bilayer formation on the surface of gold nanoparticles.	81
Determination of secondary structure of peptides bound to gold nanoparticles.....	90
Conclusion	92
References.....	92
Chapter 3 - A study of the cellular uptake of magnetic Branched Amphiphilic Peptide Capsules	97
Introduction.....	97
Materials and methods	100
Chemical reagents and cell lines.....	100
Synthesis of Branched Amphiphilic Peptide- Magnetic Nanobeads (BAPc-MNBs). 100	

Synthesis of water-filled Rhodamine labeled Branched Amphiphilic Peptide Capsules (Rh-BAPCs).....	102
Transmission Electron Microscopy (TEM).....	103
Dynamic light scattering (DLS) and zeta potential analysis.....	103
Uptake of BAPc-MNBs by IEC-18 and J774A.1.....	103
Quantification of BAPc-MNBs in cells by Ferene-s assay.....	106
Endocytosis inhibition study.....	107
BAPc-MNBs toxicity in IEC-18 cells.....	108
BAPc-MNBs toxicity in J774A.1 cells.....	108
Determination of Reactive Nitrogen Species (RNS)- Nitric oxide (NO) detection using Griess reagent.....	109
Determination of Reactive Oxygen Species (ROS) using DCF-DA.....	109
Prussian Blue staining of cells for visualization of magnetic nanobeads within cells.....	110
Results and discussion	111
Biophysical characterization of BAPc-MNBs	111
Uptake of BAPc-MNBs by rat ileum intestinal epithelial cells (IEC-18) and mouse macrophages (J774A.1) in vitro.....	114
Mechanism of uptake of BAPc-MNBs and Rh-BAPCs by IEC-18.....	117
Co-localization of magnetic nanobeads inside cells and their influence on cell viability and free radical generation.....	122
Conclusions.....	125
References.....	127
Chapter 4 - The biodistribution of BAPc-MNBs administered via different routes and their application in the delivery of an active peptide	133
Introduction.....	133
Materials and methods	135
Synthesis of D-p9 conjugated BAPc-MNBs and BAPCs.....	135
Determining conjugation of D-p9.....	136
In vivo tumors.....	136
Injection of nanoparticles (C57BL/6) and harvesting tissues.....	137
Treatment of mice with D-p9 conjugated BAPc-MNBs and BAPCs.....	138

Oral gavage in BALB/c	138
Intraperitoneal injection.	139
Quantification of magnetic nanoparticles in mouse tissue.	139
Results and discussion	140
Tissue distribution of magnetic nanoparticles in wild type C57BL/6 mice.	140
Tissue distribution in B16F10 melanoma tumor bearing C57BL/6 mice.	143
Tissue distribution in BALB/c mice treated with intraperitoneal injection of magnetic nanoparticles.	145
Tissue distribution in BALB/c mice administered magnetic nanoparticles orally.	147
Delivery and effect of D-p9 adducted BAPc-MNBs and BAPCs in tumor bearing mice.	148
Effect of BAPc-MNBs on the tumor microenvironment.	149
Conclusion	151
References.	152
Chapter 5 - Conclusions and future directions.	156
Future directions	157
Biocorona composition and impact on the pharmacokinetics and biodistribution.	157
Uptake and effect of BAPc-MNBs on primary cells.	158
Uptake and toxicity of BAP-AuNPs.	159
Conclusion	162
References.	163
Appendix A - Chapter 1	166
Copyrights permissions.	166
Supplementary data.	167
Appendix B - Chapter 2	168
Copyrights permissions.	168
Supplementary Data.	169
Appendix C - Chapter 3	172
Copyright Permission	172
Supplemental Data	173
Appendix D - Chapter 4.	179

Supplemental Data 179

List of Figures

Figure 1.1. Nanoparticle (NP) - bioconjugates	4
Figure 1.2. Experimental factors impacting in vitro studies	21
Figure 1.3. Localization of NPs in tissues and the physiological barriers to their uptake.....	37
Figure 1.4. Bio-interactions of nanoparticles.....	41
Figure 2.1. Characterization of dodecanethiol protected gold nanoparticles, surface modified with Branched Amphiphilic Peptides (BAPs)	74
Figure 2.2. Characterization of aqueous, citrate capped gold nanoparticles	76
Figure 2.3. Fluorescence response for different concentration of bis(Ac- F _{CN} LIVIGSII)-K-K ₄ -C- CONH ₂ peptide added to gold nanoparticle surface	78
Figure 2.4. TEM and UV-Vis spectral analysis of BAP monolayer adducted gold nanoparticles	80
Figure 2.5. TEM images and UV-Vis spectra of bis(Ac-FLIVIGSII)-K-K ₄ -CONH ₂ BAP bilayer adducted gold nanoparticles.....	83
Figure 2.6. Thermogravimetric Analysis (TGA) of gold nanoparticles modified with BAPs	85
Figure 2.7. Forster Resonance Energy Transfer (FRET) demonstrating formation of BAP bilayer on gold nanoparticles	88
Figure 2.8. Circular Dichroism spectra analysis of peptides bound to AuNPs.....	91
Figure 3.1. Biophysical characterization of BAPc-MNBs.....	112
Figure 3.2. Schematic representation of water-filled BAPCs and BAPc-MNBs	114
Figure 3.3. Uptake of BAPc-MNBs and magnetic nanobeads by IEC-18 and J774A.1 cell.....	116
Figure 3.4. Endocytosis inhibition assay to determine uptake mechanism of 50 nm BAPc-MNBs by IEC-18.....	119
Figure 3.5.. Endocytosis inhibition assay to determine mechanism of rhodamine labelled BAPCs uptake by IEC-18	121
Figure 3.6. Cell viability assay and reactive oxygen species (ROS) assay to determine toxicity of BAPc-MNBs to cells.....	123
Figure 3.7. Prussian blue staining for visualization of magnetic nanobeads in J774A.1. and IEC- 18 cells	125
Figure 4.1. Tissue distribution of magnetic nanoparticles in wild type C57BL/6 mice	143

Figure 4.2. Tissue distribution of magnetic nanoparticles in B16F10 melanoma tumor bearing mice.....	145
Figure 4.3. Tissue distribution of BAPc-MNBs injected i.p. in BALB/c mice.....	146
Figure 4.4. Tissue distribution of BAPc-MNBs administered orally to BALB/c mice.....	147
Figure 4.5. Delivery of D-p9 peptide using BAPc-MNBs and BAPCs as delivery systems.....	149
Figure 4.6. Effect of different treatments on the tumor microenvironment.....	151
Figure 5.1. Cellular uptake and distribution of BAP-AuNPs	161
Figure A.1. Copyrights to Chapter 1 from © Elsevier.....	166
Figure A.2. Interplay between various factors affecting the nano-bio interactions.....	167
Figure B.1. Copyrights to Chapter 2 from © American Chemical Society (ACS).....	168
Figure B.2. Schematic model for BAP-AuNP synthesis	169
Figure B.3. Dynamic Light Scattering (DLS) data and UV-Vis Spectra for BAP-AuNPs	169
Figure B.4. NMR data for removal of TFA salts from peptides.....	170
Figure B.5. MALDI-TOF mass spectra of peptides	171
Figure C.1. Copyright permission for Chapter 3 from © American Chemical Society (ACS).	172
Figure C.2. TEM images of aggregates of BAPc-MNBs	173
Figure C.3. Dynamic light scattering and zeta potential analysis of 50nm MNBs.....	173
Figure C.4. Efficiency of cell sorting using a magnetic separator.....	174
Figure C.5. Effect on cell viability after inhibitor treatment	175
Figure C.6. Effect of inhibitors on uptake of Rh-BAPCs in IEC-18 using flow cytometry analysis.....	175
Figure C.7. Summary of endocytosis inhibition data for BAPc-MNBs and Rh-BAPCs uptake, obtained using UV/Vis based quantification method and confocal imaging.....	176
Figure C.8. Brightfield images for endocytosis inhibition assay to determine mechanism of rhodamine labelled BAPCs uptake by IEC-18	177
Figure C.9. Nitric oxide species (NO) released by cells in response to magnetic nanoparticles.....	178
Figure D.1. Tissue distribution of D-p9 conjugated BAPc-MNBs in C57BL/6 mice.....	179
Figure D.2. Tumor growth curve in mice treated with different doses of BAPc-MNBs for 24 h and 48 h.....	179

List of Tables

Table 1.1. Applications of nanoparticles with different biocompatible surface ligands	12
Table 1.2. Summary of studies on effects of NPs in vitro ‘and’ in vivo	15
Table 1.3. Effect of nanoparticles on cellular toxicity and viability.....	25
Table 1.4. Endocytosis of Nanoparticles	29
Table 1.5. Immunogenicity of nanoparticles	32
Table 1.6. Biodistribution, systemic toxicity and immune response to nanoparticles in vivo	40
Table 3.1. Summary of treatments to determine uptake of BAPc-MNBs by IEC-18 and J774A.1 cells in DMEM 10% serum media and OptiMEM® 5% serum media	105
Table 3.2. Size and zeta potential data for BAPc-MNBs determined by dynamic light scattering and transmission electron microscopy	112
Table 4.1. Treatment of C57BL/6 mice with magnetic nanoparticles.....	138
Table 4.2. Treatment of tumor bearing C57BL/6 mice with D-p9	138
Table B.1. Summary of Gold Nanoparticle properties determined using DLS	170

Acknowledgements

First and foremost, I would like to thank my advisor, Prof. John M. Tomich, for his enormous support and guidance. I am grateful to him for giving me the opportunity and freedom to explore and pursue my ideas and for having trust in me. Over these years, as a mentor, he has taught me a lot of valuable lessons about science and beyond science, which has helped me grow and be independent. A big thank you to my co-advisor, mentor and collaborator, Prof. Sherry D. Fleming, for her immense support and guidance and for considering me as one of her lab members. She has been able to make me like immunology, which I thought was an impossible task, until now. She has always lent me a listening ear and a helping hand. The role played by my advisor and co-advisor in my overall development is immeasurable. I would like to thank all my committee members, Prof. Michal Zolkiweski, Prof. Lawrence Davis and Prof. Peking Fong, for guiding me, providing their insights and in positively influencing my doctoral journey. I thank Dr. Brian Lubbers, my external chairperson, for the help on the day of the defense.

The former and current members of the Tomich Lab - Susan Whitaker, Dr. Pinakin Sukthankar, Dr. Sheila Barros, Dr. Adriana Avila Flores, Benjamin Katz, Patrick Corn and all undergraduates who have directly or indirectly helped my research and made the lab a great place to be. Special thanks to Susan Whitaker for synthesizing peptides and helping me around the lab and with learning new techniques. I thank Jen Rowe, Haley Smalley and Miaomiao Wu from the Fleming Lab for all their help with the mice studies, cell cultures and for making me feel like one amongst them. I would like to acknowledge and thank the undergraduates, Joshua Lingo and Balthazar Martinez, who put in painstaking efforts into processing the mice tissue samples which helped in the fast progress of my research. Dr. Adriana Avila Flores and the Flores lab members at Auburn University- Jonathan Roberts and Nitish Kunte, were instrumental

in the development of and successful publication of my second research paper. I would like to acknowledge Dr. Wayne D. Hunter and Dr. Katherine Horak at USDA for collaborating with us and being a pleasure to work with. Thank you to every member of the Department of Biochemistry- professors, staff, graduate and undergraduate students, alike, who have influenced my journey in some way or the other. My colleagues/ co-graduate student friends who have been there to discuss science, to take a break from work and to help each other in any way possible.

My parents and sister although, thousands of miles away, have stood by me through thick and thin. They have always been encouraging of my pursuits and them being there for me, made this journey far easier. My parents and my grandmothers' lives have been a big inspiration which gave me the will power, courage and perseverance to come far away from home to Kansas, to pursue my dreams. Thank you to all my friends and well-wishers across the world. And a big thank you to my friends, Charu and Nadeem, who have been pillars of support away from home at Manhattan and the reason for me being sane.

Thank you to all the scientists and non-scientists in my life, the K-State family, the acquaintances and people whom I have never met or will meet, but have influenced my life, knowingly or unknowingly, making my journey as a graduate student beautiful and memorable.

Dedication

I dedicate this thesis to my Mom (Parvathy Natarajan), Dad (K.K. Natarajan), Sister (Namrata Natarajan) and my Grandmothers (Pattu Krishnan and Radha Natraj).

Chapter 1 - Understanding the influence of experimental factors on bio-interactions of nanoparticles: Towards improving correlation between in vitro and in vivo studies

This chapter has been reproduced with permission from - Natarajan, P.; & Tomich, J. M., Understanding the influence of experimental factors on bio-interactions of nanoparticles: Towards improving correlation between in vitro and in vivo studies Archives of Biochemistry and Biophysics 2020, 694, 108592. <https://doi.org/10.1016/j.abb.2020.108592>. © 2020 Elsevier

Introduction

The term nanotechnology was coined by Prof. Norio Taniguchi in 1974 and is defined as the science, engineering and technology conducted at the nanoscale i.e. 1 to 100 nm. The nanoscale materials generally referred to as nanoparticles (NPs) are highly desirable because of their small size, optical properties, high surface area to volume ratio and their multifunctional nature. Bionanotechnology comprises research at the interface of nanotechnology and biology² that has established a niche in biomedical sciences. Liposomes³⁻⁶, peptide-based⁷⁻⁹ and synthetic polymer-based¹⁰⁻¹², three-dimensional macromolecular assemblies and nanocages¹³⁻¹⁵ are examples of hollow/porous core NPs. Solid core NPs may be composed of inorganic metals such as iron oxide, gold, silver, platinum, silicon, quantum dots, titanium dioxide, gadolinium, selenium, copper oxide, zinc oxide or metallic hybrids, or organic carbon nanoparticles. The surfaces of inorganic NPs are generally modified with synthetic or naturally occurring polymers and/or monomers which may be of biological origin such as peptides, proteins, carbohydrates, lipids, DNA, RNA, PNA, aptamers, hybrid bio-synthetic molecules and others. These relatively flexible capping ligands improve the stability, biocompatibility and functionalize the NPs for

various applications or for further modifications. **Figure 1.1** depicts the various components and configurations of nanoparticle-bioconjugates.

Drugs that have poor pharmacodynamics can be delivered using NPs that may overcome these shortcomings by improving their half-lives, stabilities and bioavailabilities.¹⁷ However, their use is not limited to drug delivery systems (DDS). Their other applications include use as optical imaging agents and analytical probes/biosensors, thus making them suitable theranostics agents.¹⁸⁻²¹ Fifty-one nanomedicines have been approved since 1995 by FDA for clinical use with ~77 products in clinical trials as of 2016.²² Owing to their potential, nanomaterials are being utilized in the recent fight against SARS-CoV-2.^{23, 24} Gold nanoparticles based immunoassays have been developed that enable rapid detection of SARS-CoV-2 infected asymptomatic patients or individuals showing mild symptoms.^{25, 26} An mRNA vaccine which went into Phase 1 clinical trial in March 2020, codes for the prefusion stabilized spike protein of SARS-Cov-2 and it is encapsulated in lipid nanoparticles which serve as effective delivery agents.²⁷

The focus of this review is on gold and iron oxide NPs which are the top 2 inorganic NPs in clinical trials (**Figure 1.1D**). Iron oxide NPs are the only metal-containing NPs that have received approval to date for clinical use and most of them are MRI contrast agents.²² Gold nanoparticles (AuNPs) exhibit plasmon resonance which can be followed using UV-Vis spectrophotometric detection assays^{28, 29}, surface-enhanced Raman spectroscopy (SERS)³⁰ and confocal/ luminescence microscopy.^{31, 32} The magnetic iron oxide nanoparticles (FeONPs), also commonly called superparamagnetic iron oxide nanoparticles (SPIONs) are used as contrast agents for magnetic resonance imaging (MRI),^{33, 34} for bio-detection such as tracking the implanted stem cells in vitro³⁵, in binding assays and hyperthermia^{36, 37} and magnetic field guided drug delivery²¹ in cancer treatment. Besides, the electron dense gold and iron NPs are

used widely in electron microscopy analyses. Au-Magnetite composites used in (SERS) analyses improve the intracellular signal intensity essential to studying interactions of NPs with biomolecules.³⁰

Delivery systems must be non-toxic by themselves, should not be cleared quickly from the body and trigger adverse immunological responses. It, therefore, becomes vital to understand their interactions at a molecular level, to determine how suitable they are for delivery and determine the applications for which they are best suited. The review is divided into four sections which discuss the (I) synthesis and functionalizing of NPs, (II) the discrepancies observed between the effects of NPs *in vitro* and *in vivo*, followed by a detailed review of (III) *in vitro* and (IV) *in vivo* studies of gold and iron oxide NPs, which demonstrate the need to carefully consider experimental factors to improve the correlation between *in vitro* and *in vivo* studies. This review also presents recent *in vitro* and *in vivo* studies that assess the biosafety/toxicity of NPs and the influence of surface ligands on nano-bio interactions such as uptake and immune response. We will emphasize the importance of standardization in nanotechnology with a focus on the experimental parameters since they have a significant impact on the outcome of studies. Standardization is essential to make valid comparisons between studies and to prevent redundancy in research which help develop the field of nanomedicine.^{38, 39}

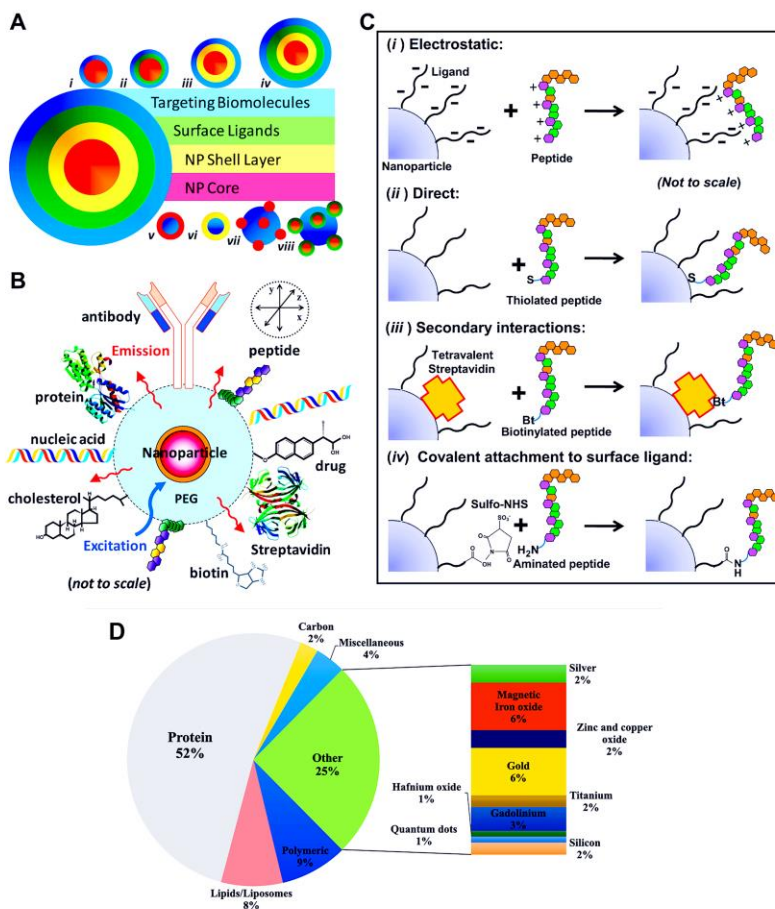


Figure 1.1. Nanoparticle (NP) - bioconjugates

(A) A nano-bioconjugate can be composed of varied components of fundamentally different origin. This figure presents these components and their configurations: (i) Biomolecule interacting with NP core, (ii) biomolecule interacting with a NP core via intermediate ligands, (iii) biomolecule interacting with NP shell layer that surrounds the NP core, (iv) biomolecule interacting with NP shell layer/NP core via intermediate ligands, (v) porous NP core containing entrapped biomolecules, (vi) porous or hollow NP core containing entrapped biomolecules surrounded by a NP shell layer, (vii) NP core (or NP core/NP shell structures) particles smaller in size than the much larger biomolecule, (viii) NP core (or NP core/NP shell structures) particles smaller in size than the much larger biomolecule attached via intermediate ligands. (B) A representative NP decorated with multiple functional molecules (e.g., nucleic acids, proteins, drugs, peptides). NPs have great potential since they can provide multiple functions in one active platform. (C) The four general schemes routinely used for the conjugation of peptides to NP materials. These schemes are also representative of the type of interactions involved in the binding of biomolecules in general to NPs. (D) Distribution of types of nanoparticles in clinical trials, explored for use as nanomedicines. Data was obtained in April 2020, from clinicaltrials.gov using the search term ‘nanoparticles’. This distribution is representative of active clinical trial studies using nanoparticles as drug delivery systems or imaging agents. Inorganic/metallic NPs in trial have been further categorized based upon their composition.

Adapted with permission from Sapsford, K. E et al.¹ Analyzing nanomaterial bioconjugates: a review of current and emerging purification and characterization techniques. *Anal Chem* 2011, 83 (12), 4453-88. Copyright (2020) American Chemical Society. Permission for part of the figure obtained from IOP publishing, Aubin-Tam et al.¹⁶. Structure and function of nanoparticle-protein conjugates. *Biomedical Materials*, 3(3). © IOP Publishing. Reproduced with permission. All rights reserved

Synthesis and functionalization of iron oxide and gold nanoparticles with biocompatible ligands

The basic principle of NPs syntheses is to promote nucleation of the monomeric element (e.g. lipids for liposomes and metal ions for inorganic metal NPs), facilitating their assembly in a controlled manner to form stable and well-structured entities with narrow size distributions. Multiple routes and techniques used in NP syntheses have been established that are broadly categorized as chemical, physical and biological. Most chemical and biological methods use facile synthesis techniques that are easily controlled and reproducible, yet low in cost and scalable.⁴⁰ Functionalization of NPs has proved essential as they affect stability in the presence of salts and prevent aggregation over time, thereby increasing their shelf-life. They may also have other purposes including- promoting cellular uptake, co-functionalization to promote the delivery of drugs and nucleic acids, use in biochemical assays serving as binding partners, and provide additional functionalities to the delivery system. There are a wide range of biocompatible molecules used to functionalize the NPs for use in nanomedicine which have been divided into 5 major categories in this review. (**Table 1.1**) The surface composition of NPs is an important factor influencing their overall behavior. Understanding their surface chemistry is therefore essential.

The synthesis method determines how the assembled surface can be further modified with desired molecules for downstream applications. One step syntheses involve the use of functionalizing molecules that serve as both, nucleation and capping agents.⁴¹⁻⁴³ Widely used Turkevich⁴¹ and Brust-Schiffrin⁴⁴ methods for AuNP synthesis contain reducing citrate molecules⁴² and hydrophobic thiol ligands such as dodecanethiol⁴⁵, respectively, in the synthesis mixture which act as nucleation and capping agents. Magnetic iron oxide nanoparticles are

commonly synthesized in the presence of surfactants/ synthetic polymers such as dextran⁴³, polyvinyl alcohol⁴⁶ or as naked iron oxide nanoparticle with cationic ions bound to the surface.⁴⁷

Ligand exchange by direct substitution of surface ligands is one of the commonly used method for functionalizing NPs.⁴⁸ AuNPs form gold-thiol bonds facilitating exchange of smaller ligands such as citrate molecules with larger molecules by direct binding of ligands to NPs via Au-S bond formation (**Figure 1.1C**).^{42, 49} Naked FeONPs have a higher tendency of aggregating due to their magnetic property and are therefore stabilized by suitable surface ligands such as polymers or cross-linking molecules.⁴⁰ These NPs can be further derivatized using ligands as linkers or binding moieties that facilitate electrostatic or covalent binding of molecules. For example, nucleic acids electrostatically bind to cationic surfaces or modified polyethylene glycol (PEG-SH) which covalently binds other thiol containing molecules.¹⁹ Further, NPs can be encapsulated within liposomes which are spherical vesicles composed of amphiphilic lipids, thus imparting added functionalities to both the liposomes and the NPs.³⁻⁵

The review by Sapsford et al.² provides details about the types of surface ligands, the functionalizing chemistries and the nano-bio interfaces for different types of NPs. However, this review, does not provide adequate information on the chemistries, syntheses and characterizations of functionalized NPs. We will discuss the functionalization of NPs with biocompatible molecules in the following section.

Biodegradable polymers and carbohydrates

Synthetic polymers such as poly(glycolic acid) (PGA), poly(lactic acid) (PLA), dextran, poly(lactic-co-glycolic acid) (PLGA), polyethylene glycol (PEG), polyethyleneimine (PEI) and polyvinyl alcohol (PVA) and natural polymers with modified carbohydrate/polysaccharide

building blocks (e.g. chitosan) are used widely.⁵⁰ Mono- and oligo-saccharides such as glucose, deoxy-D-glucose, rhamnose, maltose, and lactose, are also used as capping ligands for AuNPs and FeONPs.^{37, 51, 52} General synthesis strategies involve direct synthesis of the nanoparticles in the presence of the polymers⁵³, co-precipitation of the preformed nanoparticles with polymers in an appropriate solvent⁵⁴ and grafting to/ligand stabilization technique that involves coating nanoparticles via functional groups such as thiol and amine groups to gold nanoparticles surface.⁵⁵

Biodegradable polymers are widely used as surface coatings, as they are easy to synthesize, widely studied, allow for precise chemical binding of molecules or can be modified with functional groups to bind other molecules using facile chemistries like EDC-NHS⁵⁶ and disulfide conjugations¹⁹. They have been recognized to increase the circulation time of the nanoparticles by preventing opsonization by phagocytes in vivo. Therefore, a wide range of FDA-approved nanoparticles and in vivo devices are coated with one or more of the above-mentioned polymers.⁵⁷ A recent report also suggests that PEG-like polymers may not be as inert as currently believed. Their oxidative degradation in vivo can lead to detrimental effects on the cell membrane and affect signal transduction pathways.⁵⁸ Therefore, recent emphasis has been on the use of natural or synthetic biocompatible surface coatings which display minimal adverse effects.

Lipids and liposomes

Lipid amphiphiles comprised of one acyl chain generally form micelles while those with two acyl chains assemble into bilayer-like membrane vesicles called liposomes. Commonly, lipid formulations yield self-assembled structures that are greater than 100 nm. The first liposomal

formulation to be approved by the FDA was Doxil in 1995, subsequently⁹ additional liposomal formulations with active ingredients (AIs) have been approved.⁵⁹ Single chained lipid amphiphiles such as lysophosphatidylcholine and two-chained DOPC, POPC⁶⁰, as well as cholesterol and/or their mixtures have been incorporated into liposomes³, polymeric liposomes⁶ (polymer modified lipid components) and to functionalize inorganic core NPs.

A reverse phase evaporation method that involves exchanging the existing surface ligands with lipids in an organic solvent followed by transfer to an aqueous solvent, is commonly used for lipid membrane assembly on NPs. This technique has been employed in the synthesis of hybrid lipid bilayer coatings on NPs where inner and outer layer have different compositions.^{6, 60} Another common technique involves adsorption of liposomes⁴, on the NPs where the charged head moieties interact with the surface and encapsulate the NPs within liposomes.⁵ However, lipid membranes often have low stability in solution due to fusion, leading to increases in the particle size.⁶¹ This can be remedied by increasing the surface charges that promote repulsion between particles or by incorporating spacers such as PEG that sterically hinder particle association. These methods improve colloidal stability.

Peptides and amino acids

There are innumerable synthetic and naturally occurring peptides composed of different permutations and combinations of amino acids that have been used to coat NPs. In addition to the 20 amino acids encoded by the universal genetic code, other commercially available unique amino acids have been utilized. Depending on the chosen amino acids different functional and structural properties have been observed. With their chemically addressable functional groups, they are easily modified or adducted and they also allow for stoichiometric control of attached

targeting/therapeutic molecules for in vivo delivery. Ligand-exchange, direct binding and assembly and covalent binding to functional moieties are the synthesis approaches commonly utilized to functionalize NPs with peptides (**Figure 1.1C**). Although amines bind to the gold surfaces, the strength of Au-N (~4 kJ/mol) bond is much weaker than the Au-thiol bond (137 kJ/mol) that is commonly used to bind cysteine containing peptides under appropriate conditions.^{49, 55, 62}

Cell penetrating peptides like HIV-1 derived TAT peptide⁶³ promote the uptake of molecules or complexes that cannot penetrate the cell membrane efficiently by themselves. They are therefore used to co-functionalize the surface of nanoparticles and are widely explored for delivery of nanoparticles in radiation therapy⁶³, chemotherapy⁶⁴, cancer theranostics⁶⁵ and other targeted therapies.^{66, 67} Another class of peptides called self-assembling peptides generally consist of amphiphiles that can assemble on the surface of the nanoparticles to form a membrane called self-assembling monolayers (SAMs) similar to lipids. A library of the self-assembling peptides developed by Chee et al. have phosphate groups that promote binding with iron oxide nanoparticles.⁶⁸ and have been demonstrated to form stable monolayers on their surface. The self-assembling branched amphiphilic peptides (BAPs)^{69, 70} form water-filled, bilayer delimited cationic vesicles called BAPCs, like liposomes, and have also been conjugated to AuNPs and FeONPs.⁴⁹ These NPs with the peptide bilayer mimic the vesicles and also possess the inherent properties of iron oxide and gold NPs such as electron dense core, magnetism and plasmon resonance, thus making them useful probes for imaging and to study their nano-bio interactions.⁷¹

Antibodies and proteins

Specific proteins can be used to functionalize NPs for targeted delivery or to serve as binding partners in assays. Abraxane® is an FDA-approved chemotherapeutic drug that consists of nanoparticle albumin bound (nab)-paclitaxel. Albumin is an abundant serum protein used as surface coating for NPs as it improves bioavailability, has low immunogenicity and good biocompatibility.^{72, 73} Nab-paclitaxel and its variations comprise a major percentage of the protein-based nanomedicines in clinical trials (**Figure 1.1D**). This success has fostered the use of albumin as a surface coating for additional NPs delivery systems.⁷⁴⁻⁷⁶

Antibodies/immunoglobulins are widely used due to their high specificity in detecting and binding to specific antigens and have been successfully employed for disease treatments as antibody drug conjugates (ADCs), four of which are commercially available.⁷⁷ Since protein structure defines function, any structural alterations due to temperature transitions or pH, limit the chemistries available for attachment to NPs. General strategies for binding antibodies and proteins to inorganic surfaces therefore include covalent binding to a modified surface^{78, 79, 80} or by physical adsorption promoted by electrostatic interactions.⁷⁹ The orientation of the antibody is more important for its functioning than its coverage on the surface and hence orienting covalent binding strategies are more widely employed.⁷⁹

Finetti et al.⁸⁰ used “click” chemistry to immobilize anti CD-63 and anti-rabbit-IgG on the surface of AuNPs. Thus, using the benefits of click chemistry, antibodies immobilized NPs can be produced for a wide range of applications. Antibody immobilized AuNPs are also widely used in immunostaining for analysis using electron microscopy, and plasmon resonance mediated confocal imaging.^{31, 81, 82} Antibodies tagged with fluorescence molecule on AuNPs allows for dual imaging, reducing cost and time.

Nucleic acids/ aptamers

NPs are commonly coated with nucleic acids such as DNA, dsRNA, ssRNA, siRNA, mRNA, and microRNA, as they facilitate the delivery of the nucleic acids into cells or for use in binding assays. DNA grafted polymers such as poly (acrylic acid) embedded DNA are also used for functionalizing nanoparticles as they facilitate polyvalent DNA nanostructure formation.⁸³ A common strategy for functionalizing NPs with nucleic acids is to utilize the electrostatic interactions between the negatively charged nucleic acids and cationic NPs which mediates their adsorption to NPs.^{84, 85} This does not require extensive modification of the nucleic acids.⁸⁶ Recently nucleic acids have also been identified as templates that control and facilitate inorganic NPs synthesis.⁸⁷ Aptamers that bind with high affinity and specificity to proteins and peptides are commonly conjugated to AuNPs and FeONPs for detection of molecules using colorimetric binding assays^{88, 89} and magnetic isolation⁹⁰, respectively.

Table 1.1 summarizes the varied biomedical applications of FeONPs and AuNPs with the different biocompatible ligands discussed here.

Table 1.1. Applications of nanoparticles with different biocompatible surface ligands

Category of functionalizing molecules	Nanoparticles & Functionalizing molecules	Applications	References
Polymers & carbohydrates	FeONPs + PEG variations (NHS-PEG-SH, PEG-SH)	Magnet guided delivery, MRI, Probes for cancer imaging	Lee et al. ¹⁹ , Xu et al. ⁵⁶ , Gao et al. ⁵⁵
	AuNPs + 2-deoxyglucose	Theranostics	Suvarna et al. ⁵²
Lipids & Liposomes	AuNPs + Soybean lecithin, cholesterol liposome	Photothermal treatment	Xing et al. ³
	AgNPs/AuNPs + POPC, POPG, Cholesterol lipid bilayer	SERS probe	Bhowmik et al. ⁴
	AuNPs + DC-Chol, DOPE, Chol FeONPs + OQLCS polymeric liposomes	siRNA delivery MRI	Kong et al. ⁵ Liao et al. ⁶
Peptides	FeONPs + TAT CPP	ROS induced radiation, Dox-delivery	Hauser et al. ⁶³ , Morshed et al. ⁶⁴
	FeONPs + H625-CPP	MRI, Far red imaging, hyperthermia, drug delivery	Perillo et al. ⁶⁵
	AuNPs + Penetratin peptide	Photothermal, NIR	Yin et al. ⁶⁷
	AuNPs, FeONPs + BAPs	CT, confocal imaging, probes for molecular interactions, cell sorting and quantification	Natarajan et al. ^{49, 71}
Proteins & Antibodies	AuNPs + albumin variants (BSA, albumin, Nab-paclitaxel)	photothermal chemotherapy, anticancer drug delivery	Nosrati et al. ⁷³ , Ruttala et al. ⁷⁵ , Vismara et al. ⁷⁶
	FeONPs + Anti-Her2, ScFvEGFR	Targeted MRI	Chen et al. ⁷⁸
Nucleic acids	PEI-siRNA	siRNA delivery	Wang et al. ⁸⁵
	AuNPs + Aptamers	LSPR mediated colorimetric detection	Lia et al. ⁸⁸ , Huang et al. ⁸⁹
	FeONPs + Aptamers	Detection of biological molecules	Fernandez et al. ⁹⁰

POPC, 1-palmitoyl-2-oleoyl-sn-glycero-3-phosphocholine; POPG, 1-palmitoyl-2-oleoyl-sn-glycero-3-phosphoglycerol; DOPE, Dioleoylphosphatidylethanolamine; OQLCS, octadecyl-quaternized lysine modified chitosan; TAT, Transactivator of transcription; CPP, Cell penetrating peptide; ScFvEGFR, short chain variable, anti-EFGR

Correlation and discrepancies between in vitro and in vivo studies

In vitro studies are often indicators of potential outcomes in animal studies and provide mechanistic information at the cellular level. They allow researchers to explore the effect of different doses, chemicals at relatively lower cost and reduced time. They also allow for probing the underlying mechanisms leading to toxicity, immunogenicity, metabolic changes and analyzing gene expression profiles. These cell culture studies reduce the number and cost of animals required to statistically assess the effect of NPs.⁹¹ NPs on the other hand encounter a very complex environment in vivo which cannot be mimicked accurately in vitro. And therefore, there are obvious discrepancies due to these inherent differences between in vitro and in vivo environments. Khlebtsov et al.⁹² have examined the lack of correlation between in vitro and in vivo behavior of NPs. They emphasize on the need for systematization of data obtained from various studies on NPs, to gain a fundamental understanding of factors affecting their bio-interactions.

The inconsistencies observed between their effects in vitro and in vivo is also due to differences in experimental factors.⁹³⁻⁹⁷ For example, one basic consideration is to use the cell lines/ primary cell types for in vitro studies that belong to the same species that is being investigated in vivo. Surprisingly, this is overlooked often.^{93, 94, 96} Zhang et al.⁹⁸ observed inconsistencies where PEG-AuNPs were cleared quickly from circulation in mice even though in vitro studies demonstrated their reduced uptake by RAW 264.7 mouse macrophages. Review of literature available suggests that there are two main reasons for the discrepancies observed – (i) lack of fundamental understanding of the effect of NP's properties on biointeractions and (ii) lack of standardization / differences in experimental parameters.⁹² Therefore, one must take caution before extrapolating in vitro results to the NPs behavior in vivo. This review focusses on

understanding the impact of the experimental factors to aid in setting standards for assessing NPs and thus, help in improving the positive correlation between in vitro and in vivo studies as well as to make fair comparison between studies.

There are hundreds of reports on the toxicity of NPs in vitro ‘or’ in vivo but very few recent studies have compared their effects in vitro ‘and’ in vivo. **Table 1.2** summarizes the studies belonging to latter group.

Table 1.2. Summary of studies on effects of NPs in vitro ‘and’ in vivo

NPs	Surface coating	Cells	Animal model & strain	Route of administration	Conclusion	Ref
AuNPs	Citrate	HepG2 HT29	Wistar rats	Intraperitoneal (i.p.)	No effect was observed on cytokines secretion & other serum contents in vivo but damage to genetic material by smaller NPs, observed in vitro	Lopez-Chaves et al. ⁹³
IONPs	PEI & PEG	RAW264.7 SKOV-3	BALB/c	Intravenous (i.v.)	PEI-IONPs >> toxic to cells in vitro & ↑↑ toxicity in vivo causing death of mice at specific dosage Size & surface functionalization have a huge impact on the cellular uptake, toxicity, tissue distribution & clearance in vivo	Feng et al. ⁹⁹
AuNPs & Nanorods	Polyallylamine hydrochloride (PAH)	C3H fibroblasts HTC	Wistar rats	Oral	Some adverse effect on liver cells in vitro & oxidative stress and inflammation in vivo. No major adverse effects observed in vivo	Bernardi et al. ⁹⁶
AuNPs	PEG	RAW264.7	Swiss mice	i.v.	Dramatically lower uptake of NPs in vitro but fast clearance of NPs in vivo. No correlation between in vitro and in vivo data	Zhang et al. ⁹⁸

Nano-bio interactions in vitro

Recent reviews by Foroozandeh et al.¹⁰⁰ and Behzadi et al.¹⁰¹ discussed the effect of nanoparticle physicochemical properties such as size, shape, surface composition on their uptake and intracellular trafficking. Unfortunately, few articles discuss the effect of experimental parameters on cellular uptake. In the following section the importance of carefully selecting cell lines, determining effect of dosage, time and media type in understanding NP interactions will be discussed. We also review recent studies that explore cellular uptake routes, immune responses and toxicity induced by AuNPs and FeONPs with different surface compositions.

Influence of various experimental parameters

Cells and culturing techniques

Cell lines used to study NPs are commonly selected based on availability; they should be chosen based on the applications of NPs and the expected in vivo exposure.¹⁰² Several studies have shown that nanoparticle uptake and toxicity profiles vary between cell lines, cell sub-types and to some extent between species.¹⁰²⁻¹⁰⁶ The uptake of NPs is also dependent on cell-specific functions.¹⁰⁷

Although immortalized cell lines are easier to maintain, readily accessible and widely studied, they differ from cells in vivo due to repeated in vitro manipulations and the initial immortalization itself.¹⁰² Joris et al.¹⁰² observed that mouse and human neural stem cells clearly showed a more pronounced effect of exposure to FeONPs in terms of toxicity, mitochondrial activity, calcium homeostasis and ROS generation in comparison to neural progenitor and cancer cell lines. The phenotype expressed by cell lines and the processing of NPs differed dramatically from primary cells of similar origin. Therefore, studies in cell lines cannot be considered a final

endpoint. No one cell line will emerge as a universal one but, by testing nano-safety in multiple cell types, one increases the power of prediction for in vitro utility and safety.

The reported cell lines have been classified according to cell culture methods-- as traditional or non-traditional. Non-traditional cell culturing methods such as 3D cell cultures¹⁰³, transwell membrane set-up¹⁰⁸ and sandwich cultured cells⁹¹ are being actively used to better mimic in vivo conditions.¹⁰⁹ Larger NPs which are usually heavier, have a propensity to sediment over time and in a 2D cell culture set up this influences the uptake of NPs to a great extent.^{103, 107, 108} Bancos et al.¹⁰⁸ used a transwell membrane set up for the RAW 264.7 cell line, to study the uptake of 10 nm citrate capped AuNPs and compare it with their uptake in a 2D cell culture and in cell suspension. There was an obvious effect of sedimentation of NPs on the cellular uptake. The cells in the transwell set-up which encountered NPs suspended in media only, incorporated the least number of AuNPs compared to their 2D counterpart and cells in suspension which internalized the highest number of NPs by 24 h. Besides, a transwell set-up facilitates co-culturing of multiple cell types simultaneously, to evaluate the effect of NPs treatment on the crosstalk between the cell types or to study transcytosis.¹¹⁰⁻¹¹²

Three-D cell cultures that make use of a scaffold increase the surface area of exposure, while only ~50% area is available in a 2D cell culture. The MD1-MB231 breast cancer cells in 2D culture, in comparison to their 3D counterpart, had increased viability and showed a lesser change in the cytoplasmic actin network that plays a major role in intracellular processes.¹⁰³ Thus, the toxicity of the NPs could be underestimated by testing their effect in just 2D cell cultures and immortalized cell lines. In vivo, NPs and drugs have a tendency to accumulate in the liver generally, which clears foreign materials and thus, the liver is an important tissue to consider for studying NPs. The sandwich hepatocyte culture model uses primary hepatocytes,

grown between two layers of collagen that keeps them competent and polarized with functional bile networks and helps to assess the hepatotoxicity of drugs and NPs accurately.¹¹³ While 3-D cultures mimic the in vivo environment more closely not all labs have transitioned to this approach. Traditional 2D cultures still predominate in the current literature.

Media composition and protein corona

Cell culture media composition varies depending upon the requirements of each cell line. Examples of two commonly used cell culture media are Dulbecco's Modified Eagle Medium (DMEM) and Roswell Park Memorial Institute Medium (RPMI), which vary from the human and mouse plasma in glucose and ion concentrations.¹¹⁴ Sodium, calcium, bicarbonate, chloride, sulfate and glucose are at significantly higher concentrations in DMEM in comparison to RPMI. Media composition plays a crucial role since the NPs interact with and bind the various medium components including fetal bovine serum (FBS) proteins that help to maintain normal growth and proliferation of cells. The formation of this surface coating, called the biocorona, is dependent upon the physicochemical properties of the NPs and affects their uptake. The protein components of the biocorona have been widely explored but other components such as lipids, nucleotides and ions, are poorly characterized.¹¹⁵ Biodistribution of NPs in vivo is also affected by the biocorona. With the different compositions of serum in vivo and cell culture medium, there will be differences observed in the uptake of NPs.^{97, 116}

Maiorano et al.¹⁰⁴ studied the biophysical characteristics of 15 nm - 80 nm citrate-AuNPs in DMEM and RPMI supplemented with 10% FBS. AuNPs in RPMI showed an abrupt increase in diameter, due to formation of protein corona in 1 h of incubation after which it remained constant up to 100 h. AuNPs in DMEM showed a gradual increase in diameter to 200 nm and

then plateaued since the protein corona volume was independent of AuNP size, unlike NPs in RPMI. RPMI increased the interparticle interactions while AuNPs in DMEM were more stable due to the large protein corona which reduces interparticle interactions. Gunnarsson et al.²⁸ observed a similar effect where AuNPs pre-exposed to protein poor medium had a higher tendency to aggregate than in protein rich medium. Interestingly, 15 nm AuNPs exerted more adverse effects on cells in RPMI in comparison to DMEM. Hence, while designing and implementing studies, we should consider the choice of cell culture media which is crucial.¹¹⁷

Another non-trivial factor to be considered is the method by which NPs are administered as documented by Moore et al.¹⁰⁷ When poly(vinylpyrrolidone) (PVP) coated AuNPs were administered as a concentrated bolus directly to J774A.1 mouse macrophages, the protein corona formation was 2-fold higher than AuNPs pre-mixed with media. The macrophages also phagocytosed more AuNPs administered as a concentrated dose in comparison to the pre-mixed AuNPs. This study emphasizes how a minor detail such as the initial administration of NPs can affect the outcome of the study. Thus, to be able to compare studies between research groups, we should consider every minor detail and develop a robust analytical method. Due to a lack of standardized/universal methods of testing NPs, it is difficult to compare and obtain a better understanding of NPs bio-interactions.

Dosage and time

The effect of NP concentration and incubation times on cells is difficult to determine based on the many published protocols. Most studies used NPs in the nM to μ M range²⁸ and tested their effect using a single dosage over 24 to 72 h. Time can be a limiting factor since cells overgrow and lose viability over time. Cells in vivo encounter NPs not as a single high dose but

at diluted concentrations for a longer period of time. This can lead to higher cumulative doses. FeONPs bound anticancer agents are being explored to achieve selective accumulation of these agents in tumor which might require them to be administered in multiple doses. Thus, it involves repeated exposure over long periods to the NPs. For example, chemotherapeutic agents like doxorubicin are administered at 60-75 mg/m² dose at regular intervals of 21 days.^{21, 33-35, 91} Hence, more studies are needed to assess the effect of repeated exposure to NPs at prescribed intervals.⁹¹

Gokduman et al.⁹¹ studied the effect of single or cumulative dose of varying concentrations of SPIONs on hepatocytes over a period of 7 days. Although no significant difference was observed between LD₅₀ for the single or cumulative doses, loss of hepatocyte functions was observed after 48 h in the cumulative treatment. Similarly, Lotsch et al.¹¹⁸ used 0.1 nM of AuNPs to mimic unintended environmental exposure and assessed the effects of acute versus chronic exposure (up to 2 weeks) to AuNPs on human dermal fibroblasts (HDF) at a genetic level. Proliferation and viability of HDF cells remained unaffected over 14 days but acute exposure to PEG-AuNPs nanorods induced a measurable difference in the gene expression, while the cells developed an adaptive response to the chronic exposure. Exposure levels can vary greatly between clinical applications and environmental exposures. Thus, the type of dosage (acute vs chronic), the level and time of exposure to NPs should not set arbitrarily but by a selective process, keeping the future applications of NPs under consideration, to make a fair and relevant comparison between in vitro and in vivo studies.

Xu et al.¹¹⁹ conducted a hierarchical cluster analysis of a library of 21 gold nanoparticles with different physicochemical properties. Unlike experimental studies which demonstrated a strong correlation between individual physicochemical properties and biological effect, the

correlation analysis suggested that no such conclusion could be drawn. Rather the crosstalk between various physicochemical factors governs the bio-interactions of NPs. Thus, different experimental factors (**Figure 1.2**) and a combination of NPs physicochemical properties appear to play a significant role.

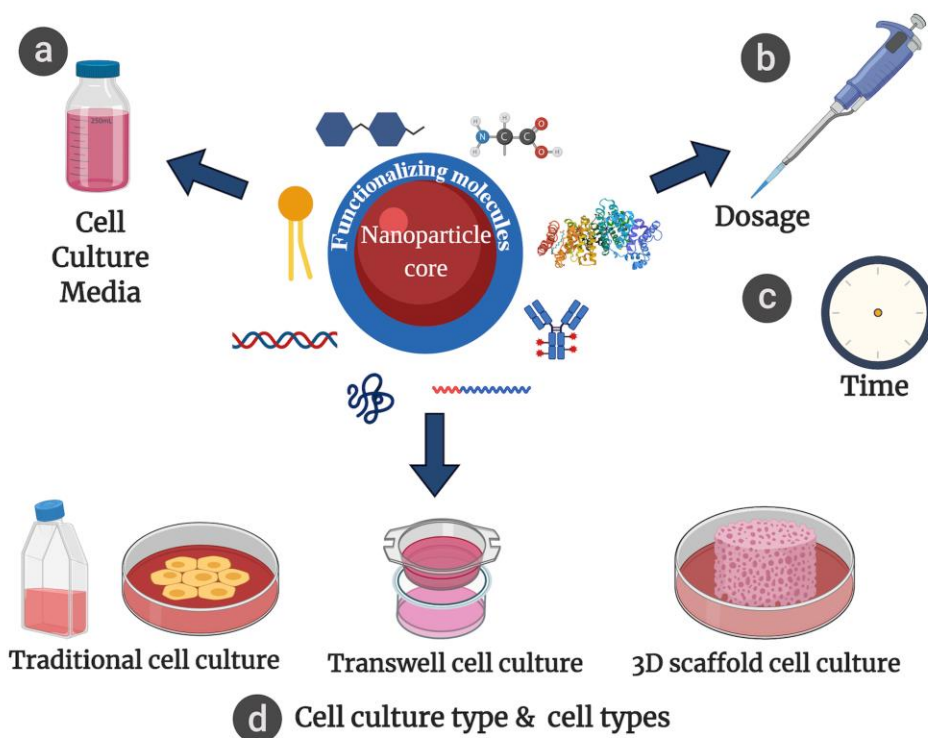


Figure 1.2. Experimental factors impacting in vitro studies

(a) Cell culture medium determines the biocorona formation around NPs. (b) Dosage, exposure type and (c) time should be chosen based on intended applications and potential exposure levels. (d) Cell culture methods, cell types and cell origin are the other factors that must be carefully selected to accurately determine the net effect of NPs.

Influence of NPs with different surface compositions on cellular interactions

Toxicity of NPs and their effect on Reactive Oxygen Species (ROS) generation

Cell viability tests are widely used to assess the toxicity of NPs. This typically involves a single dose of NPs followed by short-term evaluations of viability. Whereas, in vivo studies focus on studying the systemic effects and accumulation of NPs. Therefore, there is an apparent

disconnect between most in vitro and in vivo studies.¹²⁰ Reactive oxygen species produced by cells in response to NPs is a potent early marker for nanoparticle toxicity.^{94, 98, 114, 115} Transition metals such as iron (Fe^{+2}) in FeONPs can generate ROS by reacting with hydrogen peroxide (H_2O_2) to form hydroxyl free radical ($\text{OH}\bullet$) through the Fenton reaction.^{94, 116, 117} These can disrupt the mitochondrial activity, cause damage to DNA and lead to lipid peroxidation which destabilizes the cell membrane making it more susceptible to oxidation and may lead to rearrangement of lipid rafts, thus, affecting cell signaling.¹¹⁶⁻¹¹⁸ Organs such as the brain can be affected significantly due to their high lipid composition, reduced available antioxidants and high oxygen tensions than other tissues.¹¹⁹ Oxidative stress exerted by NPs may be inevitable in some cases and can be ameliorated by the naturally occurring antioxidants⁹⁴ or by supplementation with antioxidants such as thymoquinone to reduce these effects.¹²¹

Feng et al.⁹⁹ observed that cationic PEI coated FeONPs were endocytosed in high numbers compared to PEG-FeONPs and were more toxic to cells as they dramatically reduced cell viability in a concentration dependent manner. Increased ROS generation that disrupted the cell cycle by arresting cells in G2-phase cell cycle, led to apoptosis. Genotoxicity induced by the PEI-FeONPs was observed to be an indirect effect and not due to direct interaction with the DNA.⁹⁹ In contrast 60 nm 'naked' FeONPs intercalated with DNA base pairs in primary lymphocytes and generated high levels of ROS that reduced the cell viability.¹²¹ Micronucleus formation and chromosomal abnormalities were observed in rats, further suggesting the naked FeONPs were genotoxic. Therefore, surface composition can play an important role in preventing excessive cellular damage by influencing the subcellular localization and intracellular processing.^{122, 123}

Different cell types have varied antioxidizing abilities. For instance, macrophages have higher resistance to ROS and thus, high ROS levels do not significantly affect their viability.⁹⁹ FeONPs and AuNPs might interfere with colorimetric cell viability assays, due to their strong absorbance, light scattering or plasmon resonance in the visible light range.^{94, 124} This leads to under or over estimating the viability of cells if suitable controls are not in place. Hence, NPs may seemingly be non-toxic based on the cell viability and ROS analysis but may cause changes to cellular and molecular responses such as but not limited to impaired calcium homeostasis, perturbed mitochondrial activity, morphological changes affecting the functioning of intracellular pathways, disruption of protein-protein interactions, ER stress induced by unfolded protein response, and differences in genomic profiles which are not detectable by these conventional assays.^{102, 118} A better analysis beyond just toxic and non-toxic is essential to describe redox effects triggered by NPs. Gokduman et al.⁹¹ also hypothesized based on the ROS generation profile that instead of using absolute values, one should consider the time period at which there are logarithmic increases in ROS, since it will be more sensitive for early detection of NPs induced cytotoxicity. **Table 1.3** summarizes the cellular toxicity induced by NPs with identical or different surface chemistries and how they may differ based on the experimental factors.

The introduction of most types of foreign species warrants a response from a biological system. It is essential that one ascertain the overall effect of NPs, before concluding they are safe to use. Standardization of detection techniques and measuring harmful nano-bio interactions is absolutely essential for the advancement of bionanotechnology.^{38, 118} Recognizing this need, the International standards organization (ISO) established a committee in 2005 for standardization in nanotechnology.¹²⁵ The FDA also set up a nanotechnology task force to identify approaches to

ensure safe use of nanomaterials.¹²⁶ Therefore, a continued collaborative effort will hopefully help in advancing nanotechnology in the treatment of diseases.

Table 1.3. Effect of nanoparticles on cellular toxicity and viability

NP	Surface coating	Cell line	Media	Dosage	Time of exposure	Changes observed leading to cellular toxicity	Reference
6 nm SPIONs	Citrate	HL60 in suspension MDA-MB231 (2D) (3D) bEnd3	RPMI	0-150 µg/mL	24 h	Cells in 2D culture less affected than cells in 3D ↑ Surface area of exposure = ↑ toxicity	Milla et al. ¹⁰³
15 nm, 40 nm, 80 nm AuNPs	Citrate	Hela U937	DMEM & RPMI	1 pM - 1 nM	48 h & 96 h	Viability of HeLa cells ↓ than U937 AuNPs in RPMI more toxic to cells than AuNPs in DMEM	Maiorano et al. ¹⁰⁴
10 nm AuNPs	Citrate	HUVECs	DMEM	0-64 µg/mL	24 h	↓ cell viability at 5% serum in comparison to 10% serum ↑ uptake in low serum media	Gunduz et al. ¹²⁰
AuNPs	Nanospheres with Citrate & PAA Nanorods with PAA & PEG	Human dermal fibroblasts	DMEM	0.1 nM Acute vs chronic exposure	24 h (Acute) 3, 7, 14 days (Chronic)	AuNPs were generally non-toxic Uptake: PAA rods > PAA spheres > citrate spheres ~ PEG rods Gene expression changes observed ↑ in nonchronic exposure Cells developed adaptive response to chronic exposure, PEG rods ↑ gene expression changes	Falagan-Lotsch et al. ¹¹⁸
~4 nm AuNPs	polymer PMA	hNSC mNSC ReNcell	DMEM	0-150 nM	24 h	AuNPs were more toxic than FeONPs to all cells Primary stem cells more susceptible to FeONPs induced toxicity	Joris et al. ¹⁰²
~4 nm SPIONs		C17.2 LA-N-2 Neuro-2A				Human cells morphology was affected more than mouse cells in general	
10 nm SPIONs	Proprietary ligands	Primary rat hepatocytes	DMEM	0-400 µg/mL Acute vs Cumulative dose	24 h & 48 h	Cell viability ↓ with ↑ concentrations in single dose vs cumulative treatment Cumulative dosage more deleterious to hepatocyte functioning and metabolic competency All treatments induced ROS production	Gokduman et al. ⁹¹
10 nm & 30 nm FeONPs	PEG & PEI	RAW 264.7 SKOV	DMEM	0- 400 µg/mL	1, 2, 4, 16 h	PEI FeONPs more toxic than PEG FeONPs PEI FeONPs ↑ ROS, Apoptosis PEG FeONPs induced autophagy	Feng et al. ⁹⁹
60 nm FeONPs	Naked	Rat primary lymphocytes	RPMI	0 - 800 µg/mL	24 h	↓ cell viability, ↑ ROS, ↑ Genotoxicity	Ansari et al. ¹²¹
~ 16 nm FeONPs	DHCA	Human bone derived mesenchymal stem cells	MEM	0-1000 Fe µg/mL	1, 4, 24 h	Moderate effect on cell viability ↑ ROS	Hachani at al. ⁹⁴

Cellular uptake mechanism and pathways

Cells may use an active, energy dependent endocytic pathway or energy independent passive diffusion to internalize NPs. **Table 1.4** summarizes the uptake pathways used by nanoparticles with different surface chemistries in various cell types. Endocytosis is broadly classified as – Clathrin mediated endocytosis (CME), caveolae mediated endocytosis (CvME), macropinocytosis and clathrin and caveolae independent endocytosis. Phagocytosis is a type of endocytic pathway which is only employed by immune cells such as macrophages, neutrophils and dendritic cells.¹²⁷

Cargo is transported intracellularly in endocytic vesicles formed by cell membrane invaginations. Endocytic vesicles can be classified based on the protein markers on the vesicle membrane associated with the endocytic pathway, further influencing the cargo's intracellular sorting. **(Figure 1.4)** CME and macropinocytosis promote the fusion of endocytic vesicles with the highly acidic lysosomes (~ pH 5) that can cause degradation of the functionalizing ligands and NPs themselves. While the cargo transported in the caveosomes, enter the Golgi and endoplasmic reticulum, bypassing the lysosomes. CvME also favor transcytosis like in the case of Nab-paclitaxel.¹²⁷⁻¹³⁰ Some oncology and viral medications such as trastuzumab emtansine (T-DMI)¹³¹ and chloroquine¹³², respectively, target the endocytosis pathways. Hence, studying the mechanism of uptake is important for the fundamental understanding of nano-bio interactions and drug delivery.

Chemical inhibitors of endocytosis are commonly used to study the endocytic uptake pathways. Some inhibitors may have a generalized inhibitory effect while some are relatively more specific. Methyl- β -cyclodextrin although commonly used as an inhibitor of CvME, it can also inhibit cholesterol dependent clathrin and caveolin independent pathways.¹³³ Similarly,

dynasore may inhibit dynamin independent endocytic pathways as well.¹³⁴ Therefore, the chemical inhibitors should be selected wisely and the results should be interpreted appropriately. siRNA mediated knockdown of proteins, essential to specific endocytic routes on the other hand is less ambiguous than chemical inhibitors.¹³⁵ In some cases other endocytic pathways may be upregulated to compensate for inhibition of one pathway. Although the net uptake of NPs may seemingly be unaffected, one should not discount changes in the uptake mechanism.^{71, 135, 136}

Endocytosis of NPs is time dependent.¹³⁷ He et al.¹³⁸ observed that although the uptake of cationic CALRRRRRRRR (R8) peptide functionalized AuNPs was slower in comparison to the hydrophobic CALNNPFVYLI (PFV) peptide coated AuNPs, in the initial one hour, their net uptake was higher at the end of 12 h of incubation. IEC-18 epithelial cells also seemed to use different endocytosis pathways to internalize peptide bilayer coated FeONPs in a time dependent manner.⁷¹ The surface composition plays a crucial role since they may also help in endosomal escape as observed for highly cationic NPs.^{70, 139}

Different cell types may use different endocytic pathways for the uptake of the same NPs¹⁴⁰ and a single cell type may use multiple pathways for the uptake of NPs.⁷¹ Srijampa et al.¹⁴¹ identified that monocytes and macrophages generally studied for their phagocytic response may also use other endocytosis pathways alongside phagocytosis for NPs uptake. b.End endothelial cells internalized more of the negatively charged FeONPs in comparison to epithelial cells, using CvME, which was enhanced in the endothelial cells since they overexpressed the caveolin-1 protein.¹⁴² R8-AuNPs used energy independent direct translocation alongside CME and macropinocytosis to enter tumor cells.¹³⁸

PEG is commonly used to improve the circulation time of NPs but it also prevents their cellular uptake to a large extent. The hydration shell of PEG prevents opsonization of NPs

thereby preventing direct interaction with model liposomes used to determine interactions between membrane lipid components and surface ligands. CPP-PEG capped AuNPs on the other hand interacted efficiently with the lipid bilayer inserting themselves into the membrane.¹³⁸ The initial interactions or binding of the functionalizing molecules to the cell surface dictate the subsequent internalization events.¹⁴³ The NPs may be recognized by receptors which recruit proteins like clathrin, actin, dynamin that direct encapsulation in vesicles for internalization. For instance, glucose coated AuNPs developed to actively target aggressive head and neck tumors for computed tomography (CT) imaging, were endocytosed within 3 min of incubation by tumor cell lines which expressed high levels of GLUT-1 transporter, using CME.¹³⁰

Table 1.4. Endocytosis of Nanoparticles

NP	Surface coating	Cells	Inhibition mediated by	Uptake route	Reference
AuNPs	Glucose	A431 A549 PC3 B16F10 LNCaP 3T3	Chemical inhibitors	GLUT-1 transporter mediated, CME & CvME Lower uptake in GLUT-1 low cell lines via diffusion	Dreifuss et al. ¹³⁰
AuNPs	PEG-SH - Cell penetrating peptides (CPP)	A549 B16F10	Chemical inhibitors	CME & Macropinocytosis	He et al. ¹³⁸
AuNPs	PEI-PEG + pDNA	HeLa	Chemical inhibitors	CME	Li et al. ¹⁴⁴
AuNPs	His-PIMA-PEG-OCH ₃ /NH ₂ + SVS-1 antimicrobial peptide	HeLa CHO	Temperature	Energy independent, non-endocytic route	Kapur et al. ¹⁴⁵
FeONPs	Siloxane with free -COO groups	Primary human lung cells b. End MDCK	Chemical inhibitors & Temperature	CvME	Sun et al. ¹⁴²
SPIONs	silane/silica with free -COO groups PEG	HeLa	siRNA silencing	CvME & CDC42 mediated fluid phase endocytosis	Bohmer et al. ¹³⁵
SPIONs	PEG + Folic Acid + Fluorophores	HeLa MCF-7 MDA-MB435	Chemical inhibitors	CME CME & ↓ CvME	Vannier et al. ¹⁴⁶
SPIONs	Sienna + (Trademarked)	A549 MDA HeLa THP-1	siRNA silencing	CvME & Macropinocytosis CME, Macropinocytosis & Phagocytosis	Guggenheim et al. ¹⁴⁰
AuNPs	citrate	HUVECs	Chemical inhibitors	Macropinocytosis	Gunduz et al. ¹²⁰
SPIONs	Branched amphiphilic peptide bilayer coated magnetic nanobeads (BAPc-MNBs)	IEC-18	Chemical inhibitors	CvME, CME, Macropinocytosis (1 h) Clathrin caveolae independent endocytosis (4 h)	Natarajan et al. ⁷¹

Immune responses to NPs

NPs can elicit an immune response by interfering and interacting with intracellular signaling pathways directly or indirectly via the reactive oxygen and nitrogen species produced. For example, the transition metals on the surface of NPs or in SPIONs generate ROS as described previously, which triggers a pro-inflammatory response.^{147, 148} Cytokines and chemokines are used as indicators of an immune response since they are immune cell secretions or they are secreted by other cells to attract immune cells, in response to invading pathogens or foreign substances.¹⁴⁹ NPs may also cause changes in the conformation or cause unfolding of proteins binding them and trigger the immune system to react to the altered-self molecules.¹⁵⁰

NPs with the same core composition and size but different surface coatings can elicit different immune responses.¹⁵¹ Anionic hydrophilic ligand coated AuNPs did not affect LPS stimulated J774A.2 and RAW 264.7 macrophages, while hydrophobic ligands and tetraethylene glycol coated AuNPs elicited an anti-inflammatory response. PEI-SPIONs interacted with the TLR4 receptor on macrophages and activated them, while negatively charged dextran and DMSA coated SPIONs had negligible effects. This indicates that surface charge may have influenced the observed immune response.¹⁵² **Table 1.5** summarizes studies on the immunogenicity of NPs with varied surface compositions.

The immunogenicity of the NPs may also be used advantageously, as in tumor therapy and vaccine development.^{110, 153, 154} FDA-approved Ferumoxytol is an iron supplement used commonly to treat chronic kidney disease and the formulation contains SPIONs coated with polyglucose sorbitol carboxymethyl ether. Zanganeh et al.¹¹⁰ demonstrated that cancer cells treated with Ferumoxytol attracted M1 macrophages. An mRNA transcriptome analysis confirmed M1 related TNF- α and CD86 overexpression along with reduction in anti-

inflammatory M2 related CD206 and IL-10 expression. The pro-inflammatory response was beneficial as they prevented tumor growth by inducing tumor cell cytotoxicity, mediated by an increase in caspase-3 activity in cancer cells and a 16-fold increase in hydroxyl ($\cdot\text{OH}$) radicals.¹¹⁰

AuNPs have been explored as adjuvants by Dykman et al.¹⁵⁴ and Niikura et al.¹⁵³ The average antibody titers in response to BSA and the bacterial CpG antigens increased substantially when they were coupled to 15 and 50 nm AuNPs, in combination or individually.¹⁵⁴ Niikura et al. also used AuNPs as adjuvants and coated them with West Nile virus envelope (WNVE) protein. They observed increased anti-WNVE titers and inflammatory cytokine production by bone-marrow derived dendritic cells, when treated with WNVE-AuNPs. Thus, NPs are good immune potentiators and may serve as two-in-one adjuvant and vaccine delivery platforms. All in all, understanding the effect of NPs on immune response can also help us determine their potential applications and how to counter their effects.

Table 1.5. Immunogenicity of nanoparticles

NP	Surface coating	Cells/Cell line	Changes in secreted cytokines, chemokines & iNOS	Type of overall response	References
FeONPs	Polyglucose sorbitol carboxymethyl ether	RAW 264.7	TNF- α \uparrow , IL-10 \downarrow , iNOS \uparrow	Pro-inflammatory, M1 macrophages polarization	Zanganeh et al. ¹¹⁰
FeONPs	Ovalbumin	RAW 264.7	TNF- \uparrow , IL-6 \uparrow , IFN- γ \uparrow	Pro-inflammatory, NPs behave as adjuvants	Zhao et al. ¹⁵⁵
		DC2.4			
SPIONs	PEI- stabilized with: Zonyl-FSA Surfactant Pluronic-F127 surfactant	SVEC	TNF- α \uparrow , IL-6 \uparrow , IL-23 \uparrow , CCL1 \uparrow , CCL4 \uparrow , CCL5 \uparrow , TGF- β \downarrow , iNOS \uparrow	Pro-inflammatory, reduced cell migration	Mulens-Arias et al. ¹⁵²
		HUVECs	CCL2 \uparrow , CCL5 \uparrow , CXCL12 \uparrow , IL-23A & TNF- α levels unchanged, slight \uparrow TGF- β 1 & VEGFA	Pro-inflammatory, reduced angiogenesis	
		THP-1	IL-1 β \uparrow , Il-6 \uparrow , TNF- α \uparrow , CCL2 \uparrow , IL-12 \downarrow	Pro-inflammatory & altered M2 macrophages function	
AuNPs	Hydrophilic zwitterionic polymer (ZDiMe)	J774.2 & RAW 264.7	TNF- α unchanged	Neutral response	Moyano et al. ¹⁵¹
	Hydrophobic zwitterionic polymer (ZDiPen)		TNF- α \downarrow	Anti-inflammatory	
	Tetraethylene glycol modified		TNF- α \downarrow	Anti-inflammatory	

Nano – biointeractions in vivo

The NPs bio-interactions in the complex in vivo environment are dependent on their physicochemical properties, contributing to their translocation to the different organs and tissues and ultimate clearance.^{97, 156} Therefore, it is vital to discern the relationship between the NPs and the interactions with endogenous molecules that influence their biodistribution. In this section, the effects are discussed relative to different administration routes on tissue distribution, their systemic toxicity profiles and the immune responses generated in vivo. The in vivo studies reviewed here are limited to animals of the *Mus* and *Rattus* genus.

Effect of route of administration on biodistribution of NPs

NPs can be administered via different routes, namely- intravenous (i.v.), intramuscular (i.m.), transdermal (across the skin), subcutaneous (under the skin), intradermal (into skin), epicutaneous (on the skin), intratumoral, intraperitoneal (i.p.), intracerebral and oral delivery. The route of administration has an obvious role to play on the tissue distribution which is generally chosen based on the end application of NPs. However, i.v. injections are used more commonly since they can provide a near instantaneous response and is suitable for delivery of materials that cannot be absorbed efficiently or that can undergo proteolytic or pH disruption. Another major advantage of i.v. injections is the increased bioavailability of drugs.¹⁵⁷ The animal model selected for a particular study may influence the administration route.¹⁵⁸ Intramuscular delivery in mice is generally not recommended as their muscles are small, making it difficult to get reproducible results.¹⁵⁹ The genetic background of animals will also show variations in NPs interactions due to differences in their response to foreign molecules. The C57BL/6 and the BALB/c mice, for example, fundamentally exhibit different immune responses that could affect

their adaptive immunity. C57Bl/6 and BALB/c are prototypical, Th1 and Th2 type mouse strains, respectively, and therefore can have an altered response to NPs.¹⁶⁰

When NPs are administered, they have to cross various hurdles before they reach the target. They have to overcome primary defense barriers such as the gastrointestinal, circulation barriers and skin barriers depending upon the route of administration.¹⁶¹ A significant percentage of administered NPs reach the tissue but they have other hurdles to overcome, such as being sequestered by resident macrophages of the mononuclear phagocytic system (MPS) like Kupffer cells in liver, macrophages in the marginal zone or the red-pulp region of the spleen and alveolar macrophages in lungs.^{99, 156, 162-164} Larger NPs are typically metabolized in the liver and secreted into bile for excretion, while smaller NPs may be filtered out through the kidneys.¹⁶⁵⁻¹⁶⁷ PEI and PEG coated SPIONs when injected i.v. into SKOV-3 tumor bearing mice were cleared from circulation within 24 h of injection and accumulated primarily in liver, spleen and tumor with trace amounts found in lungs, heart and kidneys. PEI-FeONPs accumulated the least in tumors but had increased uptake in the kidneys, suggesting faster clearance from the body.⁹⁹ Faster clearance from circulation causes reduced accumulation in the tumor, as also noted by Bailly et al.¹⁶⁸

Meta-analysis conducted demonstrated that only 0.7% of total administered NPs reach tumor. Removal of Kupffer cells increased the uptake of NPs to only 2% from 0.7% in tumors. Therefore, although sequestration by macrophages in the liver affects the bioavailability of NPs, one needs to look at other organs and their effect on delivery of NPs to disease sites such as tumor.¹⁶⁴ Thus, sequestration of NPs can affect their ability to deliver therapeutics to target cells. A research group at the FDA was interested in understanding the effect of repeated doses of 10 nm AuNPs on the MPS and their importance in clearance of the NPs.¹⁶² They hypothesized that

chronic exposure to NPs would lead to saturation of the MPS system and, thus, lead to unforeseen toxicity or changes. However, 8 weeks of chronic exposure to 10 mg/kg AuNPs in BALB/c mice did not establish a steady state in the MPS i.e. they were not saturated. AuNPs accumulated the most in the liver, followed by spleen, causing tissue discoloration. The carcass showed high amounts of AuNPs due to possible accumulation in lymph nodes.

There is a complex interplay between size¹⁶⁹, charge¹⁵⁶, functionalizing molecules⁹⁷ and composition of the metallic core¹⁷⁰ that affects the tissue distribution and indirectly their use as imaging agents.¹⁶⁹ Sharma et al.¹⁵⁶ observed that cationic FeONPs accumulated mainly in lungs while the same size anionic FeONPs functionalized with carboxymethyl dextran, accumulated in the spleen and liver. The ligand density on NPs also have an effect as discerned by Xue et al.¹⁷¹ Intravenously injected 15 and 22 nm FeONPs with 2 kDa or 5 kDa PEG (i.e. different densities of PEG coating) showed obvious differences in tissue distribution. Although the lower MW PEGs covering NPs were cleared faster from blood, they persisted the longest in liver and spleen.

There has been an increase in studies exploring intradermal delivery using microneedles as it is minimally invasive.¹⁷² Dur et al.¹⁷³ delivered proinsulin peptide using glucose, mannose and GSH functionalized AuNPs to generate immune tolerance and prevent or delay onset of type 1 diabetes. They used intradermal delivery with the aim of delivering them to antigen presenting Langerhans cells in the skin, thus, generating an appropriate response from T-cells. The 5 nm AuNPs were distributed through the reticular dermis to the basement membrane zone and in keratinocytes, Langerhans cells and dermal cells, within 4 h but the colloidal 50 nm AuNPs were retained in the dermis. Repeated subcutaneous injections of similarly sized (~13 nm) iron oxide-zinc core-shell NPs delivering tumor antigens into dendritic cells, led to the accumulation of the NPs at the injection site and not in other tissues. Thus, the NPs were not effectively distributed

and therefore required further modifications to prevent accumulation at the injection site .¹⁷⁴

Hence, we see that the interplay between various factors including the administration method affect the successful delivery of the NPs and the outcome of NPs mediated drug delivery.

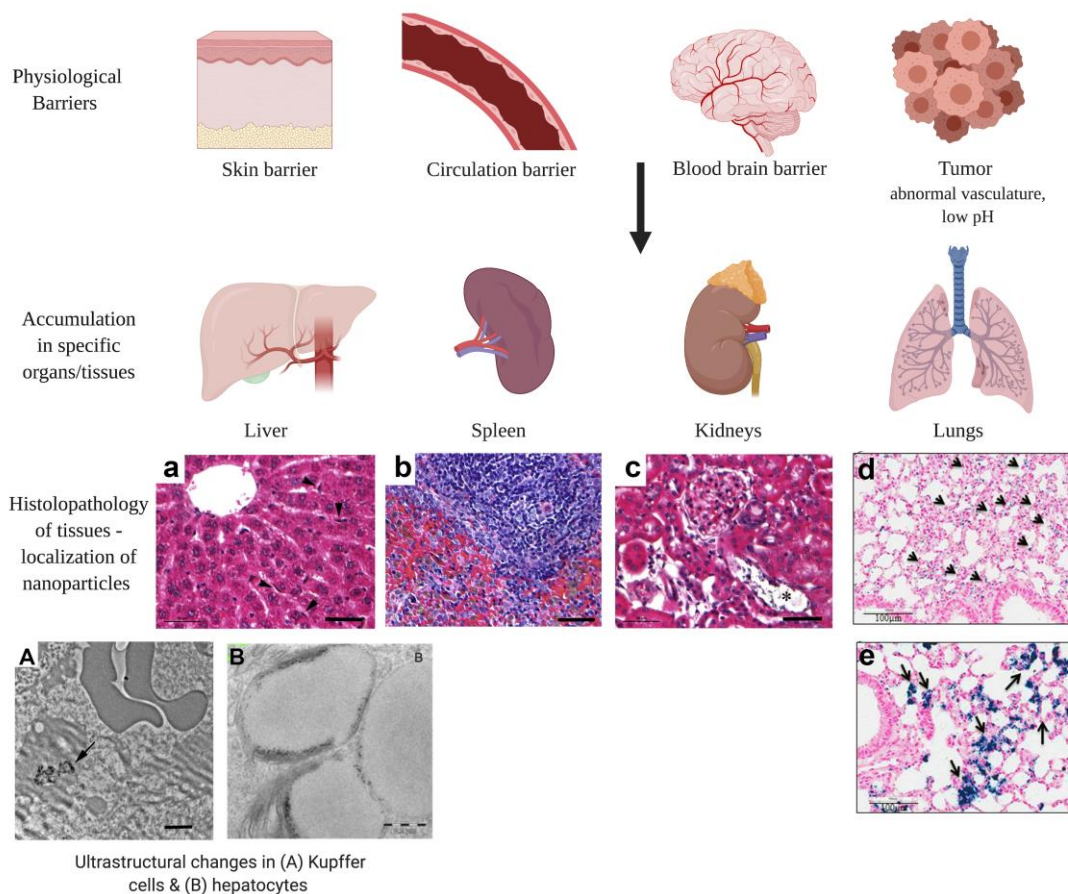


Figure 1.3. Localization of NPs in tissues and the physiological barriers to their uptake

Biodistribution of NPs in organs/tissues is influenced by their ability to cross the various physiological barriers. Sequestration by macrophages of the mononuclear phagocytic system (MPS) causes faster clearance of NPs from circulation and they accumulate mainly in organs such as liver and spleen. Histopathological & electron microscopy analyses provide information on the localization of NPs within tissues i.e. accumulation of NPs in specific cells, extracellular or in interstitial spaces as well as sub-cellular localization, morphological changes and damage to tissues and cells. H & E staining of NPs treated - (a) Liver showing FeONPs localized in Kupffer cells, (b) Spleen with increased macrophages in the red-pulp area, (c) Kidneys showing slight degeneration of tubular epithelial cells cytoplasm, (d) and (e) Lungs with NPs localized in the alveolar epithelium and interstitial spaces, respectively. Electron micrographs show accumulation of NPs in the (A) cytoplasm of Kupffer cells and (B) lipid droplets of the hepatocytes.

Adapted and reprinted (a), (b), (c) from *Nanomedicine-Nanotechnology Biology and Medicine*.12 (6), Sabareeswaran, A.; Ansar, E.; Varma, P.; Mohanan, P.; Kumary, T., Effect of surface-modified superparamagnetic iron oxide nanoparticles (SPIONS) on mast cell infiltration: An acute in vivo study, with permission from Elsevier. © (2016) (d),(e) *Scientific Reports*, Sharma, A.; Comejo, C.; Mihalic, J.; Geyh, A.; Bordelon, D.; Korangath, P.; Westphal, F.; Gruettner, C.; Ivkov, R., Physical characterization and in vivo organ distribution of coated iron oxide nanoparticles. © (2018) Springer Nature. (A) & (B) . *Nanomedicine-Nanotechnology Biology and Medicine*, 14 (1), Lopez-Chaves, C.; Soto-Alvaredo, J.; Montes-Bayon, M.; Bettmer, J.; Llopis, J.; Sanchez-Gonzalez, C., Gold nanoparticles: Distribution, bioaccumulation and toxicity. In vitro and in vivo studies, with permission from Elsevier. © (2018)

Systemic toxicity and immune response to NPs

In vitro studies can guide one in explaining the effects of NPs in vivo. For instance, ROS and RNS generated in response to NPs activates the cells and induces secretion of cytokines/chemokines. **(Figure 1.4)** This leads further to the infiltration of immune cells, which may cause tissue necrosis or induce apoptosis of cells causing organ damage. Thus, the immune response to the NPs can lead to a cascade of events that induces toxicity. In vivo, toxicity is determined by assessing ultrastructural changes in the tissues **(Figure 1.3)**, comparing cytokine levels and other molecular markers in serum and analyzing blood cell counts (hematology)¹⁷¹, which may be direct or indirect indicators of tissue damage and systemic toxicity.

Sharma et al.¹⁵⁶ observed infiltration of cells in the lungs of PEG-PEI FeONPs treated mice. Sub-chronic exposure to AuNPs caused edema in alveolar septa of lungs, enlargement of kidney corpuscles, infiltration of Kupffer cells in liver sinusoids and mild hyperplasia in spleen.¹⁷⁵ Mast cells infiltration in organs in response to coated and uncoated SPIONs, alongside macrophages was reported for the first time by Sabareeswaran et al.¹⁶³ Mast cells are actively involved in the secretion of active molecules that induce inflammation, necrosis and even allergic reactions. Hematoxylin and eosin (H&E) staining and TEM/SEM analysis are commonly used and allow visualization of tissue sections. The former provides information on morphological and ultrastructural changes, accumulation of NPs in specific types of cells in tissues while the sub-cellular localization and changes are generally assessed using the latter technique.⁹³ NPs induced cellular toxicity may lead to changes in cell surface area and morphology (shape) due to disruption of actin, increased lipid droplets in cytoplasm, granular cytoplasm and disrupted endosomal membrane.^{93, 156, 163} **(Figure 1.3)** Sequestration of NPs by antigen presenting cells such as macrophages although limits their biodistribution, they may have

an added advantage in applications such as vaccine delivery. Uptake of NPs by antigen presenting cells in major immune potentiating sites such as lymph nodes and spleen can induce an enhanced immune response to the antigens.¹⁷⁶ Therefore, certain NPs are can be developed for specific applications, but only with a fundamental understanding of the nano-bio interactions.

NPs that get past the MPS are internalized by other specialized cells in the tissues such as hepatocytes of epithelial origin and they may also accumulate in the extracellular/interstitial spaces in tissues.¹⁵⁶ Damage to the hepatic tissue is marked by an increase in serum alanine amino transferase (ALT) enzyme, while elevated aspartate amino transferase (AST) can be indicative of both cardiac function impairment and liver damage.¹⁷⁷ Other commonly used pharmacological indicators of implied toxicity are weight loss and serum levels of creatinine, bilirubin, blood urea nitrogen (BUN) and lactate dehydrogenase (LDH). PEG coated FeONPs caused increased metabolic stress in the liver leading to increase in serum ALT and AST.¹⁷¹ Five nm PBS stabilized AuNPs injected i.v. caused increase in ALT and AST levels in BALB/c mice¹⁷⁸ while 20 nm dextran coated AuNPs did not affect ALT and AST levels 14 days post injection.¹⁶⁸ PEI-FeONPs at 5 and 2.5 mg/kg doses were highly toxic to mice leading to death, but a dose of 1.5 mg/kg was well tolerated.⁹⁹ Sharma et al.¹⁵⁶ observed a similar effect of PEG-PEI FeONPs where 2 mg/kg dose was highly toxic to mice. Thus, NPs with different physicochemical properties exhibit different levels of toxicity and have varied effects in vivo. **Table 1.6** summarizes the biodistribution and systemic effects of NPs with different surface compositions.

Table 1.6. Biodistribution, systemic toxicity and immune response to nanoparticles in vivo

NPs	Surface coating	Animal model & strain	Route	Biodistribution	Toxicity and/or immune response		Ref
					Biochemical	Histopathological changes	
FeONPs	PEG & PEI	BALB/c	i.v.	Liver, spleen > lungs, heart, kidney	ALT↑ (PEG) LDH ↑ (PEI)	↑ macrophages in hepatic portal area	Feng et al. ⁹⁹
FeONPs	PEG-PEI, Carboxymethyl - dextran	Nude mice	i.p.	Spleen, liver (CM-dextran) Lungs (PEG-PEI)	Death at 2mg/kg PEG-PEI FeONPs dosage	PEG-PEI in lung epithelial cells & interstitial spaces but not in macrophages	Sharma et al. ¹⁵⁶
FeONPs	PAMAM dendrimer	BALB/c	i.p.	kidney, liver, lungs > tumor	↑ BUN, hyperglycemia, ↑LDH, ↑ Bilirubin	Edema & loss of cytoplasm in liver Apoptosis in cardiac tissue	Salimi et al. ¹⁷⁹
AuNPs	PBS stabilized (proprietary)	BALB/c	i.v.	liver, spleen> lung, kidney> brain, heart	Slight ↑ ALT, AST	Slight liver hemorrhage	Xia et al. ¹⁷⁸
AuNPs	Citrate	BALB/c	i.v.	Liver > spleen > lung > sternum > kidney > skin, heart, uterus, muscle, blood, brain		Discolored spleen, liver due to increased accumulation	Weaver et al. ¹⁶²
AuNPs	Dextran	Nude mice	i.v.	Liver > spleen >> tumor, lung, heart, brain	No apparent acute/chronic toxicity	Most NPs in Kupffer cells No hepatological changes or inflammation in kidney, spleen, heart	Bailly et al. ¹⁶⁸
AuNPs	Citrate	Wistar rats	i.p.	Spleen, liver, kidney, intestines	↑ lipid peroxidation & carbonylation No changes in TNF- α , IL-1 β , IL-6 and IL-10	↑ lipid droplets in hepatocytes	Lopez-Chaves et al. ⁹³

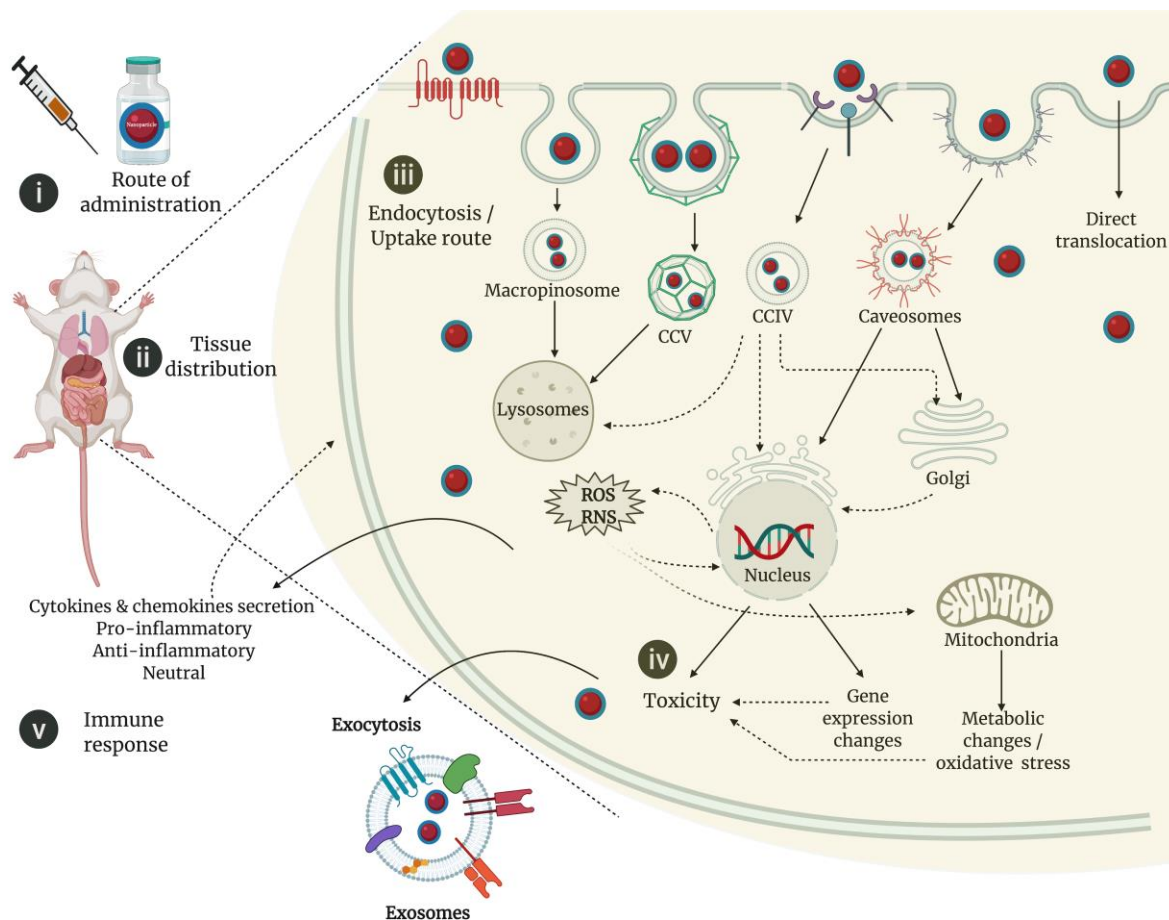


Figure 1.4. Bio-interactions of nanoparticles

Nanoparticles can be administered via different routes (i) which shapes their tissue distribution (ii). The cellular interactions of the NPs ultimately affect their fate in vivo. The physicochemical properties of the NPs impact the uptake mechanism (iii) which consecutively determines their intracellular fate. The NPs are sorted into different compartments based on the endocytic route. The NPs can affect the gene expression by directly interacting with the DNA or indirectly due the reactive oxygen species (ROS) generated. This may also lead to metabolic changes. Reactive nitrate species (RNS) produced mainly by immune cells such as macrophages and neutrophils along with the ROS are considered to be indicators of cellular activation. Altogether, the intracellular changes may cause cellular toxicity (iv) and cause an immune response by inducing changes in cytokine and chemokines secretion (v). NPs can also be exocytosed in vesicles called exosomes which may be inherently targeted to different tissues. Therefore, a cascade of events determines the bioavailability, clearance, toxicity profile and thus, the net effect of NPs.

CCV-Clathrin coated vesicles; CCIV- Clathrin caveolin independent vesicles

Conclusion

Nanoparticles developed over the past two decades are used widely in biological applications. Therefore, it has become essential to study the nano-bio interactions and understand the impact of exposure to nanoparticles. If designed optimally, in vitro studies can give a wealth of information that can be well correlated to the in vivo effects of nanoparticles, which can further help improve the success of nanomedicines. Thus, there is an increasing need for standardization in the field of bionanotechnology. Besides, understanding the limitations of the characterization techniques and cellular assays for nanomaterial assessment, identifying supplementary techniques and assays for verifying NPs bio-interactions and reasoning the use of specific experimental parameters will help achieve the goal of replacement, reduction and refinement. Most successful nanomedicines that have been approved for commercial use are relatively simple, well-described systems that have been widely studied. Given the volume of information available on different types of NPs with different physicochemical properties, a concerted effort by researchers such as depositing information on and creating a database of NPs will enable the analysis of the complex data using various computational tools available. Deciphering the complex nano-bio interactions and understanding the crosstalk between various biophysicochemical properties of nanoparticles is essential for the growth of nano-biotechnology.

References

1. Sapsford, K. E.; Tyner, K. M.; Dair, B. J.; Deschamps, J. R.; Medintz, I. L., Analyzing nanomaterial bioconjugates: a review of current and emerging purification and characterization techniques. *Anal Chem* 2011, 83 (12), 4453-88.
<https://doi.org/10.1021/ac200853a>.

2. Sapsford, K. E.; Algar, W. R.; Berti, L.; Gemmill, K. B.; Casey, B. J.; Oh, E.; Stewart, M. H.; Medintz, I. L., Functionalizing nanoparticles with biological molecules: developing chemistries that facilitate nanotechnology. *Chem Rev* 2013, 113 (3), 1904-2074. <https://doi.org/10.1021/cr300143v>.
3. Xing, S.; Zhang, X.; Luo, L.; Cao, W.; Li, L.; He, Y.; An, J.; Gao, D., Doxorubicin/gold nanoparticles coated with liposomes for chemo-photothermal synergetic antitumor therapy. *Nanotechnology* 2018, 29 (40). <https://doi.org/10.1088/1361-6528/aad358>.
4. Bhowmik, D.; Mote, K.; MacLaughlin, C.; Biswas, N.; Chandra, B.; Basu, J.; Walker, G.; Madhu, P.; Maiti, S., Cell-Membrane-Mimicking Lipid-Coated Nanoparticles Confer Raman Enhancement to Membrane Proteins and Reveal Membrane-Attached Amyloid-beta Conformation. *ACS Nano* 2015, 9 (9), 9070-9077. <https://doi.org/10.1021/acs.nano.5b03175>.
5. Kong, W.; Bae, K.; Jo, S.; Kim, J.; Park, T., Cationic Lipid-Coated Gold Nanoparticles as Efficient and Non-Cytotoxic Intracellular siRNA Delivery Vehicles. *Pharmaceutical Research* 2012, 29 (2), 362-374. <https://doi.org/10.1007/s11095-011-0554-y>.
6. Liao, Z.; Wang, H.; Lv, R.; Zhao, P.; Sun, X.; Wang, S.; Su, W.; Niu, R.; Chang, J., Polymeric Liposomes-Coated Superparamagnetic Iron Oxide Nanoparticles as Contrast Agent for Targeted Magnetic Resonance Imaging of Cancer Cells. *Langmuir* 2011, 27 (6), 3100-3105. <https://doi.org/10.1021/la1050157>.
7. Wessel, E.; Tomich, J.; Todd, R., Biodegradable Drug-Delivery Peptide Nanocapsules. *ACS Omega* 2019, 4 (22), 20059-20063. <https://doi.org/10.1021/acsomega.9b03245>.
8. Pandit, G.; Roy, K.; Agarwal, U.; Chatterjee, S., Self-Assembly Mechanism of a Peptide-Based Drug Delivery Vehicle. *ACS Omega* 2018, 3 (3), 3143-3155. <https://doi.org/10.1021/acsomega.7b01871>.
9. Bellomo, E.; Wyrsta, M.; Pakstis, L.; Pochan, D.; Deming, T., Stimuli-responsive polypeptide vesicles by conformation-specific assembly. *Nature Materials* 2004, 3 (4), 244-248. <https://doi.org/10.1038/nmat1093>.
10. Boyer, C.; Whittaker, M.; Nouvel, C.; Davis, T., Synthesis of Hollow Polymer Nanocapsules Exploiting Gold Nanoparticles as Sacrificial Templates. *Macromolecules* 2010, 43 (4), 1792-1799. <https://doi.org/10.1021/ma902663n>.
11. Shi, J.; Xiao, Z.; Votruba, A.; Vilos, C.; Farokhzad, O., Differentially Charged Hollow Core/Shell Lipid-Polymer-Lipid Hybrid Nanoparticles for Small Interfering RNA Delivery. *Angewandte Chemie-International Edition* 2011, 50 (31), 7027-7031. <https://doi.org/10.1002/anie.201101554>.
12. Kozielski, K.; Tzeng, S.; De Mendoza, B.; Green, J., Bioreducible Cationic Polymer-Based Nanoparticles for Efficient and Environmentally Triggered Cytoplasmic siRNA

- Delivery to Primary Human Brain Cancer Cells. *ACS Nano* 2014, 8 (4), 3232-3241.
<https://doi.org/10.1021/nm500704t>.
13. Wang, C.; Wang, Y.; Zhang, L.; Miron, R.; Liang, J.; Shi, M.; Mo, W.; Zheng, S.; Zhao, Y.; Zhang, Y., Pretreated Macrophage-Membrane-Coated Gold Nanocages for Precise Drug Delivery for Treatment of Bacterial Infections. *Advanced Materials* 2018, 30 (46). <https://doi.org/10.1002/adma.201804023>.
 14. Qu, F.; Jiang, H.; Yang, M., Designed formation through a metal organic framework route of ZnO/ZnCo₂O₄ hollow core-shell nanocages with enhanced gas sensing properties. *Nanoscale* 2016, 8 (36), 16349-16356. <https://doi.org/10.1039/c6nr05187a>.
 15. Li, Z.; Yu, C.; Wen, Y.; Gao, Y.; Xing, X.; Wei, Z.; Sun, H.; Zhang, Y.; Song, W., Mesoporous Hollow Cu-Ni Alloy Nanocage from Core-Shell Cu@Ni Nanocube for Efficient Hydrogen Evolution Reaction. *ACS Catalysis* 2019, 9 (6), 5084-5095.
<https://doi.org/10.1021/acscatal.8b04814>.
 16. Aubin-Tam, M.; Hamad-Schifferli, K., Structure and function of nanoparticle-protein conjugates. *Biomedical Materials* 2008, 3 (3). <https://doi.org/10.1088/1748-6041/3/3/034001>.
 17. Patra, J.; Das, G.; Fraceto, L.; Campos, E.; Rodriguez-Torres, M.; Acosta-Torres, L.; Diaz-Torres, L.; Grillo, R.; Swamy, M.; Sharma, S.; Habtemariam, S.; Shin, H., Nano based drug delivery systems: recent developments and future prospects. *Journal of Nanobiotechnology* 2018, 16. <https://doi.org/10.1186/s12951-018-0392-8>.
 18. Dixit, S.; Novak, T.; Miller, K.; Zhu, Y.; Kenney, M. E.; Broome, A. M., Transferrin receptor-targeted theranostic gold nanoparticles for photosensitizer delivery in brain tumors. *Nanoscale* 2015, 7 (5), 1782-90. <https://doi.org/10.1039/c4nr04853a>.
 19. Lee, K.; David, A.; Zhang, J.; Shin, M.; Yang, V., Enhanced accumulation of theranostic nanoparticles in brain tumor by external magnetic field mediated in situ clustering of magnetic nanoparticles. *Journal of Industrial and Engineering Chemistry* 2017, 54, 389-397. <https://doi.org/10.1016/j.jiec.2017.06.019>.
 20. Ali, A. A.; Hsu, F. T.; Hsieh, C. L.; Shiau, C. Y.; Chiang, C. H.; Wei, Z. H.; Chen, C. Y.; Huang, H. S., Erlotinib-Conjugated Iron Oxide Nanoparticles as a Smart Cancer-Targeted Theranostic Probe for MRI. *Sci Rep* 2016, 6, 36650.
<https://doi.org/10.1038/srep36650>.
 21. Salunkhe, A.; Khot, V.; Patil, S. I.; Tofail, S. A. M.; Bauer, J.; Thorat, N. D., MRI Guided Magneto-chemotherapy with High-Magnetic-Moment Iron Oxide Nanoparticles for Cancer Theranostics. *ACS Applied Bio Materials* 2020, 3 (4), 2305-2313.
<https://doi.org/10.1021/acsabm.0c00077>.
 22. Bobo, D.; Robinson, K.; Islam, J.; Thurecht, K.; Corrie, S., Nanoparticle-Based Medicines: A Review of FDA-Approved Materials and Clinical Trials to Date.

- Pharmaceutical Research 2016, 33 (10), 2373-2387. <https://doi.org/10.1007/s11095-016-1958-5>.
23. Chan, W. C. W., Nano Research for COVID-19. ACS Nano 2020, 14 (4), 3719-3720. <https://doi.org/10.1021/acsnano.0c02540>.
 24. The race against COVID-19. Nature Nanotechnology 2020, 15 (4), 239-240. <https://doi.org/10.1038/s41565-020-0680-y>.
 25. Washington University in St.Louis. "Rapid COVID-19 test based on new biolabeling technology called plasmonic-fluor." Science Daily [Online], 2020.
 26. Luan, J.; Seth, A.; Gupta, R.; Wang, Z.; Rathi, P.; Cao, S.; Derami, H.; Tang, R.; Xu, B.; Achilefu, S.; Morrissey, J.; Singamaneni, S., Ultrabright fluorescent nanoscale labels for the femtomolar detection of analytes with standard bioassays. Nature Biomedical Engineering 2020. <https://doi.org/10.1038/s41551-020-0547-4>.
 27. ClinicalTrials.gov [Internet]. Bethesda (MD): National Library of Medicine (US). 2000 Feb 29 - Identifier NCT04283461, Safety and Immunogenicity Study of 2019-nCoV Vaccine (mRNA-1273) for Prophylaxis of SARS-CoV-2 Infection (COVID-19); 2020 Feb 21 [cited 2020 May 15]; Available from: <https://clinicaltrials.gov/ct2/show/NCT04283461>.
 28. Gunnarsson, S.; Bernfur, K.; Englund-Johansson, U.; Johansson, F.; Cedervall, T., Analysis of complexes formed by small gold nanoparticles in low concentration in cell culture media. Plos One 2019, 14 (6). <https://doi.org/10.1371/journal.pone.0218211>.
 29. Javed, I.; He, J.; Kakinen, A.; Faridi, A.; Yang, W.; Davis, T.; Ke, P.; Chen, P., Probing the Aggregation and Immune Response of Human Islet Amyloid Polypeptides with Ligand-Stabilized Gold Nanoparticles. ACS Applied Materials & Interfaces 2019, 11 (11), 10462-10471. <https://doi.org/10.1021/acsmi.8b19506>.
 30. Ortas, D.; Altunbek, M.; Uzunoglu, D.; Yilmaz, H.; Cetin, D.; Suludere, Z.; Culha, M., Tracing Size and Surface Chemistry-Dependent Endosomal Uptake of Gold Nanoparticles Using Surface-Enhanced Raman Scattering. Langmuir 2019, 35 (11), 4020-4028. <https://doi.org/10.1021/acs.langmuir.8b03988>.
 31. Klein, S.; Petersen, S.; Taylor, U.; Rath, D.; Barcikowski, S., Quantitative visualization of colloidal and intracellular gold nanoparticles by confocal microscopy. Journal of Biomedical Optics 2010, 15 (3). <https://doi.org/10.1117/1.3461170>.
 32. Shah, N.; Dong, J.; Bischof, J., Cellular Uptake and Nanoscale Localization of Gold Nanoparticles in Cancer Using Label-Free Confocal Raman Microscopy. Molecular Pharmaceutics 2011, 8 (1), 176-184. <https://doi.org/10.1021/mp1002587>.
 33. Wei, H.; Bruns, O.; Kaul, M.; Hansen, E.; Barch, M.; Wisniowska, A.; Chen, O.; Chen, Y.; Li, N.; Okada, S.; Cordero, J.; Heine, M.; Farrar, C.; Montana, D.; Adam, G.; Ittrich, H.; Jasanoff, A.; Nielsen, P.; Bawendi, M., Exceedingly small iron oxide

- nanoparticles as positive MRI contrast agents. *Proceedings of the National Academy of Sciences of the United States of America* 2017, 114 (9), 2325-2330.
<https://doi.org/10.1073/pnas.1620145114>.
34. Motiei, M.; Dreifuss, T.; Betzer, O.; Panet, H.; Popovtzer, A.; Santana, J.; Abourbeh, G.; Mishani, E.; Popovtzer, R., Differentiating Between Cancer and Inflammation: A Metabolic-Based Method for Functional Computed Tomography Imaging. *ACS Nano* 2016, 10 (3), 3469-3477. <https://doi.org/10.1021/acsnano.5b07576>.
 35. Wierzbinski, K.; Szymanski, T.; Rozwadowska, N.; Rybka, J.; Zimna, A.; Zalewski, T.; Nowicka-Bauer, K.; Malcher, A.; Nowaczyk, M.; Krupinski, M.; Fiedorowicz, M.; Bogorodzki, P.; Grieb, P.; Giersig, M.; Kurpisz, M., Potential use of superparamagnetic iron oxide nanoparticles for in vitro and in vivo bioimaging of human myoblasts. *Scientific Reports* 2018, 8. <https://doi.org/10.1038/s41598-018-22018-0>.
 36. Sugumaran, P.; Liu, X.; Heng, T.; Peng, E.; Ding, J., GO-Functionalized Large Magnetic Iron Oxide Nanoparticles with Enhanced Colloidal Stability and Hyperthermia Performance. *ACS Applied Materials & Interfaces* 2019, 11 (25), 22703-22713.
<https://doi.org/10.1021/acami.9b04261>.
 37. Lartigue, L.; Innocenti, C.; Kalaivani, T.; Awwad, A.; Duque, M.; Guari, Y.; Larionova, J.; Guerin, C.; Montero, J.; Barragan-Montero, V.; Arosio, P.; Lascialfari, A.; Gatteschi, D.; Sangregorio, C., Water-Dispersible Sugar-Coated Iron Oxide Nanoparticles. An Evaluation of their Relaxometric and Magnetic Hyperthermia Properties. *Journal of the American Chemical Society* 2011, 133 (27), 10459-10472.
<https://doi.org/10.1021/ja111448t>.
 38. Mulvaney, P.; Weiss, P., Have Nanoscience and Nanotechnology Delivered? *ACS Nano* 2016, 10 (8), 7225. <https://doi.org/10.1021/acsnano.6b05344>.
 39. Gao, X.; Lowry, G., Progress towards standardized and validated characterizations for measuring physicochemical properties of manufactured nanomaterials relevant to nano health and safety risks. *Nanoimpact* 2018, 9, 14-30.
<https://doi.org/10.1016/j.impact.2017.09.002>.
 40. Ali, A.; Zafar, H.; Zia, M.; Haq, I.; Phull, A.; Ali, J.; Hussain, A., Synthesis, characterization, applications, and challenges of iron oxide nanoparticles. *Nanotechnology Science and Applications* 2016, 9, 49-67.
<https://doi.org/10.2147/NSA.S99986>.
 41. Turkevich, J.; Stevenson, P.; Hillier, J., A Study of the Nucleation and Growth Processes in the Synthesis Of Colloidal Gold. *Discussions of the Faraday Society* 1951, (11), 55.
<https://doi.org/10.1039/df9511100055>.
 42. Piella, J.; Bastus, N.; Puntès, V., Size-Controlled Synthesis of Sub-10-nanometer Citrate-Stabilized Gold Nanoparticles and Related Optical Properties. *Chemistry of Materials* 2016, 28 (4), 1066-1075. <https://doi.org/10.1021/acs.chemmater.5b04406>.

43. Naha, P.; Liu, Y.; Hwang, G.; Huang, Y.; Gubara, S.; Jonnakuti, V.; Simon-Soro, A.; Kim, D.; Gao, L.; Koo, H.; Cormode, D., Dextran-Coated Iron Oxide Nanoparticles as Biomimetic Catalysts for Localized and pH-Activated Biofilm Disruption. *ACS Nano* 2019, 13 (5), 4960-4971. <https://doi.org/10.1021/acsnano.8b08702>.
44. Brust, M.; Walker, M.; Bethell, D.; Schiffrin, D. J.; Whyman, R., Synthesis of thiol-derivatised gold nanoparticles in a two-phase Liquid–Liquid system. *Journal of the Chemical Society, Chemical Communications* 1994, (7), 2.
45. Lin, X.; Sorensen, C.; Klabunde, K., Digestive ripening, nanophase segregation and superlattice formation in gold nanocrystal colloids. *Journal of Nanoparticle Research* 2000, 2 (2), 157-164. <https://doi.org/10.1023/A:1010078521951>.
46. Mahmoudi, M.; Simchi, A.; Imani, M.; Milani, A.; Stroeve, P., Optimal Design and Characterization of Superparamagnetic Iron Oxide Nanoparticles Coated with Polyvinyl Alcohol for Targeted Delivery and Imaging. *Journal of Physical Chemistry B* 2008, 112 (46), 14470-14481. <https://doi.org/10.1021/jp803016n>.
47. Kang, Y.; Risbud, S.; Rabolt, J.; Stroeve, P., Synthesis and characterization of nanometer-size Fe₃O₄ and gamma-Fe₂O₃ particles. *Chemistry of Materials* 1996, 8 (9), 2209. <https://doi.org/10.1021/cm960157j>.
48. Davis, K.; Cole, B.; Ghelardini, M.; Powell, B.; Mefford, O., Quantitative Measurement of Ligand Exchange with Small-Molecule Ligands on Iron Oxide Nanoparticles via Radioanalytical Techniques. *Langmuir* 2016, 32 (51), 13716-13727. <https://doi.org/10.1021/acs.langmuir.6b03644>.
49. Natarajan, P.; Sukthankar, P.; Changstrom, J.; Holland, C. S.; Barry, S.; Hunter, W. B.; Sorensen, C. M.; Tomich, J. M., Synthesis and Characterization of Multifunctional Branched Amphiphilic Peptide Bilayer Conjugated Gold Nanoparticles. *ACS Omega* 2018, 3 (9), 11071-11083. <https://doi.org/10.1021/acsomega.8b01633>.
50. Muddineti, O.; Ghosh, B.; Biswas, S., Current trends in using polymer coated gold nanoparticles for cancer therapy. *International Journal of Pharmaceutics* 2015, 484 (1-2), 252-267. <https://doi.org/10.1016/j.ijpharm.2015.02.038>.
51. Katti, K. K.; Kattumuri, V.; Bhaskaran, S.; Katti, K. V.; Kannan, R., Facile and General Method for Synthesis of Sugar Coated Gold Nanoparticles. *Int J Green Nanotechnol Biomed* 2009, 1 (1), B53-B59. <https://doi.org/10.1080/19430850902983848>.
52. Suvarna, S.; Das, U.; Sunil, K.; Mishra, S.; Sudarshan, M.; Das Saha, K.; Dey, S.; Chakraborty, A.; Narayana, Y., Synthesis of a novel glucose capped gold nanoparticle as a better theranostic candidate. *Plos One* 2017, 12 (6). <https://doi.org/10.1371/journal.pone.0178202>.
53. Tang, J.; Fu, X.; Ou, Q.; Gao, K.; Man, S.; Guo, J.; Liu, Y., Hydroxide assisted synthesis of monodisperse and biocompatible gold nanoparticles with dextran. *Materials*

- Science & Engineering C-Materials For Biological Applications 2018, 93, 759-767.
<https://doi.org/10.1016/j.msec.2018.08.045>.
54. Ahmed, A.; Ibteisam, E.; Vincenzo, T.; Luca, M.; Snow, S.; C., G. M., A simple and efficient method for polymer coating of iron oxide nanoparticles. *Journal of Drug delivery science and technology* 2020, 55.
<https://doi.org/https://doi.org/10.1016/j.jddst.2019.101460>.
 55. Gao, J.; Huang, X.; Liu, H.; Zan, F.; Ren, J., Colloidal Stability of Gold Nanoparticles Modified with Thiol Compounds: Bioconjugation and Application in Cancer Cell Imaging. *Langmuir* 2012, 28 (9), 4464-4471. <https://doi.org/10.1021/la204289k>.
 56. Xu, P.; Shen, Z.; Zhang, B.; Wang, J.; Wu, R., Synthesis and characterization of superparamagnetic iron oxide nanoparticles as calcium-responsive MRI contrast agents. *Applied Surface Science* 2016, 389, 560-566.
<https://doi.org/10.1016/j.apsusc.2016.07.160>.
 57. Lombardo, D.; Kiselev, M.; Caccamo, M., Smart Nanoparticles for Drug Delivery Application: Development of Versatile Nanocarrier Platforms in Biotechnology and Nanomedicine. *Journal of Nanomaterials* 2019. <https://doi.org/10.1155/2019/3702518>.
 58. Ulbricht, J.; Jordan, R.; Luxenhofer, R., On the biodegradability of polyethylene glycol, polypeptoids and poly(2-oxazoline)s. *Biomaterials* 2014, 35 (17), 4848-4861.
<https://doi.org/10.1016/j.biomaterials.2014.02.029>.
 59. Center for Drug Evaluation and Research, Orange Book: Approved Drug Products with Therapeutic Equivalence Evaluations. 40th ed.; Rockville, Md.: U.S. Dept. of Health and Human Services, Food and Drug Administration, Center for Drug Evaluation and Research, Office of Pharmaceutical Science, Office of Generic Drugs.: 2020.
 60. Luchini, A.; Vitiello, G., Understanding the Nano-bio Interfaces: Lipid-Coatings for Inorganic Nanoparticles as Promising Strategy for Biomedical Applications. *Frontiers in Chemistry* 2019, 7. <https://doi.org/10.3389/fchem.2019.00343>.
 61. Holland, J.; Hui, C.; Cullis, P.; Madden, T., Poly(ethylene glycol)-lipid conjugates regulate the calcium-induced fusion of liposomes composed of phosphatidylethanolamine and phosphatidylserine. *Biochemistry* 1996, 35 (8), 2618-2624.
<https://doi.org/10.1021/bi952000v>.
 62. Romero, J.; Hodak, J.; Rodriguez, H.; Gonzalez, M., Silicon Quantum Dots Metal-Enhanced Photoluminescence by Gold Nanoparticles in Colloidal Ensembles: Effect of Surface Coating. *Journal of Physical Chemistry C* 2018, 122 (47), 26865-26875.
<https://doi.org/10.1021/acs.jpcc.8b09310>.
 63. Hauser, A.; Mitov, M.; Daley, E.; McGarry, R.; Anderson, K.; Hilt, J., Targeted iron oxide nanoparticles for the enhancement of radiation therapy. *Biomaterials* 2016, 105, 127-135. <https://doi.org/10.1016/j.biomaterials.2016.07.032>.

64. Morshed, R. A.; Muroski, M. E.; Dai, Q.; Wegscheid, M. L.; Auffinger, B.; Yu, D.; Han, Y.; Zhang, L.; Wu, M.; Cheng, Y.; Lesniak, M. S., Cell-Penetrating Peptide-Modified Gold Nanoparticles for the Delivery of Doxorubicin to Brain Metastatic Breast Cancer. *Mol Pharm* 2016, 13 (6), 1843-54.
<https://doi.org/10.1021/acs.molpharmaceut.6b00004>.
65. Perillo, E.; Herve-Aubert, K.; Allard-Vannier, E.; Falanga, A.; Galdiero, S.; Chourpa, I., Synthesis and in vitro evaluation of fluorescent and magnetic nanoparticles functionalized with a cell penetrating peptide for cancer theranosis. *Journal of Colloid and Interface Science* 2017, 499, 209-217. <https://doi.org/10.1016/j.jcis.2017.03.106>.
66. Silva, S.; Almeida, A.; Vale, N., Combination of Cell-Penetrating Peptides with Nanoparticles for Therapeutic Application: A Review. *Biomolecules* 2019, 9 (1).
<https://doi.org/10.3390/biom9010022>.
67. Yin, T.; Xie, W.; Sun, J.; Yang, L.; Liu, J., Penetratin Peptide-Functionalized Gold Nanostars: Enhanced BBB Permeability and NIR Photothermal Treatment of Alzheimer's Disease Using Ultralow Irradiance. *ACS Applied Materials & Interfaces* 2016, 8 (30), 19291-19302. <https://doi.org/10.1021/acsami.6b05089>.
68. Chee, H.; Gan, C.; Ng, M.; Low, L.; Fernig, D.; Bhakoo, K.; Paramelle, D., Biocompatible Peptide-Coated Ultrasmall Superparamagnetic Iron Oxide Nanoparticles for In Vivo Contrast-Enhanced Magnetic Resonance Imaging. *ACS Nano* 2018, 12 (7), 6480-6491. <https://doi.org/10.1021/acs.nano.7b07572>.
69. Sukthankar, P.; Avila, L. A.; Whitaker, S. K.; Iwamoto, T.; Morgenstern, A.; Apostolidis, C.; Liu, K.; Hanzlik, R. P.; Dadachova, E.; Tomich, J. M., Branched amphiphilic peptide capsules: cellular uptake and retention of encapsulated solutes. *Biochim Biophys Acta* 2014, 1838 (9), 2296-305.
<https://doi.org/10.1016/j.bbamem.2014.02.005>.
70. Sukthankar, P.; Gudlur, S.; Avila, L. A.; Whitaker, S. K.; Katz, B. B.; Hiromasa, Y.; Gao, J.; Thapa, P.; Moore, D.; Iwamoto, T.; Chen, J.; Tomich, J. M., Branched oligopeptides form nanocapsules with lipid vesicle characteristics. *Langmuir* 2013, 29 (47), 14648-54. <https://doi.org/10.1021/la403492n>.
71. Natarajan, P.; Roberts, J. D.; Kunte, N.; Hunter, W. B.; Fleming, S. D.; Tomich, J. M.; Avila, L. A., A Study of the Cellular Uptake of Magnetic Branched Amphiphilic Peptide Capsules. *Mol Pharm* 2020. <https://doi.org/10.1021/acs.molpharmaceut.0c00393>.
72. Zhang, L.; Han, F., Protein coated gold nanoparticles as template for the directed synthesis of highly fluorescent gold nanoclusters. *Nanotechnology* 2018, 29 (16).
<https://doi.org/10.1088/1361-6528/aaae47>.
73. Nosrati, H.; Sefidi, N.; Sharafi, A.; Danafar, H.; Kheiri Manjili, H., Bovine Serum Albumin (BSA) coated iron oxide magnetic nanoparticles as biocompatible carriers for curcumin-anticancer drug. *Bioorg Chem* 2018, 76, 501-509.
<https://doi.org/10.1016/j.bioorg.2017.12.033>.

74. Von Hoff, D.; Ervin, T.; Arena, F.; Chiorean, E.; Infante, J.; Moore, M.; Seay, T.; Tjulandin, S.; Ma, W.; Saleh, M.; Harris, M.; Reni, M.; Dowden, S.; Laheru, D.; Bahary, N.; Ramanathan, R.; Taberner, J.; Hidalgo, M.; Goldstein, D.; Van Cutsem, E.; Wei, X.; Iglesias, J.; Renschler, M., Increased Survival in Pancreatic Cancer with nab-Paclitaxel plus Gemcitabine. *New England Journal of Medicine* 2013, 369 (18), 1691-1703. <https://doi.org/10.1056/NEJMoa1304369>.
75. Ruttala, H.; Ramasamy, T.; Poudel, B.; Ruttala, R.; Jin, S.; Choi, H.; Ku, S.; Yong, C.; Kim, J., Multi-responsive albumin-lonidamine conjugated hybridized gold nanoparticle as a combined photothermal-chemotherapy for synergistic tumor ablation. *Acta Biomaterialia* 2020, 101, 531-543. <https://doi.org/10.1016/j.actbio.2019.11.003>.
76. Vismara, E.; Bongio, C.; Coletti, A.; Edelman, R.; Serafini, A.; Mauri, M.; Simonutti, R.; Bertini, S.; Urso, E.; Assaraf, Y.; Livney, Y., Albumin and Hyaluronic Acid-Coated Superparamagnetic Iron Oxide Nanoparticles Loaded with Paclitaxel for Biomedical Applications. *Molecules* 2017, 22 (7). <https://doi.org/10.3390/molecules22071030>.
77. Collins, D.; Bossenmaier, B.; Kollmorgen, G.; Niederfellner, G., Acquired Resistance to Antibody-Drug Conjugates. *Cancers* 2019, 11 (3). <https://doi.org/10.3390/cancers11030394>.
78. Chen, H.; Wang, L.; Yu, Q.; Qian, W.; Tiwari, D.; Yi, H.; Wang, A.; Huang, J.; Yang, L.; Mao, H., Anti-HER2 antibody and ScFvEGFR-conjugated antifouling magnetic iron oxide nanoparticles for targeting and magnetic resonance imaging of breast cancer. *International Journal of Nanomedicine* 2013, 8, 3781-3794. <https://doi.org/10.2147/IJN.S49069>.
79. Oliveira, J.; Prado, A.; Keijok, W.; Antunes, P.; Yapuchura, E.; Guimaraes, M., Impact of conjugation strategies for targeting of antibodies in gold nanoparticles for ultrasensitive detection of 17 beta-estradiol. *Scientific Reports* 2019, 9. <https://doi.org/10.1038/s41598-019-50424-5>.
80. Finetti, C.; Sola, L.; Pezzullo, M.; Prosperi, D.; Colombo, M.; Riva, B.; Avvakumova, S.; Morasso, C.; Picciolini, S.; Chiari, M., Click Chemistry Immobilization of Antibodies on Polymer Coated Gold Nanoparticles. *Langmuir* 2016, 32 (29), 7435-7441. <https://doi.org/10.1021/acs.langmuir.6b01142>.
81. Kijanka, M.; van Donselaar, E.; Muller, W.; Dorresteyn, B.; Popov-Celeketic, D.; el Khattabi, M.; Verrips, C.; Henegouwen, P.; Post, J., A novel immuno-gold labeling protocol for nanobody-based detection of HER2 in breast cancer cells using immuno-electron microscopy. *Journal of Structural Biology* 2017, 199 (1), 1-11. <https://doi.org/10.1016/j.jsb.2017.05.008>.
82. El-Sayed, I.; Huang, X.; El-Sayed, M., Surface plasmon resonance scattering and absorption of anti-EGFR antibody conjugated gold nanoparticles in cancer diagnostics: Applications in oral cancer. *Nano Letters* 2005, 5 (5), 829-834. <https://doi.org/10.1021/nl050074e>.

83. Hu, X.; Kim, C.; Albert, S.; Park, S., DNA-Grafted Poly(acrylic acid) for One-Step DNA Functionalization of Iron Oxide Nanoparticles. *Langmuir* 2018, 34 (47), 14342-14346. <https://doi.org/10.1021/acs.langmuir.8b03119>.
84. Nash, J.; Tucker, T.; Therriault, W.; Yingling, Y., Binding of single stranded nucleic acids to cationic ligand functionalized gold nanoparticles. *Biointerphases* 2016, 11 (4). <https://doi.org/10.1116/1.4966653>.
85. Wang, R.; Degirmenci, V.; Xin, H.; Li, Y.; Wang, L.; Chen, J.; Hu, X.; Zhang, D., PEI-Coated Fe₃O₄ Nanoparticles Enable Efficient Delivery of Therapeutic siRNA Targeting REST into Glioblastoma Cells. *International Journal of Molecular Sciences* 2018, 19 (8). <https://doi.org/10.3390/ijms19082230>.
86. Galli, M.; Guerrini, A.; Cauteruccio, S.; Thakare, P.; Dova, D.; Orsini, F.; Arosio, P.; Carrara, C.; Sangregorio, C.; Lascialfari, A.; Maggioni, D.; Licandro, E., Superparamagnetic iron oxide nanoparticles functionalized by peptide nucleic acids. *RSC Advances* 2017, 7 (25), 15500-15512. <https://doi.org/10.1039/C7RA00519A>.
87. Berti, L.; Burley, G., Nucleic acid and nucleotide-mediated synthesis of inorganic nanoparticles. *Nature Nanotechnology* 2008, 3 (2), 81-87. <https://doi.org/10.1038/nnano.2007.460>.
88. Liu, B.; Huang, R.; Yu, Y.; Su, R.; Qi, W.; He, Z., Gold Nanoparticle-Aptamer-Based LSPR Sensing of Ochratoxin A at a Widened Detection Range by Double Calibration Curve Method. *Frontiers in Chemistry* 2018, 6. <https://doi.org/10.3389/fchem.2018.00094>.
89. Huang, C.; Huang, Y.; Cao, Z.; Tan, W.; Chang, H., Aptamer-modified gold nanoparticles for colorimetric determination of platelet-derived growth factors and their receptors. *Analytical Chemistry* 2005, 77 (17), 5735-5741. <https://doi.org/10.1021/ac050957q>.
90. Fernandez, R.; Umasankar, Y.; Manickam, P.; Nickel, J.; Iwasaki, L.; Kawamoto, B.; Todoki, K.; Scott, J.; Bhansali, S., Disposable aptamer-sensor aided by magnetic nanoparticle enrichment for detection of salivary cortisol variations in obstructive sleep apnea patients. *Scientific Reports* 2017, 7. <https://doi.org/10.1038/s41598-017-17835-8>.
91. Gokduman, K.; Bestepe, F.; Li, L.; Yarmush, M.; Usta, O., Dose-, treatment- and time-dependent toxicity of superparamagnetic iron oxide nanoparticles on primary rat hepatocytes. *Nanomedicine* 2018, 13 (11), 1267-1284. <https://doi.org/10.2217/nnm-2017-0387>.
92. Khlebtsov, N.; Dykman, L., Biodistribution and toxicity of engineered gold nanoparticles: a review of in vitro and in vivo studies. *Chemical Society Reviews* 2011, 40 (3), 1647-1671. <https://doi.org/10.1039/c0cs00018c>.
93. Lopez-Chaves, C.; Soto-Alvaredo, J.; Montes-Bayon, M.; Bettmer, J.; Llopis, J.; Sanchez-Gonzalez, C., Gold nanoparticles: Distribution, bioaccumulation and toxicity. In

- vitro and in vivo studies. *Nanomedicine-Nanotechnology Biology and Medicine* 2018, 14 (1), 1-12. <https://doi.org/10.1016/j.nano.2017.08.011>.
94. Hachani, R.; Birchall, M.; Lowdell, M.; Kasparis, G.; Tung, L.; Manshian, B.; Soenen, S.; Gsell, W.; Himmelreich, U.; Gharagouzloo, C.; Sridhar, S.; Thanh, N., Assessing cell-nanoparticle interactions by high content imaging of biocompatible iron oxide nanoparticles as potential contrast agents for magnetic resonance imaging. *Scientific Reports* 2017, 7. <https://doi.org/10.1038/s41598-017-08092-w>.
 95. Kumar, K.; Moitra, P.; Bashir, M.; Kondaiah, P.; Bhattacharya, S., Natural tripeptide capped pH-sensitive gold nanoparticles for efficacious doxorubicin delivery both in vitro and in vivo. *Nanoscale* 2020, 12 (2), 1067-1074. <https://doi.org/10.1039/c9nr08475d>.
 96. Cancino-Bernardi, J.; Marangoni, V.; Besson, J.; Cancino, M.; Natali, M.; Zucolotto, V., Gold-based nanospheres and nanorods particles used as theranostic agents: An in vitro and in vivo toxicology studies. *Chemosphere* 2018, 213, 41-52. <https://doi.org/10.1016/j.chemosphere.2018.09.012>.
 97. Stepien, G.; Moros, M.; Perez-Hernandez, M.; Monge, M.; Gutierrez, L.; Fratila, R.; Heras, M.; Guillen, S.; Lanzarote, J.; Solans, C.; Pardo, J.; de la Fuente, J., Effect of Surface Chemistry and Associated Protein Corona on the Long-Term Biodegradation of Iron Oxide Nanoparticles In Vivo. *ACS Applied Materials & Interfaces* 2018, 10 (5), 4548-4560. <https://doi.org/10.1021/acsami.7b18648>.
 98. Zhang, Y.; Liu, A. T.; Cornejo, Y. R.; Van Haute, D.; Berlin, J. M., A Systematic comparison of in vitro cell uptake and in vivo biodistribution for three classes of gold nanoparticles with saturated PEG coatings. *PLoS One* 2020, 15 (7), e0234916. <https://doi.org/10.1371/journal.pone.0234916>.
 99. Feng, Q.; Liu, Y.; Huang, J.; Chen, K.; Xiao, K., Uptake, distribution, clearance, and toxicity of iron oxide nanoparticles with different sizes and coatings. *Sci Rep* 2018, 8 (1), 2082. <https://doi.org/10.1038/s41598-018-19628-z>.
 100. Foroozandeh, P.; Aziz, A. A., Insight into Cellular Uptake and Intracellular Trafficking of Nanoparticles. *Nanoscale Res Lett* 2018, 13 (1), 339. <https://doi.org/10.1186/s11671-018-2728-6>.
 101. Behzadi, S.; Serpooshan, V.; Tao, W.; Hamaly, M. A.; Alkawareek, M. Y.; Dreaden, E. C.; Brown, D.; Alkilany, A. M.; Farokhzad, O. C.; Mahmoudi, M., Cellular uptake of nanoparticles: journey inside the cell. *Chem Soc Rev* 2017, 46 (14), 4218-4244. <https://doi.org/10.1039/c6cs00636a>.
 102. Joris, F.; Valdeperez, D.; Pelaz, B.; Soenen, S.; Manshian, B.; Parak, W.; De Smedt, S.; Raemdonck, K., The impact of species and cell type on the nanosafety profile of iron oxide nanoparticles in neural cells. *Journal of Nanobiotechnology* 2016, 14. <https://doi.org/10.1186/s12951-016-0220-y>.

103. Milla, M.; Yu, S.; Laromaine, A., Parametrizing the exposure of superparamagnetic iron oxide nanoparticles in cell cultures at different in vitro environments. *Chemical Engineering Journal* 2018, 340, 173-180. <https://doi.org/10.1016/j.cej.2017.12.070>.
104. Maiorano, G.; Sabella, S.; Sorce, B.; Brunetti, V.; Malvindi, M.; Cingolani, R.; Pompa, P., Effects of Cell Culture Media on the Dynamic Formation of Protein-Nanoparticle Complexes and Influence on the Cellular Response. *ACS Nano* 2010, 4 (12), 7481-7491. <https://doi.org/10.1021/nn101557e>.
105. Pannico, M.; Calarco, A.; Peluso, G.; Musto, P., Functionalized Gold Nanoparticles as Biosensors for Monitoring Cellular Uptake and Localization in Normal and Tumor Prostatic Cells. *Biosensors-Basel* 2018, 8 (4). <https://doi.org/10.3390/bios8040087>.
106. Poller, J.; Zaloga, J.; Schreiber, E.; Unterweger, H.; Janko, C.; Radon, P.; Eberbeck, D.; Trahms, L.; Alexiou, C.; Friedrich, R., Selection of potential iron oxide nanoparticles for breast cancer treatment based on in vitro cytotoxicity and cellular uptake. *International Journal of Nanomedicine* 2017, 12, 3207-3220. <https://doi.org/10.2147/IJN.S132369>.
107. Moore, T.; Urban, D.; Rodriguez-Lorenzo, L.; Milosevic, A.; Crippa, F.; Spuch-Calvar, M.; Balog, S.; Rothen-Rutishauser, B.; Lattuada, M.; Petri-Fink, A., Nanoparticle administration method in cell culture alters particle-cell interaction. *Scientific Reports* 2019, 9. <https://doi.org/10.1038/s41598-018-36954-4>.
108. Bancos, S.; Tyner, K., Evaluating the effect of assay preparation on the uptake of gold nanoparticles by RAW264.7 cells. *Journal of Nanobiotechnology* 2014, 12. <https://doi.org/10.1186/s12951-014-0045-5>.
109. Frohlich, E., Comparison of conventional and advanced in vitro models in the toxicity testing of nanoparticles. *Artificial Cells Nanomedicine and Biotechnology* 2018, 46, 1091-1107. <https://doi.org/10.1080/21691401.2018.1479709>.
110. Zanganeh, S.; Hutter, G.; Spitler, R.; Lenkov, O.; Mahmoudi, M.; Shaw, A.; Pajarinen, J.; Nejadnik, H.; Goodman, S.; Moseley, M.; Coussens, L.; Daldrup-Link, H., Iron oxide nanoparticles inhibit tumour growth by inducing pro-inflammatory macrophage polarization in tumour tissues. *Nature Nanotechnology* 2016, 11 (11), 986-994. <https://doi.org/10.1038/NNANO.2016.168>.
111. Wahab, R.; Kaushik, N.; Khan, F.; Kaushik, N.; Lee, S.; Choi, E.; Al-Khedhairi, A., Gold quantum dots impair the tumorigenic potential of glioma stem-like cells via beta-catenin downregulation in vitro. *International Journal of Nanomedicine* 2019, 14, 1131-1148. <https://doi.org/10.2147/IJN.S195333>.
112. Lichtenstein, D.; Ebmeyer, J.; Meyer, T.; Behr, A.; Kastner, C.; Bohmert, L.; Juling, S.; Niemann, B.; Fahrenson, C.; Selve, S.; Thunemann, A.; Meijer, J.; Estrela-Lopis, I.; Braeuning, A.; Lampen, A., It takes more than a coating to get nanoparticles through the intestinal barrier in vitro. *European Journal of Pharmaceutics and Biopharmaceutics* 2017, 118, 21-29. <https://doi.org/10.1016/j.ejpb.2016.12.004>.

113. Yang, K.; Guo, C.; Woodhead, J.; St Claire, R.; Watkins, P.; Siler, S.; Howell, B.; Brouwer, K., Sandwich-Cultured Hepatocytes as a Tool to Study Drug Disposition and Drug-Induced Liver Injury. *Journal of Pharmaceutical Sciences* 2016, 105 (2), 443-459. <https://doi.org/10.1016/j.xphs.2015.11.008>.
114. McKee, T. J.; Komarova, S. V., Is it time to reinvent basic cell culture medium? *Am J Physiol Cell Physiol* 2017, 312 (5), C624-C626. <https://doi.org/10.1152/ajpcell.00336.2016>.
115. Lima, T.; Bernfur, K.; Vilanova, M.; Cedervall, T., Understanding the Lipid and Protein Corona Formation on Different Sized Polymeric Nanoparticles. *Sci Rep* 2020, 10 (1), 1129. <https://doi.org/10.1038/s41598-020-57943-6>.
116. Sakulphu, U.; Mahmoudi, M.; Maurizi, L.; Salaklang, J.; Hofmann, H., Protein Corona Composition of Superparamagnetic Iron Oxide Nanoparticles with Various Physico-Chemical Properties and Coatings. *Scientific Reports* 2014, 4. <https://doi.org/10.1038/srep05020>.
117. Petri-Fink, A.; Steitz, B.; Finka, A.; Salaklang, J.; Hofmann, H., Effect of cell media on polymer coated superparamagnetic iron oxide nanoparticles (SPIONs): Colloidal stability, cytotoxicity, and cellular uptake studies. *European Journal of Pharmaceutics and Biopharmaceutics* 2008, 68 (1), 129-137. <https://doi.org/10.1016/j.ejpb.2007.02.024>.
118. Falagan-Lotsch, P.; Grzincic, E.; Murphy, C., One low-dose exposure of gold nanoparticles induces long-term changes in human cells. *Proceedings of the National Academy of Sciences of the United States of America* 2016, 113 (47), 13318-13323. <https://doi.org/10.1073/pnas.1616400113>.
119. Xu, M.; Soliman, M.; Sun, X.; Pelaz, B.; Feliu, N.; Parak, W.; Liu, S., How Entanglement of Different Physicochemical Properties Complicates the Prediction of in Vitro and in Vivo Interactions of Gold Nanoparticles. *ACS Nano* 2018, 12 (10), 10104-10113. <https://doi.org/10.1021/acsnano.8b04906>.
120. Gunduz, N.; Ceylan, H.; Guler, M.; Tekinay, A., Intracellular Accumulation of Gold Nanoparticles Leads to Inhibition of Macropinocytosis to Reduce the Endoplasmic Reticulum Stress. *Scientific Reports* 2017, 7. <https://doi.org/10.1038/srep40493>.
121. Ansari, M.; Parveen, N.; Ahmad, M.; Wani, A.; Afrin, S.; Rahman, Y.; Jarneel, S.; Khan, Y.; Siddique, H.; Tabish, M.; Shadab, G., Evaluation of DNA interaction, genotoxicity and oxidative stress induced by iron oxide nanoparticles both in vitro and in vivo: attenuation by thymoquinone. *Scientific Reports* 2019, 9. <https://doi.org/10.1038/s41598-019-43188-5>.
122. Mahmoudi, M.; Simchi, A.; Vali, H.; Imani, M.; Shokrgozar, M.; Azadmanesh, K.; Azari, F., Cytotoxicity and Cell Cycle Effects of Bare and Poly(vinyl alcohol)-Coated Iron Oxide Nanoparticles in Mouse Fibroblasts. *Advanced Engineering Materials* 2009, 11 (12), B243-B250. <https://doi.org/10.1002/adem.200990035>.

123. Kharazian, B.; Lohse, S.; Ghasemi, F.; Raoufi, M.; Saei, A.; Hashemi, F.; Farvadi, F.; Alimohamadi, R.; Jalali, S.; Shokrgozar, M.; Hadipour, N.; Ejtehadi, M.; Mahmoudi, M., Bare surface of gold nanoparticle induces inflammation through unfolding of plasma fibrinogen. *Scientific Reports* 2018, 8. <https://doi.org/10.1038/s41598-018-30915-7>.
124. Bessar, H.; Venditti, I.; Benassi, L.; Vaschieri, C.; Azzoni, P.; Pellacani, G.; Magnoni, C.; Botti, E.; Casagrande, V.; Federici, M.; Costanzo, A.; Fontana, L.; Testa, G.; Mostafa, F. F.; Ibrahim, S. A.; Russo, M. V.; Fratoddi, I., Functionalized gold nanoparticles for topical delivery of methotrexate for the possible treatment of psoriasis. *Colloids Surf B Biointerfaces* 2016, 141, 141-147. <https://doi.org/10.1016/j.colsurfb.2016.01.021>.
125. Benko, H., ISO Technical Committee 229 Nanotechnologies. In *Metrology and Standardization for Nanotechnology : Protocols and Industrial Innovations*, Mansfield, E.; Kaiser, D. L.; Fujita, D.; Van de Voorde, M., Eds. John Wiley & Sons, Incorporated: 2017; p 629.
126. Nanotechnology Fact Sheet, U.S. Food and Drug Administration, FDA, 23 March 2018, <https://www.fda.gov/science-research/nanotechnology-programs-fda/nanotechnology-fact-sheet>.
127. Sahay, G.; Alakhova, D. Y.; Kabanov, A. V., Endocytosis of nanomedicines. *J Control Release* 2010, 145 (3), 182-95. <https://doi.org/10.1016/j.jconrel.2010.01.036>.
128. Zhang, S.; Gao, H.; Bao, G., Physical Principles of Nanoparticle Cellular Endocytosis. *ACS Nano* 2015, 9 (9), 8655-71. <https://doi.org/10.1021/acs.nano.5b03184>.
129. Xiang, S.; Tong, H.; Shi, Q.; Fernandes, J.; Jin, T.; Dai, K.; Zhang, X., Uptake mechanisms of non-viral gene delivery. *Journal of Controlled Release* 2012, 158 (3), 371-378. <https://doi.org/10.1016/j.jconrel.2011.09.093>.
130. Dreifuss, T.; Ben-Gal, T.; Shamalov, K.; Weiss, A.; Jacob, A.; Sadan, T.; Motiei, M.; Popovtzer, R., Uptake mechanism of metabolic-targeted gold nanoparticles. *Nanomedicine* 2018, 13 (13), 1535-1549. <https://doi.org/10.2217/nmm-2018-0022>.
131. Verma, S.; Miles, D.; Gianni, L.; Krop, I.; Welslau, M.; Baselga, J.; Pegram, M.; Oh, D.; Dieras, V.; Guardino, E.; Fang, L.; Lu, M.; Olsen, S.; Blackwell, K.; Grp, E. S., Trastuzumab Emtansine for HER2-Positive Advanced Breast Cancer. *New England Journal of Medicine* 2012, 367 (19), 1783-1791. <https://doi.org/10.1056/NEJMoa1209124>.
132. Yang, N.; Shen, H., Targeting the Endocytic Pathway and Autophagy Process as a Novel Therapeutic Strategy in COVID-19. *International Journal of Biological Sciences* 2020, 16 (10), 1724-1731. <https://doi.org/10.7150/ijbs.45498>.
133. Rodal, S. K.; Skretting, G.; Garred, O.; Vilhardt, F.; van Deurs, B.; Sandvig, K., Extraction of cholesterol with methyl-beta-cyclodextrin perturbs formation of clathrin-

- coated endocytic vesicles. *Mol Biol Cell* 1999, 10 (4), 961-74.
<https://doi.org/10.1091/mbc.10.4.961>.
134. Preta, G.; Cronin, J. G.; Sheldon, I. M., Dynasore - not just a dynamin inhibitor. *Cell Commun Signal* 2015, 13, 24. <https://doi.org/10.1186/s12964-015-0102-1>.
135. Bohmer, N.; Jordan, A., Caveolin-1 and CDC42 mediated endocytosis of silica-coated iron oxide nanoparticles in HeLa cells. *Beilstein Journal of Nanotechnology* 2015, 6, 167-176. <https://doi.org/10.3762/bjnano.6.16>.
136. Vercauteren, D.; Vandenbroucke, R. E.; Jones, A. T.; Rejman, J.; Demeester, J.; De Smedt, S. C.; Sanders, N. N.; Braeckmans, K., The use of inhibitors to study endocytic pathways of gene carriers: optimization and pitfalls. *Mol Ther* 2010, 18 (3), 561-9. <https://doi.org/10.1038/mt.2009.281>.
137. Sasso, L.; Purdie, L.; Grabowska, A.; Jones, A. T.; Alexander, C., Time and cell-dependent effects of endocytosis inhibitors on the internalization of biomolecule markers and nanomaterials. *Journal of Interdisciplinary Nanomedicine* 2018. <https://doi.org/https://doi.org/10.1002/jin2.39>.
138. He, B.; Yang, D.; Qin, M.; Zhang, Y.; Dai, W.; Wang, X.; Zhang, Q.; Zhang, H.; Yin, C., Increased cellular uptake of peptide-modified PEGylated gold nanoparticles. *Biochemical and Biophysical Research Communications* 2017, 494 (1-2), 339-345. <https://doi.org/10.1016/j.bbrc.2017.10.026>.
139. Erazo-Oliveras, A.; Muthukrishnan, N.; Baker, R.; Wang, T. Y.; Pellois, J. P., Improving the endosomal escape of cell-penetrating peptides and their cargos: strategies and challenges. *Pharmaceuticals (Basel)* 2012, 5 (11), 1177-209. <https://doi.org/10.3390/ph5111177>.
140. Guggenheim, E.; Rappoport, J.; Lynch, I., Mechanisms for cellular uptake of nanosized clinical MRI contrast agents. *Nanotoxicology* 2020. <https://doi.org/10.1080/17435390.2019.1698779>.
141. Srijampa, S.; Buddhisa, S.; Ngernpimai, S.; Sangiamdee, D.; Chompoosor, A.; Tippayawat, P., Effects of Gold Nanoparticles with Different Surface Charges on Cellular Internalization and Cytokine Responses in Monocytes. *BioNanoScience* 2019, 9 (3), 580-586. <https://doi.org/10.1007/s12668-019-00638-8>.
142. Sun, Z.; Worden, M.; Wroczynskyj, Y.; Manna, P.; Thliveris, J.; van Lierop, J.; Hegmann, T.; Miller, D., Differential internalization of brick shaped iron oxide nanoparticles by endothelial cells. *Journal of Materials Chemistry B* 2016, 4 (35), 5913-5920. <https://doi.org/10.1039/c6tb01480a>.
143. Francia, V.; Montizaan, D.; Salvati, A., Interactions at the cell membrane and pathways of internalization of nano-sized materials for nanomedicine. *Beilstein Journal of Nanotechnology* 2020, 11, 338-353. <https://doi.org/10.3762/bjnano.11.25>.

144. Li, A.; Qiu, J.; Zhou, B.; Xu, B.; Xiong, Z.; Hao, X.; Shi, X.; Cao, X., The gene transfection and endocytic uptake pathways mediated by PEGylated PEI-entrapped gold nanoparticles. *Arabian Journal of Chemistry* 2020, 13 (1), 2558-2567. <https://doi.org/10.1016/j.arabjc.2018.06.009>.
145. Kapur, A.; Wang, W.; Diaz Hernandez, J.; Medina, S.; Schneider, J.; Mattoussi, H., Anti-microbial peptide facilitated cytosolic delivery of metallic gold nanomaterials. *SPIE*: 2018; Vol. 10507,
146. Allard-Vannier, E.; Herve-Aubert, K.; Kaaki, K.; Blondy, T.; Shebanova, A.; Shaitan, K.; Ignatova, A.; Saboungi, M.; Feofanov, A.; Chourpa, I., Folic acid-capped PEGylated magnetic nanoparticles enter cancer cells mostly via clathrin-dependent endocytosis. *Biochimica Et Biophysica Acta-General Subjects* 2017, 1861 (6), 1578-1586. <https://doi.org/10.1016/j.bbagen.2016.11.045>.
147. Manke, A.; Wang, L.; Rojanasakul, Y., Mechanisms of Nanoparticle-Induced Oxidative Stress and Toxicity. *Biomed Research International* 2013. <https://doi.org/10.1155/2013/942916>.
148. Premasekharan, G.; Nguyen, K.; Contreras, J.; Ramon, V.; Leppert, V.; Forman, H., Iron-mediated lipid peroxidation and lipid raft disruption in low-dose silica-induced macrophage cytokine production. *Free Radical Biology and Medicine* 2011, 51 (6), 1184-1194. <https://doi.org/10.1016/j.freeradbiomed.2011.06.018>.
149. Elsabahy, M.; Wooley, K. L., Cytokines as biomarkers of nanoparticle immunotoxicity. *Chem Soc Rev* 2013, 42 (12), 5552-76. <https://doi.org/10.1039/c3cs60064e>.
150. Neagu, M.; Piperigkou, Z.; Karamanou, K.; Engin, A.; Docea, A.; Constantin, C.; Negrei, C.; Nikitovic, D.; Tsatsakis, A., Protein bio-corona: critical issue in immune nanotoxicology. *Archives of Toxicology* 2017, 91 (3), 1031-1048. <https://doi.org/10.1007/s00204-016-1797-5>.
151. Moyano, D.; Liu, Y.; Ayaz, F.; Hou, S.; Puangploy, P.; Duncan, B.; Osborne, B.; Rotello, V., Immunomodulatory Effects of Coated Gold Nanoparticles in LPS-Stimulated In Vitro and In Vivo Murine Model Systems. *Chem* 2016, 1 (2). <https://doi.org/10.1016/j.chempr.2016.07.007>.
152. Mulens-Arias, V.; Rojas, J.; Sanz-Ortega, L.; Portilla, Y.; Perez-Yague, S.; Barber, D., Polyethylenimine-coated superparamagnetic iron oxide nanoparticles impair in vitro and in vivo angiogenesis. *Nanomedicine-Nanotechnology Biology and Medicine* 2019, 21. <https://doi.org/10.1016/j.nano.2019.102063>.
153. Niikura, K.; Matsunaga, T.; Suzuki, T.; Kobayashi, S.; Yamaguchi, H.; Orba, Y.; Kawaguchi, A.; Hasegawa, H.; Kajino, K.; Ninomiya, T.; Ijio, K.; Sawa, H., Gold Nanoparticles as a Vaccine Platform: Influence of Size and Shape on Immunological Responses in Vitro and in Vivo. *ACS Nano* 2013, 7 (5), 3926-3938. <https://doi.org/10.1021/nm3057005>.

154. Dykman, L.; Staroverov, S.; Fomin, A.; Khanadeev, V.; Khlebtsov, B.; Bogatyrev, V., Gold nanoparticles as an adjuvant: Influence of size, shape, and technique of combination with CpG on antibody production. *International Immunopharmacology* 2018, 54, 163-168. <https://doi.org/10.1016/j.intimp.2017.11.008>.
155. Zhao, Y.; Zhao, X.; Cheng, Y.; Guo, X.; Yuan, W., Iron Oxide Nanoparticles-Based Vaccine Delivery for Cancer Treatment. *Molecular Pharmaceutics* 2018, 15 (5), 1791-1799. <https://doi.org/10.1021/acs.molpharmaceut.7b01103>.
156. Sharma, A.; Cornejo, C.; Mihalic, J.; Geyh, A.; Bordelon, D.; Korangath, P.; Westphal, F.; Gruettner, C.; Ivkov, R., Physical characterization and in vivo organ distribution of coated iron oxide nanoparticles. *Scientific Reports* 2018, 8. <https://doi.org/10.1038/s41598-018-23317-2>.
157. Chenthamara, D.; Subramaniam, S.; Ramakrishnan, S. G.; Krishnaswamy, S.; Essa, M. M.; Lin, F.-H.; Qoronfleh, M. W., Therapeutic efficacy of nanoparticles and routes of administration. *Biomaterials Research* 2019, 23 (1), 20. <https://doi.org/10.1186/s40824-019-0166-x>.
158. Turner, P.; Brabb, T.; Pekow, C.; Vasbinder, M., Administration of Substances to Laboratory Animals: Routes of Administration and Factors to Consider. *Journal of the American Association For Laboratory Animal Science* 2011, 50 (5), 600-613.
159. Shimizu, S., Routes of Administration. In *The Laboratory Mouse (Handbook)*, Elsevier: 2004; pp 527 - 541.
160. Watanabe, H.; Numata, K.; Ito, T.; Takagi, K.; Matsukawa, A., Innate immune response in Th1- and Th2-dominant mouse strains. *Shock* 2004, 22 (5), 460-466. <https://doi.org/10.1097/01.shk.0000142249.08135.e9>.
161. Meng, H.; Leong, W.; Leong, K.; Chen, C.; Zhao, Y., Walking the line: The fate of nanomaterials at biological barriers. *Biomaterials* 2018, 174, 41-53. <https://doi.org/10.1016/j.biomaterials.2018.04.056>.
162. Weaver, J.; Tobin, G.; Ingle, T.; Bancos, S.; Stevens, D.; Rouse, R.; Howard, K.; Goodwin, D.; Knapton, A.; Li, X.; Shea, K.; Stewart, S.; Xu, L.; Goering, P.; Zhang, Q.; Howard, P.; Collins, J.; Khan, S.; Sung, K.; Tyner, K., Evaluating the potential of gold, silver, and silica nanoparticles to saturate mononuclear phagocytic system tissues under repeat dosing conditions. *Particle and Fibre Toxicology* 2017, 14. <https://doi.org/10.1186/s12989-017-0206-4>.
163. Sabareeswaran, A.; Ansar, E.; Varma, P.; Mohanan, P.; Kumary, T., Effect of surface-modified superparamagnetic iron oxide nanoparticles (SPIONS) on mast cell infiltration: An acute in vivo study. *Nanomedicine-Nanotechnology Biology and Medicine* 2016, 12 (6), 1523-1533. <https://doi.org/10.1016/j.nano.2016.02.018>.
164. Tavares, A.; Poon, W.; Zhang, Y.; Dai, Q.; Besla, R.; Ding, D.; Ouyang, B.; Li, A.; Chen, J.; Zheng, G.; Robbins, C.; Chan, W., Effect of removing Kupffer cells on

- nanoparticle tumor delivery. Proceedings of the National Academy of Sciences of the United States of America 2017, 114 (51), E10871-E10880.
<https://doi.org/10.1073/pnas.1713390114>.
165. Gaharwar, U. S.; Meena, R.; Rajamani, P., Biodistribution, Clearance And Morphological Alterations Of Intravenously Administered Iron Oxide Nanoparticles In Male Wistar Rats. *Int J Nanomedicine* 2019, 14, 9677-9692.
<https://doi.org/10.2147/IJN.S223142>.
 166. Gomez-Vallejo, V.; Puigivila, M.; Plaza-Garcia, S.; Szczupak, B.; Pinol, R.; Murillo, J.; Sorribas, V.; Lou, G.; Veintemillas, S.; Ramos-Cabrer, P.; Llop, J.; Millan, A., PEG-copolymer-coated iron oxide nanoparticles that avoid the reticuloendothelial system and act as kidney MRI contrast agents. *Nanoscale* 2018, 10 (29), 14153-14164.
<https://doi.org/10.1039/c8nr03084g>.
 167. Higbee-Dempsey, E. M.; Amirshaghghi, A.; Case, M. J.; Bouché, M.; Kim, J.; Cormode, D. P.; Tsourkas, A., Biodegradable Gold Nanoclusters with Improved Excretion Due to pH-Triggered Hydrophobic-to-Hydrophilic Transition. *Journal of the American Chemical Society* 2020, 142 (17), 7783-7794.
<https://doi.org/10.1021/jacs.9b13813>.
 168. Bailly, A.; Correard, F.; Popov, A.; Tselikov, G.; Chaspoul, F.; Appay, R.; Al-Kattan, A.; Kabashin, A.; Braguer, D.; Esteve, M., In vivo evaluation of safety, biodistribution and pharmacokinetics of laser-synthesized gold nanoparticles. *Scientific Reports* 2019, 9.
<https://doi.org/10.1038/s41598-019-48748-3>.
 169. Dong, Y.; Hajfathalian, M.; Maidment, P.; Hsu, J.; Naha, P.; Si-Mohamed, S.; Breuilly, M.; Kim, J.; Chhour, P.; Douek, P.; Litt, H.; Cormode, D., Effect of Gold Nanoparticle Size on Their Properties as Contrast Agents for Computed Tomography. *Scientific Reports* 2019, 9. <https://doi.org/10.1038/s41598-019-50332-8>.
 170. Yang, L.; Kuang, H.; Zhang, W.; Aguilar, Z.; Wei, H.; Xu, H., Comparisons of the biodistribution and toxicological examinations after repeated intravenous administration of silver and gold nanoparticles in mice. *Scientific Reports* 2017, 7.
<https://doi.org/10.1038/s41598-017-03015-1>.
 171. Xue, W.; Liu, Y.; Zhang, N.; Yao, Y.; Ma, P.; Wen, H.; Huang, S.; Luo, Y.; Fan, H., Effects of core size and PEG coating layer of iron oxide nanoparticles on the distribution and metabolism in mice. *International Journal of Nanomedicine* 2018, 13, 5719-5731.
<https://doi.org/10.2147/IJN.S165451>.
 172. Niu, L.; Chu, L.; Burton, S.; Hansen, K.; Panyam, J., Intradermal delivery of vaccine nanoparticles using hollow microneedle array generates enhanced and balanced immune response. *Journal of Controlled Release* 2019, 294, 268-278.
<https://doi.org/10.1016/j.jconrel.2018.12.026>.
 173. Dur, M.; Nikolic, T.; Stefanidou, M.; McAteer, M.; Williams, P.; Mous, J.; Roep, B.; Kochba, E.; Levin, Y.; Peakman, M.; Wong, F.; Dayan, C.; Tatovic, D.; Coulman, S.;

- Birchall, J.; Consortium, E.-A., Conjugation of a peptide autoantigen to gold nanoparticles for intradermally administered antigen specific immunotherapy. *International Journal of Pharmaceutics* 2019, 562, 303-312. <https://doi.org/10.1016/j.ijpharm.2019.03.041>.
174. Yun, J. W.; Yoon, J. H.; Kang, B. C.; Cho, N. H.; Seok, S. H.; Min, S. K.; Min, J. H.; Che, J. H.; Kim, Y. K., The toxicity and distribution of iron oxide-zinc oxide core-shell nanoparticles in C57BL/6 mice after repeated subcutaneous administration. *J Appl Toxicol* 2015, 35 (6), 593-602. <https://doi.org/10.1002/jat.3102>.
175. Aravinthan, A.; Kamala-Kannan, S.; Govarathanan, M.; Kim, J., Accumulation of biosynthesized gold nanoparticles and its impact on various organs of Sprague Dawley rats: a systematic study. *Toxicology Research* 2016, 5 (6), 1530-1538. <https://doi.org/10.1039/c6tx00202a>.
176. Diaz-Arévalo, D.; Zeng, M., Nanoparticle-based vaccines: opportunities and limitations. In *Nanopharmaceuticals*, Shegokar, R., Ed. Elsevier: 2020.
177. Esani, M., The Physiological Sources of, Clinical Significance of, and Laboratory-Testing Methods for Determining Enzyme Levels. *Labmedicine* 2014, 45 (1), E16-E18. <https://doi.org/10.1309/LMBR83WM3GNJEDLS>.
178. Xia, Q.; Huang, J.; Feng, Q.; Chen, X.; Liu, X.; Li, X.; Zhang, T.; Xiao, S.; Li, H.; Zhong, Z.; Xiao, K., Size- and cell type-dependent cellular uptake, cytotoxicity and in vivo distribution of gold nanoparticles. *International Journal of Nanomedicine* 2019, 14, 6957-6970. <https://doi.org/10.2147/IJN.S214008>.
179. Salimi, M.; Sarkar, S.; Fathi, S.; Alizadeh, A.; Saber, R.; Moradi, F.; Delavari, H., Biodistribution, pharmacokinetics, and toxicity of dendrimer-coated iron oxide nanoparticles in BALB/c mice. *International Journal of Nanomedicine* 2018, 13, 1483-1493. <https://doi.org/10.2147/IJN.S157293>.
180. Farokhzad, O.; Langer, R., Impact of Nanotechnology on Drug Delivery. *ACS Nano* 2009, 3 (1), 16-20. <https://doi.org/10.1021/nn900002m>.

Chapter 2 - Synthesis and characterization of multifunctional Branched Amphiphilic Peptide bilayer conjugated gold nanoparticles

This chapter has been reproduced with permission from - Natarajan, P.; Sukthankar, P.; Changstrom, J.; Holland, C. S.; Barry, S.; Hunter, W. B.; Sorensen, C. M.; Tomich, J. M., Synthesis and Characterization of Multifunctional Branched Amphiphilic Peptide Bilayer Conjugated Gold Nanoparticles. ACS Omega 2018, 3 (9), 11071-11083.

<https://pubs.acs.org/doi/full/10.1021/acsomega.8b01633>. © 2018 American Chemical Society.

Further permissions related to the material excerpted here should be directed to the ACS.

Introduction

Branched Amphiphilic Peptides (BAPs) - bis(Ac-FLIVI)-K-K₄-CONH₂ and bis(Ac-FLIVIGSII)-K-K₄-CONH₂ spontaneously assemble at room temperature in an aqueous solution to form cationic capsules (vesicle like spherical structures) called Branched Amphiphilic Peptide Capsules (BAPCs). The origin of BAPs can be traced to an internal peptide segment (underlined), derived from the pore-lining segment of the L-type calcium channel (DPWNVFDFLIVIGSIIDVILSE).¹ When chemically synthesized, the cleaved deprotected peptide forms insoluble mechanically resistant clumps upon desiccation.² This property was ascribed to strong cohesive forces between the peptides and thus tested initially for peptide adhesion strength. Optimization of these sequences for solubility and functionality led to the creation of BAPs¹. We have previously explored the effects of solvent, temperature, pH, peptide composition, potentially destabilizing agents such as chaotropes, commercial proteases and peptide ratios on BAPCs stability, structure and assembly.²⁻⁵

Our studies show that the molecular architecture of BAPCs resembles liposomes i.e. bilayer membrane delimited vesicles. Few peptide amphiphiles self-assemble into stable bilayer membranes and/or form polymeric vesicles/capsules.⁶⁻⁸ S/TEM imaging data supported by coarse-grained modeling study suggested that BAPs form bilayer delimited capsules.^{2,3} However, no direct experimental evidence has been generated to document the existence of the bilayer. In this study, we used nanoparticles whose surface served as a scaffold to conjugate the inner leaflet. Excess peptide, delivered under controlled conditions, formed the outer leaflet of the bilayer. Self-assembly of the peptides into a bilayer on the nanoparticle surface was driven by the switch from organic to aqueous solvent, similar to the transition that leads to BAPC formation.^{1,2} This study reports the evidence that BAPs assemble as peptide bilayers in water and has led to the development of a gold nanoparticle conjugated multifunctional peptide bilayer complex, described for the first time to our knowledge.

Gold nanoparticles (AuNPs) were chosen for their favorable properties that allow for the monitoring of bilayer formation. These properties include- stability, inertness, ease of synthesis, surface functionalization, easy detection of surface alterations and high electron density suitable for imaging. Firstly, gold nanoparticles of specific sizes can be readily prepared following published procedures. Furthermore, their electronic property of Localized Surface Plasmon Resonance (LSPR) is a convenient preliminary indicator of surface functionalization. The observed LSPR wavelength (λ_{LSPR}) is dependent on the shape, size and distance between the adjacent nanoparticles and is affected by changes in the electronic environment. This provides for a visual indication since the color of AuNPs changes from orangish-red (~5 nm- 40 nm) gradually to black (~100 nm) as they begin to aggregate or bind to large molecules. Functionalized AuNPs are used to bind molecules of interest that cannot conjugate directly to the

gold. This approach has led to a variety of applications ranging from fabrication of nanoelectronics⁹ to drug delivery¹⁰, bioimaging¹¹, colorimetric assays¹², detection of DNA¹³ and proteins¹⁴.

Gold nanoparticles are typically synthesized by reduction of gold chloride in the presence of a stabilizing capping reagent (i.e. the Brust-Schiffrin¹⁵, and Turkevich¹⁶ methods). Each of these techniques result in AuNPs of varying stability and sizes. Lin, Sorensen and Klabunde¹⁷, described the facile synthesis of 5 nm gold nanoparticles stabilized by dodecanethiol in toluene. They used an inverse micelle system consisting of didodecyldimethylammonium bromide (DDAB)/water/toluene followed by addition of digestive ripening agent dodecanethiol generating highly monodisperse AuNPs. These AuNPs were one of the two systems used for our study. The reduction of gold chloride (Turkevich method) by trisodium citrate in water yields ~20 nm gold nanoparticles capped with sodium-citrate molecules. Citrate stabilizes the AuNPs keeping them well dispersed. Piella J et al.¹⁸ have shown that stoichiometric amounts of tannic acid can help reduce the AuNP size to 3.5 nm known as seeds. Although, AuNPs can be synthesized using certain peptides simultaneously for reduction and capping in a reducing buffer like HEPES^{19,20}, obtaining monodispersed AuNPs using this approach is difficult. In this study, we used citrate- AuNPs synthesized using the method standardized by Piella et al.,¹⁸ as our preferred green chemistry system for the BAP bilayer conjugation.

AuNPs are most often functionalized with thiols since the AuNP surface atoms are electrophilic and have an affinity for nucleophiles like sulfur. Self-assembled monolayers on gold have been extensively studied and reviewed²¹ but the nature of the Au-thiol bond has not been determined unambiguously. However, a recent study using Atomic Force Microscopy (AFM) has shown that the Au-S bond formed, changes from coordinate to covalent as the pH of

bond formation is transitioned from acidic to alkaline.²² The BAPs were modified with a cysteine residue on their oligolysine tail to facilitate their binding to AuNPs. Using an analogous approach, we prepared bilayer coated magnetic nanoparticles. We chose to employ magnetic beads (MNBs) modified with BAPs to assess non-specific binding partners from serum and/or cytoplasm in future studies, given their ease of recovery from biological samples over conventional AuNPs. Besides, AuNPs are also known to quench fluorescence of molecules within 10 nm of their surface.²³ The MNBs also served as a control for the Forster Resonance Energy Transfer (FRET) experiment for determination of bilayer formation.

The magnetic nanoparticles generally made of ferromagnetic metals and the recently developed gold coated nanoparticles with magnetic core, are widely used for biomedical applications.²⁴⁻²⁶ Similar to AuNPs, these can be functionalized for binding different molecules. Their magnetic property makes them useful in diagnostics as their magnetic property helps recover them from complex mixtures separating them from unbound molecules. They are also used as Magnetic Resonance Imaging (MRI) agents and studies are currently being carried out to use them for drug delivery by controlling them remotely with a magnetic device.^{24, 25} The BAP conjugated MNBs could thus find various biomedical applications.

BAPCs being highly cationic are readily taken up by eukaryotic cells and escape the late endosomes leading to successful release of surface bound nucleic acids for genetic modulation. This has been demonstrated in prior studies where they have been successfully used *in vivo* to deliver an HPV-16 DNA vaccine in mice and siRNA orally in two insect species.^{27, 28} Thus, BAP bilayer conjugated AuNPs are great candidates for simultaneous delivery of desired molecules and imaging - *in vitro* and *in vivo*. The study presented has thus given us peptide bilayer

conjugated metallic nanoparticle systems that can find applications in binding assays, imaging and delivery.

Materials and methods

Solid phase peptide synthesis.

The peptides were synthesized as previously published³ using an ABI 431 automated peptide synthesizer using Fmoc chemistry on 0.1 mmol scale using CLEAR amide resin (Peptides International, Louisville, KY). For the bis(Ac-FLIVIGSII)-K-K₄-CONH₂ peptides only, the initial amino acid was added manually and was allowed to react for five minutes. Once this was completed, the resin was rinsed and capped with the acetyl capping cocktail to block any other unoccupied active sites on the resin. The remainder of the synthesis was completed on the automated peptide synthesizer. The peptides were cleaved from the resin using a solution of 92% TFA, 5% thioanisole and 2% EDT for 90 min at room temperature. The liquid was removed and poured into ice-cold diethyl ether. Three additional washes of the peptide precipitate were done with diethyl ether. The bis(Ac-FLIVI)-K-K₄-CONH₂ peptide was then suspended in distilled deionized water and lyophilized. The bis(Ac-FLIVIGSII)-K-K₄-CONH₂ peptide was dried directly from the diethyl ether without suspending in water. MALDI-TOF MS was used to ensure correct product formation with the peptide spotted in a DHB matrix (Sigma-Aldrich, St. Louis, MO) on a Bruker Ultraflex II instrument.

Synthesis of BAP-AuNPs using dodecanethiol capped gold nanoparticles.

Prior to addition of peptide to AuNPs in toluene (Fisher Scientific, Inc., New Jersey), the peptide was deprotonated by dissolving bis(Ac-FLIVIGSII)-K-K₄-C-CONH₂ peptide in water

and adjusting the pH to 14 with ammonium hydroxide (Fisher Scientific, Inc., New Jersey), incubating it for 1 hour and then drying it in vacuo. This allows the peptide to easily dissolve in toluene. A 2 - fold excess of peptide was added to the dodecanethiol capped AuNPs in toluene and then refluxed under argon for 90 min leading to substitution of the dodecanethiol with bis(Ac-FLIVIGSII)-K-K₄-C-CONH₂ peptide. This BAP monolayer conjugated AuNPs in toluene was dried in vacuum and redispersed in 50% Trifluoroethanol in water (Sigma- Aldrich, Inc., Wisconsin). The excess unreacted peptide was removed by filtering it through a 30 KDa MWCO Amicon, Ultra 0.5 mL filters (Merck, Millipore Inc., Burlington. MA). A 1.1:1.0 excess of bis(Ac-FLIVI)-K-K₄-CONH₂: bis(Ac-FLIVIGSII)-K-K₄-CONH₂ peptide was added to the BAP monolayer conjugated AuNPs with thorough mixing and dried. For Scanning Transmission Electron Microscopy (STEM) we used 30 mol% of bis(Ac-FLIVI)-K-K₄-C(CH₃Hg)-CONH₂ instead. Rehydration of this mix under mild acidic conditions gives BAP bilayer modified AuNPs.

Replacement of Trifluoroacetic Acetate (TFA-salt) peptide counter ion with chloride.

The TFA-salt replacement was carried out by the acid substitution protocol mentioned in Andrushchenko et al.³² The peptides were solubilized in a 1:1 ethanol : water solution to prevent self-assembly into capsules. Hydrochloric acid, 1mM, (Fisher Scientific, Inc., New Jersey) was added with thorough mixing, to the peptide solution. The peptide solution was then frozen at -80°C followed by lyophilization using a Lab Conco (Free Zone 2.5-liter, benchtop) freeze dryer and Savant concentrator. This process was repeated for an additional 4 times with 100 μM HCl. The complete dissolution of peptides was ensured to ensure efficient reaction. The efficiency of TFA-salt displacement from peptides by HCl was determined by 1D Fluorine (¹⁹F) NMR scans of peptides after every wash.

Synthesis of citrate capped gold nanoparticles.

The citrate capped gold nanoparticles were prepared as described in Piella et al.¹⁸ For the preparation of 3.5 nm gold nanoparticles, 100 mL of freshly prepared 2.2 mM sodium citrate (Fisher Scientific, Inc., New Jersey) solution in deionize-distilled water (DDI water) with 668 μ L of 150 mM potassium carbonate (Fisher Scientific, Inc., New Jersey) was refluxed at 70 °C in a round bottom flask, under vigorous stirring on a Corning magnetic heat-stir plate. 66.8 μ L of freshly prepared 2.5 mM tannic acid (Sigma- Aldrich, Inc., Wisconsin) was added, followed by 668 μ L of 25 mM gold chloride (HAuCl₄) (Sigma- Aldrich, Inc., Wisconsin) under vigorous stirring. The color of the solution turned from brownish - black to orangish - red in less than a minute. The solution was heated for an additional 20 minutes to ensure complete reduction of the HAuCl₄. On cooling, the citrate capped gold nanoparticles were washed using 20 mL, 10K MWCO-Omega filters (Pall Corporation Centrifugal Devices) to remove excess salts. The concentrated gold nanoparticles, free of excess salts was diluted back to its original concentration with DDI water. The UV-Vis spectrum was recorded from 200 to 800 nm at the rate of 300 nm/min and 0.5 nm data interval with baseline correction using water as the blank on Cary 50-Bio UV-Vis Spectrophotometer (Varian Inc., Palo Alto, CA).

Modification of citrate capped gold nanoparticles with peptide bilayer.

The concentration of peptide required to completely cover the surface of the gold nanoparticles was theoretically calculated to be 2 μ M for a solution containing $\sim 10^{13}$ gold nanoparticles of average size 3.6 nm. Prior to addition of the peptides, the nanoparticles were sonicated using a FS20 (Fisher Scientific, Inc., New Jersey) water bath sonicator so as to evenly disperse the nanoparticles in solution. This breaks any small clusters of nanoparticles and

therefore increases the surface area accessible for peptide binding. 0.2 mM bis(Ac-FLIVIGSII)-K-K₄-C-CONH₂ peptide (Concentration was calculated using Phe absorbance at 257.5 nm with $\epsilon=195 \text{ M}^{-1} \text{ cm}^{-1}$) in 75% ethanol water was added to the citrate capped gold nanoparticles in 75% ethanol. The organic solvent content was maintained at 75% to prevent self-assembly of the free peptides and to prevent the AuNP bound peptides from aggregating due to hydrophobic tail interactions. The AuNP- bis(Ac-FLIVIGSII)-K-K₄-C-CONH₂ peptide mix was incubated for 1 hr at room temperature with constant mixing to ensure maximum binding and coverage of the nanoparticle surface. The bis(Ac-FLIVIGSII)-K-K₄-C-CONH₂ adducted AuNP were washed by centrifugation at 37,000 RCF for 30 min in PTFE centrifuge tubes (Thermo Scientific, Nalgene Products Inc. New York) on a JA-20 rotor in a Model J2-21 Beckman centrifuge. The AuNPs were washed three times and after every wash the AuNPs were suspended in 100% ethanol. After the third wash, the AuNP- bis(Ac-FLIVIGSII)-K-K₄-C-CONH₂ was suspended in a minimal amount of 100% TFE. The (bis(Ac-FLIVIGSII)-K-K₄-CONH₂) peptide (0.2 mM) was added to the AuNP- bis(Ac-FLIVIGSII)-K-K₄-C-CONH₂ monolayer in TFE and mixed well. Excess i.e. 25 times more water was added to this TFE solution gradually so that the organic solvent concentration is below 10% and incubated for 30 min with constant mixing. The AuNP-BAPs were then washed through 10K MWCO filters to remove any excess unbound peptides and were redispersed in minimal DDW water to obtain a concentrated AuNP-BAP solution.

Transmission Electron Microscopy (TEM) and Energy Dispersive X-ray (EDX).

20 μL of the sample was placed onto a 200 sq. mesh formvar coated grid for 10 min and the excess sample was wicked off using a filter paper. Samples were given 30 min to dry completely prior to visualization. The energy of the X-ray emitted by the heavy metals i.e. gold

and mercury were detected using an EDX detector linked to the Hitachi S-4800 (Hitachi high Tech, Inc., Pleasanton, CA) S/TEM instrument.

FRET experiment.

The gold nanoparticles with the requisite peptide bilayer i.e. bis(Ac- F_{CN}LIVIGSII)-K-K₄-C-CONH₂ - bis(Ac-WLIVIGSII)-K-K₄-C-CONH₂ bilayer, were prepared in the same way as the gold nanoparticles with the BAP bilayer as mentioned above. The Magnetic Nanobeads were obtained from Ocean Nanotech (San Diego, CA). bis(Ac- F_{CN}LIVIGSII)-K-K₄-C-CONH₂ was covalently linked to the maleimide on the functionalized MNBs in 75% ethanol solution by adjusting the pH to 7.4 using 0.1 N NaOH. The MNBs were washed on an Invitrogen bead separator (Invitrogen Corp., Carlsbad, CA) and the bilayer was formed by adding excess bis(Ac-WLIVIGSII)-K-K₄-C-CONH₂ and dispersing them in water. The MNBs with the peptide bilayer were washed 3 times by giving sufficient time for the beads to separate out. The bis(Ac-FLIVIGSII)-K-K₄-C-CONH₂ modified at Phe with CN were excited at 240 nm and the emission was recorded as a scan from 250 to 500 nm on Varian Cary Eclipse Fluorescence Spectrophotometer (Varian Inc., Palo Alto, CA) at a scan rate of 600 nm/min and data interval of 1nm. The slit was adjusted between 5 and 10, as per the fluorescence intensity obtained from the sample in order to obtain significant fluorescence intensity reading. The samples were placed in a quartz cuvette with a path length of 0.3 cm (Starna Cells Inc., Atascadero, CA)

To test the effect of 100% TFE on dissociation of the outer peptide leaflet on BAP bilayer conjugated AuNPs, they were dried *in vacuo* as previously described. Neat TFE was added to them and then thoroughly mixed to completely resuspend the AuNPs. They were incubated at R.T. for 30 min. The BAP bilayer conjugated AuNPs were washed using a 30K MWCO spin

filter to remove any peptides separated from the bilayer. The NPs were again resuspended in the same volume of 100% TFE to reestablish the initial concentration. The fluorescence spectrum was then collected by excitation at 240 nm, slit = 5 and scanned for emission wavelengths between 250 to 450 nm.

CD spectroscopy measurements.

CD data was collected on a Jasco J-815 CD spectrophotometer (Jasco Analytical Instruments, Easton, MD) using a 1 mm path-length cylindrical quartz cuvette (Starna Cells Inc., Atascadero, CA). The Spectra were obtained by scanning from 260 to 190 nm at scan rate of 50 nm/min with 1 nm step intervals. The final spectra obtained was an average of five scans with the ellipticity measured in mdeg. The data was corrected for the solvent and the spectra were smoothed using a Savitsky–Golay filter on the Spectra Analysis software provided by the manufacturer (Jasco Inc., Easton, MD).

Thermo-Gravimetric Analysis (TGA).

The thermal analysis of the AuNPs with peptides was carried out using a TGA-50, Shimzadu thermogravimetric analyzer, (Shimzadu Corp., Kyoto, Japan) by increasing the temperature from 25 °C to 800 °C at the rate of 5 °C/min and nitrogen gas flow rate at 10ml/min.

Results and discussion

Generation of Branched Amphiphilic Peptide (BAP) bilayer on gold nanoparticles in toluene.

Dodecanethiol capped gold nanoparticles were initially used to prepare peptide monolayer adducted AuNPs (BAP monolayer-AuNPs) suspended in toluene.¹⁷ The BAPs used for this preparation contained an additional cysteine residue at the C-terminus (bis (Ac-FLIVIGSII)-K-K₄-C-CONH₂). These peptides were pretreated with ammonium hydroxide to deprotonate the lysyl residues, which renders the peptides fully soluble in toluene. The dodecanethiol coated AuNPs were refluxed at 70 °C with excess peptides in toluene, facilitating cysteine modified BAP monolayer self-assembly on the gold surface. Thiols with longer carbon chains displace the smaller carbon chain thiols and therefore, the thiol containing branched peptides formed a self-assembled peptide monolayer on AuNPs through this ligand substitution method. Subsequent transfer of the BAP monolayer-AuNPs into 1:1 TFE:H₂O gave a monodispersed colloidal solution of AuNPs with the branched N-terminal tails of the peptides solvent exposed. Such colloidal suspensions in sealed containers have proven to be stable for greater than six months.

The BAP monolayer adducted AuNPs in 1:1 TFE:H₂O when dried on TEM copper grid formed aggregates (**Figure 2.1A**). This is due to increase in the H₂O concentration as TFE evaporated resulting in association of the branched FLIVIGSII segments of the peptide generating the array of aggregates shown.

Water-soluble, peptide bilayer - gold nanoparticles (BAP-AuNPs) were generated by adding a 1.1:1.0 excess of bis(Ac-FLIVI)-K-K₄-CONH₂ to the bis(Ac-FLIVIGSII)-K-K₄-C-CONH₂ -adducted AuNPs in the 1:1 TFE:H₂O mixture, followed by drying slowly to reduce the

TFE concentration. The sample was subsequently fully dried and then rehydrating yielded monodispersed BAP-AuNPs (**Figure 2.1B**). The presence of excess peptides in an aqueous environment drives the hydrophobic tails of the BAPs to interact with each other, thus leading to the formation of a BAP bilayer on the gold nanoparticles. The two parent peptide sequences - bis(Ac-FLIVI)-K-K₄-CONH₂ and bis(Ac-FLIVIGSII)-K-K₄-CONH₂ were modified with fluorescent and heavy metal tags as required. The amino acid sequences of these peptides used for all experiments in this study have been summarized in (**Figure 2.1C**).

For the scanning transmission electron microscopy (STEM) studies, 30 mol% of bis (Ac-FLIVI)-K-K₄-Cys(Hg-CH₃)-CONH₂ was added to the peptide monolayer conjugated to AuNPs. Energy dispersive X-ray (EDX) analysis on a scanned single 10 nm BAP-AuNPs showed overlapping signals for the gold and the mercury containing peptide in the outer leaflet, confirming its association with the inner leaflet (**Figure 2.1D**). While most BAP-AuNPs were 5 nm in diameter a few 10 nm particles were observed. Analyses of larger sizes provided a better signal to noise ratio.

Dodecanethiol capped gold nanoparticles were initially used to prepare peptide monolayer adducted AuNPs (BAP monolayer-AuNPs) suspended in toluene.¹⁷ The BAPs used for this preparation contained an additional cysteine residue at the C-terminus (bis (Ac-FLIVIGSII)-K-K₄-C-CONH₂). These peptides were pretreated with ammonium hydroxide to deprotonate the lysyl residues, which renders the peptides fully soluble in toluene. The dodecanethiol coated AuNPs were refluxed at 70 °C with excess peptides in toluene, facilitating cysteine modified BAP monolayer self-assembly on the gold surface. Thiols with longer carbon chains displace the smaller carbon chain thiols and therefore, the thiol containing branched peptides formed a self-assembled peptide monolayer on AuNPs through this ligand substitution

method. Subsequent transfer of the BAP monolayer-AuNPs into 1:1 TFE: H₂O gave a monodispersed colloidal solution of AuNPs with the branched N-terminal tails of the peptides solvent exposed. Such colloidal suspensions in sealed containers have proven to be stable for greater than six months.

The BAP monolayer adducted AuNPs in 1:1 TFE: H₂O when dried on TEM copper grid formed aggregates (**Figure 2.1A**). This is due to increase in the H₂O concentration as TFE evaporated resulting in association of the branched FLIVIGSII segments of the peptide generating the array of aggregates shown.

Water-soluble, peptide bilayer - gold nanoparticles (BAP-AuNPs) were generated by adding a 1.1:1.0 excess of bis(Ac-FLIVI)-K-K₄-CONH₂ to the bis(Ac-FLIVIGSII)-K-K₄-C-CONH₂ -adducted AuNPs in the 1:1 TFE:H₂O mixture, followed by drying slowly to reduce the TFE concentration. The sample was subsequently fully dried and then rehydrating yielded monodispersed BAP-AuNPs (**Figure 2.1B**). The presence of excess peptides in an aqueous environment drives the hydrophobic tails of the BAPs to interact with each other, thus leading to the formation of a BAP bilayer on the gold nanoparticles. The two parent peptide sequences – bis(Ac-FLIVI)-K-K₄-CONH₂ and bis(Ac-FLIVIGSII)-K-K₄-CONH₂ were modified with fluorescent and heavy metal tags as required. The amino acid sequences of these peptides used for all experiments in this study have been summarized in (**Figure 2.1C**).

For the scanning transmission electron microscopy (STEM) studies, 30 mol% of bis (Ac-FLIVI)-K-K₄-Cys(Hg-CH₃)-CONH₂ was added to the peptide monolayer conjugated to AuNPs. Energy dispersive X-ray (EDX) analysis on a scanned single 10 nm BAP-AuNPs showed overlapping signals for the gold and the mercury containing peptide in the outer leaflet, confirming its association with the inner leaflet (**Figure 2.1D**). While most BAP-AuNPs were 5

nm in diameter a few 10 nm particles were observed. Analyses of larger sizes provided a better signal to noise ratio.

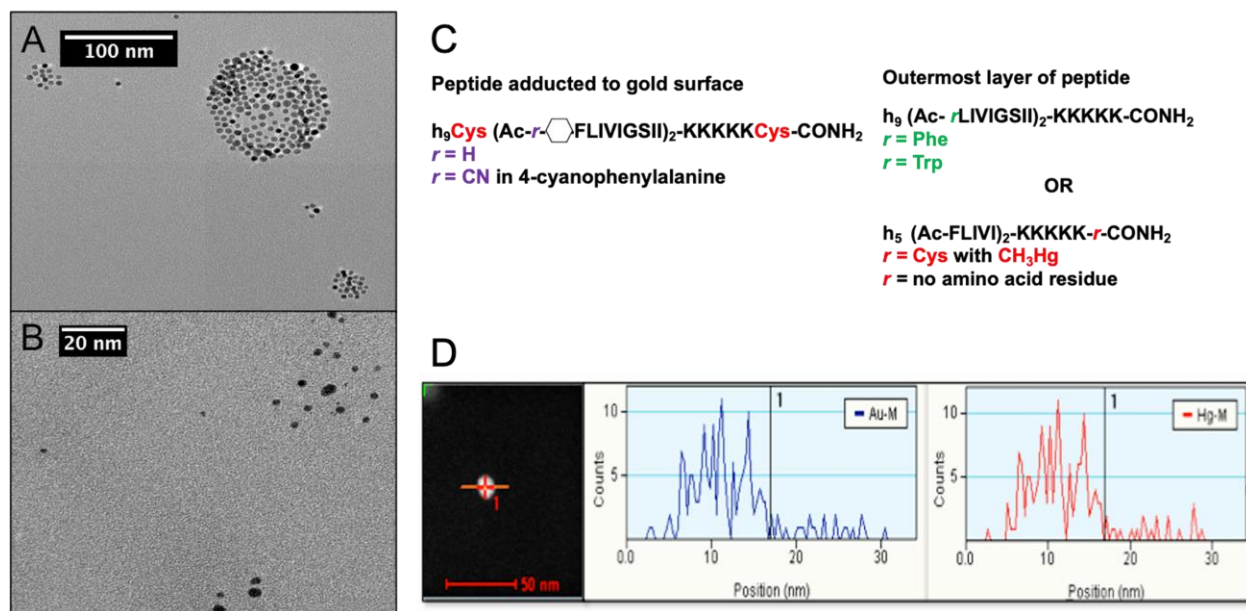


Figure 2.1. Characterization of dodecanethiol protected gold nanoparticles, surface modified with Branched Amphiphilic Peptides (BAPs)

Transmission electron microscopy (TEM) image of (A) bis(Ac-FLIVIGSII)-K-K₄-C-CONH₂ monolayer bound gold nanoparticles and (B) bis(Ac-FLIVIGSII)-K-K₄-C-CONH₂ (inner leaflet) and bis(Ac-FLIVI)-K-K₄-Cys(Hg-CH₃)-CONH₂ (outer leaflet) bilayer bound gold nanoparticles in water. (C) Amino acid residue sequence of BAPs with modified versions synthesized for use in different experiments of this study, for conjugation to the gold surface via cysteine (left) and the peptides (right) added to form the second layer. The peptides were modified with fluorescent residues such as 4-cyanophenylalanine (PheCN) and tryptophan (W) as well as heavy metals like mercury (Hg) to determine and characterize the peptide bilayer formation on gold nanoparticles. (D) Energy-dispersive X-ray (EDX) spectra showing the M shells of co-localized gold and mercury in BAP-AuNPs. The right panel shows the 10 nm Hg-labeled peptide bilayer Au particle that was scanned. The top-left panel shows the spectral counts recorded while scanning the surface of gold, while the bottom-left panel shows the spectral counts observed for mercury contained in the outer leaflet comprising solely bis(Ac-FLIVI)-K-K₄-Cys(Hg-CH₃)-CONH₂ peptide.

Aqueous citrate capped gold nanoparticles synthesis – A green chemistry approach.

Although the toluene-based system gave us the desired BAP-AuNPs, we wanted to adopt a green chemistry approach for synthesizing these nanoparticles. The TEM images of the citrate-AuNPs synthesized using a standardized protocol showed well dispersed AuNPs (Figure 2.2A,

B). The UV-Vis spectrum of the citrate-AuNPs gave a sharp localized surface plasmon resonance spectral peak at 505 nm (**Figure 2.2C**), which is in agreement with the data published by Piella et al.¹⁸ Since sodium citrate molecules are small ligands, the LSPR peak is not significantly affected by the ligand on the surface and therefore one can consider that the plasmon resonance is characteristic of the gold core itself. The TEM images were used to measure the size of the nanoparticles using ImageJ software.²⁹ The histogram (**Figure 2.2D**) plotted using the data obtained by measuring the size of ~600 citrate-AuNPs, shows a fairly monodisperse population of AuNPs with an average size of 3.56 nm and standard deviation of 0.667 nm. The number of nanoparticles synthesized in solution was determined using the absorbance at λ_{LSPR} and extinction coefficient calculated using the Eq.1-

Equation 1 $\ln \varepsilon = 3.32 \ln(d) + 10.8$

where 'd' is the diameter of the spherical AuNPs in nm and ε is the extinction coefficient of AuNP in $M^{-1} cm^{-1}$. This equation was experimentally derived by Liu et al.³⁰ where they examined three different types of capped AuNPs (citrate, olelyamine and dodecanethiol capping) to standardize the extinction coefficient values for AuNPs of different sizes and capping agents. The extinction coefficient for 3.6 nm citrate-AuNPs was calculated to be $3.44 \times 10^6 M^{-1} cm^{-1}$ using eq.1. Using Beer-Lambert's law, the average of number AuNPs in solution was calculated to be $\sim 10^{13}$ AuNPs/mL.

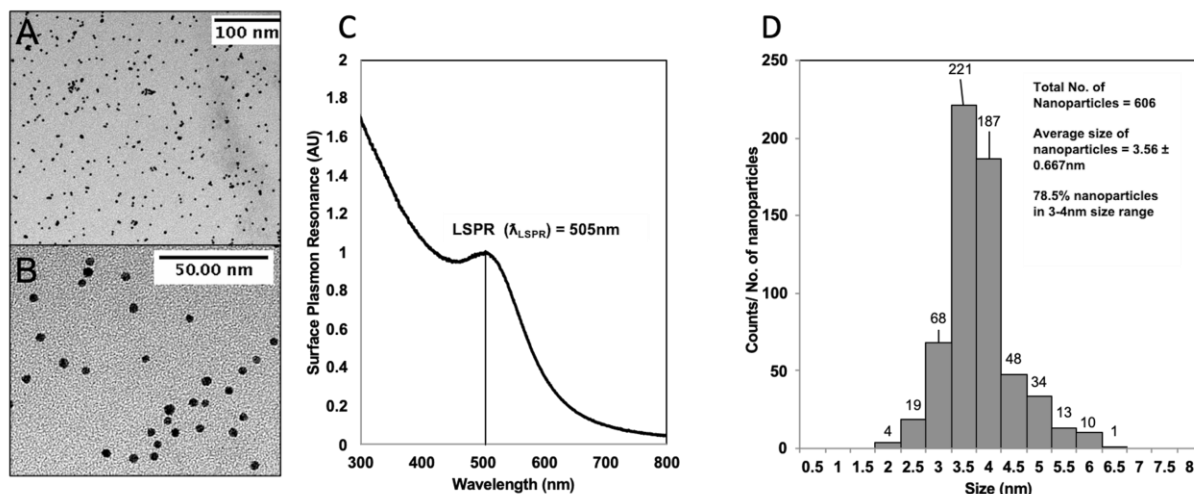


Figure 2.2. Characterization of aqueous, citrate capped gold nanoparticles

(A, B) TEM images of citrate AuNPs at two different magnifications. (C) Representative UV-Vis spectra plotted using normalized absorbance values for the AuNPs between 300 - 800 nm with Localized Surface Plasmon resonance peak (λ_{LSPR}) at 505 nm. (D) The histogram depicts the size distribution of the AuNPs. The size was calculated for ~600 AuNPs in two different TEM image fields using ImageJ software.²⁹ The histogram is unimodal showing a narrow distribution of AuNP sizes. The numbers on top of each bar represents the number of AuNPs in each class. The average size of the AuNPs calculated to be 3.56 +/- 0.667 nm with 78.5% of gold nanoparticles in the 3 to 4 nm size range.

Branched amphiphilic peptide monolayer self-assembly on citrate capped gold nanoparticles.

The BAPs were subsequently conjugated to citrate-AuNPs to form self-assembled peptide monolayer, using the same chemistry used to prepare the BAP monolayer-AuNPs previously described i.e. ligand substitution by Au-thiol bond formation but in 75% ethanol. The citrate molecules only weakly bind to Au surface and are thus displaced easily.¹⁸ The BAPs were added to the citrate-AuNPs in 75% ethanol solution to prevent self-assembly of the peptides into capsules. However, the citrate-AuNPs alone used as the control aggregated in the presence of ethanol. This was attributed to the presence of excess salts in the citrate-AuNPs solution that lead to the formation of linear aggregates in ethanol. The linear aggregates have been thought to form due to the charge on the citrate molecules leading to aggregation in a low dielectric solvent like

ethanol and increases with increase in ethanol solvent concentration.³¹ This hindered the peptide's binding to AuNPs.

To prevent the aggregation of the AuNPs in ethanol so that the entire surface of the AuNPs was accessible for the binding of the peptides, the citrate-AuNPs were washed through a 10K MWCO. Removal of the excess salts such as the unreacted gold chloride and sodium citrate prevents aggregation of the AuNPs in ethanolic solutions. However, aggregation of AuNPs was observed upon the addition of peptides to form the BAP-monolayer even after the removal of excess salt. The UV-Vis spectra showed a broad LSPR peak with high absorbance in the 600nm - 800nm region (**Figure B.3**), a characteristic of large AuNPs. This was confirmed by Dynamic Light Scattering (DLS) where large aggregates (100-2000 nm) were detected (**Figure B.3A & Table B.1**). The observation suggested that the peptides while able to displace the citrate ions were not reacting efficiently with the gold surface thus leaving much of the surface unprotected and prone to aggregation. The presence of hydrophobic trifluoroacetic acid (TFA) salts that were present as counter ions associated with the C-terminal lysines were thought to hinder the binding of peptide to the Au surface.

To address this possibility, the TFA salts were replaced with chloride. The substitution was accomplished by multiple rounds of dilute HCl washes followed by freeze-drying, as previously reported in Andrushchenko et al.³² The process was monitored by NMR following the successive decreases in the fluorine (¹⁹F) signal intensity with each washing step. By the end of the 5th wash no detectable fluorine signal was present suggesting most of the TFA salt had been exchanged with chloride (**Figure B.4**). When these chlorides containing peptides were conjugated to AuNPs we observed significant differences in the dispersion of peptide adducted AuNPs. (**Figure B.4**) The use of the peptides after chloride replacement eliminated the

aggregation of AuNPs in water/alcohol mixture. For all subsequent experiments, we therefore chose to use the chloride counter ion of peptide. In case of the peptides used in the toluene-based system, the deprotonation of the lysyl residues using ammonium hydroxide followed by freeze-drying may have caused loss of most of the TFA counter ions. Besides, the hydrophobicity of toluene coupled with refluxing at high temperature could have helped in promoting the conjugation of peptides to AuNPs. Reacting the chloride form of bis(Ac-FLIVIGSII)-K-K₄-C-CONH₂ with the citrate-AuNPs yielded the desired product as binding of excess peptide to AuNPs was evidenced by a slight color change and a red-shift in the gold plasmon wavelength. This change is indicative of a change in the electronic environment of the gold nanoparticles.

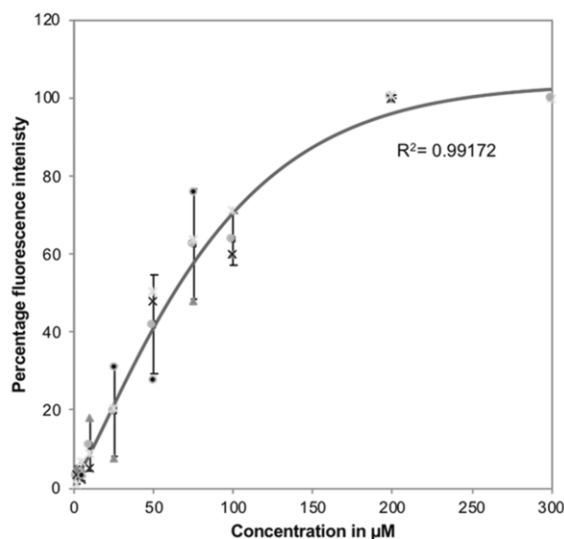


Figure 2.3. Fluorescence response for different concentration of bis(Ac- FCNLIVIGSII)-K-K₄-C-CONH₂ peptide added to gold nanoparticle surface

Different concentrations of bis(Ac- FCNLIVIGSII)-K-K₄-C-CONH₂ peptide, ranging from 2 μM to 300 μM were added to gold nanoparticles in order to determine the maximum concentration at which the gold surface is saturated with the monolayer-forming peptide. The fluorescence intensity was normalized for different batches of the samples prepared, as the percentage of fluorescence intensity of the AuNPs with maximum peptide concentration.

A titration experiment with the cysteine containing peptide bis(Ac-F_{CN}LIVIGSII)-K-K₄-C-CONH₂ was conducted to ensure complete coverage of the AuNP surface. A cyanophenylalanine (Phe_{CN}) fluorescent tag was incorporated into the peptide sequence because it does not alter the secondary structure of the peptide and can also serve as a good donor for exciting tryptophan residues by Forster Resonance Energy Transfer (FRET).³³ Increasing concentrations of the fluorescent Phe_{CN} containing peptide were tested, until no further increase in fluorescence was observed. The cyanophenylalanine group when excited at 240 nm has an emission maximum between 280-300 nm.³⁴ The concentration of the bis(Ac- F_{CN}LIVIGSII)-K-K₄-C-CONH₂ was varied from 1 μM to 0.3 mM. The BAP monolayer-AuNPs were prepared using the same protocol previously described. The fluorescence intensity of peptides bound to AuNPs did not increase beyond 0.2 mM peptide concentration and the AuNP surface appears to be saturated (**Figure 2.3**). Thus, 0.2 mM peptide concentration was used subsequently for preparation of all BAP monolayer-AuNPs.

After addition of the peptide, subsequent washes via centrifugation removed excess unbound peptide. The pelleted AuNPs were then redispersed in 100% TFE to ensure a monodispersed solution of AuNPs with the hydrophobic tails of the BAPs solvent exposed. As the dielectric of the solvent is increased by lowering the alcohol content by evaporation or dilution with water, the branched hydrophobic sequences find each other and form bilayers between adjacent AuNPs. Since the peptides are very small and lack electron density, they are invisible in the TEM images (**Figure 2.4A, B**). The TEM images of the BAP monolayer adducted AuNPs in water shows a fairly uniform spacing between the nanoparticles. This gap represents the peptide bilayer. Using these TEM images we calculated the width of the bilayer as the distance between two adjacent electron dense AuNPs. The distance between two bis(Ac-

FLIVIGSII)-K-K₄-C-CONH₂ bound AuNPs, measured for ~80 pairs of AuNPs was found to ~1.9 nm with a S.D. of 0.5 nm. The bis(Ac-FLIVIGSII)-K-K₄-C-CONH₂ BAP bilayer is tightly packed with a packing density of 0.85 and are known to form smaller BAPCs as compared to bis(Ac-FLIVI)-K-K₄-CONH₂ only bilayer with a packing density of 0.68.³⁵ Thus, when the distance between two AuNPs bound by bis(Ac-FLIVI)-K-K₄-C-CONH₂ peptides was measured, the average size of the bilayer was found to be ~2.92nm with S.D. of 0.3 nm for 80 pairs. We could see significant difference ($p \leq 0.05$, student's unpaired t-test) between the sizes of all bis(Ac-FLIVIGSII)-K-K₄-C-CONH₂ and bis(Ac-FLIVI)-K-K₄-C-CONH₂ only peptide bilayers as expected based on data from prior studies, providing further proof of peptide binding to gold nanoparticles.

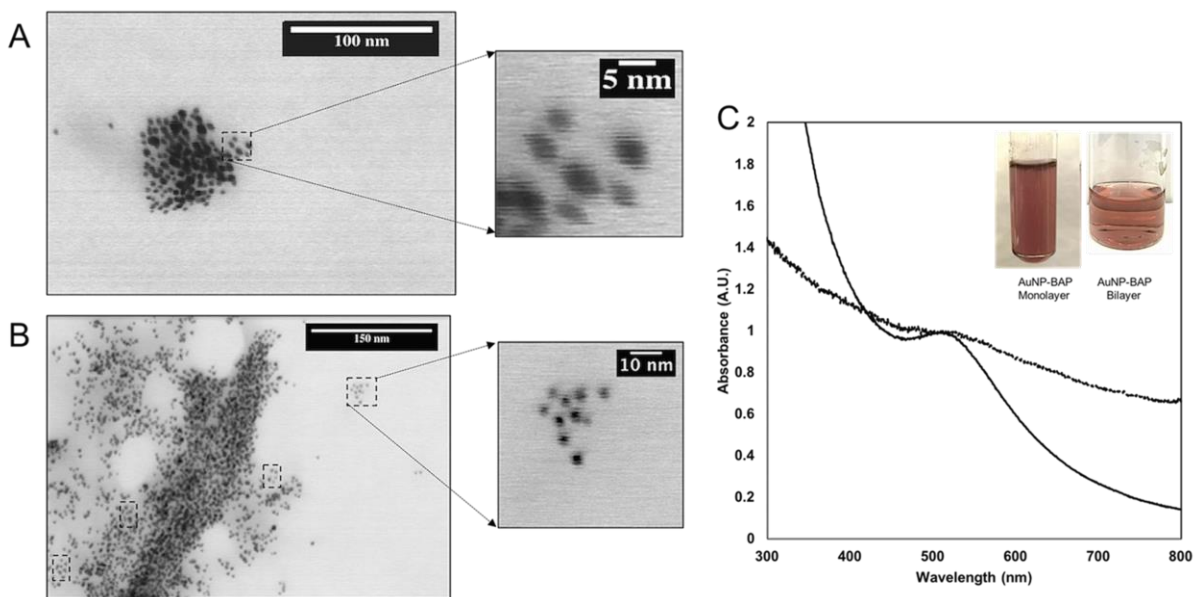


Figure 2.4. TEM and UV-Vis spectral analysis of BAP monolayer adducted gold nanoparticles

(A) TEM image showing aggregates of gold nanoparticles modified with bis(Ac-FLIVIGSII)-K-K₄-C-CONH₂ peptide monolayer in water. The distance between two nanoparticles represents the thickness of the bis(Ac-FLIVIGSII)-K-K₄-CONH₂ BAP bilayer and was measured for the uniformly spaced nanoparticles in clusters (example-dashed boxes). The average size of the bis(Ac-FLIVIGSII)-K-K₄-CONH₂ bilayer calculated for approximately 80 pairs of AuNPs is 1.95 +/- 0.5 nm. (B) TEM image

showing aggregates of bis(Ac-FLIVI)-K-K₄-C-CONH₂ monolayer adducted AuNPs in water. The average size of the bis(Ac-FLIVI)-K-K₄-CONH₂ bilayer calculated for ~80 pairs of AuNPs is 2.92 +/- 0.437 nm. The average sizes of the bilayers were statistically determined using the students unpaired t-test, p≤0.05 (C) UV-Vis spectra of BAP monolayer-AuNPs aggregate in water (grey line) and of BAP-AuNPs in water (black line) for comparison. Inset shows the clear colloidal solution of mono dispersed AuNP-BAPs (right) and the turbid AuNP-BAP monolayers in water (left).

Branched amphiphilic peptide bilayer formation on the surface of gold nanoparticles.

Peptide bilayers were assembled by adding a second layer of peptides to the BAP monolayer- AuNPs in TFE. The free peptide added to form the bilayer was added at the same concentration (0.2mM) used to saturate the surface of AuNPs, to form the peptide monolayer. The second layer in theory should require more peptide than the monolayer due to increased surface area. This peptide concentration should be ideal to form the outer leaflet on most of the monolayer coated AuNPs while simultaneously limiting formation of higher number of BAPCs by excess, unbound free peptides in solution. Assembly of the peptides occurred as the water content of the solution was gradually increased until the water content exceeds 75%, as described in Methods. This increase in the dielectric value of the solvent drives the branched hydrophobic segments of the bis(Ac-FLIVIGSII)-K-K₄-CONH₂ peptides to associate with the hydrophobic peptide tails bound to the AuNPs thus forming a bilayer. TEM images of the BAP-AuNPs (**Figure 2.5A, B**) show NPs that are fairly dispersed due to the cationic nature of the BAP-AuNP surface leading to the electrostatic repulsion of the individual particles. This was observed as a red-shift in the LSPR spectral wavelength due to the change in the electronic environment of the AuNPs, also observed as a color change in the AuNP colloidal suspension solution. The LSPR spectral position shifted from ~505 nm for citrate-AuNPs to ~514 nm for BAP-AuNPs in water. The UV-Vis spectra from five separate reactions of BAP-AuNPs, similarly prepared showed an average LSPR peak at 514.78 nm with a S.D. of 2.81 nm (**Figure 2.5 C**). Since LSPR spectral position is highly dependent on size, shape and composition as well as solvent refractive index,

an overlap in the UV-Vis spectra indicates the reproducibility of protocol. A few aggregates of BAP-AuNPs are present as seen in TEM images suggesting that some of the BAP monolayer-AuNPs were still able to interact as the water content was increased.

The bilayer modified BAP-AuNPs were vacuum dried and easily resuspended in water as fairly monodispersed particles upon rehydration. On the other hand, dried BAP monolayer - AuNPs could not be suspended in water without forming large aggregates. They precipitated out of solution to yield a colorless solution. However, dried BAP monolayer-AuNPs could be readily resuspended in 100% TFE. This difference in solvent preference of BAP monolayer-AuNPs with their exposed hydrophobic tails and bilayer modified BAP-AuNPs with their solvent exposed positively charged lysine tail, indicates that the BAPs have assembled into a bilayer on AuNP surface.

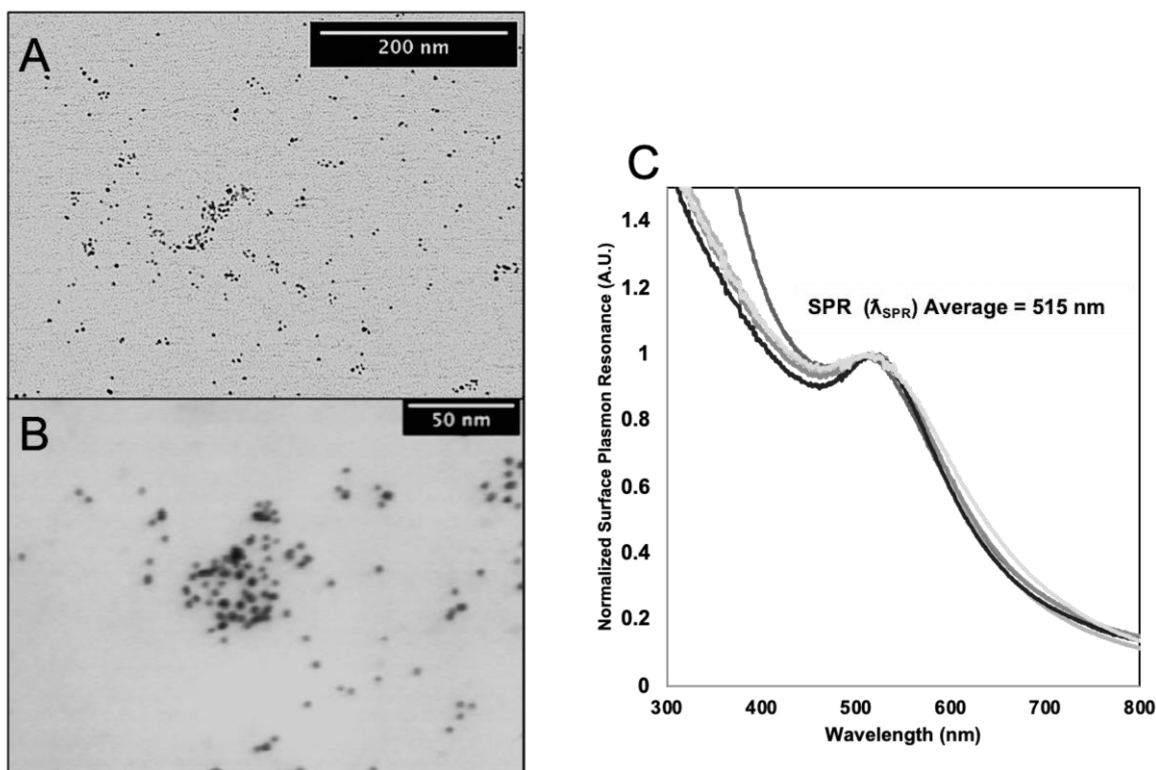


Figure 2.5. TEM images and UV-Vis spectra of bis(Ac-FLIVIGSII)-K-K₄-CONH₂ BAP bilayer adducted gold nanoparticles

(A) Representative TEM image of BAP bilayer adducted gold nanoparticles at a lower magnification capturing the well-dispersed AuNPs in a large image field. Few if any aggregates of the AuNPs are observed. (B) Relatively higher magnification TEM image of the BAP-AuNPs. (C) Overlapping UV-Vis spectra of representative three different batches of BAP-AuNPs with normalized absorbance, showing localized surface plasmon resonance peak at ~515 nm.

Thermogravimetric analyses (TGA) on both the monolayer and bilayer modified bis(Ac-FLIVIGSII)-K-K₄-C-CONH₂ NPs gave quantitative information on the number of peptides coupled to the AuNPs. Analyses to show interactions of different decomposition profiles due to difference in the nature of the bonds formed between the two peptide layers and the peptide-AuNPs were conducted. In this study after determining the initial weight of the sample, the temperature was slowly increased from R.T. to 800 °C. The amino acids decompose into CO₂ and H₂O over a particular temperature range depending on their composition. As expected, decomposition of the peptides was observed between 200 °C and 300 °C as a sharp decline in the

weight of the sample. At the end of the heating cycle the weight of the remaining sample was determined. The weight was attributed solely to the metallic nanoparticles, since the gold itself is not affected over this temperature range. The BAP monolayer-AuNPs (**Figure 2.6A**) showed ~10% weight loss between 100 °C to 200 °C which was attributed to decomposition of water absorbed by the peptides from the atmosphere. An approximate 40% weight loss was seen from 225 °C to 550 °C is due to decomposition of the BAPs. Two sharp weight loss regions are observed in this range, which could be indicative of loss of peptides binding the AuNPs with different strengths in the 225 °C to 400 °C and 400 °C to 550 °C regions. On the other hand, the bilayer modified BAP-AuNPs (**Figure 2.6B**) showed three distinct weight loss regions. The sharp decrease (~30%) from 125 °C to 200 °C cannot be attributed to water decomposition alone but also to the loss of some of the outer leaflet peptides, non-covalently binding to the BAP monolayer-AuNPs. The samples were dried completely and 30% of the weight loss cannot be from water loss alone. BAPs are rich in lysine and isoleucine which have been shown to start decomposing at a lower temperature which is ~120 °C for lysine³⁶ and ~180 °C for isoleucine³⁷, which could be contributing to a higher proportion weight loss in the 125 °C to 200°C.

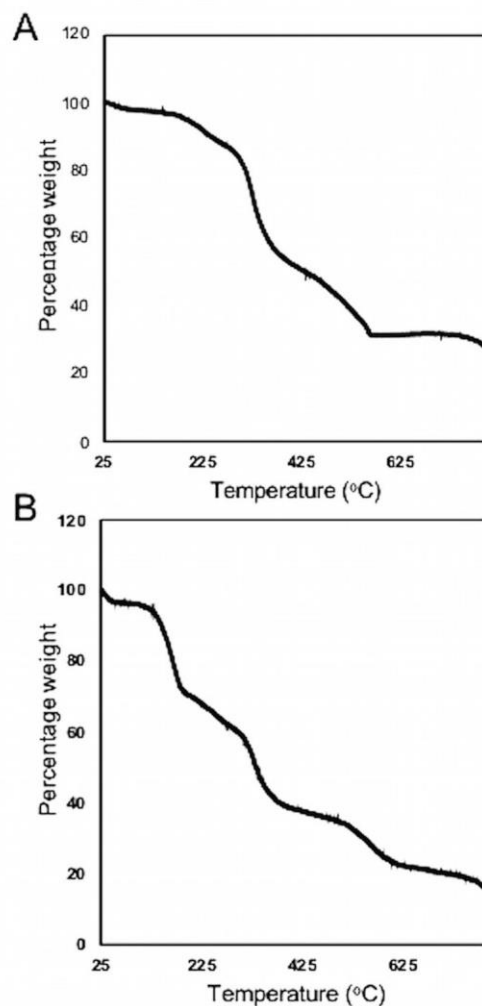


Figure 2.6. Thermogravimetric Analysis (TGA) of gold nanoparticles modified with BAPs

The TGA curve represents the percentage of the starting weight for (A) BAP monolayer-AuNPs and (B) represents BAP-AuNPs, as temperature increases from 25 °C – 800 °C. The 30% weight loss observed between 125 °C and 225 °C for the BAP-AuNPs is not observed for the BAP monolayer-AuNPs. It represents the weight loss due to decomposition of the non-covalently bound outer leaflet of the peptide bilayer.

The BAP monolayer-AuNPs TGA showed that 30% of the mass could be attributed to free AuNPs and 60% to the mass of peptides. For the bilayer modified BAP-AuNPs, 10% of the mass came from the AuNPs and 75% of the mass was from the bound peptides. This indicates that there is a stoichiometric difference for the number of peptides binding AuNPs in the monolayer and bilayer samples. The bilayer modified BAP-AuNPs show a different

decomposition and mass loss profile compared to the BAP monolayer- AuNPs providing further evidence that BAPs can be assembled into a bilayer on the surface of the gold nanoparticles.

In order to further confirm the formation of the bilayer we conducted a Forster Resonance Energy Transfer (FRET) experiment. Phe_{CN} and Trp are a FRET pair with Phe_{CN} acting as the donor and Trp as the acceptor when irradiated at 240 nm. Adding the cyano group does not appear to perturb the structure of the assembly based on CD analyses as discussed later. In addition, designing the peptides such that the fluorescent molecules are placed at the peptide-peptide interface greatly improves the FRET efficiency and gives a better understanding of distance between interacting moieties.^{33, 38} Based on our modeling studies these two residues should come in close proximity to one another when the bilayer forms.³⁵ The bis(Ac-F_{CN}LIVIGSII)-K-K₄-C-CONH₂ peptide used in the previous titration experiment was used for this FRET experiment. The bis(Ac-F_{CN}LIVIGSII)-K-K₄-C-CONH₂ monolayer was formed on the AuNP by adding saturating levels of peptide. Subsequently, bis(Ac-WLIVIGSII)-K-K₄-CONH₂ peptide was added as previously described to form the outer leaflet of the bilayer. After washing the bilayer modified BAP-AuNPs with water through 10K MWCO filter to remove any excess free peptide when they were excited at 240 nm we saw a shift in the emission peak to 360 nm, characteristic of Trp emission, instead of 290 nm which is emission from Phe_{CN} (**Figure 2.7A**). The shift can be ascribed to the FRET phenomenon where the Trp accepts the photons emitted by Phe_{CN} donor molecule at 290 nm on excitation at 240 nm and itself emits fluorescence at 360 nm. Although the Phe_{CN} fluorescence is not completely lost at 240 nm it is significantly decreased. The few aggregates that were observed in the BAP-AuNPs solution, might be contributing to the emission at 290 nm since Phe_{CN} has a higher quantum yield of 0.11 and significantly higher molar absorptivity of 13,500 M⁻¹ cm⁻¹ at 240 nm. The two emission

peaks could also be indicative of the distance between the tightly packed, interdigitating BAP bilayer showing complete overlap of the hydrophobic segments and hence a larger distance between the donor-acceptor on the opposite leaflets.

Gold nanoparticles have strong absorption in the UV range; hence it was not possible to determine the absorbance due to peptides alone accurately and therefore we could not calculate the FRET efficiency. Since they absorb in the UV range we wanted to check if gold nanoparticles themselves or with the non-fluorescent BAP bilayer bound to them have any influence on the fluorescence spectrum when excited at 240 nm. As observed (**Figure 2.7A**), no significant fluorescence signal for citrate-AuNPs alone (not shown) nor BAP(non-fluorescent)-AuNPs in water were detected. The gold nanoparticles exhibit some fluorescence and the excitation/emission wavelengths depend on the nature of the capping ligands, zeta potential and size of the nanoparticles.³⁹ However, the controls used helped us eliminate the possibility of interference by the AuNPs alone in the fluorescence emission spectral region used for analyses. The fluorescence emission profile of bis(Ac-F_{CN}LIVIGSII)-K-K₄-C-CONH₂ - bis(Ac-WLIVIGSII)-K-K₄-CONH₂ forming BAPCs in water were recorded.

The fluorescence emission profile of bis(Ac-F_{CN}LIVIGSII)-K-K₄-C-CONH₂ - bis(Ac-WLIVIGSII)-K-K₄-CONH₂ forming BAPCs in water were recorded. The fluorescence emission profile of these BAPCs as seen does not give a complete shift in emission to 360 nm (**Figure 2.7A**). We see significantly high fluorescence emission from Phe_{CN} and a slightly lower Trp fluorescence. Since there is no control over which two peptides come together in which leaflet and whether they are in proximity to themselves or the other residue, we cannot observe an enhanced FRET effect although we observe some. The bis(Ac-F_{CN}LIVIGSII)-K-K₄-C-CONH₂ - bis(Ac-WLIVIGSII)-K-K₄-CONH₂ equimolar mix in 100% TFE (monomeric peptides not

forming capsules in solution) shows that bis(Ac- F_{CN}LIVIGSII)-K-K₄-C-CONH₂ emission predominates the spectrum due to its higher quantum yield even though bis(Ac-WLIVIGSII)-K-K₄-CONH₂ by itself shows fluorescence when excited at 240 nm (not shown).³⁴

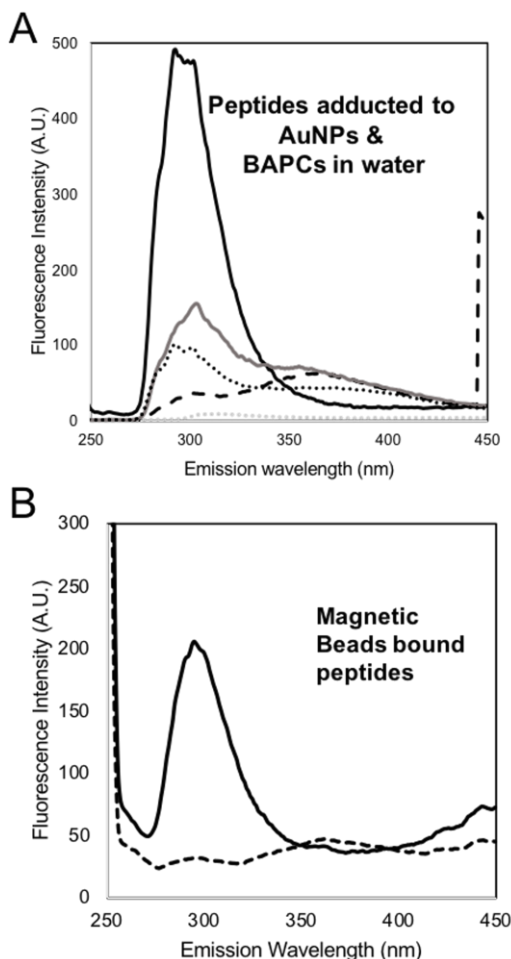


Figure 2.7. Forster Resonance Energy Transfer (FRET) demonstrating formation of BAP bilayer on gold nanoparticles

(A) Fluorescence profile for peptides binding AuNPs. bis(Ac-F_{CN}LIVIGSII)-K-K₄-C-CONH₂ adducted gold nanoparticles in 100% TFE (black bold), bis(Ac- F_{CN}LIVIGSII)-K-K₄-C-CONH₂ – bis(Ac-WLIVIGSII)-K-K₄-CONH₂ bilayer bound AuNPs (black dashed) in water and in 100% TFE (Black dotted). non-fluorescent peptide bilayer bound AuNPs i.e. bis(Ac-FLIVIGSII)-K-K₄-C-CONH₂ - bis(Ac-FLIVIGSII)-K-K₄-CONH₂ bound AuNPs (grey dotted) in water when excited at 240 nm. BAPCs prepared with bis(Ac-F_{CN}LIVIGSII)-K-K₄-C-CONH₂ and bis(Ac-WLIVIGSII)-K-K₄-CONH₂ (grey bold). Binding of bis(Ac-WLIVIGSII)-K-K₄-CONH₂ peptide causes a FRET phenomenon leading to shift in fluorescence emission from ~290 nm ($\lambda_{\text{emission}}$ for Phe_{CN}) to ~360 nm ($\lambda_{\text{emission}}$ for Trp). (B) Magnetic Nano Beads modified with maleimide groups binding bis(Ac- F_{CN}LIVIGSII)-K-K₄-C-CONH₂ (black bold) in 75% TFE and with bis(Ac- F_{CN}LIVIGSII)-K-K₄-C-CONH₂ – bis(Ac-WLIVIGSII)-K-K₄-CONH₂ bilayer (black dashed) in DI water.

We dispersed the BAP-AuNPs in 100% TFE, which should cause the outer leaflet of the bilayer on AuNPs to dissociate from the inner one due to disruption of hydrophobic interactions between the peptides as well as disrupt hydrogen bonding due to their transition back to a helical conformation. Once liberated the fluorescence emission of the free peptides, revert back to ~290 nm for the Phe_{CN}. These same conditions would also have a disruptive effect on any free BAPCs that formed in solution for the reasons previously described. Newly freed peptide bis(Ac-WLIVIGSII)-K-K₄-CONH₂, from the BAPCs should again show one emission peak at ~290nm. For this study we observed that treating the BAP-AuNPs with 100% TFE shows only a modest drop in the fluorescence intensity at 360 nm, with retention of the FRET effect (**Figure 2.7A**). The fluorescence profile of these BAP-AuNPs in 100% TFE somewhat resembled that of intact BAPCs in water. This result signifies that much of peptide bilayer bound to AuNPs was not disrupted by the solvent. We have observed this phenomenon previously for locked BAPCs described in Sukthankar et al. where the peptides adopt a structural configuration that makes them resistant to disruption by TFE.⁵ Therefore, when TFE is added the peptide bilayer conjugated to the AuNPs do not dissociate, most probably due to the nature of the strong interactions between the peptides on the gold nanoparticles.

A conjugate was also made with commercially obtained magnetic nanobeads (MNBs), which were 50 nm in size and were surface adducted with maleimide. The method uses maleimide chemistry to conjugate the cysteine of bis(Ac- F_{CN}LIVIGSII)-K-K₄-C-CONH₂ to the surface and then forms the bilayer by adding excess bis(Ac-WLIVIGSII)-K-K₄-CONH₂ as there is an increase in water concentration as mentioned before. The MNBs with BAP monolayer alone show emission at 290 nm (**Figure 2.7B**) indicating successful coupling of BAP to the surface. Addition of bis(Ac-WLIVIGSII)-K-K₄-CONH₂ shows FRET effect similar to the BAP-

AuNPs, where we see emission at 290 nm and 360 nm (**Figure 2.7B**), indicating that BAP bilayer was successfully formed. Thus, the MNBs act as a control here for bilayer formation on AuNPs. The BAP-MNBs showed a fluorescence profile similar to BAP-AuNPs separated from BAPCs in solution. The BAPCs present, if any, were separated from BAP-MNBs thoroughly, using a magnetic separator. Thus, the FRET experiment provides strong evidence that the BAPs form a bilayer on AuNP and MNB surface in an aqueous solution.

Determination of secondary structure of peptides bound to gold nanoparticles.

We wanted to compare the secondary structures of the BAPs when bound to the gold nanoparticles to that previously observed for BAPs free in solution. The tethered peptides that form the inner leaflet will not have the same ability to sample conformational space as those which are free in solution. Previously it was established that bis(Ac-FLIVIGSII)-K-K₄-CONH₂ BAPs assembled into capsules in water exhibit beta sheet secondary structure over a wide range of temperatures.⁵ Since it was established that a BAP bilayer successfully formed on the surface of AuNPs, determining the secondary structure of the inner leaflet as well as the bound bilayer was now possible. The BAP monolayer-AuNPs in 100% TFE (**Figure 2.8A**) show a secondary structure intermediate between beta-sheet and alpha helix with a broad peak ranging from 218 nm (characteristic of beta sheet) to 222 nm and a small peak at 208 nm, both of which are characteristic of alpha helix. The BAP-AuNPs in water (**Figure 2.8A**) show a strong beta -sheet characteristic with a minimum peak at 218 nm similar to BAPCs in water. Citrate-AuNPs alone are not chiral and as expected do not exhibit any ellipticity and bis(Ac-FLIVIGSII)-K-K₄-CONH₂ peptide alone in 75% TFE (**Figure 2.8B**) showed alpha-helical structure as monomeric peptides in TFE do.

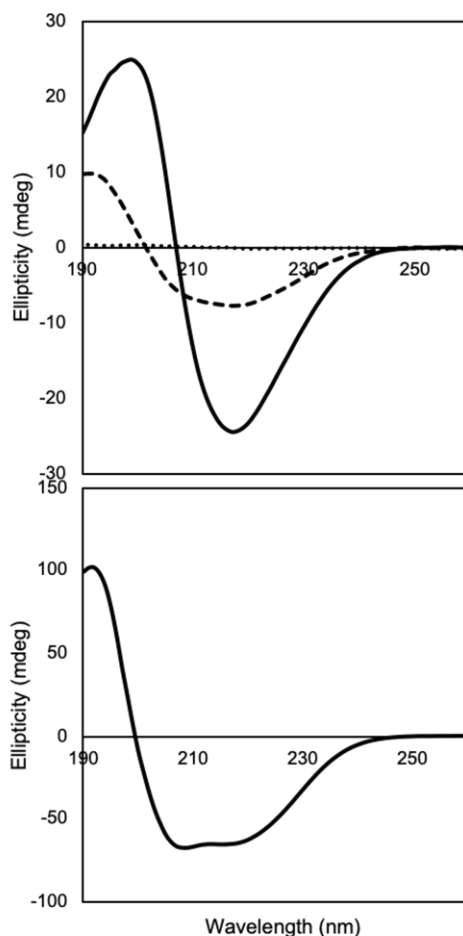


Figure 2.8. Circular Dichroism spectra analysis of peptides bound to AuNPs

(A) BAP monolayer-AuNPs (Dashed line) in 100% TFE shows slight beta characteristic as opposed to an all alpha-helix structure observed in the free monomeric BAPs. The minimum peak is broad between 215 nm and 225 nm, with minima at 222 nm and a slight peak at 208 nm. The BAP-AuNPs (bold line) on the other hand shows strong beta-sheet structure, with minima at 218nm which is the structure adopted by BAPs when they form capsules in water. Citrate - AuNPs alone were scanned (dotted line) as a control and as expected, they do not show any ellipticity (B) CD spectrum of bis(Ac-FLIVIGSII)-K-K₄-C-CONH₂ monomeric peptides in 75% TFE showing strong alpha helical characteristic.

With these results we conclude that BAPs assemble to form a bilayer in water leading to a transition in secondary structure from alpha helix to beta sheet due to inter and intramolecular interactions between peptide of the two leaflets as they are transferred from a lower dielectric to an aqueous environment.

Conclusion

Branched Amphiphilic Peptides, BAPs, assemble into a bilayer when added one leaflet at a time to gold nanoparticles, which serve as a substrate/scaffold for their formation. The self-assembly of BAPs as a bilayer is driven by the presence of water, causing the hydrophobic segments to interact with each other thus shielding them from the hydrophilic solvent. Thus, BAPs are very similar in structure to phospholipids that self-assemble to form bilayer-delimited liposomes with significant advantages over their liposome counterparts. The gold nanoparticles capped with BAP bilayer are approximately 7.5 nm in size. These assemblies being smaller in size may serve as more efficient delivery systems for surface binding molecules like nucleic acids and proteins. Since BAPs are not degraded within cells due to their unique stability as an assembly, they may provide new capping agents that prevent toxicity caused by gold nanoparticle accumulation in vivo as bioaccumulation.⁴⁰ Gold being electron dense, is a good candidate for electron beam-based imaging techniques, like micro Computed Tomography scanning.⁴¹ Therefore, BAP-AuNPs provide a system that can be used for imaging with targeted delivery simultaneously. The BAP-AuNPs described here with their bilayer forming nature can be applied to future studies in diagnostics as a delivery system in both in vitro and in vivo research.

References

1. Barros, S.; Whitaker, S.; Sukthankar, P.; Avila, L.; Gudlur, S.; Warner, M.; Beltrao, E.; Tomich, J., A review of solute encapsulating nanoparticles used as delivery systems with emphasis on branched amphipathic peptide capsules. *Archives of Biochemistry and Biophysics* 2016, 596, 22-42. <https://doi.org/10.1016/j.abb.2016.02.027>.
2. Gudlur, S.; Sukthankar, P.; Gao, J.; Avila, L. A.; Hiromasa, Y.; Chen, J.; Iwamoto, T.; Tomich, J. M., Peptide nanovesicles formed by the self-assembly of branched

- amphiphilic peptides. PLoS One 2012, 7 (9), e45374.
<https://doi.org/10.1371/journal.pone.0045374>.
3. Sukthankar, P.; Gudlur, S.; Avila, L. A.; Whitaker, S. K.; Katz, B. B.; Hiromasa, Y.; Gao, J.; Thapa, P.; Moore, D.; Iwamoto, T.; Chen, J.; Tomich, J. M., Branched oligopeptides form nanocapsules with lipid vesicle characteristics. *Langmuir* 2013, 29 (47), 14648-54. <https://doi.org/10.1021/la403492n>.
 4. Barros, S. M.; Avila, L. A.; Whitaker, S. K.; Wilkinson, K. E.; Sukthankar, P.; Beltrão, E. I. C.; Tomich, J. M., Branched Amphipathic Peptide Capsules: Different Ratios of the Two Constituent Peptides Direct Distinct Bilayer Structures, Sizes, and DNA Transfection Efficiency. *Langmuir* 2017, 33 (28), 7096-7104.
<https://doi.org/10.1021/acs.langmuir.7b00912>.
 5. Sukthankar, P.; Whitaker, S. K.; Garcia, M.; Herrera, A.; Boatwright, M.; Prakash, O.; Tomich, J. M., Thermally induced conformational transitions in nascent branched amphiphilic peptide capsules. *Langmuir* 2015, 31 (10), 2946-55.
<https://doi.org/10.1021/la504381y>.
 6. Liang, X.; Shi, B.; Wang, K.; Fan, M.; Jiao, D.; Ao, J.; Song, N.; Wang, C.; Gu, J.; Li, Z., Development of self-assembling peptide nanovesicle with bilayers for enhanced EGFR-targeted drug and gene delivery. *Biomaterials* 2016, 82, 194-207.
<https://doi.org/10.1016/j.biomaterials.2015.12.015>.
 7. Li, S.; Mehta, A.; Sidorov, A.; Orlando, T.; Jiang, Z.; Anthony, N.; Lynn, D., Design of Asymmetric Peptide Bilayer Membranes. *Journal of the American Chemical Society* 2016, 138 (10), 3579-3586. <https://doi.org/10.1021/jacs.6b00977>.
 8. Fatouros, D.; Lamprou, D.; Urquhart, A.; Yannopoulos, S.; Vizirianakis, I.; Zhang, S.; Koutsopoulos, S., Lipid-like Self-Assembling Peptide Nanovesicles for Drug Delivery. *ACS Applied Materials & Interfaces* 2014, 6 (11), 8184-8189.
<https://doi.org/10.1021/am501673x>.
 9. Homberger, M.; Simon, U., On the application potential of gold nanoparticles in nanoelectronics and biomedicine. *Philosophical Transactions of the Royal Society a-Mathematical Physical and Engineering Sciences* 2010, 368 (1915), 1405-1453.
<https://doi.org/10.1098/rsta.2009.0275>.
 10. Kalimuthu, K.; Lubin, B.; Bazylevich, A.; Gellerman, G.; Shpilberg, O.; Luboshits, G.; Firer, M., Gold nanoparticles stabilize peptide-drug-conjugates for sustained targeted drug delivery to cancer cells. *Journal of Nanobiotechnology* 2018, 16.
<https://doi.org/10.1186/s12951-018-0362-1>.
 11. Dykman, L.; Khlebtsov, N., Gold nanoparticles in biomedical applications: recent advances and perspectives. *Chemical Society Reviews* 2012, 41 (6), 2256-2282.
<https://doi.org/10.1039/c1cs15166e>.

12. Vilela, D.; Gonzalez, M.; Escarpa, A., Sensing colorimetric approaches based on gold and silver nanoparticles aggregation: Chemical creativity behind the assay. A review. *Analytica Chimica Acta* 2012, 751, 24-43. <https://doi.org/10.1016/j.aca.2012.08.043>.
13. Xia, F.; Zuo, X.; Yang, R.; Xiao, Y.; Kang, D.; Vallee-Belisle, A.; Gong, X.; Yuen, J.; Hsu, B.; Heeger, A.; Plaxco, K., Colorimetric detection of DNA, small molecules, proteins, and ions using unmodified gold nanoparticles and conjugated polyelectrolytes. *Proceedings of the National Academy of Sciences of the United States of America* 2010, 107 (24), 10837-10841. <https://doi.org/10.1073/pnas.1005632107>.
14. Valentini, P.; Pompa, P., Gold nanoparticles for naked-eye DNA detection: smart designs for sensitive assays. *RSC Advances* 2013, 3 (42), 19181-19190. <https://doi.org/10.1039/c3ra43729a>.
15. Brust, M.; Walker, M.; Bethell, D.; Schiffrin, D. J.; Whyman, R., Synthesis of thiol-derivatised gold nanoparticles in a two-phase Liquid-Liquid system. *Journal of the Chemical Society, Chemical Communications* 1994, (7), 2.
16. Turkevich, J.; Stevenson, P.; Hillier, J., A Study Of The Nucleation And Growth Processes In The Synthesis Of Colloidal Gold. *Discussions of the Faraday Society* 1951, (11), 55-&. <https://doi.org/10.1039/df9511100055>.
17. Lin, X.; Sorensen, C.; Klabunde, K., Digestive ripening, nanophase segregation and superlattice formation in gold nanocrystal colloids. *Journal of Nanoparticle Research* 2000, 2 (2), 157-164. <https://doi.org/10.1023/A:1010078521951>.
18. Piella, J.; Bastus, N.; Puntès, V., Size-Controlled Synthesis of Sub-10-nanometer Citrate-Stabilized Gold Nanoparticles and Related Optical Properties. *Chemistry of Materials* 2016, 28 (4), 1066-1075. <https://doi.org/10.1021/acs.chemmater.5b04406>.
19. Karki, I.; Wang, H.; Geise, N.; Wilson, B.; Lewis, J.; Gullion, T., Tripeptides on Gold Nanoparticles: Structural Differences between Two Reverse Sequences as Determined by Solid-State NMR and DFT Calculations. *Journal of Physical Chemistry B* 2015, 119 (36), 11998-12006. <https://doi.org/10.1021/acs.jpcc.5b04299>.
20. Serizawa, T.; Hirai, Y.; Aizawa, M., Novel Synthetic Route to Peptide-Capped Gold Nanoparticles. *Langmuir* 2009, 25 (20), 12229-12234. <https://doi.org/10.1021/la9021799>.
21. Love, J.; Estroff, L.; Kriebel, J.; Nuzzo, R.; Whitesides, G., Self-assembled monolayers of thiolates on metals as a form of nanotechnology. *Chemical Reviews* 2005, 105 (4), 1103-1169. <https://doi.org/10.1021/cr0300789>.
22. Xue, Y.; Li, X.; Li, H.; Zhang, W., Quantifying thiol-gold interactions towards the efficient strength control. *Nature Communications* 2014, 5. <https://doi.org/10.1038/ncomms5348>.
23. Schneider, G.; Decher, G.; Nerambourg, N.; Praho, R.; Werts, M.; Blanchard-Desce, M., Distance-dependent fluorescence quenching on gold nanoparticles ensheathed with

- layer-by-layer assembled polyelectrolytes. *Nano Letters* 2006, 6 (3), 530-536.
<https://doi.org/10.1021/nl052441s>.
24. Amiri, S.; Shokrollahi, H., The role of cobalt ferrite magnetic nanoparticles in medical science. *Mater Sci Eng C Mater Biol Appl* 2013, 33 (1), 1-8.
<https://doi.org/10.1016/j.msec.2012.09.003>.
 25. Reddy, L. H.; Arias, J. L.; Nicolas, J.; Couvreur, P., Magnetic nanoparticles: design and characterization, toxicity and biocompatibility, pharmaceutical and biomedical applications. *Chem Rev* 2012, 112 (11), 5818-78. <https://doi.org/10.1021/cr300068p>.
 26. Silva, S.; Tavallaie, R.; Sandiford, L.; Tilley, R.; Gooding, J., Gold coated magnetic nanoparticles: from preparation to surface modification for analytical and biomedical applications. *Chemical Communications* 2016, 52 (48), 7528-7540.
<https://doi.org/10.1039/c6cc03225g>.
 27. Avila, L. A.; Aps, L. R. M. M.; Ploscariu, N.; Sukthankar, P.; Guo, R.; Wilkinson, K. E.; Games, P.; Szoszkiewicz, R.; Alves, R. P. S.; Diniz, M. O.; Fang, Y.; Ferreira, L. C. S.; Tomich, J. M., Gene delivery and immunomodulatory effects of plasmid DNA associated with Branched Amphiphilic Peptide Capsules. *J Control Release* 2016, 241, 15-24. <https://doi.org/10.1016/j.jconrel.2016.08.042>.
 28. Avila, L. A.; Chandrasekar, R.; Wilkinson, K. E.; Balthazor, J.; Heerman, M.; Bechard, J.; Brown, S.; Park, Y.; Dhar, S.; Reeck, G. R.; Tomich, J. M., Delivery of lethal dsRNAs in insect diets by branched amphiphilic peptide capsules. *J Control Release* 2018, 273, 139-146. <https://doi.org/10.1016/j.jconrel.2018.01.010>.
 29. Rasband, W. S. ImageJ ; U.S. National Institutes of Health: Bethesda, MD, <https://imagej.nih.gov/ij/> , 1997 – 2018.
 30. Liu, X.; Atwater, M.; Wang, J.; Huo, Q., Extinction coefficient of gold nanoparticles with different sizes and different capping ligands. *Colloids and Surfaces B-Biointerfaces* 2007, 58 (1), 3-7. <https://doi.org/10.1016/j.colsurfb.2006.08.005>.
 31. Han, X.; Goebel, J.; Lu, Z.; Yin, Y., Role of Salt in the Spontaneous Assembly of Charged Gold Nanoparticles in Ethanol. *Langmuir* 2011, 27 (9), 5282-5289.
<https://doi.org/10.1021/la200459t>.
 32. Andrushchenko, V.; Vogel, H.; Prenner, E., Optimization of the hydrochloric acid concentration used for trifluoroacetate removal from synthetic peptides. *Journal of Peptide Science* 2007, 13 (1), 37-43. <https://doi.org/10.1002/psc.793>.
 33. Glasscock, J.; Zhu, Y.; Chowdhury, P.; Tang, J.; Gai, F., Using an amino acid fluorescence resonance energy transfer pair to probe protein unfolding: Application to the villin headpiece subdomain and the LysM domain. *Biochemistry* 2008, 47 (42), 11070-11076. <https://doi.org/10.1021/bi8012406>.

34. Tucker, M.; Oyola, R.; Gai, F., Conformational distribution of a 14-residue peptide in solution: A fluorescence resonance energy transfer study. *Journal of Physical Chemistry B* 2005, 109 (10), 4788-4795. <https://doi.org/10.1021/jp044347q>.
35. Jia, Z.; Whitaker, S.; Tomich, J.; Chen, J., Organization and Structure of Branched Amphipathic Oligopeptide Bilayers. *Langmuir* 2016, 32 (38), 9883-9891. <https://doi.org/10.1021/acs.langmuir.6b02421>.
36. Cao, Y.; Mu, T., Comprehensive Investigation on the Thermal Stability of 66 Ionic Liquids by Thermogravimetric Analysis. *Industrial & Engineering Chemistry Research* 2014, 53 (20), 8651-8664. <https://doi.org/10.1021/ie5009597>.
37. Dunn, M. S.; Brophy, T. W. Decomposition Points of Amino Acids. *J. Biol. Chem.* 1932, 99 , 221 – 229.
38. Rogers, J.; Lippert, L.; Gai, F., Non-natural amino acid fluorophores for one- and two-step fluorescence resonance energy transfer applications. *Analytical Biochemistry* 2010, 399 (2), 182-189. <https://doi.org/10.1016/j.ab.2009.12.027>.
39. Goldys, E.; Sobhan, M., Fluorescence of Colloidal Gold Nanoparticles is Controlled by the Surface Adsorbate. *Advanced Functional Materials* 2012, 22 (9), 1906-1913. <https://doi.org/10.1002/adfm.201102057>.
40. Lopez-Chaves, C.; Soto-Alvaredo, J.; Montes-Bayon, M.; Bettmer, J.; Llopis, J.; Sanchez-Gonzalez, C., Gold nanoparticles: Distribution, bioaccumulation and toxicity. In vitro and in vivo studies. *Nanomedicine-Nanotechnology Biology and Medicine* 2018, 14 (1), 1-12. <https://doi.org/10.1016/j.nano.2017.08.011>.
41. Alba-Tercedor, J.; Hunter, W. B.; Cicero, J. M.; Bariain, M. S.; Brown, S. J. In Use of Micro-CT to Elucidate Details of the Anatomy and Feeding of the Asian Citrus Psyllid *Diaphorina Citri* Kuwayama, 1908 (Insecta: Hemiptera, Liviidae) , *Micro-CT User Meeting 2017*; Royal Belgian Institute of Natural Science: Brussels, 2017; pp 270 – 285.

Chapter 3 - A study of the cellular uptake of magnetic Branched Amphiphilic Peptide Capsules

This chapter has been reproduced with permission from - Natarajan, P.; Roberts, J. D.; Kunte, N.; Hunter, W. B.; Fleming, S. D.; Tomich, J. M.; Avila, L. A., A Study of the Cellular Uptake of Magnetic Branched Amphiphilic Peptide Capsules. *Molecular Pharmaceutics* 2020, 17 (6), 2208–2220. <https://pubs.acs.org/doi/abs/10.1021/acs.molpharmaceut.0c00393>. © 2020 American Chemical Society.

Introduction

Self-assembled peptide nanostructures have gained increasing importance as delivery systems since they are highly biocompatible, biodegradable, and tunable. Their structure and function can be easily modified by changing the amino acid sequence and/or environment of assembly (temperature, solvent, pH).¹⁻³

For the past decade, our team has focused on studying the properties and applications of two branched amphiphilic peptides that self-assemble to form nano-capsules. They assemble into bilayer delimited vesicles called branched amphiphilic peptide capsules (BAPCs) whose molecular architecture is similar to liposomes.^{4,5} BAPCs are formed by mixing equimolar concentrations of bis-(Ac-FLIVI)-KKKKK-CONH₂ and bis-(Ac-FLIVIGSII)-KKKKK-CONH₂. They can also be prepared using either sequence individually which varies the thickness of the assembled bilayer.⁶ The size of BAPCs is controlled by temperature changes that induce a shift in the secondary structure of the peptide bilayer.⁷ Thus, BAPCs of varying size can be generated as per the requirement of a specific application.

BAPCs have been successfully used to deliver nucleic acids in different animal models. In mice, intramuscular injections of BAPCs loaded with a DNA vaccine enhanced immune

responses and controlled tumors induced by type 16 human papilloma virus (HPV-16).⁸ In insects, oral administration of BAPCs bound to dsRNA enhanced the silencing of vital genes, leading to the premature death of two species from two different orders: *Tribolium castaneum* and *Acyrtosiphon pisum*.⁹ We also reported that BAPCs are easily degraded by a common soil fungus thereby suggesting that their use would not result in any accumulation in the environment.¹⁰ Recently, we developed Branched Amphiphilic Peptide coated (BAPc) magnetic nanobeads (MNBs).¹¹ The peptide bilayer was assembled in a controlled manner i.e. one layer at a time on the magnetic bead surface. We refer to these as BAPc-MNBs. Substituting the water-filled core of BAPCs with magnetic nanobeads might provide the peptide bilayer nanocapsules with added functionalities, thereby permitting their use in a multitude of applications such as bio/immunoassays, magnetic field guided delivery in vitro and in vivo, magnetofection, magnetic resonance imaging (MRI) and hyperthermia in cancer treatment.^{1, 12-14} Nonetheless, fundamental aspects of BAPc-MNBs such as cellular uptake routes have yet to be fully elucidated.

In this study, the cellular internalization pathways of the newly developed BAPc-MNBs were explored along with their effect on cell viability. Uptake was evaluated in two cell types: mouse macrophages (J774A.1) and rat intestinal epithelial cells (IEC-18). Ileum epithelial cells are known to be a major barrier for oral drug delivery animals. Thus, we consider that in vitro studies using the intestinal epithelial cells can serve as proof of concept of BAPCs uptake by gut cells.^{15,16,17} Foreign particles when administered in vivo commonly encounter phagocytes and therefore, we chose to study BAPc-MNBs uptake by macrophage as well.

The magnetic core allowed for easy quantification using a colorimetric assay¹⁸, offering a numerical analysis of the uptake process with a relatively simple benchtop processing. We also analyzed cellular uptake of fluorescent labeled water-filled BAPCs, to establish a comparison

between the two nanoparticles with differing cores. The fluorescent dye Rhodamine B was incorporated in the N-terminal lysine of the BAPCs forming the peptide bis-(Ac-FLIVI)-KKKKK-CONH₂. We named these modified branched amphiphilic peptide capsules as Rh-BAPCs. By using this approach, cellular internalization was monitored qualitatively using confocal microscopy and quantitatively by flow cytometry.

In general, interaction between nanomaterials and the exterior of the plasma membrane results in cell entry via endocytosis. Depending on the proteins involved in the internalization process, endocytosis can be classified as clathrin-dependent and independent endocytosis¹⁹. The clathrin-independent routes are further classified as 1) caveolae-mediated endocytosis, 2) clathrin- and caveolae-independent endocytosis and 3) macropinocytosis. To probe the dependency of these nanoparticles on these pathways, we used selective inhibitors (individually or in combination) to disrupt these endocytic routes²⁰.

Our results indicated that BAPc-MNBs and Rh-BAPCs enter epithelial cells via multiple endocytic pathways- clathrin and caveolae mediated endocytosis as well as macropinocytosis. Some differences were observed between BAPc-MNBs and Rh-BAPCs, most likely due to the different nanoparticle core (magnetic versus water-filled). We also included reactive oxygen and nitrogen species analysis (ROS/RNS) to determine the downstream effects following BAPc-MNBs internalization. Cell viability and ROS/RNS analysis suggest that BAPc-MNBs did not induce significant toxicity in epithelial cells and macrophages.

Few peptide vesicles have been reported in the literature compared to the numerous synthetic polymers capable of self-assembling into vesicles. The studies presented in this report, provided fundamental knowledge on peptide nanocapsules-based delivery systems and can lay a foundation for novel therapeutic applications.

Materials and methods

Chemical reagents and cell lines.

Ethanol (99% pure, Sigma, ChromSolv, Denatured ethanol), 4-(2-hydroxyethyl)-1-piperazineethanesulfonic acid (HEPES) (Acros Organics, ThermoFisher), Magnetic nanobeads (Ocean Nanotech, San diego, CA), Trifluoroethanol (TFE) (Tokyo Chemical Industry Ltd.), Rhodamine B (Sigma-Aldrich Corp., St. Louis, MO), 6-well plate (TPP® tissue culture plates, Sigma-Aldrich) , 2.0 mL Low binding tubes (VWR, North America), Dulbecco's modified Eagle's medium (Gibco®, Sigma-Aldrich), OptiMEM-I® (Gibco®, Sigma-Aldrich), L-Glutamine (GlutaMAX™, Sigma-Aldrich), Insulin (Bovine Pancreas, Millipore Sigma), 3-(2-Pyridyl)-5,6-di(2-furyl)-1,2,4-triazine-5', 5''-disulfuric acid disodium salt (Ferene-s, Sigma Ultra), IEC-18 (ATCC® CRL-1589™), J774A.1 (ATCC® TIB-67™), pH 7.4 Phosphate buffered Saline (PBS) with Ca⁺² and Mg⁺², L-ascorbic acid (Sigma-Aldrich), Acetate Buffer (Glacial Acetic acid, Fischer), methyl-β-cyclodextrin (Millipore Sigma), Chlorpromazine, Dynasore and Nystatin(Sigma-Aldrich), Cytochalasin D (Tocris Biosciences), 7AAD (Tonbo, San Diego, CA) , Sodium azide (Sigma-Aldrich), Dichlorofluorescein-diacetate (DCF-DA) (Sigma – Aldrich), potassium hexacyanoferrate (II) trihydrate 98.5-102% (Sigma-Aldrich), Paraformaldehyde (37% w/v, Fisher Scientific), Hema III stain (Solution 1) (Fischer Scientific).

Synthesis of Branched Amphiphilic Peptide- Magnetic Nanobeads (BAPc-MNBs).

Peptide layer on MNBs

The strategy employed to synthesize the modified branched amphiphilic peptide coated-magnetic nanobeads (BAPc-MNBs) bears some similarity with a method previously reported by Natarajan et al.¹¹ A cysteine residue was added on the oligo-lysine segment, C-terminus of bis-

(Ac-FLIVIGSII)-KKKKK-C-CONH₂ and was covalently linked to maleimide groups embedded on the magnetic nanobeads surface, in 75% Ethanol: HEPES solvent. Thus, the peptide hydrophobic chains orient themselves towards the organic solvent which promotes the peptides to adopt a helical secondary structure thereby keeping them monodispersed. Assembly of peptides into capsules only occurs when they adopt a beta structure in an aqueous solvent.

To determine whether the peptides were bound to the MNBs and assemble into a tightly packed monolayer, we substituted Phe of the peptide with its fluorescent counterpart, cyanophenylalanine (F_{CN}) i.e. bis-(Ac-F_{CN}LIVIGSII)-KKKKK-C-CONH₂, as described previously.¹¹ Varying amounts of this peptide was added to MNBs in 75% ethanol to form the inner peptide monolayer. The pH of the solution was adjusted to 7.5 using 1N NaOH and the mixture was placed on a shaker overnight at RT. The tube containing the reaction mixture was placed in a magnetic separation rack (OzBiosciences, San Diego, CA) for a minimum of 2 h and maximum MNBs were recovered after separation from excess, unbound peptides. The peptide monolayer coated MNBs were washed twice in ethanol and resuspended in 100% Trifluoroethanol (TFE). The peptide binding was measured as a function of cyanophenylalanine fluorescence at $\lambda_{\text{emission}} = 290$ nm when excited at $\lambda_{\text{excitation}}$ at 240 nm, on a Cary eclipse fluorescence spectrophotometer (Varian). Fluorescence saturation or curve flattening was observed at 600 nmoles of peptide per 0.5 mg of MNBs, which was the point at which the MNBs surface was saturated with peptides.

Synthesis of BAPc-MNBs

Peptide monolayer coated MNBs was synthesized using bis-(Ac-FLIVIGSII)-KKKKK-C-CONH₂ peptide (as the chloride salt) as described above and redispersed in 100% TFE. The second peptide bis-(Ac-FLIVIGSII)-KKKKK-CONH₂ was added to it at twice the concentration

used to form the bilayer (1200 nmoles per 0.5 mg of MNBs). Water was added to dilute the TFE (final water to TFE ratio of 9:1) and promote beta structure formation thereby allowing the branched sequences to interact and form a bilayer on the MNBs. After sitting for 20-30 minutes on the magnetic rack, the BAPc-MNBs were carefully collected and was concentrated on a rotavapor with a 40 °C water bath. Thus, the TFE was completely removed during this process and the final product i.e. BAPc-MNBs were re-dispersed in water alone. After the overnight incubation at 4 °C the BAPc-MNBs were extruded through a sterile 0.22 µM syringe filter (Millex-GS, Millipore-Sigma). This sterilizes the BAPc-MNBs and excludes any large aggregated BAPc-MNBs. The typical yield after the separation of aggregates is between 25-40%.

Synthesis of water-filled Rhodamine labeled Branched Amphiphilic Peptide Capsules (Rh-BAPCs).

Rhodamine B labeled bis(FLIVI)-K-K₄ peptide was synthesized as described in Sukthankar et al.²¹ Rh-BAPCs were prepared as indicated in Avila et al.⁸, with 30% Rhodamine B labeled bis(FLIVI)-K-K₄. Briefly, water was added dropwise to the dried peptide mixture containing equimolar concentrations of bis-(Ac-FLIVIGSII)-KKKKK-CONH₂ and bis(FLIVI)-K-K₄ (30% Rh-labeled and 20% unlabeled) and allowed to stand for 30 min at 25 °C to form the water-filled nanocapsules. Subsequently, the solution was cooled to 4 °C, and incubated for 1 h prior to returning them to room temperature for an additional 30 min. This protocol yields the conformationally constrained Rh-BAPCs.

Transmission Electron Microscopy (TEM).

Five μL of undiluted samples (50nm and 200nm BAPc-MNBs) were spotted on Parafilm paper Individual grids (Lacey F/C 200 mesh Au, Cat No. 01882G, TedPella) were carefully placed on the surface of each sample and allowed to stay in contact for ~ 5 min. Grids were then sequentially washed with 20 μL deionized water on the parafilm. Excess sample or water were removed by gently putting the side edge of grids in contact with Kim wipes. Grids were allowed to dry overnight at $\sim 50^\circ\text{C}$ in petri dishes. For imaging, grids were mounted in specimen holders specific for TEM. Conditions for imaging were set to 25 KV on a SEM Model S-4800 (Hitachi) or they were adjusted occasionally according to quality of images.

Dynamic light scattering (DLS) and zeta potential analysis.

50 nm and 200 nm BAPc-MNBs and control beads were resuspended in sterile DDI H₂O to have a final concentration of 10^9 particles/mL. Dynamic light scattering (DLS) and zeta potential (ZP) analyses were performed for nanoparticles in a 10 mm path length cuvettes (Sarstedt® Standard Cuvettes) on a Zetasizer Nano ZSP (Malvern Instruments Ltd., Westborough, MA).

Uptake of BAPc-MNBs by IEC-18 and J774A.1.

IEC-18

Rat Intestinal Epithelial Cells (IEC-18) were cultured in Dulbecco's modified Eagle's medium supplemented with 2% FBS (DMEM₂), 10% OptiMEM-I®, 3% FBS, 5% NuSerum, 2mM L-Glutamine and 180 μM Insulin. IEC-18 were seeded in a 6-well plate at 5×10^5 cells/mL and incubated overnight. After overnight incubation, the media in the wells was replaced with

fresh media and 10^4 magnetic nanobeads per cell or 17 pg /cell were added to the wells directly. Therefore, the total number of magnetic nanobeads added to each well was 5×10^9 or 8.4 μg total. Cells were then incubated at 37 °C for 4 h. Three treatments (**Table 3.1**) were performed in a plate i.e. 2 wells per treatment. The experiments were repeated three times to account for any experimental variations/errors and to test the reproducibility of data. Thus, we obtained up to 6 readings per treatment. After 4 h, the cells were briefly washed with PBS and trypsinized and pelleted.

The supernatant was stored at -80 °C for reactive nitrate species analysis as discussed later, and the pellet resuspended in 1 mL PBS by gently mixing using pipette. The number of cells in each tube were counted on a Moxi-Z™ cell counter (ORFLO technologies). The magnetic separator (Permagen® Labware) was placed in an ice bath to chill prior to sorting the cells. The tubes containing cells were placed in the separation rack on ice for 30 min. After incubating on ice, the PBS was gently aspirated without disturbing the cells adhering to the side of the tube facing the magnet.

The PBS with residual cells was transferred to another tube and the adhered cells in the tube on the magnetic rack were resuspended in 1 mL of PBS. The number of successfully separated cells containing the magnetic nanobeads were counted on the cell counter as stated before. Using this approach, we could determine the percentage of cells that took up the magnetic nanobeads. The cells were then gently spun down and the supernatant discarded. The pellets were then stored at -80 °C to determine the number of magnetic nanobeads in the cells using ferene-s assay. The same procedure was used to determine uptake of magnetic beads by IEC-18 in OptiMEM® as well as for different temperatures and times.

J774A.1

Mouse macrophages were cultured in media with same media composition as for IEC-18 with the exception of insulin, which was not required for macrophage growth. The macrophages adhere strongly to any surface and hence to ensure consistent counts of the cells, they were kept in suspension for the 20 min incubation period and in low binding tubes, to ensure consistent cell counting. 5×10^9 magnetic nanobeads were added to 5×10^5 cells in 1 mL of media, and the tube was inverted a couple of times to ensure maximal dispersion. The tubes were then placed in a 37 °C incubator on a shaker (Labquake, Barnstead Thermolyne rotator) that rotates the tubes 360°, for 20min.

Macrophages were then spun down as stated above at 4 °C. Cells were then resuspended in PBS and separated using a magnetic separation rack. For macrophage activation, the adherent cells were stimulated with 1µg/mL of lipopolysaccharide from *E.coli* O55:BS (List Biological Lab Inc.) in media for 4 h at 37 °C. The media was then replaced with fresh media without LPS to determining uptake of magnetic nanobeads by cells as previously described.

Table 3.1. Summary of treatments to determine uptake of BAPc-MNBs by IEC-18 and J774A.1 cells in DMEM 10% serum media and OptiMEM® 5% serum media

Treatments	Cell Type Tested
Only Cells	IEC-18 and J774A.1
Control beads (Only MNBs)	IEC-18 and J774A.1
BAPc-MNBs in DMEM 10% Serum Media	IEC-18 and J774A.1
BAPc-MNBs in OptiMEM® 4% Serum Media	IEC-18 only
BAPc-MNBs in DMEM 10% Serum Media with Lipopolysaccharide (LPS)	J774A.1 only

Quantification of BAPc-MNBs in cells by Ferene-s assay.

The Ferene-s chromophoric assay used was adapted from Hedayati et al.¹⁸ The 3-(2-Pyridyl)-5,6-di(2-furyl)-1,2,4-triazine-5', 5''-disulfuric acid disodium salt working solution was prepared by mixing 10 mL of 5 times working buffer 2 g L-ascorbic acid in 11 mL 2 M Acetate Buffer and 500 μ L of 0.5 M Ferene-s in DIH₂O (0.5 g in 2 mL water). The volume was subsequently brought up to 50 mL with DIH₂O. One mL of the ferene-s working solution was added to the cell pellets after bringing them to RT. The solution was vortexed and then incubated overnight in the dark at RT. This allows for the cells to break open and release the magnetic beads. The iron beads released, reacted with ferene-s leading to a measurable color change. After incubating overnight, the cells were vortexed again and the cell debris (including some magnetic beads remained bound to the cell membrane.) spun down at 16,000 rcf (Centrifuge 5415D, Eppendorf) for 3 min. The supernatant was then transferred to a 1 mL disposable cuvette and the absorbance of the solution read at 595 nm using a Varian Cary 300 UV-Vis spectrophotometer against a blank containing only the ferene-s working solution. The magnetic nanobeads in the cell supernatants were sorted on the magnetic separator overnight and quantified using ferene-s. Thus, we could determine the quantity of magnetic beads recovered from the cell supernatant after incubation with cells.

The standard curve for this assay was generated using freshly prepared 0.1 mg/mL FeCl₃ (Fischer Scientific) solution in DIH₂O. Fe standards containing 0.1 μ g, 0.2 μ g, 0.5 μ g, 1 μ g, 2 μ g, 4 μ g and 5 μ g were used. 1mL of Ferene-s solution was added to each tube with mixing and allowed to stand at RT for 30 min. In order to calculate the number of magnetic nanobeads in cell extract solution, a control tube containing a known amount of magnetic nanobeads was used along with the cell extract samples. According to the manufacturer, 1 mg of 50 nm MNB

contains 6×10^{11} beads. Using this relationship, the number of magnetic nanobeads in solution was calculated (i.e. 0.5 mg beads/mL contains 3×10^{11} beads).

Endocytosis inhibition study.

IEC-18 cell (growth as previously described) cells were used to study the effect of chemical inhibitors on the uptake of BAPc-MNBs and Rh-BAPCs. The inhibitors tested were- methyl- β -cyclodextrin (5 mM), chlorpromazine (10 μ M), Nystatin (50 μ M), Cytochalasin D (4 μ M) and dynasore (80 μ M). We also tested the combined effect of inhibitors on uptake – methyl- β -cyclodextrin + chlorpromazine, Cytochalasin D + Nystatin, Cytochalasin D + Chlorpromazine.

Prior to incubation of IEC-18 with BAPc-MNBs and Rh-BAPCs, cells were incubated with 1 mL media containing the respective inhibitor (or combinations of inhibitors) for 30 min at 37 °C. The BAPc-MNBs and Rh-BAPCs were then added to the media at 5×10^9 and 60 μ M respectively. After 1 h or 4 h of incubation time, plates were washed with PBS twice. . The analysis of BAPc-MNBs uptake was performed as previously described and Rh-BAPCs uptake was evaluated using confocal microscopy and flow cytometry. For confocal analysis, cells were fixed with paraformaldehyde (Sigma-Aldrich) for 30 min and washed twice with PBS. Subsequently, coverslips were mounted to microscope slides and imaging was carried out with a Nikon AR-1 confocal microscope. BAPCs labeled with rhodamine B were prepared as previously described by Gudlur et al. ⁴

For flow cytometry analysis, cells were detached using acutase, the well contents were loaded into a micro-centrifuge tube, centrifuged at 1500 rpm for 5 min, and were then washed twice with PBS. Flow cytometry was carried out in a MACSquant (Miltenyi Biotec, Germany) at 488 Excitation/585-640 Emission channel.

BAPc-MNBs toxicity in IEC-18 cells.

IEC-18 cells were seeded in a 12 well plate at 100,000 cells/mL and were allowed to adhere overnight prior to nanoparticle treatment. Further, cells were washed once with sterile PBS and treated with 10^4 magnetic nanobeads / cell of 50 nm MNBs and 50 nm and 200 nm of BAPc-MNBs in OptiMEM® for 4 h. Upon treatment, supernatant was removed and adherent cells were detached using accutase enzyme. The cells were collected in 1.5 mL tubes and were then spun at 1500 rpm. Next, the pellet was washed twice with PBS containing 2mM EDTA. Prior to flow cytometry analysis, 0.05 μ g of 7AAD dye was added to samples and incubated for 5-10 min. Percentage of dead cells was determined by measuring 7AAD fluorescence using flow cytometry MACSquant (Miltenyi Biotec, Germany) at 488 Excitation/655-730 Emission channel.

BAPc-MNBs toxicity in J774A.1 cells.

To test cell viability in J774A.1, we used an Abcam® cell viability kit (catalog no. ab112118) and the recommended protocol was followed. Briefly, J774A.1 cells were seeded in 96 well, clear bottom, black walled plates at 10,000 cells/well. The cells were treated with 50 nm and 200 nm BAPc-MNBs and control beads at 10000:1 bead to cell ratio as stated previously for 4 h in DMEM without phenol red. Sodium azide was used as the positive control while the negative control consisted of untreated cells. 20 μ L of the reagent compound provided in the kit was added to all wells, except one set of wells containing untreated cells to account for background due to just cells. The cells were incubated at 37 °C for 1.5 h. The absorbance was measured at 570 nm and 605 nm for each well using a Bio-rad microplate reader (Model 680). The percent cell viability was calculated as percent cell viability= $100 \times (R_{\text{sample}} - R_0) / (R_{\text{ctrl}} - R_0)$

R0), where R0= ratio of OD570/OD605 for negative control cells without the reagent, Rsample= ratio of OD570/OD605 in the presence of the test compound and Rctrl = ratio of OD570/OD605 in the absence of the test compound.

Determination of Reactive Nitrogen Species (RNS)- Nitric oxide (NO) detection using Griess reagent.

IEC-18 and J774A.1 cells supernatant was collected after treatment with BAPc-MNBs for varying time periods and were used for RNS detection using Griess agent. Control beads, untreated and lipopolysaccharide treated cells served as controls for the study. 25 μM of sodium nitrite was serially diluted in the appropriate cell media to generate a standard curve in the 12.5 μM to 0.195 μM range. Cell supernatants (150 μL) were placed in duplicates in the 96 well plate. A volume of 150 μL of the Griess reagent (1% sulfanilamide + 0.1% naphthylene diamine dihydrochloride + 2.5% H_3PO_4) was added to each well and incubated at RT for 10 min. The absorbance was read using a plate reader (Bio-Rad Model680 microplate reader) at 550 nm. The data was analyzed using Microplate Manager 5.2 software.

Determination of Reactive Oxygen Species (ROS) using DCF-DA.

IEC-18 and J774A.1 cells were seeded at 10^5 cells per well in a clear bottom, black walled, 96 well plate. The cells were allowed to adhere overnight and washed with Hanks buffered salt solution (HBSS). 20mM stock (1000X) Dichlorofluorescein-diacetate (DCF-DA) was prepared in neat DMSO. Fresh solution of 1X DCF-DA was prepared in HBSS and added to the cells for a final concentration of 20 μM . The cells were incubated for 30min in the 37 $^\circ\text{C}$ incubator and the supernatant was discarded. DMEM without phenol red was added to the cells followed by addition of 50 nm BAPc-MNBs and control beads at 10000:1 beads to cell ratio.

Negative control included untreated cells. Positive control cells were treated with a final concentration of 10 μ M hydrogen peroxide. The cells were treated with the magnetic nanobeads for 4 h and 24 h at 37 °C. The fluorescence was scanned from 500 nm – 600 nm with excitation wavelength of 495 nm using Cary eclipse fluorescence spectrophotometer (Varian) with plate reader accessory. The normalized fluorescence was calculated as the ratio of the fluorescence intensity of the treated cells to negative control cells minus the autofluorescence of cells not treated with DCF-DA and magnetic nanobeads. A ratio of > 1 suggests increased fluorescence in comparison to the negative control and indicates release of reactive oxygen species.

Prussian Blue staining of cells for visualization of magnetic nanobeads within cells.

In order to visualize the magnetic beads within cells, potassium hexacyanoferrate (II) trihydrate 98.5-100% was used to stain the magnetic iron nanobeads within cells. For the purpose of staining, IEC-18 and J774A.1 cells were cultured as described previously. After incubation with magnetic nanobeads for the different times at 37 °C, the supernatant was collected in 2 mL tubes and the cells were washed with PBS while adhering to the plate. The cells were then fixed with 3% paraformaldehyde in PBS by adding 1mL of 3% Paraformaldehyde (PFA) in each well and incubating for 30 min at RT. After the 30 min incubation, the PFA was removed by aspiration and the cells were washed with PBS.

Fresh stain was prepared by mixing equal volumes of 10% Potassium Ferrocyanide solution (5 g in 50 mL DDI H₂O) and 20% HCl (Add 10 mL HCl to 15 mL DDI H₂O and bringing the volume to 50 mL with DDI H₂O). One mL of the fresh acidified potassium Ferrocyanide solution was added to the wells and allowed to incubate at 37 °C for 30 min. The solution was then aspirated and the cells washed with water to remove excess stain. Cells were

counterstained for 30 sec using Hema III stain (Solution 1) which stains the cytoplasm pink. The excess of stain was washed out with water. The cells were imaged using a light microscope (Olympus KX31) and a Digital sight DS-5M Nikon lens placed on the eyepiece and connected to Nikon DS-L1 screen, for capturing the images.

Results and discussion

Biophysical characterization of BAPc-MNBs

Two sizes of magnetic iron nanobeads (MNBs) (50 and 200 nm diameter), were used in this study. The branched amphiphilic peptide bilayer on the MNBs was formed as described before.¹¹ We determined the concentration of peptide required to form a monolayer i.e. to saturate the surface by titrating the MNBs with varying concentrations of the inner leaflet peptide, containing the fluorescent amino acid residue, cyanophenylalanine (F_{CN}), in 75% ethanol:HEPES as described in methods. Six hundred nmoles of peptide per 0.5 mg of 50 nm MNBs was required to form the monolayer (**Figure 3.1A**).

The formation of a second peptide layer on magnetic nanobeads in water was confirmed using Förster resonance energy transfer (FRET) analysis as demonstrated in Natarajan et al.¹¹ The peptide forming the inner layer i.e. binding directly to the MNBs surface were modified to have the fluorescent amino acid - cyanophenylalanine in place of the N-terminal phenylalanine. The phenylalanine of peptides in the outer layer were substituted with the fluorescent aromatic amino acid, tryptophan. Cyanophenylalanine when excited with light of wavelength 240 nm, emits light at ~290 nm which is close to the excitation wavelength of tryptophan.²² Thus, the formation of the bilayer was determined using the inherently fluorescent amino acids which do not cause change in the secondary structure of the peptide. Further, the BAPc-MNBs were

purified (i.e. separated from the aggregates) by placing them on a magnetic separation rack for a specific amount of time, as shown in **Figure C.2**.

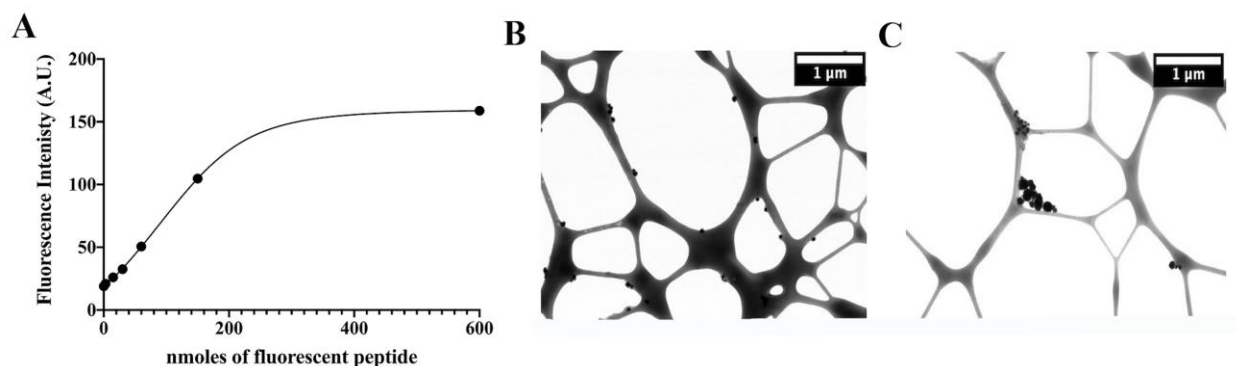


Figure 3.1. Biophysical characterization of BAPc-MNBs

(A) Representative graph showing titration of MNBs with bis-(Ac-F_{CN}LIVIGSII)-KKKKK-C-CONH₂ that demonstrates the saturation of MNB surface with the fluorescent peptide at 600 nmols of peptide per 0.5 mg of magnetic nanobeads. The cyanophenylalanine residue of the modified peptide sequence emits fluorescence close to 290 nm when excited by light of wavelength 240 nm. Transmission Electron Microscopy (TEM) images of (B) 50 nm and (C) 200 nm BAPc-MNBs on Lacey TEM grids, shows well dispersed magnetic Nanobeads.

Table 3.2. Size and zeta potential data for BAPc-MNBs determined by dynamic light scattering and transmission electron microscopy

Nanoparticle	Size by TEM	Hydrodynamic size by DLS	Polydispersity Index (PDI)	Zeta Potential
50nm BAPc-MNBs	50nm	208nm	<0.2	+23.1mV
200nm BAPc-MNBs	200nm	331nm	<0.2	+37.8mV

TEM images of the 50 nm and 200 nm BAPc-MNBs showed dispersed magnetic nanobeads lining the edges of the lacey TEM grid (**Figure 3.1B, C**). Few, if any, BAPc-MNB clusters were observed as a result of the drying process in the grid. Dynamic light scattering (DLS) size analysis indicated that the hydrodynamic size of BAPc-MNBs synthesized using the 50 nm and 200 nm MNBs were 208 nm and 331 nm, respectively (**Table 3.2**), while the

commercially supplied 50 nm MNBs displayed a hydrodynamic radius of ~80 nm (**Figure C.3A**). The polydispersity index of BAPc-MNBs was < 0.2 which is indicative of monodispersed nanoparticles.²³ The intrinsic property of large nanoparticles such as irregularity in shape and the modified surface coating changes the solvation sphere around the nanoparticles increasing the apparent hydrodynamic size of the nanoparticles and thus contributes to the apparent disparity in size between TEM and DLS.²⁴ Zeta potential analysis further confirmed the presence of the BAP-bilayer on MNBs. Zeta potential of MNBs prior to peptide bilayer coating is -30.9 mV, indicating that their surface charge is negative. (**Figure C.3B**) BAPc-MNBs with 50 nm and 200 nm cores by contrast have a zeta potential of +23.1 mV and +37.8 mV, respectively (**Table 3.2**). This suggests that the BAPc-MNBs are positively charged due to the oligo-lysine tails of the peptides present on the outer, solvent-exposed layer of the nanoparticles. For the sake of simplicity, we refer to the TEM size (50 nm and 200 nm) of BAPc-MNBs in further experiments. In **Figure 3.2**, we compare the structure of BAPc-MNBs and fluorescent rhodamine labeled water-filled Rh-BAPCs.

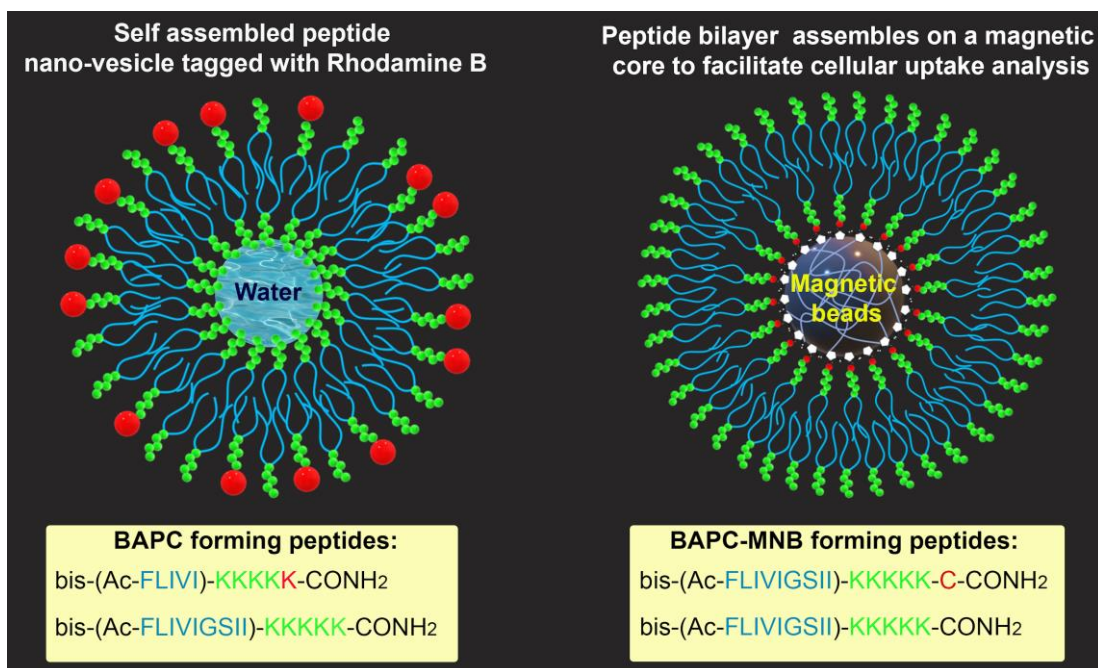


Figure 3.2. Schematic representation of water-filled BAPCs and BAPc-MNBs

Left panel: water-filled BAPCs and the amino acid sequence of the capsules forming peptides. The lysine tagged with rhodamine has been represented in red. Right panel: BAPc-MNBs and the sequence of the bilayer forming peptides. Cysteine (in red) is covalently bound to the maleimide groups embedded in the dextran coating, on the surface of the magnetic nanobeads. The poly-lysine tail has been indicated in green and the hydrophobic tail in blue.

Uptake of BAPc-MNBs by rat ileum intestinal epithelial cells (IEC-18) and mouse macrophages (J774A.1) in vitro

Cellular uptake of BAPc-MNBs was quantified in IEC-18 and J774A.1. Different parameters were taken into consideration for this analysis, such as size of BAPc-MNBs and the percentage of serum present in the cell culture media (**Figure 3.3A-C**). IEC-18 cells exposed to ~50 nm and ~200 nm BAPc-MNBs for 4 h at 37 °C showed increased uptake (~ 2.5-fold) in media containing only 4% of serum (OptiMEM®) compared with DMEM supplemented media containing up to 10% of serum. The composition of OptiMEM® probably improved uptake by IEC-18, in part, due to the reduced number of serum proteins adsorbed to the surface of BAPc-MNBs. This behavior is analogous to other cationic liposomes and nanoparticles, which have

been shown to have better transfection efficiency and/or uptake in reduced-serum media.²⁵⁻²⁷

With respect to the nanoparticle size, quantitative analysis shows IEC-18 cells internalize significantly more ~50 nm BAPc-MNBs than ~200 nm BAPc-MNBs in both cell culture media. **(Figure 3.3A-B)**. Similar results have been reported by Foged et al.²⁸ with polystyrene nanoparticles in dendritic cells as well as by Oh et al.²⁹ with positively charged gold nanoparticles of varying sizes, in which smaller nanoparticles are internalized by cells more efficiently than larger nanoparticles.³⁰

Mouse macrophages (J774A.1) treated under similar experimental conditions used for IEC-18, showed that nanoparticle size did not affect the number of nanoparticles internalized by this cell type, in DMEM 10% Serum **(Figure 3.3A-B)**. Addition of lipopolysaccharides (LPS) to this media yielded similar results **(Figure 3.3C)**. LPS induces production of pro-inflammatory cytokines such as IL-1 β and IL-6, activating the macrophages and upregulating phagocytosis of the foreign particles.³¹ Toll-like receptor-4 (TLR-4) is a LPS receptor and since LPS stimulation did not increase uptake of the beads, we concluded that the uptake of BAPc-MNBs and bare MNBs (control beads) was not TLR-4 mediated or low levels of LPS were present which led to endotoxin tolerance. For both cell types, critical controls (i.e. control beads, untreated cells) were included in all the uptake studies.

Uptake of BAPc-MNBs in IEC-18 and J774A.1 cells was quantified using the ferene-s based spectrophotometric assay.¹⁸ Ferene-s is a triazine compound that binds to iron, allowing the colorimetric detection of iron by measuring the absorbance at 595 nm. The iron content from magnetic beads internalized by treated cells was determined by subtracting the background iron from negative control. Since the iron content of each magnetic nanoparticle is known the number of magnetic nanoparticles internalized can be ascertained. Loss of beads was observed for some

treatments, possibly due to a percentage of the beads binding to the cell membrane (or organelle membranes). However, quantification of BAPc-MNB in the cell membrane would lead to inclusion of not just the internalized beads but also the cell membrane bound nanoparticles. This would not be an accurate representation of internalized BAPc-MNBs in the cytosol and therefore, insoluble membranes or cell debris that reacted with ferene-s were spun down prior to spectrophotometric measurements and hence not detected in the assay. However, we can estimate the number of cell membrane-bound nanoparticles by subtracting the nanobeads quantified in the cytosol from the nanobeads recovered i.e in media. (Figure C.4A)

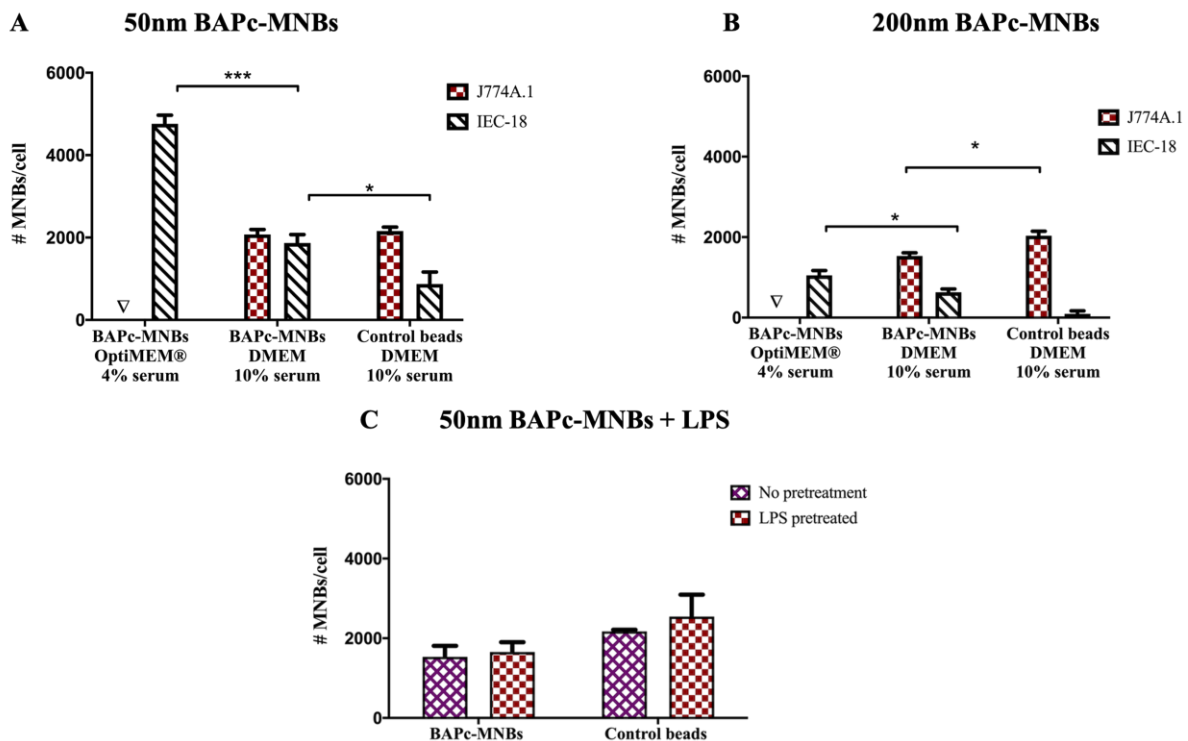


Figure 3.3. Uptake of BAPc-MNBs and magnetic nanobeads by IEC-18 and J774A.1 cell

IEC-18 and J774A.1 cells were incubated with BAPc-MNBs of different sizes and control beads for 4 h in DMEM 10% serum or OptiMEM® 4% serum. The untreated cells were the negative controls. (A) 50 nm BAPc-MNBs internalized by IEC-18 and J774A.1, (B) 200 nm BAPc-MNBs internalized by IEC-18 and J774A.1 and (C) 50 nm BAPc-MNBs internalized by J774A.1 in the presence or absence of Lipopolysaccharide (LPS). ∇J774A.1 treated with OptiMEM® could not be analyzed for uptake ANOVA followed by Bonferroni's posttest was applied for statistical analysis. n=5 (ns=not significant, *p-value<0.05, **p-value<0.01, ***p-value<0.001).

Mechanism of uptake of BAPc-MNBs and Rh-BAPCs by IEC-18.

The effect of different endocytic inhibitors on BAPc-MNBs and Rh-BAPCs uptake was tested in IEC-18 cells. Elucidation of cellular internalization mechanisms can help to determine the sub-cellular processing of the nanoparticles and their potential downstream effects. To inhibit clathrin mediated endocytosis we used chlorpromazine (Cpz) and dynasore. Methyl- β -cyclodextrin (M- β -CD) and nystatin were used to inhibit caveolae mediated endocytosis. M- β -CD is commonly used as an inhibitor for caveolae mediated endocytosis by sequestering cholesterol which in turn perturbs plasma membrane fluidity in lipid rafts. However, there is growing evidence that suggests M- β -CD can also inhibit clathrin mediated endocytosis and macropinocytosis, making it a non-specific inhibitor.^{32, 33} Thus, we also used Nystatin, which is more specific towards caveolae mediated endocytosis. Dynasore is a dynamin inhibitor known to be less specific towards clathrin mediated endocytosis³⁴, therefore, it was used in combination with chlorpromazine (Cpz). To prevent macropinocytosis, we treated cells with Cytochalasin D (Cyt D), which is specific towards macropinocytosis and phagocytosis because it induces depolymerization of actin filaments which are essential for coating the macropinosomes.³⁵ A viability assay was performed to ensure that the selected concentrations of all the inhibitors were nontoxic for cells. **(Figure C.5).**

IEC-18 cells were incubated at 1 h and 4 h in the presence of inhibitors and BAPc-MNBs or Rh-BAPCs. Cellular uptake was monitored using microscopy, flow cytometry and UV/Vis spectroscopy. We selected the 50 nm BAPc-MNBs since uptake appeared to be more efficient, as discussed in previous section. Quantitative analysis by UV/Vis spectroscopy suggested that at 1 h, BAPc-MNBs uptake was reduced in the presence of M- β -CD + Cpz as well as Cytochalasin D + Cpz **(Figure 3.4A-B)**. This significant reduction in uptake only in the presence of

combinatorial treatments indicates that BAPc-MNBs enter cells via multiple endocytic pathways simultaneously and, disrupting one pathway might cause the upregulation of other active pathways. However, excluding M- β -CD, other inhibitors had no significant effect on the uptake of the 50 nm BAPc- MNBs when incubated with cells for 4 h (**Figure 3.4C-D**). We believe that the combinatorial treatments did not elicit a stronger effect because Cpz (clathrin inhibitor) did not have a significant impact on the uptake of BAPc-MNBs. It is also possible that BAPc-MNBs may be endocytosed via a clathrin and caveolae independent pathway at this incubation time. This pathway is independent of dynamin function and caveolae dependent microdomains but majorly dependent on the cell membrane cholesterol which affects membrane fluidity.^{19,36, 37} Cells may also be using an energy-dependent pathway which is unaffected by the chemical inhibitors used in this study, over 1 h of incubation with BAPc-MNBs.

Some individual treatments with inhibitors such as Nystatin revealed higher uptake (120%) compared with the “No inhibitor” group. It has been reported in the literature that inhibition of a single endocytic pathway can up-regulate another pathway.³⁸ Thus, inhibition of caveolae mediated endocytosis by Nystatin may have increased internalization via macropinocytosis. Moreover, one cell type can sometimes endocytose the same nanoparticle using multiple pathways, as nanoparticle formulations are often made up of a group of heterogeneous particles, which makes the process more complicated to be analyzed.³⁹

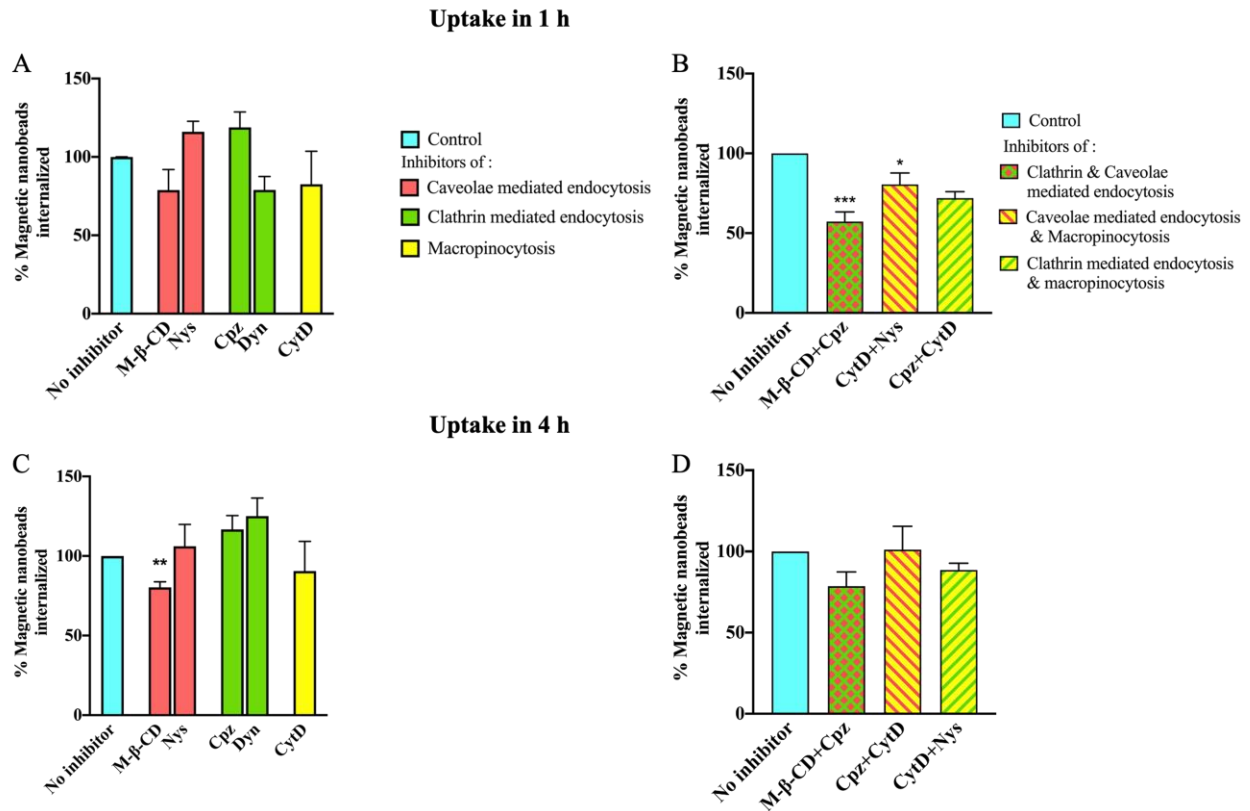


Figure 3.4. Endocytosis inhibition assay to determine uptake mechanism of 50 nm BAPc-MNBs by IEC-18

(A) and (B) IEC-18 incubated for 1 h with BAPc-MNBs + single and combinatorial inhibitor treatments respectively. (C) and (D) IEC-18 incubated for 4 h with BAPc-MNBs + single and combinatorial inhibitor treatments respectively. ANOVA followed by Bonferroni's posttest was applied for statistical analysis. (ns=not significant, *p-value<0.05, **p-value<0.01, ***p-value<0.001).

Rh-BAPCs (~ 50 nm) were subjected to similar experimental conditions used for BAPc-MNBs. Confocal imaging showed that water-filled Rh-BAPCs internalization in IEC-18 was inhibited by Nystatin, Cpz, CytD, Cpz + Cytochalasin D, M-β-CD + Cpz and to some degree with M-β-CD after 1 h of incubation (Figure 3.5). These results confirm that at 1 h internalization occurs via multiple pathways. After 4 h of incubation, uptake was inhibited only by Cytochalasin D + Cpz and to some degree by Cpz, showing that at longer incubation times clathrin mediated endocytosis and macropinocytosis are the major uptake pathways for Rh-BAPCs (Figure 3.5). Flow cytometry was used as well to verify results obtained by confocal

microscopy. This analysis also showed a significant decrease in the uptake of fluorescent BAPCs in the presence of Cpz and Cpz + Cytochalasin D, which agreed with confocal analysis (**Figure C.6A-B**). Nevertheless, a limitation of this analytical technique is that Rh-BAPCs trapped or bound to the cell membrane can result in the detection of a false positive for cells that did not actually uptake the nanoparticles. Therefore, results from this analysis should be always complemented with a secondary technique.

Endocytosis of nanoparticles is a complex process involving several proteins that play a role in the identification of the cargo and subsequent internalization via vesicle formation.^{39, 40} In the case of BAPCs, different cores (magnetic vs water) and sizes influenced the uptake route. These discrepancies were noticeable at both incubation times and **Figure C.7** summarizes the effect of endocytic inhibitors on BAPc-MNBs and Rh-BAPCs. Recent discoveries also indicated that incubation time with inhibitors may be cell type and nanoparticle size dependent, therefore a careful optimization would be required for each system.^{41, 42} Review of literature suggest that endocytosis of nanomaterials can take around 20-30 min or the whole process can take up to 4 h,¹¹ besides different uptake routes can be activated depending on the exposure time to nanoparticles.³¹

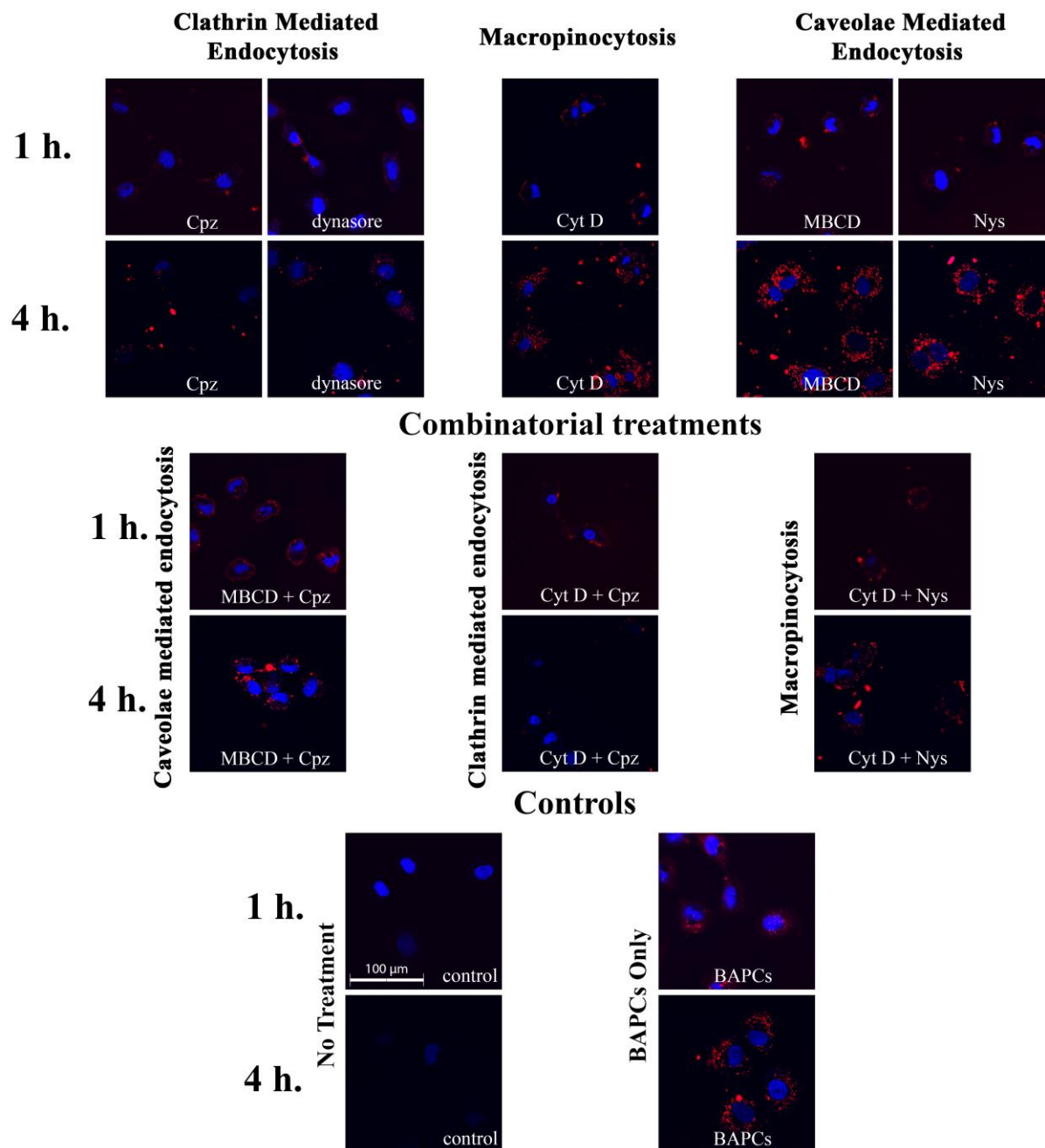


Figure 3.5.. Endocytosis inhibition assay to determine mechanism of rhodamine labelled BAPCs uptake by IEC-18

IEC-18 cells incubated with rhodamine BAPCs for 1 h and 4 h after preincubation with respective inhibitors of endocytosis. Inhibitors used are indicated in the bottom right corner of each micrograph. The pathway inhibited has been indicated above the micrographs for individual inhibitor treatments. For combinatorial treatments, the micrographs are placed directly below one pathway inhibited and to the right of the other pathway inhibited. The time of incubation is indicated to the left of the micrographs. Control group were cells treated exclusively with saline solution (PBS) and served as a positive control. BAPCs only group was not exposed to inhibitors. Bright field images showing cell boundaries are shown in **Figure C.8**.

Co-localization of magnetic nanobeads inside cells and their influence on cell viability and free radical generation.

Toxicity of BAPc-MNBs in IEC-18 cells was evaluated by flow cytometry. This is a rapid and reliable method to quantify cell viability.⁴³ Dead cells are identified by the fluorochrome 7-AAD, which binds to the DNA of damaged cells. As a result, those cells emit fluorescence at 647 nm and are identified as non-viable cells. As seen in **Figure 3.6A**, viability of IEC-18 treated with 50 nm BAPc-MNBs was minimally affected (<5% cell mortality). However, the number of non-viable cells increased at bead to cell ratios of 10000:1 for the 200 nm BAPc-MNBs. Due to some degree of cellular stickiness observed in macrophages, we did not use the 7AAD dye-based flow cytometry assay used to determine cell viability. Instead we used an MTT-like assay kit available commercially, which is claimed to be more sensitive than the traditional MTT assay for determining the macrophages viability.⁴⁴ The viability of macrophages treated with 50 nm and 200 nm BAPc-MNBs as well as the control MNBs was not significantly affected. Sodium azide (0.04 mM) was used to generate a positive control group, as it is cytotoxic and results in significant cell death. Thus, 50 nm BAPc-MNBs do not have an adverse effect on the viability of IEC-18 and J774A.1 cells (**Figure 3.6B**).

Reactive oxygen species generated by cells in response to nanoparticles is also a potent early marker for nanoparticle toxicity.^{45, 46} Transition metals such as iron (Fe^{+2}) in iron oxide nanoparticles can generate ROS by reacting with hydrogen peroxide (H_2O_2) to form hydroxyl free radical ($\text{OH}\cdot$) which is called the Fenton reaction.^{45, 47} These can disrupt the mitochondrial activity, cause damage to DNA and cause lipid peroxidation. This in turn destabilizes the cell membrane making it more susceptible to oxidation.^{47, 48} Phagocytes generate reactive nitrogen species (RNS) owing to their inducible nitric oxide synthase (iNOS) activity in response to

activation by foreign molecules.⁴⁷ Therefore, measuring ROS/RNS generated by epithelial cells and macrophages will help us determine the downstream effects of BAPc-MNBs from a toxicity perspective. Reactive oxygen species (ROS) were detected using Dichlorofluorescein-diacetate (DCF-DA) fluorescence assay. The release of reactive oxygen species causes increase in fluorescence of membrane permeable DCF-DA. BAPc-MNBs do not cause a significant increase in the ROS (**Figure 3.6C, D**) in either epithelial cells or macrophages. Similarly, no reactive nitrogen species (RNS) were detected in IEC-18 and J774A.1 cells treated with BAPc-MNBs. (**Figure C.9**)

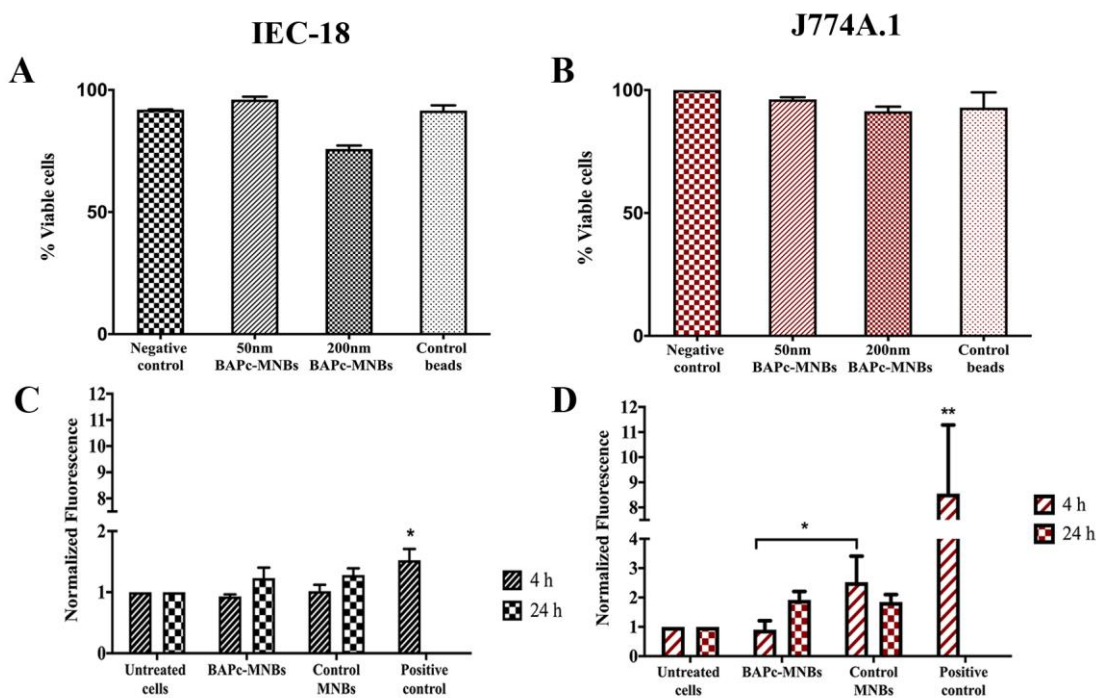


Figure 3.6. Cell viability assay and reactive oxygen species (ROS) assay to determine toxicity of BAPc-MNBs to cells

Flow cytometry analysis using 7AAD was used to determine cell viability of (A) IEC-18, treated with 50nm and 200nm BAPc-MNBs and control MNBs at 10000:1, beads to cell ratio. Negative control=No treatment. (B) Cell viability of J774A.1 cells were determined using an MTT like assay. The cells were treated with 50nm and 200nm BAPc-MNBs and control MNBs at 10000:1, beads to cell ratio. Reactive oxygen species generated by (C) IEC-18 and (D) J774A.1 cells after 4h and 24 h incubation with 10000:1 beads to cells, as determined by DCF-DA fluorescence-based assay. A normalized fluorescence greater

than 1 signifies higher ROS generated in comparison to untreated cells. Negative control=No treatment , Positive control = treated with hydrogen peroxide. (* p-value < 0.05, ** p-value < 0.01, n=4)

To verify that BAPc-MNBs gain access to IEC-18 and J774A.1 cytosolic space, cells were stained by incubation with Prussian blue (**Figure 3.7A-B**). This staining method uses an inorganic compound, potassium ferrocyanide, along with hydrochloric acid to permeate the fixed cells and bind to iron, developing a Prussian blue colored pigment. Thus, from these observations we confirmed that BAPc-MNBs and the control MNBs co-localized within IEC-18 and J774A.1 without affecting their morphology, growth or survival rate.

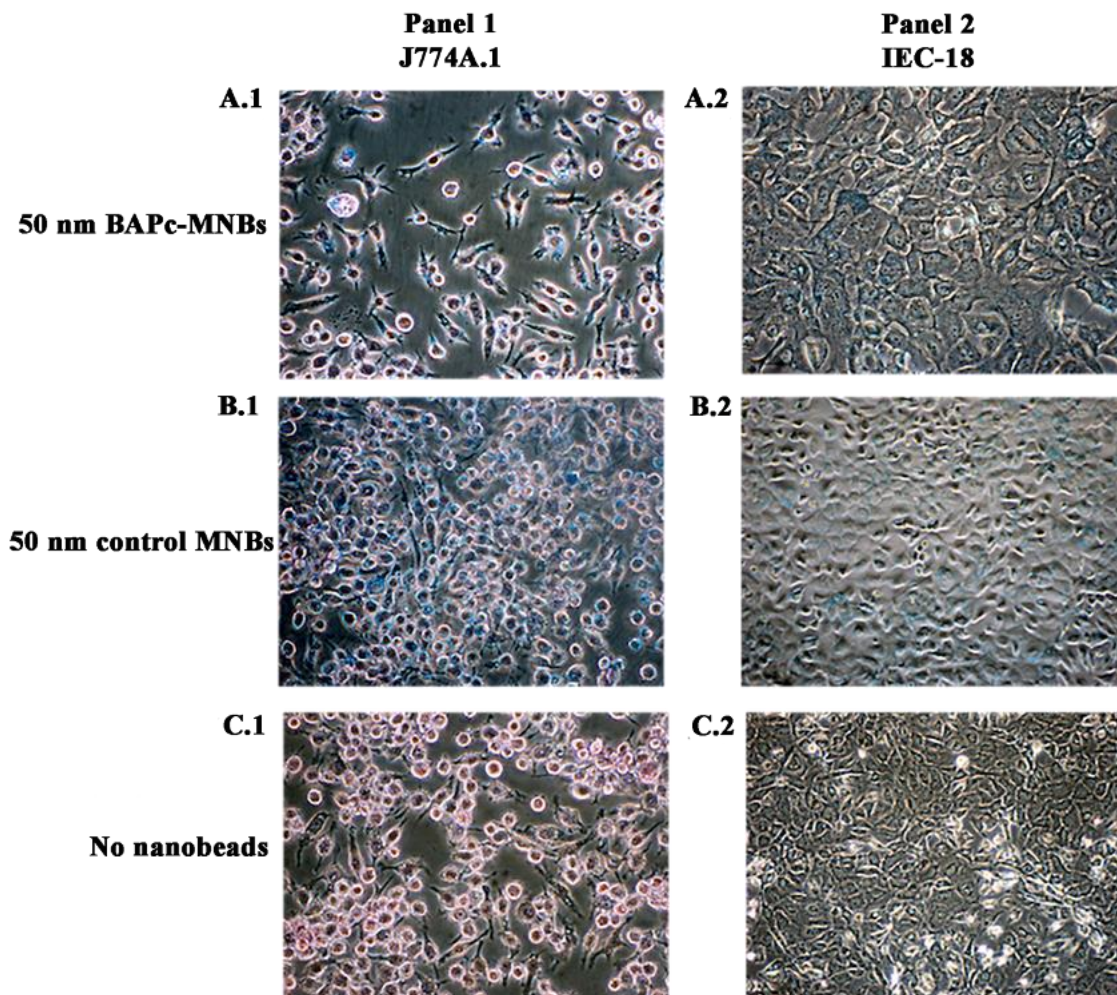


Figure 3.7. Prussian blue staining for visualization of magnetic nanobeads in J774A.1. and IEC-18 cells

The cells incubated with magnetic nanobeads at 10000:1, bead to cell ratio were imaged using an Optical light microscope (45X magnification for J774A.1 & 20X for IEC-18), to visualize the magnetic nanobeads internalized by cells as blue aggregates. (Panel 1) J774A.1 macrophage with (A.1) BAPc-MNBs, (B.1) MNBs and (C.1) no nanobeads; counter stained with Hema Stain® solution I (stains cytoplasm pink). (Panel 2) IEC-18 epithelial cells with (A.2) BAPc-MNBs, (B.2) MNBs and (C.2) no beads.

Conclusions

In summary, we studied the endocytic uptake routes of BAPc-MNBs in epithelial cells. The magnetic beads facilitated the separation and sorting of the cells that have internalized BAPCs and allowed us to quantify nanoparticles per cell using the ferene-s method. Results

indicated that after exposing cells to BAPc-MNBs for 1 h, the preferable route of entrance is clathrin and caveolae mediated endocytosis and macropinocytosis. Most likely these routes act synergistically. At 4 h, caveolae mediated endocytosis appeared to be the predominant pathway. However, future studies will elucidate and confirm if BAPc-MNBs may be endocytosed via a clathrin and caveolae independent pathway at this incubation time. This pathway is independent of dynamin function and caveolae dependent microdomains, but it is highly dependent on the cell membrane cholesterol which affects membrane fluidity.

We compared uptake results of BAPc-MNBs with water-filled Rh-BAPCs using the same incubation periods. Confocal imaging showed that at 1 h internalization is similar to BAPc-MNBs. However, after 4 h of incubation, uptake was inhibited only by Cytochalasin D + Cpz and to some extent by Cpz, showing that at longer incubation times clathrin mediated endocytosis and macropinocytosis are the major uptake pathways for Rh-BAPCs. These slight variances observed mostly at longer incubation times can be attributed to the type of nanoparticle used (BAPCs with different cores). Similar discrepancies have been reported for other nanoparticles with different cores ⁴⁵.

The study also demonstrated that while epithelial cells preferentially internalize BAPc-MNBs over unmodified control beads, macrophages indiscriminately phagocytose the magnetic beads with different surface compositions. Uptake also appeared to be more efficient for 50 nm BAPc-MNBs than 200 nm BAPc-MNBs in epithelial cells and hence 50 nm BAPc-MNBs were used to determine the endocytic uptake mechanism. Cell viability was carefully assayed and we confirmed that it is minimally affected by BAPc-MNBs as < 5% of non-viable cells were detected using flow cytometry and MTT analysis in IEC-18 and macrophages, respectively. In

addition, BAPc-MNBs did not significantly induce ROS generation in the cell lines we tested. i.e. induce oxidative stress, that could cause damage to the DNA and mitochondria.

We have also explored different techniques in this study and have therefore been able to weigh their advantages and disadvantages. Peptide bilayer coated magnetic beads are quantitative tools, however, a limitation of this technique is the exclusion of BAPc-MNBs bound to the cell membrane. Confocal imaging allows for visual analysis with the limitation that it is not quantitative. Flow cytometry on the other hand is not very suitable for the kind of study conducted here given that interference was observed from membrane embedded fluorescent particles. Overall, applying different methods helps to compensate for each other's limitation.

Biophysical characterization of BAPc-MNBs confirmed the presence of the peptide bilayer coating on MNBs and the homogeneity/ monodispersity of the nanoparticles. Thus, we have described herein, a relatively easy and reliable method to synthesize cationic peptide bilayer coated magnetic nanoparticles. We explored the similarities and differences between the magnetic and water-filled core BAPCs in cell culture, for their use in other applications in vitro and in vivo. This study brings us a step closer to understanding BAPCs and their interactions with cells, that will allow us to further investigate the potential of magnetic and water-filled core BAPCs in therapeutic applications.

References

1. Bull, S. R.; Guler, M. O.; Bras, R. E.; Meade, T. J.; Stupp, S. I., Self-assembled peptide amphiphile nanofibers conjugated to MRI contrast agents. *Nano Lett* 2005, 5 (1), 1-4. <https://doi.org/10.1021/nl0484898>.
2. Cui, H.; Webber, M. J.; Stupp, S. I., Self-assembly of peptide amphiphiles: from molecules to nanostructures to biomaterials. *Biopolymers* 2010, 94 (1), 1-18. <https://doi.org/10.1002/bip.21328>.

3. Matson, J. B.; Stupp, S. I., Self-assembling peptide scaffolds for regenerative medicine. *Chem Commun (Camb)* 2012, 48 (1), 26-33. <https://doi.org/10.1039/c1cc15551b>.
4. Gudlur, S.; Sukthankar, P.; Gao, J.; Avila, L. A.; Hiromasa, Y.; Chen, J.; Iwamoto, T.; Tomich, J. M., Peptide nanovesicles formed by the self-assembly of branched amphiphilic peptides. *PLoS One* 2012, 7 (9). <https://doi.org/e45374.10.1371/journal.pone.0045374>.
5. Sukthankar, P.; Gudlur, S.; Avila, L. A.; Whitaker, S. K.; Katz, B. B.; Hiromasa, Y.; Gao, J.; Thapa, P.; Moore, D.; Iwamoto, T.; Chen, J.; Tomich, J. M., Branched oligopeptides form nanocapsules with lipid vesicle characteristics. *Langmuir* 2013, 29 (47), 14648-54. <https://doi.org/10.1021/la403492n>.
6. Barros, S. M.; Avila, L. A.; Whitaker, S. K.; Wilkinson, K. E.; Sukthankar, P.; Beltrão, E. I. C.; Tomich, J. M., Branched Amphiphilic Peptide Capsules: Different Ratios of the Two Constituent Peptides Direct Distinct Bilayer Structures, Sizes, and DNA Transfection Efficiency. *Langmuir* 2017, 33 (28), 7096-7104. <https://doi.org/10.1021/acs.langmuir.7b00912>.
7. Sukthankar, P.; Whitaker, S. K.; Garcia, M.; Herrera, A.; Boatwright, M.; Prakash, O.; Tomich, J. M., Thermally induced conformational transitions in nascent branched amphiphilic peptide capsules. *Langmuir* 2015, 31 (10), 2946-55. <https://doi.org/10.1021/la504381y>.
8. Avila, L. A.; Aps, L. R. M. M.; Ploscariu, N.; Sukthankar, P.; Guo, R.; Wilkinson, K. E.; Games, P.; Szoszkiewicz, R.; Alves, R. P. S.; Diniz, M. O.; Fang, Y.; Ferreira, L. C. S.; Tomich, J. M., Gene delivery and immunomodulatory effects of plasmid DNA associated with Branched Amphiphilic Peptide Capsules. *J Control Release* 2016, 241, 15-24. <https://doi.org/10.1016/j.jconrel.2016.08.042>.
9. Avila, L. A.; Chandrasekar, R.; Wilkinson, K. E.; Balthazor, J.; Heerman, M.; Bechard, J.; Brown, S.; Park, Y.; Dhar, S.; Reeck, G. R.; Tomich, J. M., Delivery of lethal dsRNAs in insect diets by branched amphiphilic peptide capsules. *J Control Release* 2018, 273, 139-146. <https://doi.org/10.1016/j.jconrel.2018.01.010>.
10. Wessel, E. M.; Tomich, J. M.; Todd, R. B., Biodegradable Drug-Delivery Peptide Nanocapsules. *ACS Omega* 2019, 4 (22), 20059-20063. <https://doi.org/10.1021/acsomega.9b03245>.
11. Natarajan, P.; Sukthankar, P.; Changstrom, J.; Holland, C. S.; Barry, S.; Hunter, W. B.; Sorensen, C. M.; Tomich, J. M., Synthesis and Characterization of Multifunctional Branched Amphiphilic Peptide Bilayer Conjugated Gold Nanoparticles. *ACS Omega* 2018, 3 (9), 11071-11083. <https://doi.org/10.1021/acsomega.8b01633>.
12. Ali, A. A.; Hsu, F. T.; Hsieh, C. L.; Shiau, C. Y.; Chiang, C. H.; Wei, Z. H.; Chen, C. Y.; Huang, H. S., Erlotinib-Conjugated Iron Oxide Nanoparticles as a Smart Cancer-Targeted Theranostic Probe for MRI. *Sci Rep* 2016, 6, 36650. <https://doi.org/10.1038/srep36650>.

13. McFadden, C.; Mallett, C. L.; Foster, P. J., Labeling of multiple cell lines using a new iron oxide agent for cell tracking by MRI. *Contrast Media Mol Imaging* 2011, 6 (6), 514-22. <https://doi.org/10.1002/cmml.456>.
14. Reddy, L. H.; Arias, J. L.; Nicolas, J.; Couvreur, P., Magnetic nanoparticles: design and characterization, toxicity and biocompatibility, pharmaceutical and biomedical applications. *Chem Rev* 2012, 112 (11), 5818-78. <https://doi.org/10.1021/cr300068p>.
15. Lundquist, P.; Artursson, P., Oral absorption of peptides and nanoparticles across the human intestine: Opportunities, limitations and studies in human tissues. *Adv Drug Deliv Rev* 2016, 106 (Pt B), 256-276. <https://doi.org/10.1016/j.addr.2016.07.007>.
16. Simovic, S.; Song, Y.; Nann, T.; Desai, T. A., Intestinal absorption of fluorescently labeled nanoparticles. *Nanomedicine* 2015, 11 (5), 1169-78. <https://doi.org/10.1016/j.nano.2015.02.016>.
17. Kyoung, K. S.; Kenichi, S.; Hana, C.; Yu, Y. S.; You, B. H., Oral Nanoparticles Exhibit Specific HighEfficiency Intestinal Uptake and Lymphatic Transport. *ACS Nano* 2018, 12 (9), 7. <https://doi.org/10.1021/acsnano.8b04315>.
18. Hedayati, M.; Abubaker-Sharif, B.; Khattab, M.; Razavi, A.; Mohammed, I.; Nejad, A.; Wabler, M.; Zhou, H.; Mihalic, J.; Gruettner, C.; DeWeese, T.; Ivkov, R., An optimised spectrophotometric assay for convenient and accurate quantitation of intracellular iron from iron oxide nanoparticles. *Int J Hyperthermia* 2018, 34 (4), 373-381. <https://doi.org/10.1080/02656736.2017.1354403>.
19. Sahay, G.; Alakhova, D. Y.; Kabanov, A. V., Endocytosis of nanomedicines. *J Control Release* 2010, 145 (3), 182-95. <https://doi.org/10.1016/j.jconrel.2010.01.036>.
20. Mercer, J.; Helenius, A., Virus entry by macropinocytosis. *Nat Cell Biol* 2009, 11 (5), 510-20. <https://doi.org/10.1038/ncb0509-510>.
21. Sukthankar, P.; Avila, L. A.; Whitaker, S. K.; Iwamoto, T.; Morgenstern, A.; Apostolidis, C.; Liu, K.; Hanzlik, R. P.; Dadachova, E.; Tomich, J. M., Branched amphiphilic peptide capsules: cellular uptake and retention of encapsulated solutes. *Biochim Biophys Acta* 2014, 1838 (9), 2296-305. <https://doi.org/10.1016/j.bbamem.2014.02.005>.
22. Tucker, M.; Oyola, R.; Gai, F., Conformational distribution of a 14-residue peptide in solution: A fluorescence resonance energy transfer study. *Journal of Physical Chemistry B* 2005, 109 (10), 4788-4795. <https://doi.org/10.1021/jp044347q>.
23. Danaei, M.; Dehghankhold, M.; Ataei, S.; Hasanzadeh Davarani, F.; Javanmard, R.; Dokhani, A.; Khorasani, S.; Mozafari, M. R., Impact of Particle Size and Polydispersity Index on the Clinical Applications of Lipidic Nanocarrier Systems. *Pharmaceutics* 2018, 10 (2). <https://doi.org/10.3390/pharmaceutics10020057>.

24. Lim, J.; Yeap, S. P.; Che, H. X.; Low, S. C., Characterization of magnetic nanoparticle by dynamic light scattering. *Nanoscale Res Lett* 2013, 8 (1), 381. <https://doi.org/10.1186/1556-276X-8-381>.
25. Johnstone, S. A.; Masin, D.; Mayer, L.; Bally, M. B., Surface-associated serum proteins inhibit the uptake of phosphatidylserine and poly(ethylene glycol) liposomes by mouse macrophages. *Biochim Biophys Acta* 2001, 1513 (1), 25-37. [https://doi.org/10.1016/s0005-2736\(01\)00292-9](https://doi.org/10.1016/s0005-2736(01)00292-9).
26. Xiao, K.; Li, Y.; Luo, J.; Lee, J. S.; Xiao, W.; Gonik, A. M.; Agarwal, R. G.; Lam, K. S., The effect of surface charge on in vivo biodistribution of PEG-oligocholeic acid based micellar nanoparticles. *Biomaterials* 2011, 32 (13), 3435-46. <https://doi.org/10.1016/j.biomaterials.2011.01.021>.
27. Zhang, X. X.; Prata, C. A.; Berlin, J. A.; McIntosh, T. J.; Barthelemy, P.; Grinstaff, M. W., Synthesis, characterization, and in vitro transfection activity of charge-reversal amphiphiles for DNA delivery. *Bioconjug Chem* 2011, 22 (4), 690-9. <https://doi.org/10.1021/bc1004526>.
28. Foged, C.; Brodin, B.; Frokjaer, S.; Sundblad, A., Particle size and surface charge affect particle uptake by human dendritic cells in an in vitro model. *Int J Pharm* 2005, 298 (2), 315-22. <https://doi.org/10.1016/j.ijpharm.2005.03.035>.
29. Oh, E.; Delehanty, J. B.; Sapsford, K. E.; Susumu, K.; Goswami, R.; Blanco-Canosa, J. B.; Dawson, P. E.; Granek, J.; Shoff, M.; Zhang, Q.; Goering, P. L.; Huston, A.; Medintz, I. L., Cellular uptake and fate of PEGylated gold nanoparticles is dependent on both cell-penetration peptides and particle size. *ACS Nano* 2011, 5 (8), 6434-48. <https://doi.org/10.1021/nn201624c>.
30. Thurn, K. T.; Brown, E.; Wu, A.; Vogt, S.; Lai, B.; Maser, J.; Paunesku, T.; Woloschak, G. E., Nanoparticles for applications in cellular imaging. *Nanoscale Res Lett* 2007, 2 (9), 430-41. <https://doi.org/10.1007/s11671-007-9081-5>.
31. Wu, T. T.; Chen, T. L.; Chen, R. M., Lipopolysaccharide triggers macrophage activation of inflammatory cytokine expression, chemotaxis, phagocytosis, and oxidative ability via a toll-like receptor 4-dependent pathway: validated by RNA interference. *Toxicol Lett* 2009, 191 (2-3), 195-202. <https://doi.org/10.1016/j.toxlet.2009.08.025>.
32. Dutta, D.; Donaldson, J. G., Search for inhibitors of endocytosis: Intended specificity and unintended consequences. *Cell Logist* 2012, 2 (4), 203-208. <https://doi.org/10.4161/cl.23967>.
33. Rodal, S. K.; Skretting, G.; Garred, O.; Vilhardt, F.; van Deurs, B.; Sandvig, K., Extraction of cholesterol with methyl-beta-cyclodextrin perturbs formation of clathrin-coated endocytic vesicles. *Mol Biol Cell* 1999, 10 (4), 961-74. <https://doi.org/10.1091/mbc.10.4.961>.

34. Preta, G.; Cronin, J. G.; Sheldon, I. M., Dynasore - not just a dynamin inhibitor. *Cell Commun Signal* 2015, 13, 24. <https://doi.org/10.1186/s12964-015-0102-1>.
35. Mäger, I.; Langel, K.; Lehto, T.; Eiríksdóttir, E.; Langel, U., The role of endocytosis on the uptake kinetics of luciferin-conjugated cell-penetrating peptides. *Biochim Biophys Acta* 2012, 1818 (3), 502-11. <https://doi.org/10.1016/j.bbamem.2011.11.020>.
36. Damm, E. M.; Pelkmans, L.; Kartenbeck, J.; Mezzacasa, A.; Kurzchalia, T.; Helenius, A., Clathrin- and caveolin-1-independent endocytosis: entry of simian virus 40 into cells devoid of caveolae. *J Cell Biol* 2005, 168 (3), 477-88. <https://doi.org/10.1083/jcb.200407113>.
37. dos Santos, T.; Varela, J.; Lynch, I.; Salvati, A.; Dawson, K. A., Effects of transport inhibitors on the cellular uptake of carboxylated polystyrene nanoparticles in different cell lines. *PLoS One* 2011, 6 (9). <https://doi.org/e24438.10.1371/journal.pone.0024438>.
38. Robinson, M.; Watts, C.; Zerial, M., Membrane dynamics in endocytosis. *Cell* 1996, 84 (1), 13-21. [https://doi.org/10.1016/S0092-8674\(00\)80988-5](https://doi.org/10.1016/S0092-8674(00)80988-5).
39. Foroozandeh, P.; Aziz, A. A., Insight into Cellular Uptake and Intracellular Trafficking of Nanoparticles. *Nanoscale Res Lett* 2018, 13 (1), 339. <https://doi.org/10.1186/s11671-018-2728-6>.
40. Kuhn, D. A.; Vanhecke, D.; Michen, B.; Blank, F.; Gehr, P.; Petri-Fink, A.; Rothen-Rutishauser, B., Different endocytotic uptake mechanisms for nanoparticles in epithelial cells and macrophages. *Beilstein J Nanotechnol* 2014, 5, 1625-36. <https://doi.org/10.3762/bjnano.5.174>.
41. Ivanov, A. I., Pharmacological inhibition of endocytic pathways: is it specific enough to be useful? *Methods Mol Biol* 2008, 440, 15-33. https://doi.org/10.1007/978-1-59745-178-9_2.
42. Sasso, L.; Purdie, L.; Grabowska, A.; Jones, A. T.; Alexander, C., Time and cell-dependent effects of endocytosis inhibitors on the internalization of biomolecule markers and nanomaterials *Journal of Interdisciplinary Nanomedicine* 2018. <https://doi.org/10.1002/jin2.39>.
43. Chan, L. L.; McCulley, K. J.; Kessel, S. L., Assessment of Cell Viability with Single-, Dual-, and Multi-Staining Methods Using Image Cytometry. *Methods Mol Biol* 2017, 1601, 27-41. https://doi.org/10.1007/978-1-4939-6960-9_3.
44. Mosmann, T., Rapid colorimetric assay for cellular growth and survival: application to proliferation and cytotoxicity assays. *J Immunol Methods* 1983, 65 (1-2), 55-63. [https://doi.org/10.1016/0022-1759\(83\)90303-4](https://doi.org/10.1016/0022-1759(83)90303-4).
45. Gokduman, K.; Bestepe, F.; Li, L.; Yarmush, M.; Usta, O., Dose-, treatment- and time-dependent toxicity of superparamagnetic iron oxide nanoparticles on primary rat

- hepatocytes. *Nanomedicine* 2018, 13 (11), 1267-1284. <https://doi.org/10.2217/nmm-2017-0387>.
46. Feng, Q.; Liu, Y.; Huang, J.; Chen, K.; Xiao, K., Uptake, distribution, clearance, and toxicity of iron oxide nanoparticles with different sizes and coatings. *Sci Rep* 2018, 8 (1), 2082. <https://doi.org/10.1038/s41598-018-19628-z>.
 47. Manke, A.; Wang, L.; Rojanasakul, Y., Mechanisms of Nanoparticle-Induced Oxidative Stress and Toxicity. *Biomed Research International* 2013. <https://doi.org/10.1155/2013/942916>.
 48. Ansari, M.; Parveen, N.; Ahmad, M.; Wani, A.; Afrin, S.; Rahman, Y.; Jarneel, S.; Khan, Y.; Siddique, H.; Tabish, M.; Shadab, G., Evaluation of DNA interaction, genotoxicity and oxidative stress induced by iron oxide nanoparticles both in vitro and in vivo: attenuation by thymoquinone. *Scientific Reports* 2019, 9. <https://doi.org/10.1038/s41598-019-43188-5>.

Chapter 4 - The biodistribution of BAPc-MNBs administered via different routes and their application in the delivery of an active peptide

Introduction

Branched amphiphilic peptide coated magnetic nanobeads (BAPc-MNBs) are readily taken up by mammalian cells via multiple endocytic routes in a time dependent manner.¹ They induce a pro-inflammatory response in mouse macrophages (J774A.1) and rat intestinal epithelial cells (IEC-18), in vitro. However, the immune response generated to BAPc-MNBs in IEC-18 is dose dependent and only the highest dosage of the magnetic nanoparticles induces a significant response. The cell viability of epithelial cells and macrophages is unaffected by BAPc-MNBs, although they induced increased ROS production in macrophages. Thus, BAPc-MNBs are suitable candidates to be further explored for in vivo applications.

Nanoparticles (NPs) encounter a very complex environment in vivo, which determines their tissue distribution, bioavailability and clearance from the system.^{2,3} Depending upon the route of administration, the initial interactions of NPs vary and affect their overall pharmacokinetics and biodistribution. We therefore chose to study the effect of different administration routes on BAPc-MNBs biodistribution, to determine the most suitable route of administration, beneficial for specific applications. The tissue distribution of BAPc-MNBs was determined in C57BL/6 mice injected with NPs intravenously (i.v.) and in BALB/c mice, administered with NPs intraperitoneally (i.p.) and using the oral gavage method. C57BL/6 and BALB/c mice typically exhibit a Th1 type and Th2 type response, respectively.⁴ The innate

response is generally pro-inflammatory in nature in C57BL/6 mice and anti-inflammatory in BALB/c mice.⁵

NPs are not readily absorbed in the intestine of animals which is a major barrier to oral delivery.^{6, 7} The biocompatible molecules such as peptides and proteins are acted upon by peptidases and acidic digestive juices (pH 2) proving to be a major hurdle in oral delivery.⁸ However, oral intake of drugs is preferred by the end user and thus, researchers continually work to design nanoparticle-drug conjugates that are effective when administered orally.⁹ BAPCs are unaffected by mammalian proteinases and are not denatured within mammalian cells.^{10, 11} BAPCs conjugated with dsRNA have been successfully delivered in liquid and solid insect diets to *Tribolium castaneum* and *Acyrtosiphon pisum*.¹² *Tribolium* shows a gradual increase from pH 5.6 to pH 7.5 in the anterior to posterior midgut, similar to mammalian intestines in pH, with the exception that their GI system is far less complex.^{13, 14} We therefore hypothesized that BAPC-MNBs may be able to cross the acidic stomach to be absorbed into the mammalian system through the intestinal barrier.

BAPCs have effectively delivered nucleic acids bound to their surface.^{12, 15, 16} We are yet to explore their delivery of other surface adducted biomolecules. In this study, we explored the applicability of BAPC-MNBs to deliver a 9-residue peptide. Retro-inverso D-amino acids containing peptide (RD-p9; SHAEVTYSS) is a oligo peptide derived from the tail region of β 2-glycoprotein I (β 2-GPI) binding domain V, which inserts itself into the lipid membrane.^{17, 18} β 2-GPI binds to anionic lipids in hypoxic cells and causes a conformational change in the protein, exposing domains I-II which binds naturally occurring antibodies and triggers antibody dependent complement activation and inflammation.¹⁹⁻²¹ The Fleming group has demonstrated that RD-p9 can prevent intestinal ischemia/reperfusion induced injury when injected during

ischemia¹⁸ or early during reperfusion.¹⁷ Recent evidence suggests that RD-p9 peptide effectively reduces melanoma tumor growth in mice by competing with β 2-GPI to bind endothelial cells. It prevents migration of endothelial cells in vitro and alters the vasculature markers and reduces angiogenesis in vivo. RD-p9 reduces the abnormal vasculature in tumors and thus inhibits tumor growth.²²

We hypothesized that BAPc-MNBs could deliver a slightly different peptide D-p9 peptide that reduces tumor growth while increasing the bioavailability of D-p9. D-p9 (SSYTVEAHS) consists of the D-amino acids in the coded N to C sequence, unlike RD-p9 and is observed to have the same effect on melanoma tumor growth. Along with BAPc-MNBs, fluorescent water-soluble dye filled 25 nm BAPCs were used to deliver D-p9. BAPc-MNBs showed variations in tissue distribution in mice with and without subcutaneously injected melanoma tumors. i.p. injections of BAPc-MNBs was slightly more successful in distributing the nanoparticles, in comparison to their oral delivery in BALB/c mice. D-p9 delivery using the BAPc-MNBs and BAPCs delivery systems was inconclusive and further studies are required to verify the delivery of D-p9 and the effect on tumor growth.

Materials and methods

Synthesis of D-p9 conjugated BAPc-MNBs and BAPCs.

BAPc-MNBs and BAPCs were synthesized as described previously.¹ One mg/mL Alexa Fluor ® 488 was used instead of rhodamine for encapsulation in BAPCs. The outer peptide layer of BAPc-MNBs and BAPCs was composed of a mix of bis (Ac-FLIVIGSII)-KKKKK-CONH₂ and bis(Ac-FLIVIGSII)-KKKKK-C-CONH₂ in approximately 2:1 ratio. The peptide solution added during the outer peptide layer formation in water, consisted of 1/3rd bis(Ac-FLIVIGSII)-

KKKKK-C-CONH₂. For BAPCs synthesis, 33% of the peptide solution used contained bis (Ac-FLIVIGSII)-KKKKK-C-CONH₂. D-p9 peptide was modified to have a cysteine residue on its C-terminal in place of the serine. D-p9 was coupled to BAPc-MNBs and BAPCs via a disulfide bond. And the disulfide bond formation was mediated by reacting BAPCs and BAPc-MNBs in DI water containing 2% DMSO and ten times excess of D-p9, overnight, with mixing at room temperature. The BAPc-MNBs and BAPCs solution was diluted in water to prevent overcrowding of the NPs and thus allowing D-p9 conjugation while preventing aggregation of the NPs. Three to four washes were performed to BAPCs using a 30K MWCO filter and to BAPc-MNBs using magnetic separation, to remove any excess unbound D-p9.

Determining conjugation of D-p9.

The peptide bilayer on BAPc-MNBs and BAPCs was separated in neat trifluoroethanol to yield monomeric peptides. The coupling of D-p9 was verified by detecting the mass of the coupled D-p9 peptide and bis (Ac-FLIVIGSII)-KKKKK-C-CONH₂ i.e. sum of the peptide masses, using a Bruker MALDI-TOF Ultraflex III mass spectrophotometer. One microliter of the peptide solution was spotted on the plate with 1 μ L of 2,5 -dihydroxybenzoic acid (DHB) and the reflectron mode was used on the instrument to detect the lower mass range peptides.

In vivo tumors.

C57Bl/6 mice (Jax.org) were bred and maintained in the Division of Biology at Kansas State University. Male and female mice were kept in a 12 h light/dark cycle with constant access to rodent food and water. All procedures were approved by the Institutional Animal Care and Use Committee (IACUC) (Protocol # 4220) and were in compliance with the Animal Welfare

Act. Four to five weeks old, C57BL/6 mice were used for all studies. 2×10^6 B16F10 mouse melanoma tumor cells suspended 1:1 in Matrigel (Corning) were injected sub-cutaneous on the ventral side in the thoracic region of the mice. The mice were weighed and tumor growth was monitored every day. Tumor size was measured and recorded using Vernier calipers as length \times width \times height. The tumor was excised on day 10, the ex-vivo tumor volume and diameter was calculated and pictures were captured. The weight of the tumor was recorded and arbitrarily divided into two. One half of the tumor was snap dried using liquid nitrogen and the other half of the tumor was used to collect tumor secretions, ex vivo. The secretions were collected by incubating the tumor at 37 °C in 1 mL of freshly oxygenated, Tyrode's solution for 20 min. The tissue and supernatant were separated and stored at -80 °C for further analysis. Milliplex® mouse cytokines/chemokine panel (MCYTOMAG 70K, Mag Panel, 7plex) was used to analyze the secretions.

Injection of nanoparticles (C57BL/6) and harvesting tissues.

The mice were anaesthetized using isoflurane prior to the injection of 100 μ L of nanoparticles dispersed in 0.15 M saline intravenously (retro-orbital). The treatments that the mice were subjected to is indicated in **Table 4.1**. The tissues (spleen, lungs, kidneys, heart, brain, intestines, thymus, tumor, blood, urine, feces) were harvested at appropriate time points, their weights were recorded, washed in saline and stored for further analysis. Tissues from mice treated with Alexa Fluor® 488 encapsulated BAPCs were embedded in OCT for sectioning and imaging.

Table 4.1. Treatment of C57BL/6 mice with magnetic nanoparticles

Treatment	Without tumor		With tumor		Total no. of mice
	24 h	48 h	24 h	48 h	
Saline Control	6		6		12
2×10 ¹⁰ BAPc-MNBs (Low dose)	4	4	4	4	16
1×10 ¹¹ BAPc-MNBs (High dose)	4	4	4	4	16
2×10 ¹⁰ control beads (Low dose)	4	4	4	4	16
					60

Treatment of mice with D-p9 conjugated BAPc-MNBs and BAPCs.

The tumor bearing mice were injected with 100 µL of 40µM D-p9, D-p9 conjugated, 1 × 10¹¹ BAPc-MNBs and 0.25 mM BAPCs, on Day 3 after tumor injection. The organs were harvested on Day 10. The treatments and controls are as stated below in **Table 4.2**.

Table 4.2. Treatment of tumor bearing C57BL/6 mice with D-p9

Treatment	No. of mice
Saline Control	5
BAPc-MNBs	5
BAPCs	5
D-p9	5
BAPc-MNBs + D-p9	5
BAPCs + D-p9	5
	30

Oral gavage in BALB/c .

A total of 18 animals were used for oral gavage studies. Animals were fasted overnight but had free access to water. Six animals were sham gavaged and euthanized at 48 h. to each mouse. To gavage, mice were lightly anesthetized using isoflurane and 2×10¹¹ BAPc-MNBs

were administered with a max volume 200 μ L. Six mice were euthanized at 24 h post-gavage and six at 48 h post-gavage. Tissues were removed and stored at -80 $^{\circ}$ C.

Intraperitoneal injection.

For IP injections, mice were restrained in the head down position. A total of 18 animals were used for the study. The appropriate landmarks were identified and the lower right quadrant was sterilized using isopropyl alcohol. Using a 25-30-gauge needle, 2×10^{11} BAPc-MNBs were administered in a volume of $\leq 1\%$ kg body weight. Mice were returned to their individual cages and monitored until normal behavior is observed. Organs were harvested 24 h and 48 h after administration and stored at -80 $^{\circ}$ C.

Quantification of magnetic nanoparticles in mouse tissue.

The tissues were homogenized in 0.1M tris buffered saline (TBS) containing 1% Tween-20 (Sigma-Aldrich) using a pre-programmed gentleMACSTM dissociator (Miltenyi Biotec). The tissue homogenate was collected in 1.5mL Eppendorf vials and placed on a magnetic separator (Permagen), overnight for separation and collection of magnetic nanoparticles. The tissue homogenate was discarded and the magnetic beads were resuspended in DI water. Five μ L of 5 mg/mL Proteinase K (Sigma-Aldrich) was added to digest any protein bound to the NPs, before aliquoting the collected magnetic nanobeads into a 96 well plate and placing them on handheld magnets, overnight for separation at 37 $^{\circ}$ C. The magnetic beads were washed in DI water and quantified using the ferene-s assay as described previously in Natarajan et al.¹. The iron quantified was normalized using the weight of the tissue, for the ease of comparison.

Results and discussion

Tissue distribution of magnetic nanoparticles in wild type C57BL/6 mice.

BAPc-MNBs administered IV at low and high doses were localized significantly in spleen, lungs and heart, 24 h after injection (**Figure 4.1A, B, D, E**). The iron content in each organ was represented as microgram of iron detected per gram of tissue/organ. The highest amount of BAPc-MNBs were present in the spleen at 24 h and reduced significantly by 48 h (**Figure 4.1D, E**). Thus, BAPc-MNBs were distributed to the spleen, lungs and heart in significantly high amounts when injected IV in C57BL/6 mice. NPs were injected through the retro-orbital venous which empties into the external jugular vein and connects to the subclavian vein, carrying the NPs to the heart.²² Intestines also showed the presence of BAPc-MNBs either 24 h or 48 h after injection. The magnetic nanoparticles could not be detected in significant amounts in blood and excretory products (**Figure 4.1G, H**). Thus, BAPc-MNBs and control beads were cleared from circulation and deposited in various tissues within 24 h. Mice treated with the control beads that had no peptide bilayer coating on them were observed to be in significantly lower numbers in the spleen while no statistically significant amounts could be detected in other tissues except for the intestines (**Figure 4.1C, F, I**).

The mouse spleen on an average weighs about 0.1 grams. The average iron content in the spleen of a wild-type mouse treated with low and high dose of BAPc-MNBs for 24 h was 150 $\mu\text{g/g}$ (**Figure 4.1D**) and 350 $\mu\text{g/g}$ (**Figure 4.1E**), which amounts to 15 μg and 35 μg net iron in the spleen, respectively. BAPc-MNBs consistently accumulated in high numbers in the spleen at different treatment doses and times. Spleen is a highly vascular organs that acts as a blood filter and receives about 4.8% of the total cardiac output.^{23, 24} The blood carrying foreign molecules enters through the splenic artery and distributed further through a highly organized vascular

system to the white pulp and the marginal zone. Once through the marginal zone about 90% of the total splenic blood flow passes through the adjacent venous sinuses continuous with the marginal zone while some enter the meshwork of the red pulp.²³ The marginal zone macrophages can capture BAPc-MNBs or some can be retained by the macrophages in the red pulp for slow destruction. BAPc-MNBs persist in the spleen after 24 h of injection but ~50% reduction is observed indicating clearance and/or escape of BAPc-MNBs from the spleen by 48 h. An average of 25% BAPc-MNBs were retained in the spleen 7 days after injection in tumor bearing mice suggesting slow clearance of the NPs from the system.(**Figure D.1**)

Positively charged nanoparticles upon parenteral administration are often sequestered by macrophages in the lungs, liver and spleen, which are collectively termed as the Mononuclear phagocytic system (MPS).²⁵ This may explain the increased number of BAPc-MNBs in the lungs and spleen. The liver although does not show significant number of NPs in the quantitative analysis, visual observation during magnetic beads sorting from tissues clearly indicates presence of BAPc-MNBs either in the liver or the liver circulatory system. Thus, false negative results were obtained probably due to the limitation of the quantitative spectrophotometric assay used for analysis. Therefore, the ferene-s quantitative technique²⁶ used to determine tissue distribution needs to be complemented with another quantitative techniques such as ICP-MS³ or qualitative imaging analysis such as MRI²⁷, fluorescence live imaging²⁸ or Prussian blue staining³ of tissue sections for iron content analysis. However, in comparison to the spleen, the liver accumulated significantly lower levels of BAPc-MNBs per gram of the tissue. As the size of NPs increases in vivo due to protein corona formation and subsequent aggregation, fewer NPs are phagocytosed by kuppfer cells in the liver and more are retained in the spleen.^{24, 29} Tissue distribution is dependent on the nanoparticle size and the heterogenous nature of the NPs due to in vivo

interactions with serum proteins leads to differences in the retention of magnetic nanoparticles in different organs.

Some animals treated with 1×10^{11} BAPc-MNBs showed extremely high BAPc-MNBs (172 $\mu\text{g/g}$ and 92 $\mu\text{g/g}$) in the lungs at 24 h and 48 h after injection. These were outliers and were excluded from the analysis (**Figure 4.1B**). This suggests that the sample size needs to be increased to further verify and understand the factors affecting the distribution drastically in the lungs. BAPc-MNBs and control beads without the peptide bilayer were cleared from the system through the intestines, which showed significantly high levels of iron content in comparison to the saline control. The enterohepatic circulation transports secreted bile from the liver to the intestines for lipid digestion and absorption of nutrients. The bile transporters are conserved between humans and mice but the bile composition varies between the two species.³⁰ BAPc-MNBs and control beads might be transported to the intestines via the enterohepatic circulation, facilitating their clearance from the system.

Control beads showed some differences in the tissue distribution in comparison to BAPc-MNBs. (**Figure 4.1C, F, I**) Higher amounts of control beads were observed in the liver, kidneys and intestines while significantly less quantity was detected in the spleen when compared to BAPc-MNBs. Increased levels in intestines in comparison to the liver and lungs 24 h after injection may indicate faster clearance of the control beads from the system. Thus, we observe a difference in the tissue distribution of magnetic nanoparticles with the same core size but different surface composition and charge.

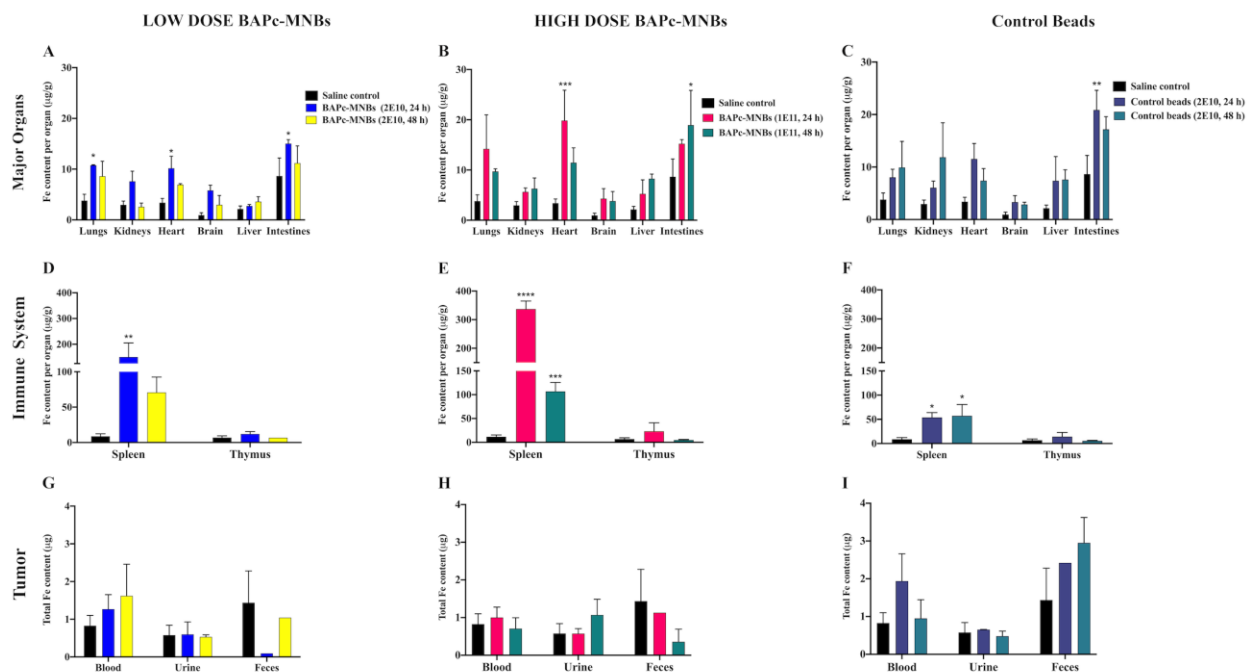


Figure 4.1. Tissue distribution of magnetic nanoparticles in wild type C57BL/6 mice

Iron content in major organs (A) (B) (C), organs of the immune system (D) (E) (F) and body fluids / excretory products (G) (H) (I) was determined 24 h and 48 h after injecting low dose (2×10^{10}) of BAPc-MNBs, control beads without peptide bilayer and high dose (1×10^{11}) of BAPc-MNBs. $n = 3$, 2-way ANOVA statistical analysis, Dunnett's multiple comparison test for statistical hypothesis testing. p -value : * < 0.05 , ** < 0.01 , *** < 0.001 , **** < 0.0001

Tissue distribution in B16F10 melanoma tumor bearing C57BL/6 mice.

Tumor bearing mice showed a similar tissue distribution to the wild type non-tumor bearing mice. A significant proportion of BAPc-MNBs were localized in the spleen followed by the lungs and heart (Figure 4.2A, B, D, E). The major difference between the tumor and non-tumor mice was the quantity of localized magnetic nanoparticles. The distribution of beads was not consistent with the dosage of NPs administered since the spleen, lungs, liver, excretory and digestive organs showed comparatively similar levels of iron content, 24 h and 48 h after injection of low or high doses of BAPc-MNBs. Iron from the control beads could not be detected in any of the organs sampled including the body fluids and excretory products (Figure 4.2C, F, I, L).

The presence of a subcutaneously injected melanoma tumor, thus, affected the tissue distribution of BAPc-MNBs and the control beads. The spleen showed significantly ($p < 0.001$) lesser number of NPs between the melanoma tumor bearing mice and mice without tumors which were treated with a high dose of BAPc-MNBs for 24 h. (**Figure 4.1, 4.2**) Kai et al.³¹ noted that the tumor causes global immune changes which can cause faster clearance of the NPs from the system. BAPc-MNBs may have thus been cleared faster in the tumor bearing mice treated with high dosage of the nanoparticles. Control beads were not present at detectable levels in the tissues analyzed, including the spleen, suggesting that they may be cleared almost instantaneously or faster than BAPc-MNBs. Iron content was increased in tumors harvested 24 h after treatment of mice with low dose of BAPc-MNBs only (**Figure 4.2G**). This is consistent with the idea that the presence of tumor accelerates the clearance of NPs.

Only an average of 25% of the total administered magnetic nanobeads was detected in the tissues of the C57BL/6 mice, with and without tumor. The NPs may have been deposited in other tissues that were not analyzed, such as bones which have previously been demonstrated to accumulate small amounts of the actinium encapsulated BAPCs¹⁰ or in lymph nodes, adipose tissue etc. BAPCs being smaller in size (25 nm) were observed to be in circulation 24 h after administration¹⁰ unlike the heavy, solid core magnetic BAPc-MNBs which were cleared within 24 h from circulation.

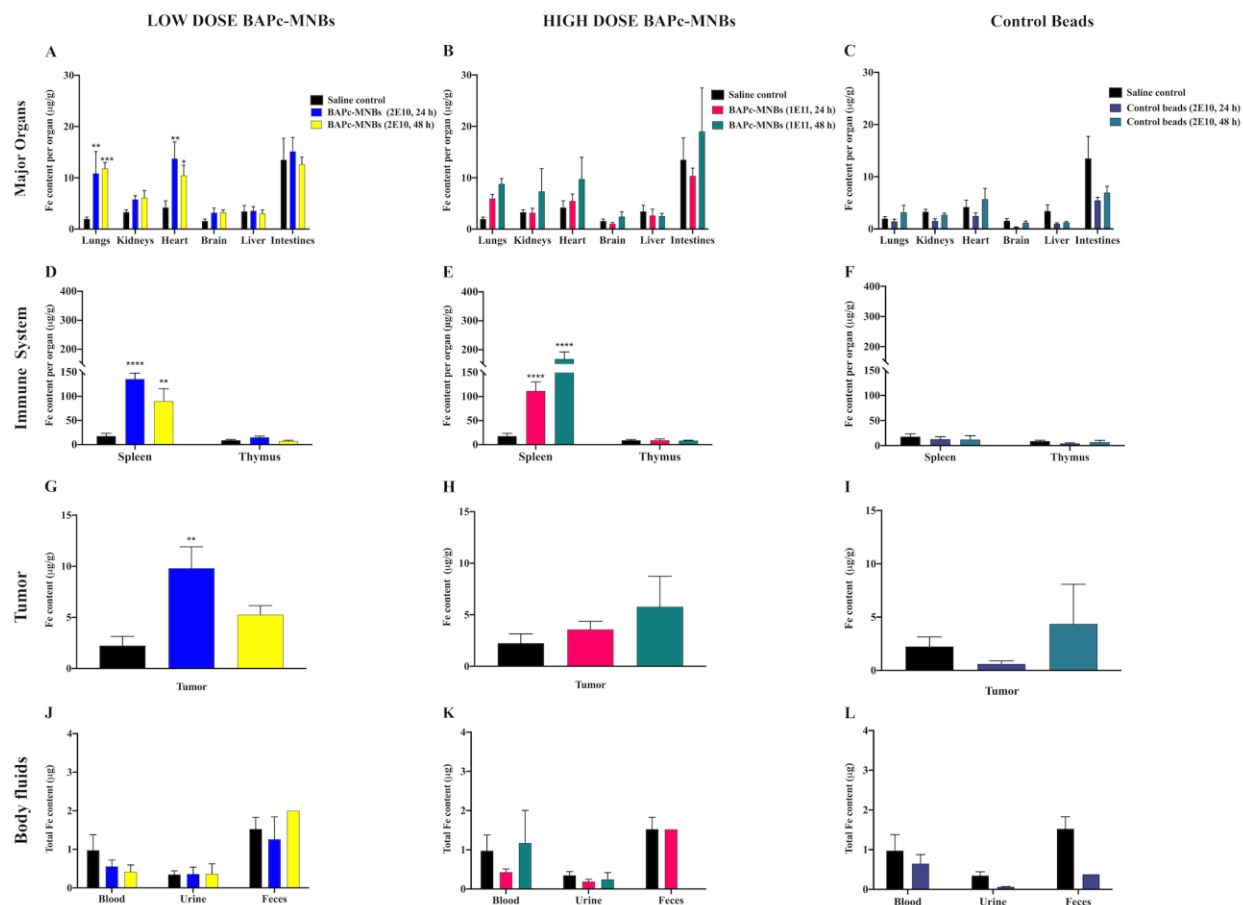


Figure 4.2. Tissue distribution of magnetic nanoparticles in B16F10 melanoma tumor bearing mice

Iron content in major organs (A) (B) (C), organs of the immune system (D) (E) (F), tumor (G) (H) (I) and body fluids / excretory products (J) (K) (L) was determined 24 h and 48 h after injecting low dose (2×10^{10}) of BAPc-MNBs, control beads without peptide bilayer and high dose (1×10^{11}) of BAPc-MNBs. $n = 4$, 2-way ANOVA statistical analysis, Dunnett's multiple comparison test for statistical hypothesis testing. p-value: * < 0.05 , ** < 0.01 , *** < 0.001 , **** < 0.0001

Tissue distribution in BALB/c mice treated with intraperitoneal injection of magnetic nanoparticles.

IP injections are commonly used for treatment of localized infections and abdominal malignancies. BAPc-MNBs were majorly detected in the spleen and to some extent in the stomach after 24 h and 48 h of IP injections (Figure 4.3B, C). The lungs, heart and thymus also showed increased numbers but it was not statistically significant (Figure 4.3A, B). The magnetic

NPs were not found in circulation, 24 h after injection. (Figure 4.3D). BAPc-MNBs (2×10^{11}) injected intraperitoneally in BALB/c mice accumulated mainly in the spleen followed by the stomach.(Figure 4.3B, C)

NPs administered IP diffuse across the mesothelium but may not be able to diffuse across the endothelium in the connective under the mesothelial layer due to the tight junctions. However, they can enter the lymphatic system through larger openings in the peritoneum called the stomata.³² Thus, BAPc-MNBs may have been distributed to the organs via the lymphatic system after IP injections. However, not all the NPs administered were detected and only a small percentage of it was found in the spleen and the stomach

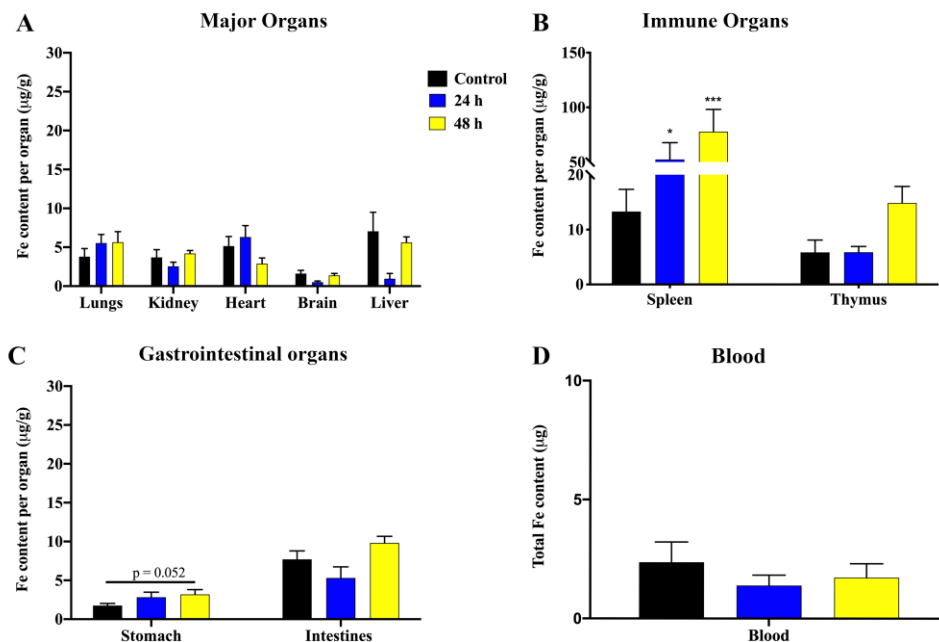


Figure 4.3. Tissue distribution of BAPc-MNBs injected i.p. in BALB/c mice

Iron content in major organs (A), organs of the immune system (B), Gastrointestinal system (C) and blood (D) was determined 24 h and 48 h after injecting high dose (2×10^{11}) of BAPc-MNBs. n = 5, 2-way ANOVA statistical analysis, Dunnett's multiple comparison test for statistical hypothesis testing. p-value: * <0.05, ** <0.01, *** <0.001, **** < 0.0001

Tissue distribution in BALB/c mice administered magnetic nanoparticles orally.

BAPc-MNBs administered orally using the gavage method were only found in significant numbers in lungs of BALB/c mice after 24 h (**Figure 4.4A**). Thus, oral delivery using the gavage method was unsuccessful in delivering BAPc-MNBs to all the organs tested. The net iron content detected in all other organs was not significantly different from the control which indicates that BAPc-MNBs were either present at very low undetectable levels or not present in the tissues analyzed. (**Figure 4.4**) Significant number of BAPc-MNBs were detected in the lungs 24 h after administration which may have been due to aspiration of the NPs during gavage using a feeding tube.

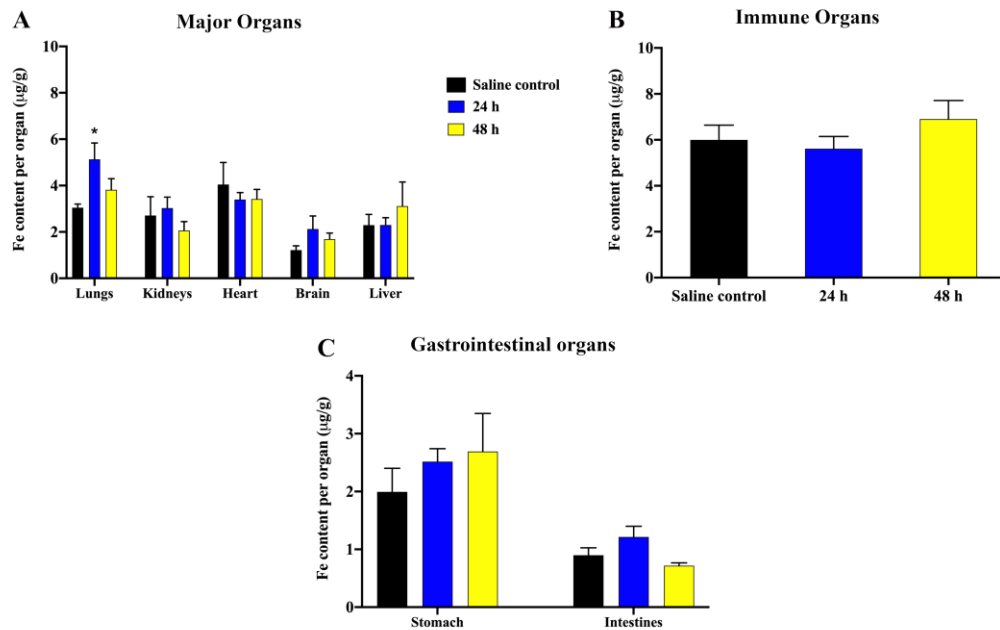


Figure 4.4. Tissue distribution of BAPc-MNBs administered orally to BALB/c mice

Iron content in major organs (A), organs of the immune system (B) and Gastrointestinal system (C) was determined 24 h and 48 h after administering high dose (2×10^{11}) of BAPc-MNBs. $n = 5$, 2-way ANOVA statistical analysis, Dunnett's multiple comparison test for statistical hypothesis testing. p-value: * <0.05 , ** <0.01 , *** <0.001 , **** <0.0001

Delivery and effect of D-p9 adducted BAPc-MNBs and BAPCs in tumor bearing mice.

Mice injected with B16F10 tumor cells were treated with D-p9 conjugated BAPc-MNBs and BAPCs. The tumor growth curve generated based on the tumor volume recorded for days 1 to 10 demonstrated the effect of D-p9 on tumor growth and indirectly, the efficiency of BAPc-MNBs and BAPCs in delivering D-p9. D-p9 did not reduce tumor growth significantly in comparison to the saline control when delivered using BAPc-MNBs and BAPCs or in the unconjugated form. (**Figure 4.5A, B**) Ex-vivo tumor volume analysis on Day 10 further show that BAPc-MNBs and BAPCs conjugated D-p9 as well as D-p9 alone was not successful in reducing the tumor growth. (**Figure 4.5C**) However, BAPc-MNBs injected on Day 3 after tumor injection seemingly reduced tumor growth in comparison to the saline control (p -value = 0.0964) (**Figure 4.5C, E**). Some NPs by themselves may have an anti-tumor effect due to their potential to polarize tumor associated macrophages to assume M1 phenotype i.e. be pro-inflammatory and thus, reduce tumor growth.^{33, 34} Thus, BAPc-MNBs may help in alleviating tumor growth when delivered in conjunction with anti-tumorigenic therapeutics due to their observed effect on the melanoma tumor growth by themselves.

The effect of D-p9 treatments was not consistent and varied extensively, as also observed in the ex-vivo tumor visualizations. (**Figure 4.5D, E**) The tumor growth analysis curve did not provide conclusive data due to large deviations in the tumor volume observed. (**Figure D.2**) D-p9 did not reduce tumor growth when delivered in the unconjugated form i.e. only the peptide or using BAPc-MNBs and BAPCs as delivery vehicles. (**Figure 4.5**) Instead, BAPc-MNBs + D-p9 significantly increased tumor growth. Experiments conducted to study the function of D-p9 demonstrated its inability to prevent endothelial cell migration in the wound assay. Further

analysis using D-p9 peptide recleaved in the strong trifluoroacetic acid seemed to marginally improve their function. Thus, this demonstrated that the D-p9 delivered to mice contained uncleaved protecting groups on the peptide which inhibited their function. Besides, D-p9 may have not worked since the R-groups are misaligned in comparison to the L-peptide and that is why the retro-D sequence (RD-p9) should be used instead. Therefore, future experiments will help ascertain the potential of BAPc-MNBs and BAPCs in delivering functionally stable RD-p9.

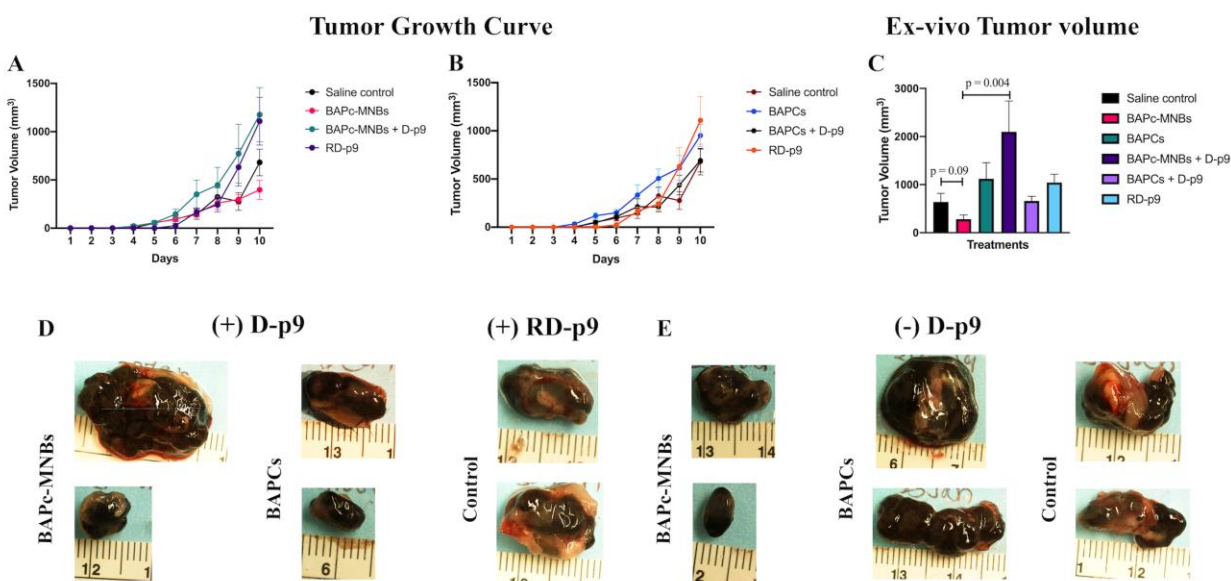


Figure 4.5. Delivery of D-p9 peptide using BAPc-MNBs and BAPCs as delivery systems.

Tumor growth was monitored and recorded from Day 1 after B16F10 cells injection to Day 10, before harvesting the tumor. The growth of tumor in mice treated with BAPc-MNBs + D-p9 and controls (A), BAPCs + D-p9 and controls (B) on Day 3 of tumor injection is expressed as the tumor volume. The tumor volume measured ex-vivo (C) after extraction on Day 10 demonstrates the effect of different treatments on tumor growth in mice. The ex-vivo tumor images captured for mice treated with (D) and without D-p9 (E), conjugated to BAPc-MNBs, BAPCs or unconjugated.

Effect of BAPc-MNBs on the tumor microenvironment.

The effect of BAPc-MNBs administered to tumor bearing mice was determined by analyzing the tumor secretions for secreted cytokines and chemokines. Significant increase in IL-1 β was observed in mice treated with 1×10^{11} BAPc-MNBs for 24 h (Figure 4.6A) while no

significant IL-1 β secretions were detected for other treatments. IL-10 was significantly reduced 48 h after 1×10^{11} BAPc-MNBs injection (**Figure 4.6B**). No significant changes were observed in the levels of KC, MCP-1, MIP-2, RANTES and TNF- α secreted by the tumor in response to treatment with different doses of BAPc-MNBs for 24 h and 48 h. Analysis of tumor secretions from mice treated on day 3 with and without D-p9 conjugated variants does not show any significant difference in cytokines secreted per mg of tumor. (**Figure 4.6F**)

IL-1 β is an inflammatory cytokine that promotes tumor metastasis and growth while IL-10 is anti-inflammatory cytokine which polarizes the tumor associated macrophages (TAMs) to assume M2 phenotype.³⁵ Thus, BAPc-MNBs can aid in reducing tumor growth via the effect on TAMs by reducing the anti-inflammatory cytokine, may promote tumor growth due to increased IL-1 β or may have neutral effect due to antagonizing effect of the cytokines secreted.

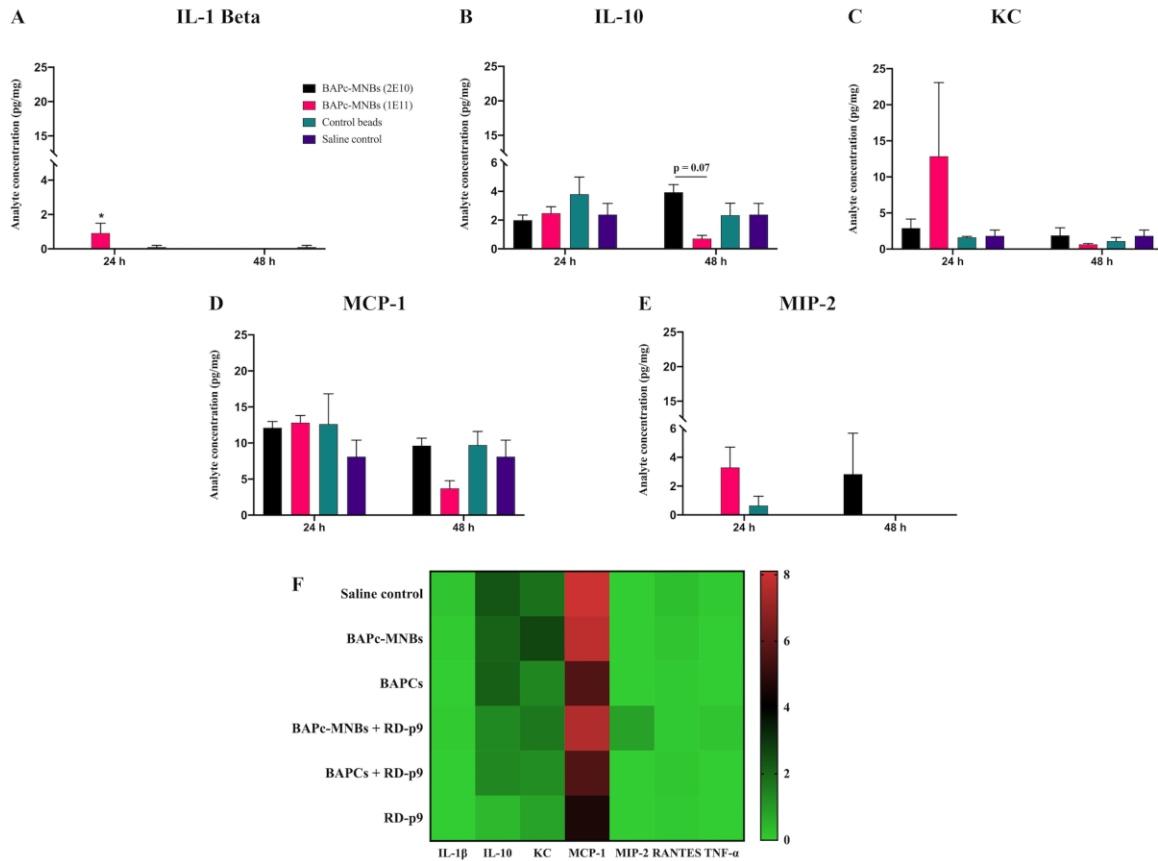


Figure 4.6. Effect of different treatments on the tumor microenvironment

(A) IL-1 β , (B) IL-10, (C) KC, (D) MCP-1 and (E) MIP-2, cytokines secreted by tumors in response to treatment of C57BL/6 mice with low and high doses of BAPc-MNBs for 24 h to 48 h. (F) Heat map of the cytokines levels in the tumor secretions of mice treated with D-p9 conjugated BAPc-MNBs and BAPCs and other controls

Conclusion

BAPc-MNBs were distributed widely to various organs when injected i.v. in C57BL/6 mice and were cleared from circulation within 24 h of administration. Some BAPc-MNBs were eliminated from the system via the intestines. Spleen was found to accumulate the highest amount of BAPc-MNBs in BALB/c and C57BL/6 mice. BAPc-MNBs may aid in tumor growth reduction. Although, melanoma tumor growth reducing peptide, D-p9, did not function as expected, future studies will help discern the effect of BAPc-MNBs and BAPCs conjugated D-p9

or RD-p9. Thus, BAPc-MNBs may be suitable agents that can be used for delivering therapeutic molecules via parenteral administration routes.

References

1. Natarajan, P.; Roberts, J. D.; Kunte, N.; Hunter, W. B.; Fleming, S. D.; Tomich, J. M.; Avila, L. A., A Study of the Cellular Uptake of Magnetic Branched Amphiphilic Peptide Capsules. *Mol Pharm* 2020. <https://doi.org/10.1021/acs.molpharmaceut.0c00393>.
2. Gaharwar, U. S.; Meena, R.; Rajamani, P., Biodistribution, Clearance And Morphological Alterations Of Intravenously Administered Iron Oxide Nanoparticles In Male Wistar Rats. *Int J Nanomedicine* 2019, 14, 9677-9692. <https://doi.org/10.2147/IJN.S223142>.
3. Feng, Q.; Liu, Y.; Huang, J.; Chen, K.; Xiao, K., Uptake, distribution, clearance, and toxicity of iron oxide nanoparticles with different sizes and coatings. *Sci Rep* 2018, 8 (1), 2082. <https://doi.org/10.1038/s41598-018-19628-z>.
4. Watanabe, H.; Numata, K.; Ito, T.; Takagi, K.; Matsukawa, A., Innate immune response in Th1- and Th2-dominant mouse strains. *Shock* 2004, 22 (5), 460-466. <https://doi.org/10.1097/01.shk.0000142249.08135.e9>.
5. Shi, H.; Ebrahim, A.; Berger, E., A Contrast in Pathogenic Responses between C57BL/6J and BALB/cJ Mice Using a Model of Retinal Injury. *American Journal of Pathology* 2018, 188 (12), 2717-2728. <https://doi.org/10.1016/j.ajpath.2018.08.010>.
6. Simovic, S.; Song, Y.; Nann, T.; Desai, T. A., Intestinal absorption of fluorescently labeled nanoparticles. *Nanomedicine* 2015, 11 (5), 1169-78. <https://doi.org/10.1016/j.nano.2015.02.016>.
7. Kyoung, K. S.; Kenichi, S.; Hana, C.; Yu, Y. S.; You, B. H., Oral Nanoparticles Exhibit Specific HighEfficiency Intestinal Uptake and Lymphatic Transport. *ACS Nano* 2018, 12 (9), 7. <https://doi.org/10.1021/acs.nano.8b04315>.
8. Lundquist, P.; Artursson, P., Oral absorption of peptides and nanoparticles across the human intestine: Opportunities, limitations and studies in human tissues. *Adv Drug Deliv Rev* 2016, 106 (Pt B), 256-276. <https://doi.org/10.1016/j.addr.2016.07.007>.
9. Kim, K.; Suzuki, K.; Cho, H.; Youn, Y.; Bae, Y., Oral Nanoparticles Exhibit Specific High-Efficiency Intestinal Uptake and Lymphatic Transport. *ACS Nano* 2018, 12 (9), 8893-8900. <https://doi.org/10.1021/acs.nano.8b04315>.
10. Sukthankar, P.; Avila, L. A.; Whitaker, S. K.; Iwamoto, T.; Morgenstern, A.; Apostolidis, C.; Liu, K.; Hanzlik, R. P.; Dadachova, E.; Tomich, J. M., Branched

- amphiphilic peptide capsules: cellular uptake and retention of encapsulated solutes. *Biochim Biophys Acta* 2014, 1838 (9), 2296-305.
<https://doi.org/10.1016/j.bbamem.2014.02.005>.
11. Gudlur, S.; Sukthankar, P.; Gao, J.; Avila, L. A.; Hiromasa, Y.; Chen, J.; Iwamoto, T.; Tomich, J. M., Peptide nanovesicles formed by the self-assembly of branched amphiphilic peptides. *PLoS One* 2012, 7 (9), e45374.
<https://doi.org/10.1371/journal.pone.0045374>.
 12. Avila, L. A.; Chandrasekar, R.; Wilkinson, K. E.; Balthazor, J.; Heerman, M.; Bechard, J.; Brown, S.; Park, Y.; Dhar, S.; Reeck, G. R.; Tomich, J. M., Delivery of lethal dsRNAs in insect diets by branched amphiphilic peptide capsules. *J Control Release* 2018, 273, 139-146. <https://doi.org/10.1016/j.jconrel.2018.01.010>.
 13. Fallingborg, J., Intraluminal pH of the human gastrointestinal tract. *Danish Medical Bulletin* 1999, 46 (3), 183-196.
 14. Vinokurov, K.; Elpidina, E.; Zhuzhikov, D.; Oppert, B.; Kodrik, D.; Sehnal, F., Digestive proteolysis organization in two closely related tenebrionid beetles: red flour beetle (*tribolium castaneum*) and confused flour beetle (*Tribolium confusum*). *Archives of Insect Biochemistry and Physiology* 2009, 70 (4), 254-279.
<https://doi.org/10.1002/arch.20299>.
 15. Avila, L. A.; Aps, L. R.; Sukthankar, P.; Ploscariu, N.; Gudlur, S.; Šimo, L.; Szoszkiewicz, R.; Park, Y.; Lee, S. Y.; Iwamoto, T.; Ferreira, L. C.; Tomich, J. M., Branched amphiphilic cationic oligopeptides form peptiplexes with DNA: a study of their biophysical properties and transfection efficiency. *Mol Pharm* 2015, 12 (3), 706-15.
<https://doi.org/10.1021/mp500524s>.
 16. Avila, L. A.; Aps, L. R. M. M.; Ploscariu, N.; Sukthankar, P.; Guo, R.; Wilkinson, K. E.; Games, P.; Szoszkiewicz, R.; Alves, R. P. S.; Diniz, M. O.; Fang, Y.; Ferreira, L. C. S.; Tomich, J. M., Gene delivery and immunomodulatory effects of plasmid DNA associated with Branched Amphiphilic Peptide Capsules. *J Control Release* 2016, 241, 15-24. <https://doi.org/10.1016/j.jconrel.2016.08.042>.
 17. Pope, M. R.; Bukovnik, U.; Tomich, J. M.; Fleming, S. D., Small β 2-glycoprotein I peptides protect from intestinal ischemia reperfusion injury. *J Immunol* 2012, 189 (10), 5047-56. <https://doi.org/10.4049/jimmunol.1200290>.
 18. Fleming, S. D.; Pope, M. R.; Hoffman, S. M.; Moses, T.; Bukovnik, U.; Tomich, J. M.; Wagner, L. M.; Woods, K. M., Domain V peptides inhibit beta2-glycoprotein I-mediated mesenteric ischemia/reperfusion-induced tissue damage and inflammation. *J Immunol* 2010, 185 (10), 6168-78. <https://doi.org/10.4049/jimmunol.1002520>.
 19. McDonnell, T.; Wincup, C.; Buchholz, I.; Pericleous, C.; Giles, I.; Ripoll, V.; Cohen, H.; Delcea, M.; Rahman, A., The role of beta-2-glycoprotein I in health and disease associating structure with function: More than just APS. *Blood Reviews* 2020, 39.
<https://doi.org/10.1016/j.blre.2019.100610>.

20. Agar, C.; van Os, G. M.; Mörgelin, M.; Sprenger, R. R.; Marquart, J. A.; Urbanus, R. T.; Derksen, R. H.; Meijers, J. C.; de Groot, P. G., Beta2-glycoprotein I can exist in 2 conformations: implications for our understanding of the antiphospholipid syndrome. *Blood* 2010, 116 (8), 1336-43. <https://doi.org/10.1182/blood-2009-12-260976>.
21. Gropp, K.; Weber, N.; Reuter, M.; Micklisch, S.; Kopka, I.; Hallstrom, T.; Skerka, C., beta(2)-glycoprotein I, the major target in antiphospholipid syndrome, is a special human complement regulator. *Blood* 2011, 118 (10), 2774-2783. <https://doi.org/10.1182/blood-2011-02-339564>.
22. Cook, M. J., *The anatomy of the laboratory mouse*. Elsevier: Jackson Laboratories, Bar Harbor, Maine, 2005.
23. Cesta, M., Normal structure, function, and histology of the spleen. *Toxicologic Pathology* 2006, 34 (5), 455-465. <https://doi.org/10.1080/01926230600867743>.
24. Cataldi, M.; Vigliotti, C.; Mosca, T.; Cammarota, M.; Capone, D., Emerging Role of the Spleen in the Pharmacokinetics of Monoclonal Antibodies, Nanoparticles and Exosomes. *International Journal of Molecular Sciences* 2017, 18 (6). <https://doi.org/10.3390/ijms18061249>.
25. Blanco, E.; Shen, H.; Ferrari, M., Principles of nanoparticle design for overcoming biological barriers to drug delivery. *Nature Biotechnology* 2015, 33 (9), 941-951. <https://doi.org/10.1038/nbt.3330>.
26. Hedayati, M.; Abubaker-Sharif, B.; Khattab, M.; Razavi, A.; Mohammed, I.; Nejad, A.; Wabler, M.; Zhou, H.; Mihalic, J.; Gruettner, C.; DeWeese, T.; Ivkov, R., An optimised spectrophotometric assay for convenient and accurate quantitation of intracellular iron from iron oxide nanoparticles. *Int J Hyperthermia* 2018, 34 (4), 373-381. <https://doi.org/10.1080/02656736.2017.1354403>.
27. Dreifuss, T.; Ben-Gal, T.; Shamalov, K.; Weiss, A.; Jacob, A.; Sadan, T.; Motiei, M.; Popovtzer, R., Uptake mechanism of metabolic-targeted gold nanoparticles. *Nanomedicine* 2018, 13 (13), 1535-1549. <https://doi.org/10.2217/nnm-2018-0022>.
28. Meng, F.; Wang, J.; Ping, Q.; Yeo, Y., Quantitative Assessment of Nanoparticle Biodistribution by Fluorescence Imaging, Revisited. *ACS Nano* 2018, 12 (7), 6458-6468. <https://doi.org/10.1021/acsnano.8b02881>.
29. De Jong, W.; Hagens, W.; Krystek, P.; Burger, M.; Sips, A.; Geertsma, R., Particle size-dependent organ distribution of gold nanoparticles after intravenous administration. *Biomaterials* 2008, 29 (12), 1912-1919. <https://doi.org/10.1016/j.biomaterials.2007.12.037>.
30. Li, J.; Dawson, P., Animal models to study bile acid metabolism. *Biochimica Et Biophysica Acta-Molecular Basis of Disease* 2019, 1865 (5), 895-911. <https://doi.org/10.1016/j.bbadis.2018.05.011>.

31. Kai, M.; Brighton, H.; Fromen, C.; Shen, T.; Luft, J.; Luft, Y.; Keeler, A.; Robbins, G.; Ting, J.; Zamboni, W.; Bear, J.; DeSimone, J., Tumor Presence Induces Global Immune Changes and Enhances Nanoparticle Clearance. *ACS Nano* 2016, 10 (1), 861-870. <https://doi.org/10.1021/acsnano.5b05999>.
32. Lee, G.; Han, S.; Inocencio, I.; Cao, E.; Hong, J.; Phillips, A.; Windsor, J.; Porter, C.; Trevaskis, N., Lymphatic Uptake of Liposomes after Intraperitoneal Administration Primarily Occurs via the Diaphragmatic Lymphatics and is Dependent on Liposome Surface Properties. *Molecular Pharmaceutics* 2019, 16 (12), 4987-4999. <https://doi.org/10.1021/acs.molpharmaceut.9b00855>.
33. Korangath, P.; Barnett, J. D.; Sharma, A.; Henderson, E. T.; Stewart, J.; Yu, S.-H.; Kandala, S. K.; Yang, C.-T.; Caserto, J. S.; Hedayati, M.; Armstrong, T. D.; Jaffee, E.; Gruettner, C.; Zhou, X. C.; Fu, W.; Hu, C.; Sukumar, S.; Simons, B. W.; Ivkov, R., Nanoparticle interactions with immune cells dominate tumor retention and induce T cell-mediated tumor suppression in models of breast cancer. *Science Advances* 2020, 6 (13), 1601. <https://doi.org/10.1126/sciadv.aay1601>.
34. Zanganeh, S.; Hutter, G.; Spitler, R.; Lenkov, O.; Mahmoudi, M.; Shaw, A.; Pajarinen, J.; Nejadnik, H.; Goodman, S.; Moseley, M.; Coussens, L.; Daldrup-Link, H., Iron oxide nanoparticles inhibit tumour growth by inducing pro-inflammatory macrophage polarization in tumour tissues. *Nature Nanotechnology* 2016, 11 (11), 986-994. <https://doi.org/10.1038/NNANO.2016.168>.
35. Mantovani, A.; Barajon, I.; Garlanda, C., IL-1 and IL-1 regulatory pathways in cancer progression and therapy. *Immunological Reviews* 2018, 281 (1), 57-61. <https://doi.org/10.1111/imr.12614>.

Chapter 5 - Conclusions and future directions

Branched amphiphilic peptides capsules (BAPCs) are a relatively new (i.e. about a decade old) peptide-based delivery system. Their physiochemical properties have been studied to date using experimental, biophysical and biocomputational techniques to understand the nature of and interaction between the peptides forming the bilayer, which confers them with unique properties.¹⁻⁴ BAPCs are stable at high temperatures, resistant to most proteinases and have a long shelf-life either dry or in solution. Water molecules are able to cross the peptide bilayer spontaneously unlike salts/ions which gives BAPCs filter-like properties.⁵ The unusual stability may also stem from their ability to contract and expand in environments with different osmotic pressure. Recent studies demonstrate that BAPCs can be degraded by a common soil fungus suggesting that BAPCs do not pose an environmental hazard.⁶ BAPCs do not denature to release the encapsulated contents in mammalian cells and this property has been used to the advantage to carry radionuclides for tumor therapy.² All together, branched amphiphilic peptides have unique properties which is being exploited further to develop a successful delivery system. Current studies are aimed at acquiring fundamental knowledge about BAPCs as well as developing and discovering applications for which they are best suited.

Substituting the water-filled core of BAPCs with a metallic gold or iron oxide core provides added functionality to BAPCs. As a part of this doctoral project I have developed BAP-AuNPs and BAPc-MNBs which are ~7.5 nm and ~50nm in size, respectively. They can be used as imaging probes and the BAPc-MNBs can also be used for magnetic sorting and quantification.^{7, 8} BAPc-MNBs are readily internalized by mammalian cells and have been successfully used as quantification tools to probe their cellular uptake routes and subcellular localization. They are not significantly toxic to cells and show dose and time dependent effect on

the immune response, in vitro.⁷ They also serve as useful probes for determining their biodistribution. They are widely distributed in vivo to major organs and are excreted through the intestines. Thus, BAPc-MNBs have served as useful quantitative tools to study the bio-nano interactions of the branched amphiphilic peptides.

Branched amphiphilic peptides capsules (BAPCs) have shown great potential in delivering surface bound nucleic acids (ssRNA, dsDNA, mRNA) and they are being explored for vaccine development.⁹⁻¹¹ As discussed previously, preliminary data suggests that BAPc-MNBs may have adjuvant like properties, further strengthening their use for vaccine development (**Figure 4.6**).¹²⁻¹⁴ Therefore, BAPCs, BAP-AuNPs and BAPc-MNBs can be used for a wide range of applications. But prior to that it is essential to obtain further understanding of their fundamental interactions with the biological system to ensure that they are minimally toxic and to improve their pharmacokinetics. In the following section I discuss further experimentation and future directions for the development of the delivery system.

Future directions

Biocorona composition and impact on the pharmacokinetics and biodistribution.

The binding of biomolecules to the surface of NPs has a major impact on their fate in vitro and in vivo. The binding of endogenous biomolecules in tissues and cells to the surface of the BAPCs promotes alternate interactions with cells and other biomolecules.¹⁵ They cause an increase in the hydrodynamic size of the NPs and most likely decrease original cationic charge which causes a change in their biophysical properties and influences their biodistribution.¹⁶ The corona formed may consist of proteins, carbohydrates, lipids, nucleic acids and other salts. The biocorona consists of two parts – the hard corona which is composed of molecules that bind

irreversibly to their surface and the soft corona which includes molecules binding reversibly to the hard corona, thus forming a dynamic system explained by the Vroman effect.¹⁵ Albumin binding to NPs has been observed to reduce the NPs uptake by phagocytic and non-phagocytic cells while in some cases the unfolding of albumin by certain NPs exposes epitopes which leads to their recognition by scavenger receptors and uptake by the macrophages.¹⁷ This is an example of how the binding of proteins can impact NPs cellular uptake.

By identifying the components of the biocorona on BAPc-MNBs we can deduce the mechanism of their cellular uptake and their possible in vivo effects. We can thus make informed modifications to the peptide bilayer to improve their pharmacokinetics. Interspersing PEG groups in the peptide bilayer is an example of a surface modification which might help prolong their circulation time while preserving the properties of the branched amphiphilic peptides. On the other hand, binding of the serum components may also provide protection to the NPs as they may be otherwise marked as endogenous molecules.¹⁷ Serum free cell culture media increases the uptake of the NPs and induces toxicity due to overload of NPs.¹⁸ The reduced uptake of biomolecules coated NPs may be another way of preventing significant cellular toxicity. Hence, studying the biocorona formation on NPs and their composition can be very informative.

Uptake and effect of BAPc-MNBs on primary cells.

As discussed previously, studies in cell lines are a good starting point but studying the effect of NPs on primary cells is essential. Biodistribution data suggests that BAPc-MNBs accumulate in spleen, liver, lungs and heart. Thus, primary dendritic cells, monocytes, Kupffer cells, hepatocytes, alveolar macrophages, lung epithelial cells and cardiomyocytes should be considered for assessing the effects of BAPc-MNBs.

Uptake and toxicity of BAP-AuNPs.

BAP-AuNPs have laid the foundation to the development of metallic nanoparticles with covalently bound branched amphiphilic peptide bilayer. However, one major drawback of BAP-AuNPs is the presence of water-filled BAPCs along with them. BAPCs formed due to the presence of excess peptide form BAPCs in water which is easily washed off using a magnetic separator from BAPc-MNBs solution. However, we still have to find a technique/ method to separate BAP-AuNPs from BAPCs.

Preliminary analysis suggests that BAP-AuNPs do not significantly affect viability of human embryonic kidney cells (HEK293T) when treated with 10^9 to 10^{11} nanoparticles, (**Figure 5.1A**) i.e. BAP-AuNPs did not induce significant cytotoxicity up to $1:10^6$, cells to nanoparticle ratio. The highest dose of BAP-AuNPs used to treat the cells was 10,000-fold higher than BAPc-MNBs, which was the most lethal to the cells i.e. 10^9 BAPc-MNBs and 10^{11} BAP-AuNPs were the highest concentration that did not significantly affect cell viability. Thus, BAP-AuNPs can be used to further study their uptake and applications. Citrate-AuNPs did not affect cell viability at all doses tested and this may be due to reduced uptake of negatively charged nanoparticles by cells in comparison to cationic nanoparticles which are readily taken up by cells in significantly larger numbers.

In another preliminary study, *Triboleum castaenum* larvae were allowed to feed on flour premixed and dried with 10^{10} BAP-AuNPs per mg of flour, from 1 h to 24 h at 8 h intervals. The larvae were sectioned at respective time points and imaged using confocal microscopy at 561 nm. BAP-AuNPs ingested by the larvae showed strong signals at 561 nm and 488 nm band pass. (**Figure 5.1B, D**) While citrate-AuNPs spotted directly on the slide showed strong signal only at 561 nm. (**Figure 5.1C, E**) The shift in surface plasmon resonance of AuNPs observed due to

binding of surface molecules could lead to the differences between the wavelengths at which BAP-AuNPs and citrate-AuNPs scatter light, which is captured for confocal microscopy. Similar observations have been made by Tsai et al.¹⁹ and Thompson et al.²⁰ where they using laser scanning confocal microscopy to capture the light emitted by AuNPs due to their surface plasmon resonance. However, additional controls are required to understand and interpret the observed effects, unambiguously.

These preliminary data suggest that further studies are required to understand the changes in the optical properties of BAP-AuNPs and to study their biological interactions so that they can be used in the future for *in vitro* and *in vivo* applications.

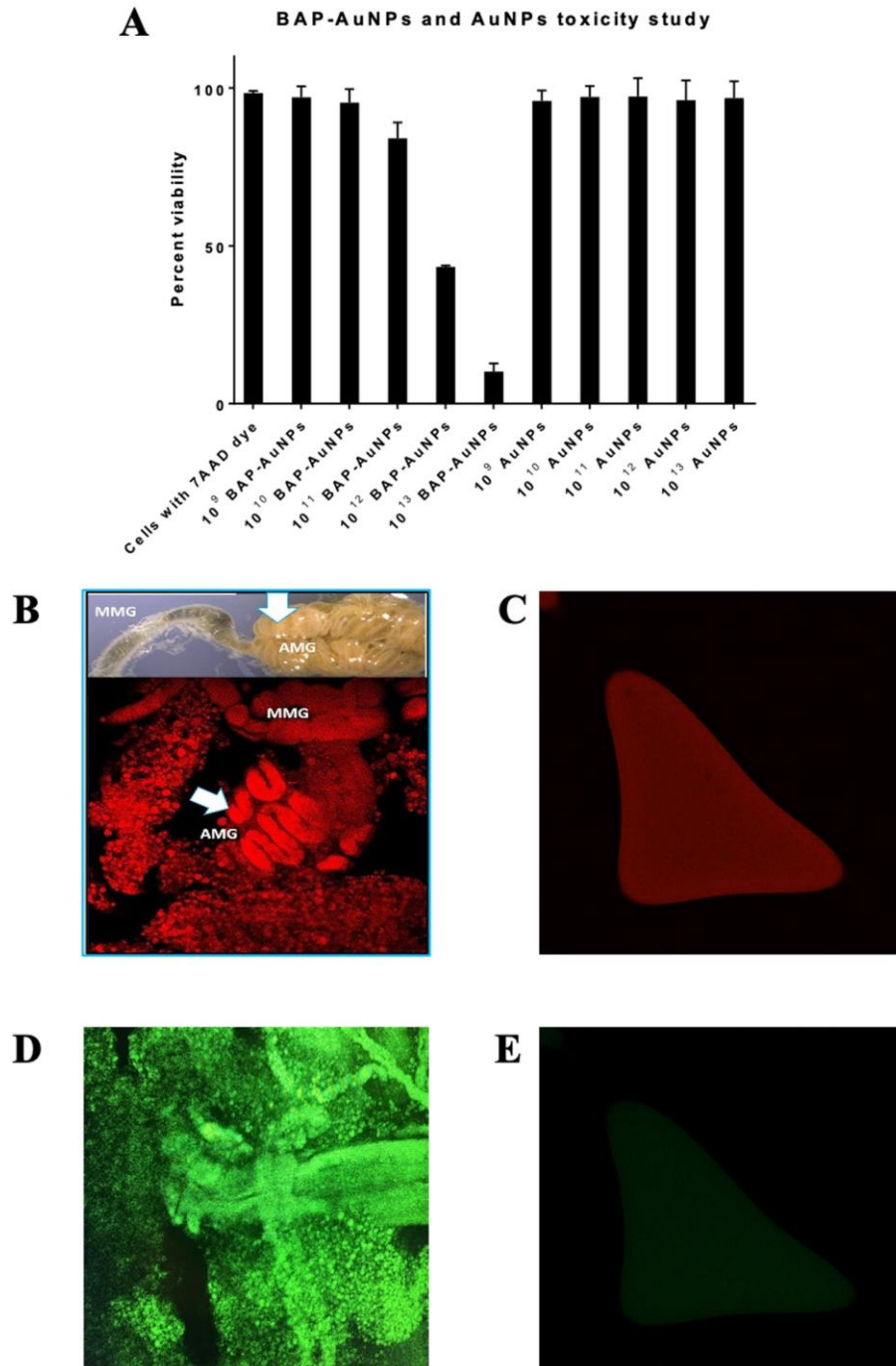


Figure 5.1. Cellular uptake and distribution of BAP-AuNPs

Cell viability of 10^5 HEK293T cells treated with 10^9 to 10^{13} BAP-AuNPs and citrate-AuNPs (no peptides) was determined by flow cytometry analysis using 7AAD dye (**A**). Tissue sections of *Triboleum castaneum* larvae that fed for 16h on flour containing BAP-AuNPs, imaged using Zeiss confocal microscope at 561 nm wavelength narrow band pass (**B**) and 488 nm wavelength band pass (**D**) show intense illumination of middle midgut (MMG) and anterior midgut (AMG) region. BAP-AuNPs are also observed in the surrounding fat bodies. Citrate-AuNPs control show intense signals only at 561 nm (**C**)

but not at 488nm wavelength (**E**). Negative control larvae i.e. larvae feeding on normal flour without gold nanoparticles showed minimal background at the wavelengths used for imaging.

BAPc-MNBs have been used to deliver surface bound peptides for reducing melanoma tumor growth. As discussed earlier, further experimentation using RD-p9 conjugated BAPc-MNBs and BAPCs will help determine whether they are suitable for the effective delivery of the surface bound molecule and in reducing tumor growth. The therapeutic peptide conjugated nanoparticles were administered as a one-time dose on day 3 after subcutaneous injection of the tumor cells. Approximately 1/3rd of the surface exposed peptides i.e. peptides in the outer layer of the branched amphiphilic peptide bilayer were conjugated to the nonameric peptide.

To determine the optimal dose and injection time, it is necessary to test the effect of BAPc-MNBs with different surface coverage of RD-p9, different doses (less than or more than 10¹¹ BAPc-MNBs, as used in the original experiment) and injected on different days i.e. between 1 -10 days after tumor injection. RD-p9 is effective in melanoma tumor reduction when injected on multiple days for e.g. days 3, 5, 7, 9 or days 1-4, 5,7 and 9. We hypothesized that BAPc-MNBs could reduce the number of injections required to effectively reduce tumor growth. Thus, by varying the above-mentioned parameters we can optimize the delivery system to improve the efficiency of RDp9 in reducing melanoma tumor growth with fewer number of injections.

Conclusion

I have primarily worked on developing metallic nanoparticles coated with branched amphiphilic peptides bilayer for use as probes to study the nano-bio interactions of peptide-based delivery system and to expand on their applications. The research presented in this thesis demonstrates that BAPc-MNBs and BAP-AuNPs are useful tools. Conducting further studies to gain a fundamental understanding of the delivery system will aid in increasing the potential of

branched amphiphilic peptides as a nano-delivery system and in other allied biomedical applications.

References

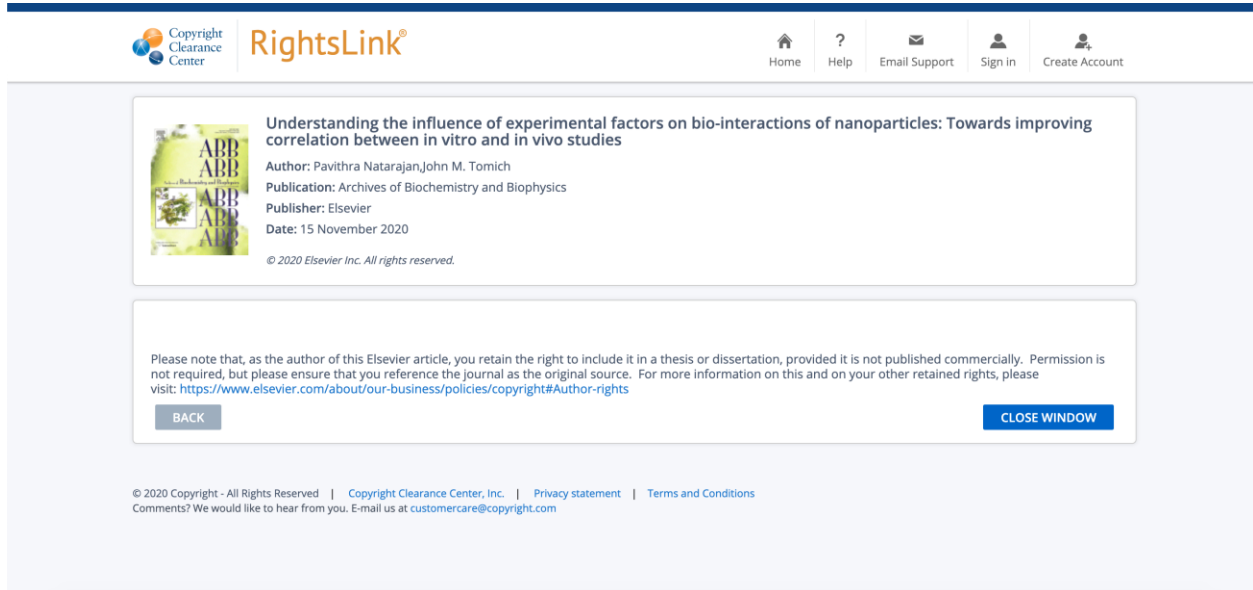
1. Gudlur, S.; Sukthankar, P.; Gao, J.; Avila, L. A.; Hiromasa, Y.; Chen, J.; Iwamoto, T.; Tomich, J. M., Peptide nanovesicles formed by the self-assembly of branched amphiphilic peptides. *PLoS One* 2012, 7 (9), e45374. <https://doi.org/10.1371/journal.pone.0045374>.
2. Sukthankar, P.; Avila, L. A.; Whitaker, S. K.; Iwamoto, T.; Morgenstern, A.; Apostolidis, C.; Liu, K.; Hanzlik, R. P.; Dadachova, E.; Tomich, J. M., Branched amphiphilic peptide capsules: cellular uptake and retention of encapsulated solutes. *Biochim Biophys Acta* 2014, 1838 (9), 2296-305. <https://doi.org/10.1016/j.bbame.2014.02.005>.
3. Sukthankar, P.; Gudlur, S.; Avila, L. A.; Whitaker, S. K.; Katz, B. B.; Hiromasa, Y.; Gao, J.; Thapa, P.; Moore, D.; Iwamoto, T.; Chen, J.; Tomich, J. M., Branched oligopeptides form nanocapsules with lipid vesicle characteristics. *Langmuir* 2013, 29 (47), 14648-54. <https://doi.org/10.1021/la403492n>.
4. Sukthankar, P.; Whitaker, S. K.; Garcia, M.; Herrera, A.; Boatwright, M.; Prakash, O.; Tomich, J. M., Thermally induced conformational transitions in nascent branched amphiphilic peptide capsules. *Langmuir* 2015, 31 (10), 2946-55. <https://doi.org/10.1021/la504381y>.
5. Jia, Z.; Whitaker, S.; Tomich, J.; Chen, J., Organization and Structure of Branched Amphiphilic Oligopeptide Bilayers. *Langmuir* 2016, 32 (38), 9883-9891. <https://doi.org/10.1021/acs.langmuir.6b02421>.
6. Wessel, E.; Tomich, J.; Todd, R., Biodegradable Drug-Delivery Peptide Nanocapsules. *ACS Omega* 2019, 4 (22), 20059-20063. <https://doi.org/10.1021/acsomega.9b03245>.
7. Natarajan, P.; Roberts, J. D.; Kunte, N.; Hunter, W. B.; Fleming, S. D.; Tomich, J. M.; Avila, L. A., A Study of the Cellular Uptake of Magnetic Branched Amphiphilic Peptide Capsules. *Mol Pharm* 2020. <https://doi.org/10.1021/acs.molpharmaceut.0c00393>.
8. Natarajan, P.; Sukthankar, P.; Changstrom, J.; Holland, C. S.; Barry, S.; Hunter, W. B.; Sorensen, C. M.; Tomich, J. M., Synthesis and Characterization of Multifunctional Branched Amphiphilic Peptide Bilayer Conjugated Gold Nanoparticles. *ACS Omega* 2018, 3 (9), 11071-11083. <https://doi.org/10.1021/acsomega.8b01633>.
9. Avila, L. A.; Aps, L. R.; Sukthankar, P.; Ploscariu, N.; Gudlur, S.; Šimo, L.; Szoszkiewicz, R.; Park, Y.; Lee, S. Y.; Iwamoto, T.; Ferreira, L. C.; Tomich, J. M., Branched amphiphilic cationic oligopeptides form peptiplexes with DNA: a study of their

- biophysical properties and transfection efficiency. *Mol Pharm* 2015, 12 (3), 706-15.
<https://doi.org/10.1021/mp500524s>.
10. Avila, L. A.; Aps, L. R. M. M.; Ploscariu, N.; Sukthankar, P.; Guo, R.; Wilkinson, K. E.; Games, P.; Szoszkiewicz, R.; Alves, R. P. S.; Diniz, M. O.; Fang, Y.; Ferreira, L. C. S.; Tomich, J. M., Gene delivery and immunomodulatory effects of plasmid DNA associated with Branched Amphiphilic Peptide Capsules. *J Control Release* 2016, 241, 15-24. <https://doi.org/10.1016/j.jconrel.2016.08.042>.
 11. Avila, L. A.; Chandrasekar, R.; Wilkinson, K. E.; Balthazor, J.; Heerman, M.; Bechard, J.; Brown, S.; Park, Y.; Dhar, S.; Reeck, G. R.; Tomich, J. M., Delivery of lethal dsRNAs in insect diets by branched amphiphilic peptide capsules. *J Control Release* 2018, 273, 139-146. <https://doi.org/10.1016/j.jconrel.2018.01.010>.
 12. Niikura, K.; Matsunaga, T.; Suzuki, T.; Kobayashi, S.; Yamaguchi, H.; Orba, Y.; Kawaguchi, A.; Hasegawa, H.; Kajino, K.; Ninomiya, T.; Ijro, K.; Sawa, H., Gold Nanoparticles as a Vaccine Platform: Influence of Size and Shape on Immunological Responses in Vitro and in Vivo. *ACS Nano* 2013, 7 (5), 3926-3938.
<https://doi.org/10.1021/nn3057005>.
 13. Neto, L.; Zufelato, N.; de Sousa, A.; Trentini, M.; da Costa, A.; Bakuzis, A.; Kipnis, A.; Junqueira-Kipnis, A., Specific T cell induction using iron oxide based nanoparticles as subunit vaccine adjuvant. *Human Vaccines & Immunotherapeutics* 2018, 14 (11), 2786-2801. <https://doi.org/10.1080/21645515.2018.1489192>.
 14. Dykman, L.; Staroverov, S.; Fomin, A.; Khanadeev, V.; Khlebtsov, B.; Bogatyrev, V., Gold nanoparticles as an adjuvant: Influence of size, shape, and technique of combination with CpG on antibody production. *International Immunopharmacology* 2018, 54, 163-168. <https://doi.org/10.1016/j.intimp.2017.11.008>.
 15. Gupta, M.; Roy, I., How Corona Formation Impacts Nanomaterials as Drug Carriers. *Molecular Pharmaceutics* 2019, 17 (3), 725-737.
<https://doi.org/10.1021/acs.molpharmaceut.9b01111>.
 16. Gunnarsson, S.; Bernfur, K.; Englund-Johansson, U.; Johansson, F.; Cedervall, T., Analysis of complexes formed by small gold nanoparticles in low concentration in cell culture media. *Plos One* 2019, 14 (6). <https://doi.org/10.1371/journal.pone.0218211>.
 17. Obst, K.; Yealland, G.; Balzus, B.; Miceli, E.; Dimde, M.; Weise, C.; Eravci, M.; Bodmeier, R.; Haag, R.; Calderon, M.; Charbaji, N.; Hedtrich, S., Protein Corona Formation on Colloidal Polymeric Nanoparticles and Polymeric Nanogels: Impact on Cellular Uptake, Toxicity, Immunogenicity, and Drug Release Properties. *Biomacromolecules* 2017, 18 (6), 1762-1771.
<https://doi.org/10.1021/acs.biomac.7b00158>.
 18. Gunduz, N.; Ceylan, H.; Guler, M.; Tekinay, A., Intracellular Accumulation of Gold Nanoparticles Leads to Inhibition of Macropinocytosis to Reduce the Endoplasmic Reticulum Stress. *Scientific Reports* 2017, 7. <https://doi.org/10.1038/srep40493>.

19. Tsai, S.; Chen, Y.; Liaw, J., Compound cellular imaging of laser scanning confocal microscopy by using gold nanoparticles and dyes. *Sensors* 2008, 8 (4), 2306-2316. <https://doi.org/10.3390/s8042306>.
20. Thompson, K.; Harley, C.; Barthel, G.; Sanders, M.; Mesce, K., Plasmon resonance and the imaging of metal-impregnated neurons with the laser scanning confocal microscope. *Elife* 2015, 4. <https://doi.org/10.7554/eLife.09388>.

Appendix A - Chapter 1


Copyrights permissions



The screenshot displays the RightsLink interface. At the top left, there is a logo for the Copyright Clearance Center and the RightsLink® logo. To the right of these logos is a navigation menu with icons and labels for Home, Help, Email Support, Sign in, and Create Account. The main content area features a white box with a thumbnail of a journal cover on the left and text on the right. The text includes the article title, author names, publication information, and a date. Below this box is a larger white box containing a permissions notice and two buttons: 'BACK' and 'CLOSE WINDOW'. At the bottom of the page, there is a footer with copyright information and contact details.

Copyright Clearance Center RightsLink®

Home Help Email Support Sign in Create Account

 Understanding the influence of experimental factors on bio-interactions of nanoparticles: Towards improving correlation between in vitro and in vivo studies

Author: Pavithra Natarajan, John M. Tomich

Publication: Archives of Biochemistry and Biophysics

Publisher: Elsevier

Date: 15 November 2020

© 2020 Elsevier Inc. All rights reserved.

Please note that, as the author of this Elsevier article, you retain the right to include it in a thesis or dissertation, provided it is not published commercially. Permission is not required, but please ensure that you reference the journal as the original source. For more information on this and on your other retained rights, please visit: <https://www.elsevier.com/about/our-business/policies/copyright#Author-rights>

BACK CLOSE WINDOW

© 2020 Copyright - All Rights Reserved | Copyright Clearance Center, Inc. | Privacy statement | Terms and Conditions
Comments? We would like to hear from you. E-mail us at customer-care@copyright.com

Figure A.1. Copyrights to Chapter 1 from © Elsevier

Supplementary data

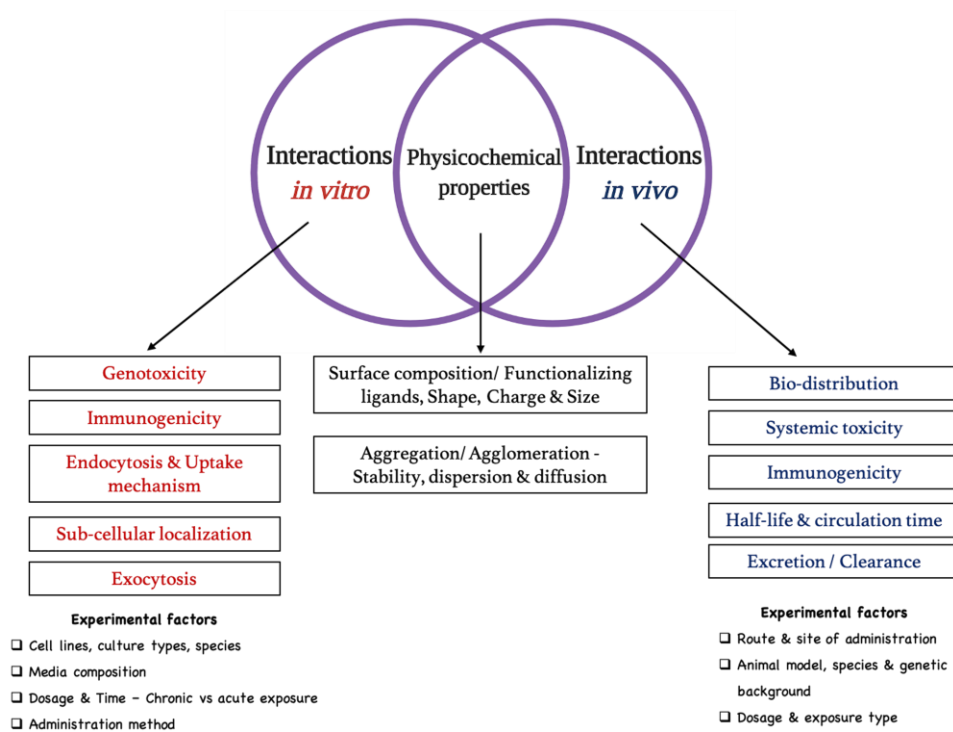


Figure A.2. Interplay between various factors affecting the nano-bio interactions

Appendix B - Chapter 2

Copyrights permissions

Tuesday, June 23, 2020 at 9:12:33 AM Central Daylight Time

Subject: Regarding Incident 3590186 -- Permission to reuse article in thesis -- DOI: 10.1021/acsomega.8b01633
Date: Sunday, June 7, 2020 at 6:06:09 PM Central Daylight Time
From: support@services.acs.org
To: Pavithra Natarajan
Priority: High
Attachments: Image-94605a22caf492830f8cbb45d292f296d983b8453d.png



Dear Pavithra Natarajan,

Your permission requested is granted and there is no fee for this reuse. In your planned reuse, you must cite the A source, add this direct link <https://pubs.acs.org/doi/full/10.1021/acsomega.8b01633>, and include a notice to reac permissions related to the material excerpted should be directed to the ACS.

If you need further assistance, please let me know.

Sincerely,

Raquel Picar-Simpson
ACS Publications Support
Customer Services & Information
Website: <https://help.acs.org/>

Incident Information:

Incident #: 3590186
Date Created: 2020-06-05T20:24:41
Priority: 3
Customer: Pavithra Natarajan
Title: Permission to reuse article in thesis -- DOI: 10.1021/acsomega.8b01633
Description: Hello,

I would like to obtain permission to reuse the entire article - <https://pubs.acs.org/doi/full/10.1021/acsomega.8b01633> for my Ph.D. thesis. I am the ori paper and since it is an author's choice article, I was redirected to email ACS services to ot Kindly advise on this matter.

Thank you,
Pavithra Natarajan

Page 1 of 2

Figure B.1. Copyrights to Chapter 2 from © American Chemical Society (ACS)

Supplementary Data

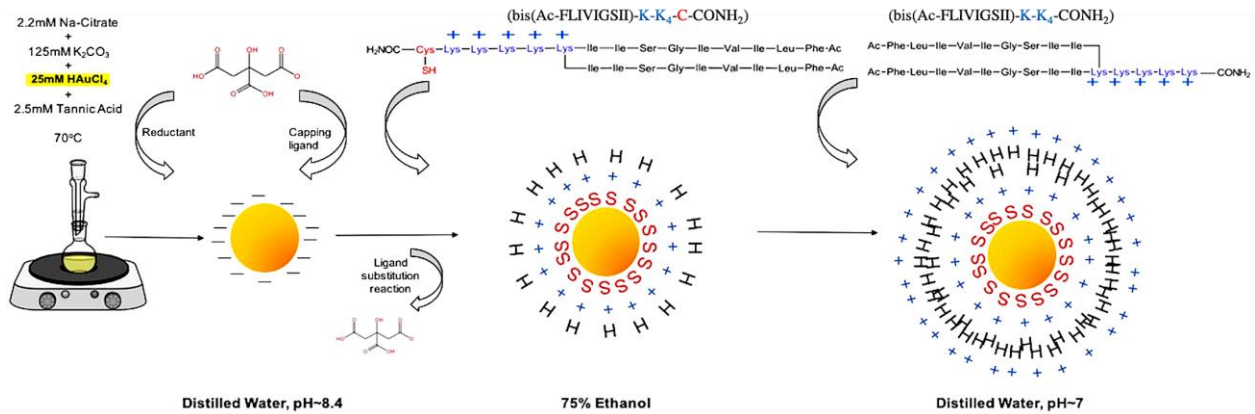


Figure B.2. Schematic model for BAP-AuNP synthesis

The scheme shows the basic principle and procedure leading to the synthesis of BAP bilayer coated AuNPs using the 3.5 nm citrate capped AuNPs synthesized. H represents the hydrophobic tail of the Branched Amphiphilic Peptides, S, the Sulphur atom of the cysteine residue on (bis(Ac-FLIVIGSII)-K-K₄-C-CONH₂), +, the positively charged lysine tail. The diagram is not drawn to scale here.

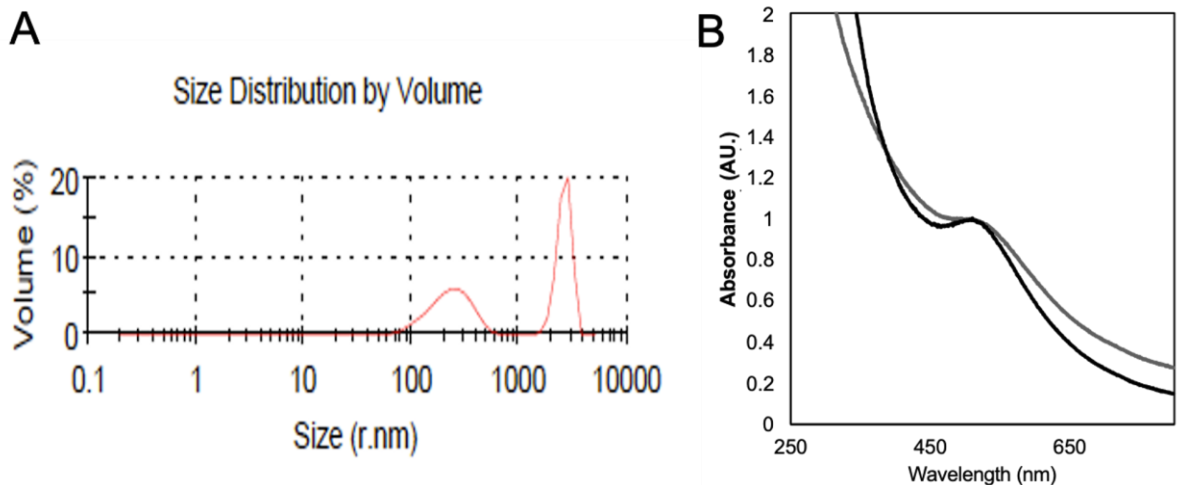


Figure B.3. Dynamic Light Scattering (DLS) data and UV-Vis Spectra for BAP-AuNPs synthesized with TFA salts containing peptides

(A) The DLS plot for size distribution (% by volume) of BAP-AuNPs prepared with TFA salts containing peptides shows large aggregates in the size range of 100 - 2000 nm. The table below (**Table B.1**) summarizes the measured parameters using DLS including the PDI and size distribution as per intensity. (B) UV-Vis spectra for BAP-AuNPs in DDI water with TFA salts containing peptides (Grey curve) and HCl washed peptides (Black). The peptides with TFA salts cause aggregation leading to a broad peak with high absorbance in the 600 - 800 nm region.

Table B.1. Summary of Gold Nanoparticle properties determined using DLS

Parameters	Values
Polydispersity Index (PDI)	0.275
Size (95% by Intensity)	199.4nm
Size (4.9% by Intensity)	2511nm
Z-Average	195nm

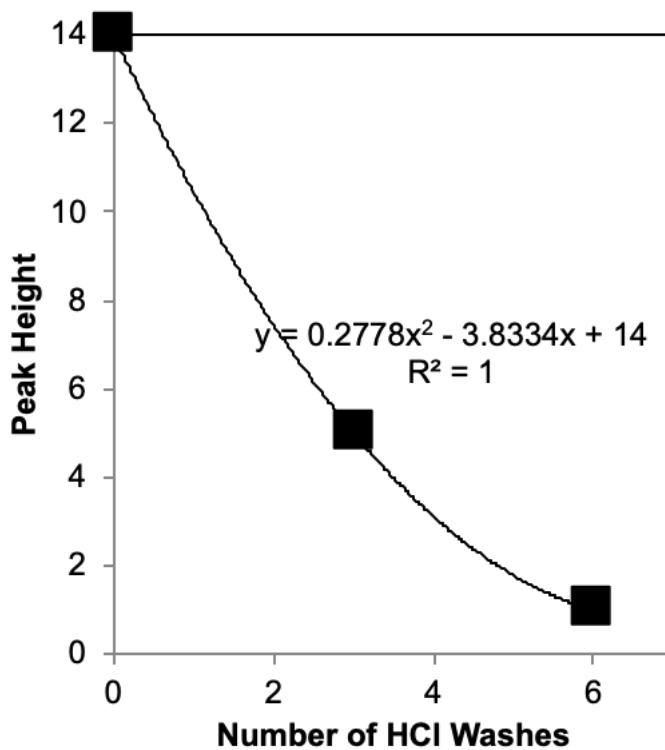


Figure B.4. NMR data for removal of TFA salts from peptides

The graph represents a decrease in the peak height for ^{19}F signal intensity as the number of washes increases.

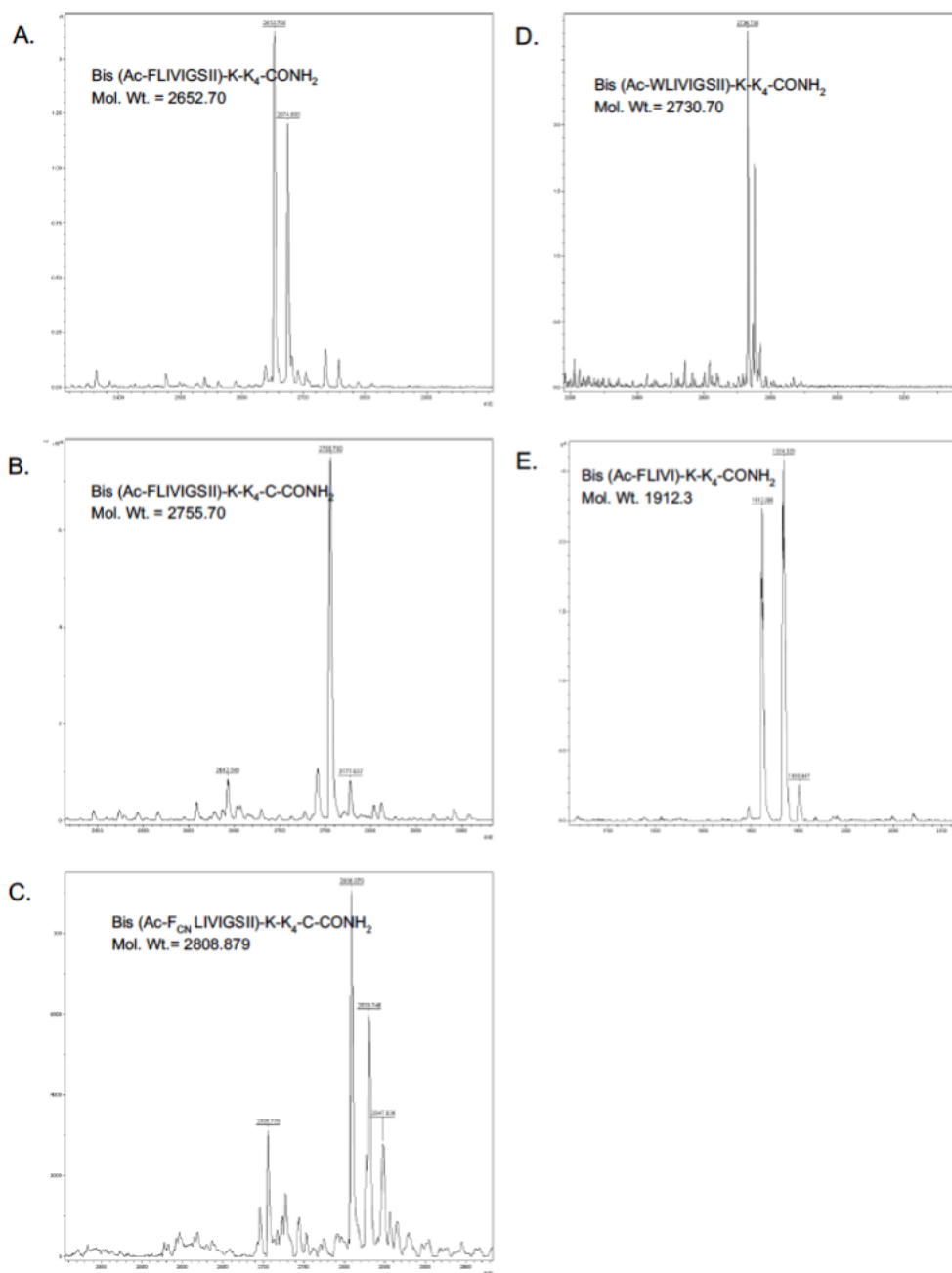


Figure B.5. MALDI-TOF mass spectra of peptides

The mass spectra for all peptides used in the study and synthesized by solid phase peptide synthesis have been shown above. Their molecular weight and amino acid sequence has been displayed inset each spectrum- **(A)** Bis (Ac- FLIVIGSII)-K-K₄-CONH₂, **(B)** Bis (Ac-FLIVIGSII)-K-K₄ -C-CONH₂ **(C)** Bis (Ac-F_{CN} LIVIGSII)-K-K₄ -C-CONH₂ **(D)** Bis (Ac-WLIVIGSII)-K-K₄-CONH₂ **(E)** Bis (Ac-FLIVI)-K-K₄ -CONH₂. The higher molecular weight peaks i.e molecular weight of peptide +22 and/or +39, in the mass spectra represent the sodium and potassium salts of the peptides, respectively.

Appendix C - Chapter 3

Copyright Permission

6/5/2020

Rightslink® by Copyright Clearance Center



RightsLink®



Home



Help



Email Support



Pavithra Natarajan ▾

A Study of the Cellular Uptake of Magnetic Branched Amphiphilic Peptide Capsules



Author: Pavithra Natarajan, Jonathan D. Roberts, Nitish Kunte, et al

Publication: Molecular Pharmaceutics

Publisher: American Chemical Society

Date: Jun 1, 2020

Copyright © 2020, American Chemical Society

PERMISSION/LICENSE IS GRANTED FOR YOUR ORDER AT NO CHARGE

This type of permission/license, instead of the standard Terms & Conditions, is sent to you because no fee is being charged for your order. Please note the following:

- Permission is granted for your request in both print and electronic formats, and translations.
- If figures and/or tables were requested, they may be adapted or used in part.
- Please print this page for your records and send a copy of it to your publisher/graduate school.
- Appropriate credit for the requested material should be given as follows: "Reprinted (adapted) with permission from (COMPLETE REFERENCE CITATION). Copyright (YEAR) American Chemical Society." Insert appropriate information in place of the capitalized words.
- One-time permission is granted only for the use specified in your request. No additional uses are granted (such as derivative works or other editions). For any other uses, please submit a new request.

[BACK](#)

[CLOSE WINDOW](#)

© 2020 Copyright - All Rights Reserved | [Copyright Clearance Center, Inc.](#) | [Privacy statement](#) | [Terms and Conditions](#)
Comments? We would like to hear from you. E-mail us at customer@copyright.com

Figure C.1. Copyright permission for Chapter 3 from © American Chemical Society (ACS)

Supplemental Data

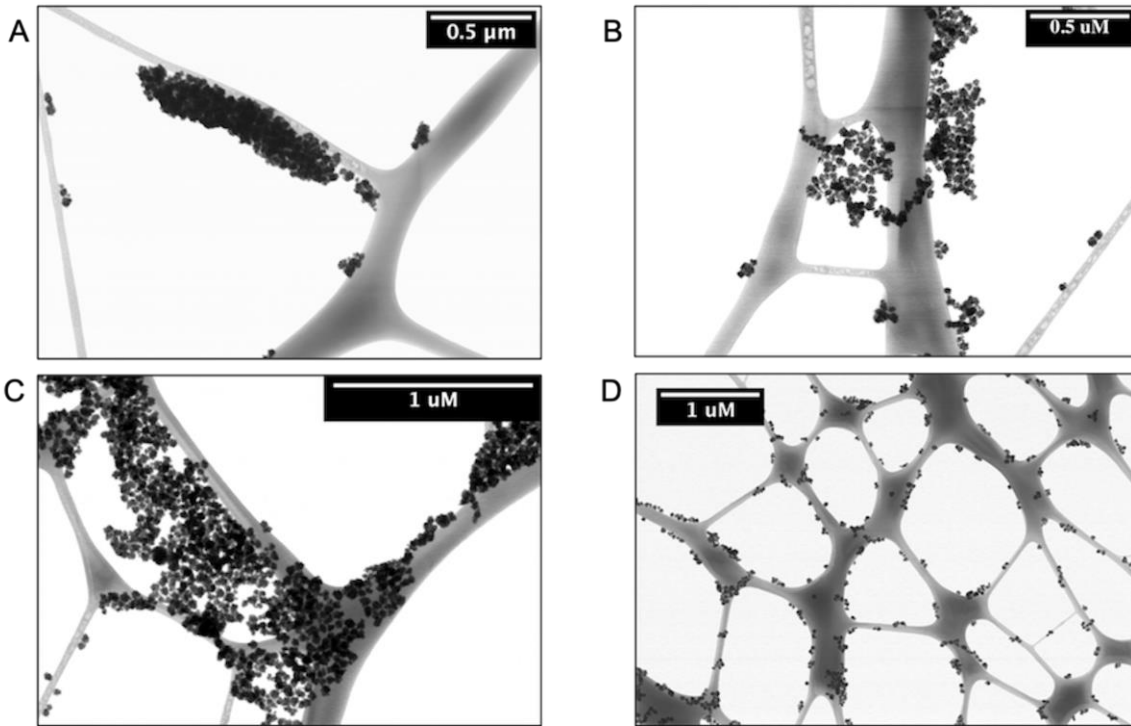


Figure C.2. TEM images of aggregates of BAPc-MNBs

Aggregates sorted on magnetic separator at different times- (A) 3min, (B) 10min, (C) 30min and (D) 60min. The images are of the nanoparticles that were bound to the magnet at the specific time points mentioned before. The density of the aggregated nanoparticles gradually decreases with time. Separation of aggregates using this technique gives well dispersed BAPc-MNBs solution with very few aggregates, as seen in (D).

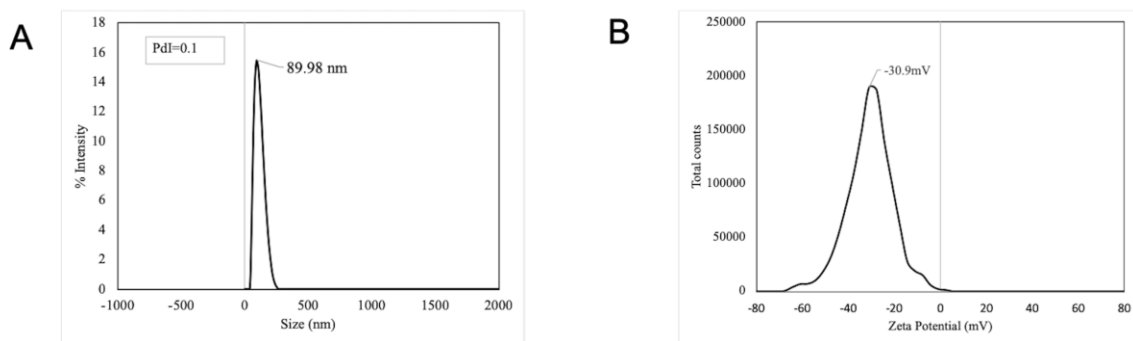


Figure C.3. Dynamic light scattering and zeta potential analysis of 50nm MNBs

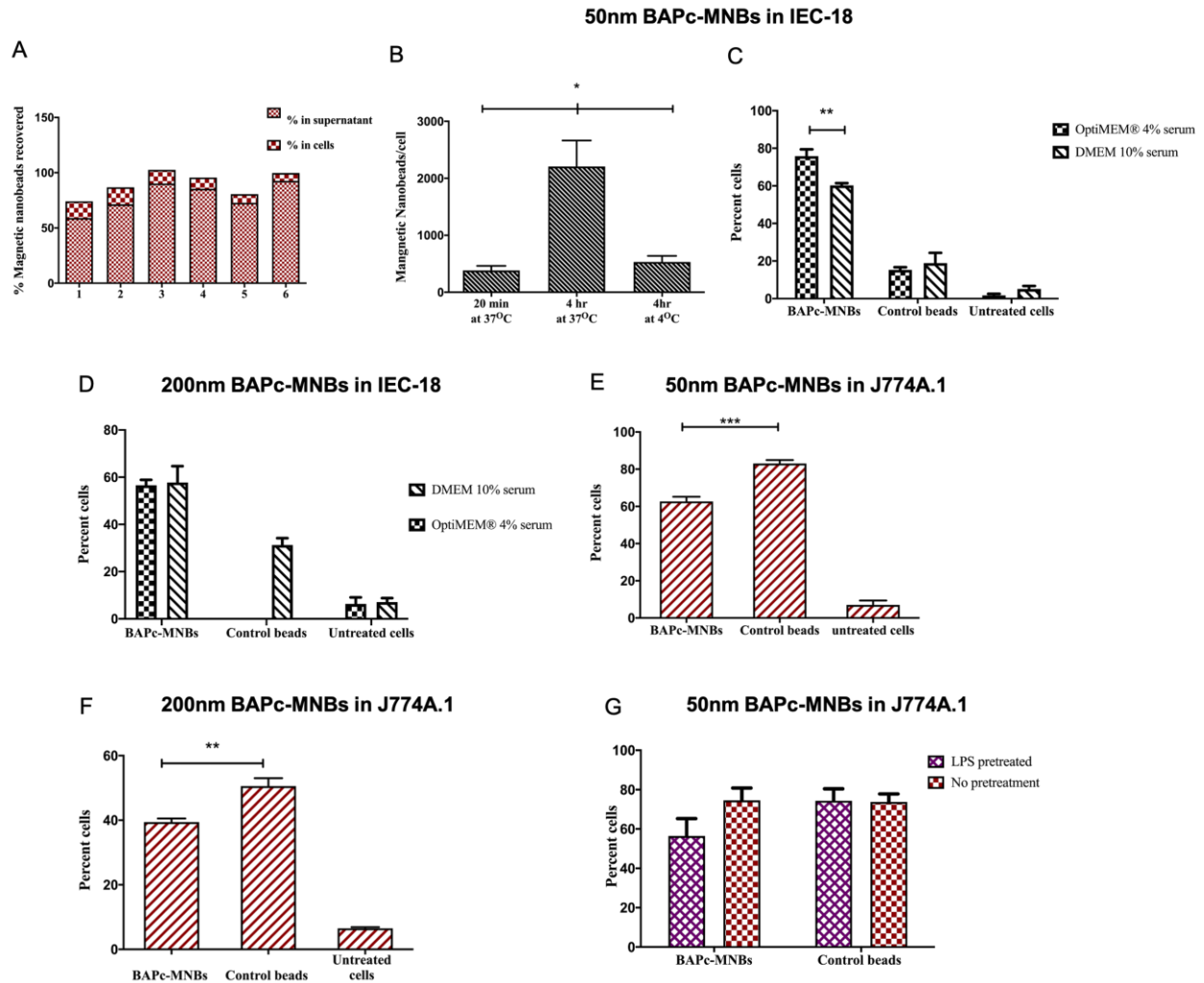


Figure C.4. Efficiency of cell sorting using a magnetic separator

(A) The total magnetic nanobeads recovered, determined by adding the amount of beads detected in cells and the beads in cell culture supernatants of J774A.1 cells, shows that ~80%- 100% of the beads added were recovered/detected using the ferene-s assay. (B) IEC-18 cells treated with BAPc-MNBs at 3 different temperature and time combinations shows that the optimal conditions for the uptake of BAPc-MNBs is for 4 h at 37°C in normal cell culture media. As expected barely any nanoparticles were taken up within 20min incubation at physiological temperature or in 4 h at 4°C. (C),(D),(E),(F)&(G) Percentage of cells sorted based upon the uptake of the magnetic nanobeads for different treatments and cell types.

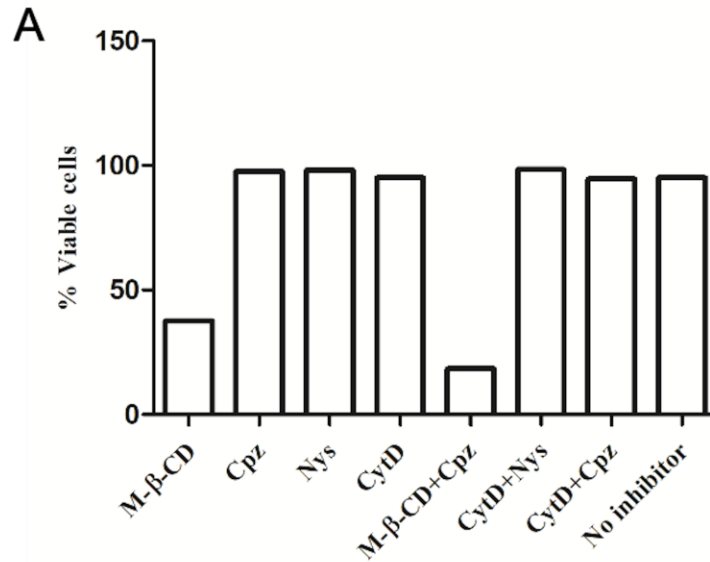


Figure C.5. Effect on cell viability after inhibitor treatment

The viability of IEC-18 cells was not affected significantly when treated with most inhibitors except when treated with 10mM M-β-CD and 10mM M-β-CD+10μM Cpz. The concentration was reduced to 5mM for M-β-CD which did not affect the viability. The rest of concentrations tested were: Cpz (20 μM), Nystatin (100 μM), Cyt D (8 μM) and dynasore (160 μM)

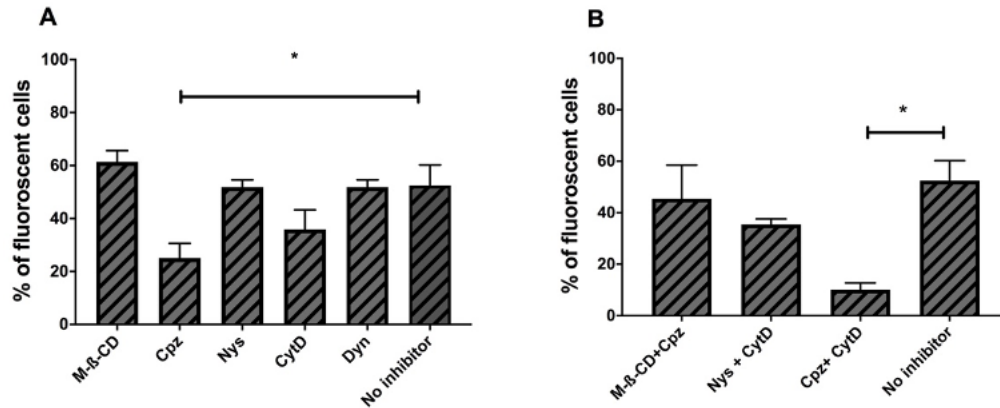


Figure C.6. Effect of inhibitors on uptake of Rh-BAPCs in IEC-18 using flow cytometry analysis

(A), (B) Rh-BAPCs incubated with IEC-18 were analyzed using flow cytometer to determine percentage of cells that have taken up the fluorescent BAPCs. The Rh-BAPCs uptake in IEC-18 was only affected in the presence of Cpz and Cpz+CytD after 4 h of incubation with these inhibitors. ANOVA followed by Bonferroni's posttest was applied for statistical analysis. (ns=not significant, *p-value<0.05, **p-value<0.01, ***p-value<0.001).

	Techniques	Time			
		1h		4h	
		Magnetic Nanobeads Quantification	Confocal Imaging	Magnetic Nanobeads Quantification	Confocal Imaging
Inhibitors	M-β-CD	✗	✓	✓	✗
	Cpz	✗	✓	✗	✓
	Nys	✗	✓	✗	✗
	CytD	✗	✓	✗	✗
	Dyn	✗	✓	✗	✗
	M-β-CD+Cpz	✓	✓	✗	✗
	Cpz+CytD	✓	✓	✗	✓
	Nys+CytD	✓	✓	✗	✗

KEY	
✗	No Inhibitor
✓	High Level inhibitor
✓	Moderate Level inhibitor
✓	Low level inhibitor

Figure C.7. Summary of endocytosis inhibition data for BAPc-MNBs and Rh-BAPCs uptake, obtained using UV/Vis based quantification method and confocal imaging

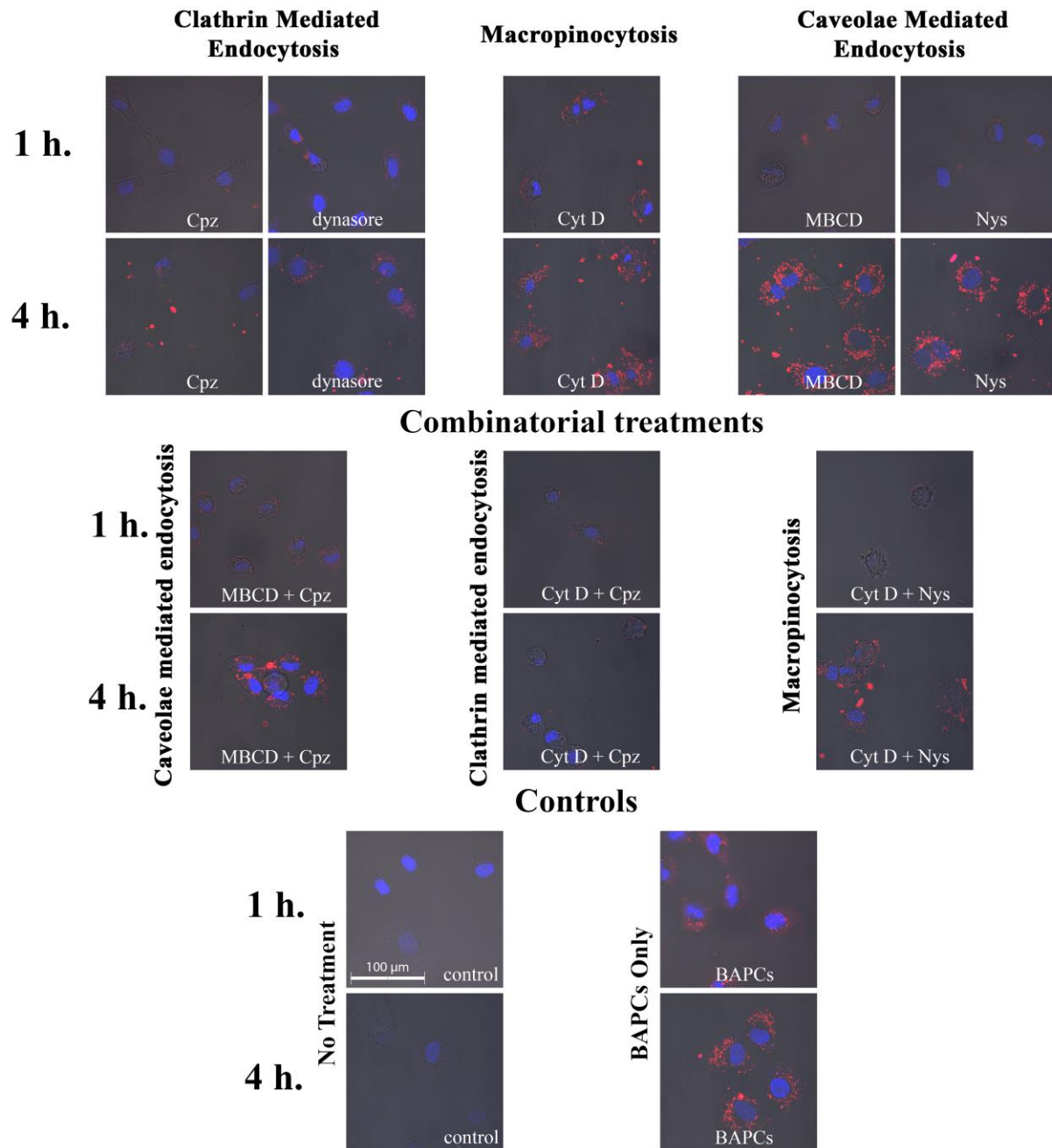


Figure C.8. Brightfield images for endocytosis inhibition assay to determine mechanism of rhodamine labelled BAPCs uptake by IEC-18

IEC-18 cells incubated with rhodamine BAPCs for 1 h. and 4 h. after preincubation with respective inhibitors of endocytosis. Inhibitors used are indicated at the bottom of each micrograph. Control group were cells treated exclusively with saline solution (PBS) and served as a positive control. BAPCs group was not exposed to inhibitors.

A

Treatment	Conc. Of Nitric Oxide released
4hr BAP-MNBs	Not Detectable
4hr MNBs	Not Detectable
4hr Controls	Not Detectable
24hr BAP-MNBs	Not Detectable
24hr MNBs	Not Detectable
24hr Control	Not Detectable
48hr BAP-MNBs	Not Detectable
48hr MNBs	Not Detectable
48hr Control	Not Detectable
LPS (positive control)	0.147 μ M

B

Treatment	Conc. Of Nitric oxide released
20min BAP-MNBs	Not detectable
20min MNBs	Not detectable
20min Controls	Not detectable
4hr BAP-MNBs	Not detectable
4hr MNBs	Not detectable
4hr Controls	Not detectable
24hr BAP-MNBs	Not detectable
24hr MNBs	Not detectable
24hr Control	Not detectable
48hr BAP-MNBs	Not detectable
48hr MNBs	Not detectable
48hr Control	0.264 μ M
LPS (positive control)	0.252 μ M

Figure C.9. Nitric oxide species (NO) released by cells in response to magnetic nanoparticles

Cell supernatants (n=2) collected at different time points and tested using the Griess reagent, shows that the nanoparticles do not induce IEC-18 and J774A.1 to release nitric oxide. Only LPS treated positive controls release NO after 4 h treatments

Appendix D - Chapter 4

Supplemental Data

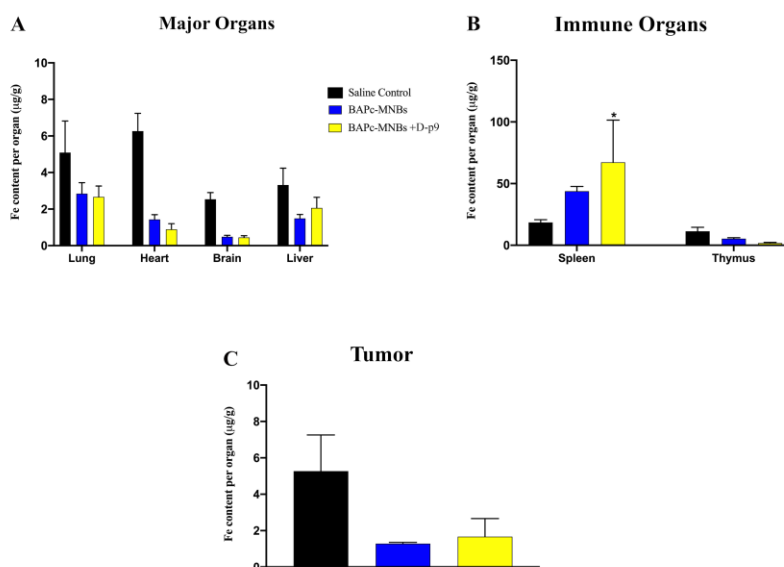


Figure D.1. Tissue distribution of D-p9 conjugated BAPc-MNBs in C57BL/6 mice

Iron content in organs comprising the reticuloendothelial (RES) system (A), immune system (B) and tumor (C) was determined after injecting BAPc-MNBs + D-p9 and BAPc-MNBs only, on Day 3 after tumor cells injection. Organs were harvested on Day 10 for analysis.

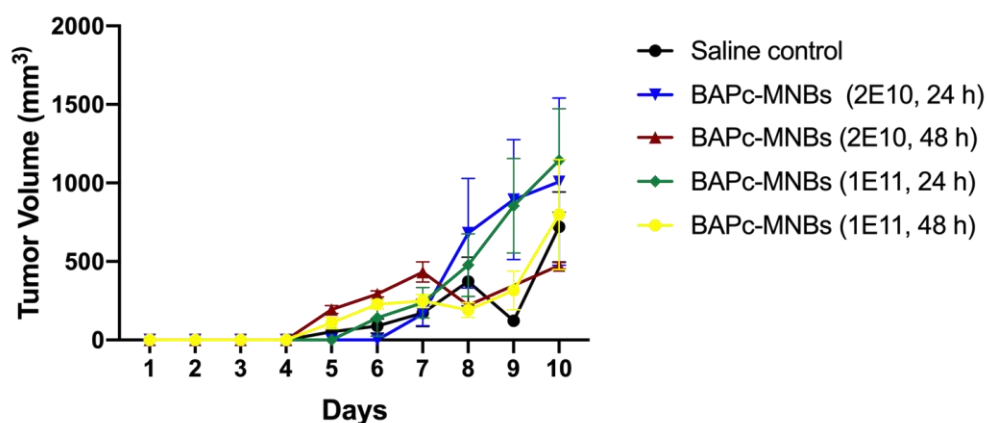


Figure D.2. Tumor growth curve in mice treated with different doses of BAPc-MNBs for 24 h and 48 h

The tumor growth was monitored and recorded from Day 1 after B16F10 tumor cells injection to Day 10, before harvesting the tumor